TOWARD A THEORY OF DIFFUSE ENERGY TRANSPORT IN LARGE IRREGULAR STRUCTURES

BY

NICHOLAS LOWELL WOLFF

DISSERTATION

Submitted in partial fulfillment of the requirements
for the degree of Doctor of Philosophy in Theoretical and Applied Mechanics
in the Graduate College of the
University of Illinois at Urbana-Champaign, 2010

Urbana, Illinois

Doctoral Committee:

Professor Richard L. Weaver, Chair and Director of Research
Associate Professor Jonathan B. Freund
Professor Glaucio H. Paulino
Professor Daniel A. Tortorelli

Abstract

We develop a “concatenation ansatz” of energy flow in large, complex structures to predict the response of a nominally diffusive system. The concatenation ansatz is inspired by statistical energy analysis (SEA) which is, in turn, based on an analogy to diffusive heat transfer. Where in heat transfer, thermal energy flows from areas of hot temperature to those of cold temperature, in SEA vibrational or acoustic energy is assumed to flow from structures or volumes with high energy density to those with low energy density. The word “ansatz” refers to a “starting assumption.” Here we make the ansatz that transport of diffuse vibrational energy over short-time intervals contains all information needed for estimates of energy flow over long times, and that these estimates can be extracted by concatenating successive copies of transport over short-time intervals. Though not based directly on an assumption of diffusion, the ansatz contains the same phase-neglecting principle as SEA and implies a diffusion limit equivalent to SEA.

In this thesis, the concatenation ansatz is tested on various benchmark systems, some typically studied using SEA, other not. We carry out direct numerical simulation (DNS) in the time domain using finite-difference and finite-element methods. We study two- and three-room systems with rooms connected by a window allowing energy to flow between them. We study a torus, a single statistically homogenous structure, which cannot be studied by SEA. We also study plates coupled by springs allowing energy to flow between the plates. This type of system is of interest to the

structures community. Finally, we study an interesting “hybrid” system consisting of two coupled systems. One system would typically be studied statistically in a framework such as SEA. The other system, not satisfying the assumptions of SEA, would typically be studied deterministically in a framework such as finite-element analysis.

Acknowledgments

This work was supported by NSF grants CMS-0201346 and CMS-0528096.

I would like to thank my adviser Prof. Richard L. Weaver. I also thank the other members of my committee: Prof. Jonathan B. Freund, Prof. Glaucio H. Paulino, and Prof Daniel A. Tortorelli.

I thank Prof. Kimberly M. Hill (currently at the University of Minnesota) and Prof. D. Scott Stewart for serving on my preliminary and qualifying exam committees, respectively.

I extend special thanks to Prof. Asan Gani Abdul-Muthalif (currently at the International Islamic University Malaysia) and Prof. Robin S. Langley of the University of Cambridge, UK, for useful discussions during my sojourn there.

Table of Contents

Chapter 1

Introduction

1.1 Background

Statistical energy analysis[1*] (SEA) is a framework that has been used since the 1960s to solve vibration and acoustics problems in large, complex structures and systems. The "brute-force" method of solving such problems is to mesh the geometry and solve the appropriate wave equation by performing direct numerical simulation (DNS), such as the finite-element method (FEM). However, it is well documented in the literature that such methods have both practical and fundamental problems.

Fahy[2] provides some motivation for SEA from an historical viewpoint. He cites an early aerospace project requiring more computational power than what was available at the time. Even though the computational techniques to rigorously determine modes of vibration to carry out DNS to predict response to forcing were available, they were impractical. There was not enough storage to handle the large number of degrees of freedom of the system. In addition, the speed at which computations could be carried out was prohibitively slow. Though computational power continues to grow today, systems can be arbitrarily large in size and can have arbitrary geometric and material complexity to outrun the state-of-the-art in computation.

*References are indicated with a superscript Arabic numeral and are listed at the end of the thesis in the order of appearance in the thesis.

He[2] goes on to note another practical problem with DNS. For example, in room acoustics, the pressure and particle velocity fields are not appropriate measures of response to sources in a room. Even if one can get such detailed local fields using available computational power, they are not effective measures of what one hears. Instead, it is more useful to study the time average of global (spatially averaged) variables such as vibrational or acoustic energy.

Indeed, in early stages of a design, analysts often want or need only a coarse understanding of the behavior of a system. They want to know only how to modify the design to optimize performance. It is a waste of time and effort to obtain detailed results that one cannot understand or will never use.

He[2] details another, more fundamental problem with detailed computation: uncertainty. For prediction, all physical systems must be modeled, and models must make some idealized approximations to reality. It is unavoidable that the precise dynamic properties of any system must be unknown to some degree. Uncertainties are introduced by many aspects of modeling, including from the system itself, such as at boundaries and material properties that get introduced from manufacturing tolerances and imperfections. Uncertainties also arise from outside the system, such as imperfect knowledge of forcing from the environment (temperature, wind, static load) and from the operators of equipment.

Problems with uncertainty are compounded at higher and higher frequencies. At any given frequency, more and more modes contribute to the response as one attempts DNS at higher frequencies.

Hodges and Woodhouse[3] stress the uncertainty in the physical structure, pointing out that modes of vibration become more sensitive to details of the modeling as the frequency increases.

They also recognize that detailed computation of a complex response may not be very illuminating or useful for insights. During early stages of a design process, engineers need a better "feel" for the physics of a system.

Woodhouse[4] gives further insight stating that numerical accuracy diminishes and becomes less reliable as one increases the number of degrees of freedom. This numerical issue is independent of, though certainly related to, the issue of increased uncertainty of system parameters and forcing at small length scales and, thus, high frequency. He also suggests that the variability in the uncertain parameters must itself be studied to gain a full understanding of the sensitivity of the system to those parameters. With computation, the usual way variability is studied is to adjust the uncertain parameters within a presumed range and perform Monte Carlo simulations. The opaqueness of the system behavior becomes more problematic the more variable parameters there are.

We offer one specific example of parameter uncertainties. Kompella and Bernhard[5] performed experiments on two large fleets of nominally identical vehicles, carefully controlling their experimental procedure. They found that the response at any given frequency in the high frequency regime varied from 10-20 dB. They concluded that noise control treatments that are effective for one vehicle may not be effective for all vehicles in a fleet, and that variability should be taken into account.

We briefly summarize by echoing the two main problems with DNS: large computational burden at high frequencies and high sensitivity to geometrical imperfections at small wavelengths. In the next section we survey the literature on one answer to these problems: statistical energy analysis.

1.2 Statistical energy analysis

1.2.1 Overview

Statistical energy analysis is one approach to solving some of the practical and fundamental problems of DNS. There is a monograph[1] containing an overview of the subject. The idea is to partition a large, complex structure into several simpler, weakly coupled substructures and define a single global variable of interest in each substructure, such as vibrational energy density. In conventional SEA, steady-state energy densities are predicted for band-limited responses in the presence of dissipation. In SEA models, it is assumed that there is equipartition of energy among modes to justify using a modal average for a "coupling loss factor" (CLF), a coefficient that determines energy flow between substructures, for each pair of substructures. A predictive SEA model therefore requires modal densities and dissipation estimates for each substructure, and estimates for these CLFs between pairs of substructures. These restrictions on SEA are discussed in more detail later in this introduction.

Statistical energy analysis exploits an analogy to heat transfer.[6] Consider two bodies in thermal communication with each other. The two bodies are small enough or have large enough conductance such that their temperatures are uniform, i.e., they are in internal thermal equilibrium. The rate of energy transfer (flux) between the two is proportional to the temperature difference and is given by Fourier's law of heat conduction,

$$q = -k\Delta T, \tag{1.1}$$

where k is the thermal conductivity between the two bodies. In the discrete case of many bodies in

thermal communication with each other, the flux from i to j is

$$q_{i\to j} = -k_{ij}\left(T_j - T_i\right), \tag{1.2}$$

with $k_{ij} = k_{ji}$. Also, if one considers conservation of energy in each body and the heat capacity model of stored thermal energy,

$$C_i \frac{\partial}{\partial t} T_i = -\sum_{j=1}^{N} q_{i\to j}, \tag{1.3}$$

where C_i is the thermal capacity of the i^{th} body, and $j = i$ is not included in the sum. Substitution of Eq. (1.2) into Eq. (1.3) allows one to construct the matrix equation

$$[C]\frac{\partial}{\partial t}\{T\} = -[k]\{T\}, \tag{1.4}$$

where $[C]$ is a diagonal matrix of heat capacities, $[k]$ is a symmetric matrix of heat conductances, and $\{T\}$ is a column array containing the temperatures of the bodies. In SEA, modal density plays the role of heat capacity, CLFs play the role of conductances, and energy density (i.e., energy per mode) plays the role of temperature.

The generalization of temperature difference to three dimensions and continuous systems is the temperature gradient, so (c.f. Eq. (1.1))

$$\{q\} = -k\nabla T, \tag{1.5}$$

where the vector $\{q\}$ has three components in the three spatial directions. Also, a consideration of

an energy control volume with the heat capacity model results in

$$\frac{\partial}{\partial t} CT = -\nabla \cdot \{q\}\,. \tag{1.6}$$

The diffusion equation

$$\frac{\partial T}{\partial t} = \alpha \nabla^2 T, \tag{1.7}$$

where $\alpha = k/C$ is the thermal diffusivity at a point, follows from substitution of Eq. (1.5) into Eq. (1.6). Throughout this thesis, what would properly be called the conduction model of Eq. (1.4) will also be referred to as "diffusion," as for Eq. (1.7).

Woodhouse[7] wrote an early attempt of a theoretical justification of SEA. He proved that the power flow between two single oscillators is exactly proportional to the energy difference between them when they are coupled by any conservative system. His work was an alternative theoretical formulation of that of Lyon and Maidanik,[8] generalizing their work. Lyon and Maidanik had proved the result for the case of coupling by a single oscillator. Woodhouse's proof also includes Scharton and Lyon's[9] result that for a system of identical oscillators all coupled in an identical way, the power flow between any two of them is exactly proportional to the energy difference between them. Woodhouse[7] also showed that the proportionality relationship does not hold with more than a single oscillator in a substructure; however, the approximation that it does hold must be made to make progress. He thus stressed the idea of partitioning a large structure into substructures by assigning degrees of freedom to the coupling and blocking them, isolating the substructures.

Woodhouse[4] also wrote an early general review of SEA without detailed analysis, aimed toward researchers who may want to know if SEA is appropriate for their particular vibration prob-

lems. He describes the analogy to heat diffusion in detail. He goes on to suggest an experimental procedure to determine if a particular system satisfies the assumptions of SEA and to determine some of the parameters required by SEA.

Dowell and Kubota[10] give a detailed derivation of the average response of a single structure due to random loading, which is used in SEA. They start with an exact modal sum and apply the assumptions that individual modes are uncorrelated with each other and that the forcing varies slowly over frequency. They then perform a spatial average over the structure. Finally, an average is taken over a frequency band (wide enough to include many modes, but narrow enough such that frequency and damping vary slowly). They go on to argue that the response everywhere is the same as the average response, so long as the source and response site are not close to each other or the response point is not close to a boundary.

Hodges and Woodhouse[3] review SEA in the larger context of random media. They briefly discuss the statistics of single, homogeneous structures, such as a plate of irregular shape. They go on to discuss the SEA formulation, taking care to state the important assumptions of the theory. Modes and forcing must be incoherent so that energies can be added, and there must be equipartition of energy amongst the modes. It may not be obvious how to partition a large system into substructures in general, and they note in particular that different mode types (e.g., extensional, torsion, and bending) may have to be treated as separate substructures. They also see as a major problem that, formally, the SEA framework is for predicting an ensemble average across similar structures that differ in precise details, but any one sample of the ensemble may behave significantly differently from the ensemble average. They also discuss Anderson localization[11] at length. In a near-periodic lattice with disorder, the modes tend to have large amplitudes in a spatially local-

ized area of the structure and be nearly zero elsewhere. This localization violates the assumptions of random modal statistics necessary for the validity of SEA, so one would expect SEA to fail in the presence of Anderson localization.

Fahy[2] provides a more critical review of SEA. He notes that there is little work on confidence estimates for the predictions made using SEA. The framework requires averages over frequency bands, so responses to single frequencies are unavailable using SEA. The global variables used in SEA do not give information about spatial fluctuations within a substructure. SEA predictions are profoundly wrong in periodic and nearly periodic structures,[12] related to Anderson localization.[11] Fahy[2] goes on to note that SEA formulations often require "indirect coupling" between two substructures that are not physically connected to produce correct predictions. Special care must be taken when a coupling element is forced close to one of its own resonant frequencies. The case of couplings that dissipate energy cannot be interpreted in the framework of SEA. Finally, coupling loss coefficients calculated theoretically by considering transmission between two infinite and/or semi-infinite substructures[13] deviate systematically from those in the finite case.

Bot[14] briefly reviews a range of energy transfer theories in structures, including SEA and similar formulations. He also develops another framework for vibrational energy transfer based on an analogy to radiative thermal transfer.

We note that, at least to some extent, the analogy of heat transfer to energy transport in vibrational systems is valid because of the wave-particle duality of physics. Heat transfer can be thought of quantum mechanical waves diffusing through the conductor or as photon billiards. Invoking the same argument, vibrational systems can be though of as solutions to the classical wave equation or as phonon billiards, as in ray acoustics. An important difference is that in SEA and other vibra-

tional energy formulations, the quantity of interest is the energy in some frequency band, not the total energy. Energy does not migrate between frequency bands in the linear vibrational systems typically analyzed with SEA.

1.2.2 Applications of diffusion models

Purely diffusive models have been used for vibrational and acoustic energy flow within single structures. For example, in solid mechanics Weaver[15] noted difficulties in conventional pulse-echo experiments and instead suggested that studying the diffuse ultrasonic wave field in a multiply scattering material may be more robust. He was chiefly concerned with deriving a diffusivity analogous to α in Eq. (1.7) in terms of material properties (shear and longitudinal wave speed and their associated attenuations).

Diffusive scattering of acoustic fields has been considered in water.[16, 17] The experimenters emphasized analogies to electron random walks and optics. Acoustic waves were allowed to scatter off of steel cylinders in water. The diffusivity constant was presented in terms of the dimension of the system, properties of the fluid, and the mean free path. Predictions were compared with experiments, and an extension to probing coarse grain steel was discussed.

Weaver and Sachse[18] performed similar experiments in water using a random system of densely packed glass beads as scatterers instead of steel cylinders.

Jia and others[19] studied diffusive ultrasound propagation in granular materials. They performed pulse-echo experiments on various configurations of glass beads. Their responses contained a well-defined reproducible early pulse followed by a diffusely scattered irregular signal that depends on the configuration of the beads.

A final example of where statistical arguments and diffusion are also used is in room acoustics.[20] Practitioners of the field are concerned with such tasks as predicting reverberation times in rooms. There is much interest in classrooms[21] and concert halls.[22]

1.2.3 Extensions of SEA

More recently, SEA has been extended to the time domain. Lai and Soom[23] studied two weakly coupled oscillators and concluded that the coupling loss factor varies in time, but the the CLF does approach its steady state value asymptotically at late time. Introducing time varying CLFs is a plausible way to better represent data instead of using constant CLFs, but, physically, it is surprising that the parameters governing energy flow should change in time-invariant systems. Time varying CLFs seem less than useful. Pennington and Ledinik[24] also considered two weakly coupled (damped) oscillators. They concluded that the approximate non-time varying CLFs are sufficient at not too early times. Indeed, the power flow from a forced oscillator to an unforced oscillator is maximum at the initiation of the source in SEA, but it is zero in the exact solution. Power is force dotted with velocity, and the velocity of the unforced system is zero at the initiation of the source. They also showed that the integral of the time history of the SEA solution and the exact solution were equal. However, in their formulation of the power balance, they used total energy in each substructure instead of energy density, so their "conduction" matrix is nonsymmetric in general, leading to a non-standard eigenvalue decomposition.

Development of a hybrid method was proposed by Langley and Bremner[25] combining deterministic and statistical frameworks. They recognize the success of DNS in systems with wavelengths long compared to the system and of SEA in systems with wavelengths short compared to

the system. They partition a system into “global” and “local” sets of degrees of freedom. The global set is associated with long wavelengths and are modeled deterministically. The local set is associated with short wavelengths and are modeled statistically. There is a single degree of freedom for each statistical substructure, and they account for the coupling between the global and local sets. The hybrid method is suitable for, say, a stiff beam with few modes in a certain frequency band coupled to a compliant plate with many overlapping modes in the same frequency band.

Catoni and others[26] have predicted variances from the mean one predicts by SEA. They write the SEA power balance in the usual way and write a perturbation expansion of the power input to each substructure. They then use the assumption of Gaussian orthogonal ensemble statistics from random matrix theory[27] for the eigenvalues of the dynamic matrices of each substructure.

Gregory and Keltie[28] have used experimental SEA. They start with a “reasonable” initial SEA modal. They then collect experimental data in the time domain from some or all of the substructures in the initial model. The eigensystem realization algorithm[29] (ERA) is used on the experimental data to reduce the model to a minimum state dimension to compensate for experimental noise. The realized system is used to update the SEA model by enforcing that the measured power input/output relationships be maintained. They concluded that they could detect changes in the experimental setup by using the same initial SEA model but constructing their updated SEA model from new experimental data taken from a subset of the substructures used to construct the initial SEA model.

One of the first uses of direct finite-element numerical calculations to estimate coupling loss factors was made by Simmons.[30] He constructed FEM models of (finite) joined plates and explic-

itly integrated the square displacement over each entire plate to calculate the energy in the plates. He then used the ratio of the energies in the plates to estimate CLFs. This FEM procedure contrasts with SEA analytic models in that it does not include an assumption that energy is transferred between semi-infinite structures the same way as between real, finite structures. The CLFs obtained by FEM are compared to those obtained by SEA and experiments. He does note that one specific model is not representative of an ensemble of such joined plates with slightly different geometry or boundary conditions. Whether CLFs obtained for a junction in isolation can be used in a large structure remains unclear.

Steel and Craik[31] compared coupling loss factors obtained from FEM with those obtained in a conventional way from SEA at low frequencies where one would expect SEA to fail due to low modal density. They found that the CLFs from FEM had large fluctuations about the SEA prediction, and that the FEM prediction was highly sensitive to boundary conditions in the frequency range that they studied.

Shankar and Keane[32] studied assemblies of beams and springs using two deterministic models, FEM and the Green's function method. They used their numerical results as a substitute for experimental data and used a procedure similar to that described by Woodhouse[4] to determine SEA coupling loss factors. They[32] discussed in detail the importance of the indirect CLFs associated with two substructures that are not physically connected. Predictions can be poor in certain circumstances if one uses only the direct CLFs, calculated no matter how accurately, between substructures that are physically connected. Direct CLFs can be calculated from analytical models, but there is no direction for calculating indirect CLFs analytically.

Shankar and Keane presented an energy flow theory applied to beams,[33] plates,[34] and a section

of a ship.[34] Their formulation involves calculating, using FEM or some other deterministic model, the eigenvalues and modes for the various substructures separately, considering free boundary conditions at the degrees of freedom that join the any particular substructure to another. Solving an eigenvalue problem on several substructures separately is computationally more efficient than calculating global modes. The degrees of freedom common to two different substructures are set equal to each other to assemble global Green's functions. With this formulation, one can calculate the power transferred from one substructure to another directly by force times velocity.

Fredö[35] used an approach to the SEA formulation similar to that of Simmons.[30] Like Simmons, he considered a finite-element model of two coupled plates and emphasized that the procedure is appropriate for individual cases as opposed to SEA which is appropriate for ensemble averages. His direct calculations of energy flow between substructures approached those predicted by SEA at high frequencies. He suggested explicitly that the coupling parameters obtained from one set of forcing can be used for other sets of forcing and in other configurations that are difficult to analyze by other means.

Mace and Shorter[36] perform analysis similar to that of Simmons,[30] but develop methods for frequency averaging and spacial averaging for random forcing. The averaging can be done analytically in pre- and post-processing for computational efficiency. They[36] also describe a formulation similar to that of Shankar and Keane,[33,34] but considering fixed boundary conditions at the shared degrees of freedom between each pair of joined subsystems instead of free boundary conditions.

Finally, Vibro-Acoustic Sciences, now a part of ESI Group, markets the software package VA One©, previously AutoSEA©, and has an ongoing effort developing semi-analytic techniques for estimating SEA parameters.

1.2.4 Our focus and organization of the thesis

We do not attempt to solve all problems associated with the statistical energy analysis modeling mentioned in our overview. Issues we address include developing methods to estimate the required parameters (e.g., coupling loss factors). As mentioned above, FEM[30–36] has been used to estimate the CLFs, though more commonly they are estimated from analytic models[13] or experimental observations.[4] Once these parameters have been estimated, solving the resulting set of differential equations is trivial. In addition SEA requires partitioning into substructures. A "correct" way to partition a system is not always obvious, or a given system may not admit any substructures at all. Moreover, SEA modeling results in only average estimates for modal energy density in substructures. The SEA framework does not include a framework to account for local variations in impedance within a substructure. Conventional SEA considers steady-state processes without transport in nonstationary situations. Finally, the variables in SEA, such as energy density and energy flux between structures, are not directly measurable. It would be preferable to have a model with variables, such as force and displacement, that are directly measurable in experiment or DNS.

The organization of the thesis is as follows. We conclude the introduction in Section 1.3 with a discussion of relevant previous work. In Chapter 2, we describe some first attempts of fitting a diffusion equation to noisy diffuse data. In Chapter 3, we describe our framework, inspired by but different from SEA, for providing descriptions of large, complex structures. In Chapters 4 through 7, we apply our framework to several systems, both typically studied by SEA and not typically studied by SEA. Finally, we offer concluding remarks and some direction for possible

future work in Chapter 8. We hope that this work is not included in a future enumeration of "bad acoustics."[37]

1.3 Previous related work

Weaver[38] predicted late-time values of average, squared, band-limited responses to transient sources in linear elastic undamped vibrational systems. We summarize his pervious work in this section. The remainder of this thesis contains theories and examples extending Weaver's work to the slow energy evolution to late-time values.

1.3.1 Mathematical preliminaries

The theory of transient behavior of such linear elastic systems is mature. The governing equations are often modeled as a set of ordinary differential equations (ODEs). In matrix form, they may be cast as

$$[K]\{u(t)\} + [M]\frac{\mathrm{d}^2}{\mathrm{d}t^2}\{u(t)\} = \{s\}B(t), \tag{1.8}$$

$$\{u(0)\} = \frac{\mathrm{d}}{\mathrm{d}t}\{u(0)\} = \{0\}, \tag{1.9}$$

where $\{u(t)\}$ is a column vector containing the response at time t, $[K]$ and $[M]$ are the symmetric (and typically sparse) stiffness and mass matrices, respectively, and $\{s\}$ is a column vector containing the spatial distribution of the transient forcing $B(t)$. The vector $\{s\}$ is normalized on $[M]$ by

$$\{s\}^T[M]\{s\} = 1, \tag{1.10}$$

where T denotes transpose; $B(t)$ is taken to be zero for $t < 0$ and $t > T_B$; and quiescent initial conditions are imposed.

The set of ODEs in Eq. (1.8) can be thought of as an approximation to a partial differential equation (PDE). An example is a spatial finite-difference mesh of masses connected by springs modeling a membrane. Such a mesh better approximates the membrane as one reduces the mesh spacing; however, we make no attempt to precisely reproduce the PDE. We would instead take our system to be the system of masses and springs, recognizing it to be a perfectly good complex system to study.

A practical computer implementation of the solution to the ODEs involves evaluating the second time derivative as finite differences. The three-step centered scheme is

$$\frac{\mathrm{d}^2}{\mathrm{d}t^2}\{u(t)\} = \frac{\{u(t-\delta t)\} - 2\{u(t)\} + \{u(t+\delta t)\}}{\delta t^2}, \tag{1.11}$$

where δt is the time step, resulting in a set of finite-difference equations

$$\{u(t+\delta t)\} = 2\{u(t)\} - \{u(t-\delta t)\} - \delta t^2 [M]^{-1} [K] \{u(t)\} + \{s\} B(t). \tag{1.12}$$

The mass matrix $[M]$ is typically diagonal, so the introduction of $[M]^{-1}$ does not pose a problem. The difference between the ODEs and the finite-difference equations is also trivial. The natural frequencies and natural modes of the ODEs are given by

$$[K]\{u\} = \omega_{\mathrm{ODE}}^2 [M]\{u\}, \tag{1.13}$$

while the natural frequencies of the finite-difference equations are given by the mapping

$$\omega_{\mathrm{FD}} = \frac{1}{\delta t} \arccos\left(1 - \frac{\omega_{\mathrm{ODE}}^2 \delta t^2}{2}\right), \tag{1.14}$$

and the natural modes remain the same. The mode shapes are determined completely by the mesh. We make no attempt to reproduce the ODEs, requiring δt to be small enough only to ensure stability.

That a finite-difference measure of energy

$$\mathcal{E}_{t+\delta t/2} \equiv \frac{\{u(t+\delta t)\}^T [K] \{u(t)\}}{2} + \frac{\{u(t+\delta t) - u(t)\}^T [M] \{u(t+\delta t) - u(t)\}}{2\delta t^2} \tag{1.15}$$

is conserved after $t = T_B$ is confirmed by substitution of Eq. (1.12) into Eq. (1.15). Checking that this measure of energy is conserved numerically during execution of a computer implementation of Eq. (1.12) is an important verification of the code.

1.3.2 Late-time asymptotic behavior

Weaver[38] showed that the average late-time squared response to band-limited source $B(t)$ can be estimated accurately by

$$\Psi_{rs,B}(t = \infty) = \frac{E_{r,B} E_{s,B}}{N_D}, \tag{1.16}$$

where the denominator

$$N_D = 2\pi^3 f_c^2 D(2\pi f_c) \int B^2(t) \mathrm{d}t \tag{1.17}$$

is proportional to the global modal density $D(\omega) = \mathrm{d}N/\mathrm{d}\omega$ and, thus, the size of the system. The terms in the numerator are calculated by

$$E_{s,B} = \int_0^{T_B} B(t) \left[\frac{\mathrm{d}}{\mathrm{d}t} \int_0^t (\{s\}^T [\mathbf{G}(t-\tau)] \{s\}) B(\tau) \mathrm{d}\tau \right] \mathrm{d}t, \tag{1.18}$$

with a similar expression for $E_{r,B}$, where $\{r\}$ has a similar definition as $\{s\}$. The quantity $E_{s,B}$ is the work done on the system by a transient band-limited force $\{s\}\, B(t)$ with center frequency f_c and time duration T_B. Only diagonal elements of the Green's function $[\mathbf{G}(t)]$ for time $t < T_B$ are required for the calculation, where diagonal is in the sense that $\mathbf{G}_{ss}(t) = \{s\}^T [\mathbf{G}(t)] \{s\}$.

We note from Weaver's work[38] that Eq. (1.18) can be written as

$$E_{s,B} = -\frac{1}{\pi} \int_0^\infty \omega |\tilde{B}(\omega)|^2 \Im \widetilde{\mathbf{G}}_{ss}(\omega) \, \mathrm{d}\omega, \tag{1.19}$$

where $\Im$ denotes imaginary part, and the tilde represents Fourier transform. Since the admittance is $\omega \left[\widetilde{\mathbf{G}}(\omega) \right]$, Eq. (1.16) can be seen to be a product of admittances. In later discussion, $E_{s,B}$ will loosely be referred to as "admittance."

The approximation of Eq. (1.16) has general utility, but it does have weaknesses. It is related to (but not strictly dependent on) equipartition. The approximation would be inaccurate if the structure is Anderson-localized.[11] (The same problem is evident in SEA.) The approximation is also inaccurate if the source and receiver are near each other or coincide. If they coincide, an ad hoc weak-localization[39] factor ranging from 2 at early times to 3 at late times may be used. Also, the theory is inapplicable in the presence of dissipation.

The work that follows addresses a different issue. Weaver's theory[38] shows that late-time

behavior is predicted from early-time responses, but it does not address transport at moderate times. However, early-time responses do show a degree of transport. If this transport can detected in a short-time DNS, then it may be possible to extrapolate it to later times. Statistical energy transport theories such as SEA are developed under the presumption that such transport is diffusive. However, a diffusion model need not look like SEA. Indeed, the theory reviewed in this section does not require the substructures that SEA requires.

Chapter 2

First attempts

Material in this chapter has been previously published by the authors Wolff and Weaver[40] by the publisher Elsevier. It is used with permission.

2.1 Two descriptions of diffusion

In order to describe the complicated dynamics of a vibrational system approximately, we adopt a diffusion-like model for energy flow. First, the form this model takes in terms of such measurable quantities as mean-square response and mean-square forcing (the quantities used in Weaver's paper[38]) is described. To the end of extracting the diffusion parameters of this measurables model, we assume that the structure does admit a division into substructures. Thus there is an exact correspondence, in this case, to SEA.

2.1.1 Description of the model in terms of measured quantities

We begin with an assumed diffusion-like energy flow equation governing the slow evolution of band-limited energy. The description is in terms of slowly time-varying mean-square displacement Ψ at each of R receivers and in terms of mean-square forcings $\{\hat{\Pi}\}$ (which may act through some of those receivers). This description does not require substructuring, so it can be applied to a dynamical system without first having to substructure it. In the absence of dissipation, the equation

takes the form

$$[\mathbf{H}]\frac{\partial}{\partial t}\{\Psi(t)\} = \left\{\hat{\Pi}(t)\right\} - [\mathbf{D}]\{\Psi(t)\}, \tag{2.1}$$

where $[\mathbf{H}]$ and $[\mathbf{D}]$ are $R \times R$, $\{\Psi\}$ contains the mean-square displacements and is $R \times 1$, and $\left\{\hat{\Pi}\right\}$ represents average band-limited force squared and is also $R \times 1$. The total number of receivers (potential sources) is denoted by R. These are the measurable quantities discussed in Weaver's paper.[38] Our ansatz is somewhat more general than SEA, albeit still diffusive. Statistical energy analysis is one special case of our theory. There is no assumption about substructures in this proposed approach: it can be applied to a dynamical system without the need to substructure it in order to define modal energy density in a substructure and coupling loss factors between substructures, and to systems that do not admit discrete substructures. Whether or not it is valid to apply a diffusion-like model at all is another matter, and a long-standing question within SEA.

We imagine having generated data $\{\Psi\}$ and $\left\{\hat{\Pi}\right\}$ by direct numerical simulation over short times. Thus it is inexpensive to employ a large number, R, of receivers; however, each source site requires a separate DNS of the impulse response of the system, so use of multiple sources is more expensive. It is desired to determine the diffusion parameters.

The matrix $[\mathbf{H}]$ must be diagonal in order that a forcing at one location does not instantaneously result in a response at another location. Any such energy transport may be restricted to be a consequence of possibly large off-diagonal elements in the construction of $[\mathbf{D}]$.

The matrix $[\mathbf{D}]$ must be symmetric as argued by reciprocity. Reciprocity between force and displacement implies reciprocity between mean-square force $\left\{\hat{\Pi}\right\}$ and mean-square displacement

$\{\Psi\}$. In the Laplace transform domain, one finds that the solution of Eq. (2.1) is

$$\{\Psi(s)\} = ([\mathbf{D}] + s[\mathbf{H}])^{-1} \left\{\hat{\Pi}(s)\right\}. \tag{2.2}$$

The matrix $([\mathbf{D}] + s[\mathbf{H}])^{-1}$ must be symmetric for all s, implying that both $[\mathbf{H}]$ and $[\mathbf{D}]$ must be symmetric.

In discussing the solution to Eq. (2.1) in the time domain, we consider the generalized eigenvalue problem

$$[\mathbf{D}]\{\mathbf{U}\} = \Lambda[\mathbf{H}]\{\mathbf{U}\} \tag{2.3}$$

with eigenpairs $(\Lambda_r, \{\mathbf{V}\}^r)$, $r = 1, 2, \ldots, R$. Since there is no dissipation, the first eigenvalue is trivial, that is, $\Lambda_1 = 0$. The eigenvectors are orthogonal and normalized:

$$\{\mathbf{V}\}^{rT}[\mathbf{H}]\{\mathbf{V}\}^q = \delta_{rq}, \tag{2.4a}$$

$$\{\mathbf{V}\}^{rT}[\mathbf{D}]\{\mathbf{V}\}^q = \Lambda_r \delta_{rq}, \tag{2.4b}$$

where the superscript T denotes transpose.

Consider the "impulsive" band-limited forcing described by

$$\left\{\hat{\Pi}(t)\right\} = \{\Pi\}\,\delta(t) \tag{2.5}$$

along with quiescent initial conditions. One finds the solution to Eq. (2.1) to be

$$\{\Psi(t)\} = \sum_{r=1}^{R} \{\mathbf{V}\}^r \{\mathbf{V}\}^{rT} \{\Pi\}\, e^{-\Lambda_r t}\Theta(t), \tag{2.6}$$

where $\Theta(t)$ is the Heaviside function. This solution is just an expansion in eigenvectors, each multiplied by a decaying exponential. As summarized above in Section 1.3, previous work by Weaver[38] shows that the mode associated with the trivial eigenvalue $\Lambda_1 = 0$ can be estimated accurately and directly from a direct numerical simulation over short-time (a length of time comparable to the inverse of the desired frequency resolution). This mode is constructed via Eq. (1.16) as

$$\mathbf{V}_r^1 = \frac{E_{r,B}}{\sqrt{2\pi^3 f_c^2 D(2\pi f_c)}}. \tag{2.7}$$

Calculating this mode for any site r requires a short-time DNS with a source at r.

2.1.2 Description of the model in terms of energy density

As in SEA we can also attempt to describe the diffusion in terms of energy flow between several (N) substructures. The governing equation is much the same as Eq. (2.1) above. It is, in the absence of dissipation,

$$[\mathbf{h}] \frac{\partial}{\partial t} \{\psi(t)\} = \{\hat{\pi}(t)\} - [\mathbf{d}] \{\psi(t)\}, \tag{2.8}$$

where $[\mathbf{h}]$ and $[\mathbf{d}]$ are $N \times N$, $\{\psi\}$ contains the modal energy densities (energy per mode) in some frequency band Δf in each substructure and is $N \times 1$, and $\{\hat{\pi}\}$ contains power, the rate at which energy is deposited into each substructure, and is also $N \times 1$. The number of substructures is denoted by N.

The matrix $[\mathbf{h}]$ is diagonal and contains the known mode counts, so these are not parameters to be extracted. Because equipartition of energy among the various modes across each substructure in a frequency band Δf is assumed in SEA, this definition implies that the left-hand side of Eq. (2.8)

can be interpreted as the time rate of change of total energy in each substructure. Through this definition $[\mathbf{d}]$ must be symmetric. setting the net energy flux from substructure b to substructure a (equal to $\mathbf{d}_{ab}\psi_b - \mathbf{d}_{ba}\psi_a$) to zero when $\psi_a = \psi_b$ implies that $[\mathbf{d}]$ is symmetric. Alternatively, one argues that the net flux is proportional (only) to the difference $\psi_a - \psi_b$.

Pinnington and Lednik[24] assumed the $[\mathbf{h}]$ matrix was the identity matrix, and $[\mathbf{d}]$ was non-symmetric. Their formulation may be obtained from our formulation Eq. (2.8) by changing the dependent variable from the modal energy densities used here to total substructure energies used there.[24]

Again, there is a set of eigenpairs $(\lambda_n, \{\mathbf{v}\}^n)$, $n = 1, 2, \ldots, N$ associated with Eq. (2.8). In the absence of dissipation, the first eigenvalue is trivial, that is $\lambda_1 = 0$. The eigenvectors are orthogonal and normalized:

$$\{\mathbf{v}\}^{nT}\,[\mathbf{h}]\,\{\mathbf{v}\}^q = \delta_{nq}, \tag{2.9a}$$

$$\{\mathbf{v}\}^{nT}\,[\mathbf{d}]\,\{\mathbf{v}\}^q = \lambda_n \delta_{nq}. \tag{2.9b}$$

The solution of Eq. (2.8) in the case of impulsive loading $\{\hat{\pi}(t)\} = \{\pi\}\,\delta(t)$ and quiescent initial conditions,

$$\{\psi(t)\} = \sum_{n=1}^{N} \{\mathbf{v}\}^n \{\mathbf{v}\}^{nT} \{\pi\}\, e^{-\lambda_n t}\Theta(t), \tag{2.10}$$

follows in exactly the same way as above for the description in terms of measured quantities. Equipartition across the entire structure at late times implies that the first eigenvector is

$$\mathbf{v}_n^1 = 1/\sqrt{\mathrm{tr}\,([\mathbf{h}])} \tag{2.11}$$

for all n. Equation (2.9a) is satisfied, so this mode is properly normalized.

Connection to the measured quantity description

If a substructured description is valid (and one can imagine systems for which it is not), there must be a connection between the measured quantities $\{\Psi\}$ and the substructures' energies $\{\psi\}$. We define $[g]$, a typically nonsquare $R \times N$ $(R \geq N)$ matrix of local frequency-dependent transducer functions and sensitivities (henceforth simply called gains) such that

$$\{\Psi(t)\} = [g]\{\psi(t)\}. \tag{2.12}$$

Elements of $[g]$ are the sensitivities of the response of the transducer to the local dynamics multiplied by the sensitivity of the local dynamics to the local geometrical details of the structure, i.e., the admittances.

That there is a unique mapping in Eq. (2.12) between substructure energy and mean square displacement at sites within the substructure is a consequence of the diffuse field assumption—that total energy is statistically equivalent to energy density samples. Cases in which the mapping is nonunique follow from failures of the diffuse field assumption, and/or poor substructuring.

Presumably, if the structures of the SEA description are geometrically separated, $[g]$ is especially simple. That is, g_{rn} is nonzero if and only if receiver r is physically located in substructure n. Geometric separation implies that each row of $[g]$ has only one nontrivial element. Unless otherwise noted in the sections to follow, such a $[g]$ is assumed, implying that the systems are such that

1. There is a strict substructuring such that the mean-square response at any given receiver is

directly proportional to the energy density in (only) that substructure.

2. It is known in which substructure each receiver is located.

These requirements will ultimately need to be relaxed if the methods are to be applied to systems that do not admit subtructuring. We will eventually want to consider fully populated $[g]$ matrices such that the response at any given receiver site may be some weighted average of the energy density in different substructures. In particular one can think of at least two counterexamples to the above assumption of the special case $[g]$.

1. One might imagine two large rooms with a small window providing the coupling between the two rooms. Presumably, if a receiver is located close to the window, the response at that site would be a weighted average of the local energy density in each room.

2. One can consider diffusion across a statistically uniform structure. Multiple scattering of waves in such systems is often described by diffusion.[15–17,19] We study such a system in Chapter 5. The concept of substructures in this pure diffusion case becomes problematic, and one would expect an SEA description to fail and the need for $[g]$ to vanish in this case.

We proceed to derive the relationship between the eigenvalues and eigenvectors of the measured-quantities description and the energy-density description. Substituting Eqs. (2.6) and (2.10) into Eq. (2.12), we have

$$\{\Psi(t)\} = \sum_{r=1}^{R} \{\mathbf{V}\}^r \{\mathbf{V}\}^{rT} \{\Pi\} e^{-\Lambda_r t} \Theta(t) = [g] \sum_{n=1}^{N} \{\mathbf{v}\}^n \{\mathbf{v}\}^{nT} \{\pi\} e^{-\lambda_n t} \Theta(t). \tag{2.13}$$

Thus it is inferred

$$\{\mathbf{V}\}^r = [g]\,\{\mathbf{v}\}^n \delta_{rn} \text{ for } r \leq N, \tag{2.14a}$$

$$[g]^T\,\{\Pi\} = \{\pi\}\,, \tag{2.14b}$$

$$\Lambda_r = \begin{cases} \lambda_n \delta_{rn} & \text{for } r \leq N \\ \infty & \text{otherwise,} \end{cases} \tag{2.14c}$$

establishing the relationships between the eigenvectors, power inputs, and eigenvalues in the measurables description and the energy-density description. In particular, the small eigenvalues ($r \leq N$) in the measured-quantities description are the same as those in the energy-density description while the large eigenvalues ($r > N$) are at least approximated to be infinite. Note that to obtain the eigenvectors in the measured space, one left-multiplies the corresponding eigenvectors in the physical space with the $[g]$ matrix in identically the same way as one obtains the $\{\Psi\}$ vector from the $\{\psi\}$ vector. Also note that Eq. (2.14a) applied to $r = 1$ allows us to solve for the elements of $[g]$, at least for the strict substructuring $[g]$, since $\{\mathbf{V}\}^1$ and $\{\mathbf{v}\}^1$ are completely known.

We can consider the orthogonality of the eigenvectors in the SEA description and in the measured-data description. We have, by substituting Eq. (2.14a) into Eq. (2.4a),

$$\{\mathbf{V}\}^{rT}\,[\mathbf{H}]\,\{\mathbf{V}\}^q = \{\mathbf{v}\}^{rT}\,[g]^T\,[\mathbf{H}]\,[g]\,\{\mathbf{v}\}^q = \delta_{rq}, \tag{2.15}$$

as well as from Eq. (2.9a)

$$\{\mathbf{v}\}^{pT}\,[\mathbf{h}]\,\{\mathbf{v}\}^s = \delta_{ps}. \tag{2.16}$$

Therefore,

$$[g]^T [\mathbf{H}] [g] = [\mathbf{h}] . \tag{2.17}$$

Equation (2.17) appears to be $N(N+1)/2$ equations (orthogonality conditions) in R unknowns (diagonal elements of $[\mathbf{H}]$). If, however, only strict substructuring is considered, inspection of Eq. (2.17) reveals that the equations associated with the off-diagonal elements of $[\mathbf{h}]$ are automatically satisfied. Then Eq. (2.17) is N equations in R unknowns, a completely determined system if there is one and only one receiver in each substructure. If there is more than one receiver in any substructure, then there is some freedom in choosing how to distribute the elements of $\mathbf{H}$ among the receiver sites in that substructure.

2.2 Case study 1: Two-room system

Our long-range desire is to be able to fit a diffusion model to short-time DNS measured data in order to predict transport dynamics over longer times. Toward this end we here generate data artificially to which to fit equations such as Eq. (2.13). The parameters of diffusion (i.e., λs, $\{\mathbf{v}\}$s, and $[g]$) will be recovered by minimizing a χ^2 quantity by adjusting the diffusion parameters, as explained below.

We consider two simple case studies, each of the strict substructuring class that maps well onto SEA. One has two substructures; the other has three. For these studies mode counts are taken as known, and admittances (i.e., $\{\mathbf{V}\}^1$) are taken as known by Weaver's procedure[38] for sites with a source. Forcing $\{\Pi\}$ would be known in a DNS simulation, so these are not fit parameters to be extracted.

2.2.1 Description of data

The data are constructed first by evaluating the SEA solution Eq. (2.10) in a simple two-substructure system. With a view toward application to data gleaned from a DNS, with inevitable stochastic fluctuations and local variations in sensitivities, we then add noise and multiply by arbitrarily specified receiver gains $[g]$. Noise is constructed independently at each r and time t such that it has fixed fractional standard deviation σ. These characteristics for noise are typical. Moreover the fractional standard deviation is $\sigma = 1/\sqrt{\Delta f \Delta t}$ in real DNS applications or measurements, where Δf is the bandwidth in a DNS or measurement, and Δt is the duration of the time window over which energies are averaged.[41,42] There is a theoretical argument[43] for this estimate, and some experimental studies are discussed by Davy.[44] Studying fluctuations from the mean is an area of active research. Some years ago there was a series of papers by Lyon[45] and Davy,[44,46,47] and more recently by Lobkis and others,[48] Langley and Cotoni,[49] and Langley and Brown.[50,51] The details of the construction of noise are in Appendix A.

Our system in the first case study is equivalent to that used to describe room acoustics in the structure pictured in Fig. 2.1 of size 400×300 with a partition along its width. The partition has a window of length $l_{12} = 0.20 \times 300 = 60$ allowing energy to flow between the two (two-dimensional) rooms. In practice, this window has to be small for "weak-coupling" but larger than a few wavelengths to avoid localization. Therefore, the parameters of Eq. (2.8) with mode counts

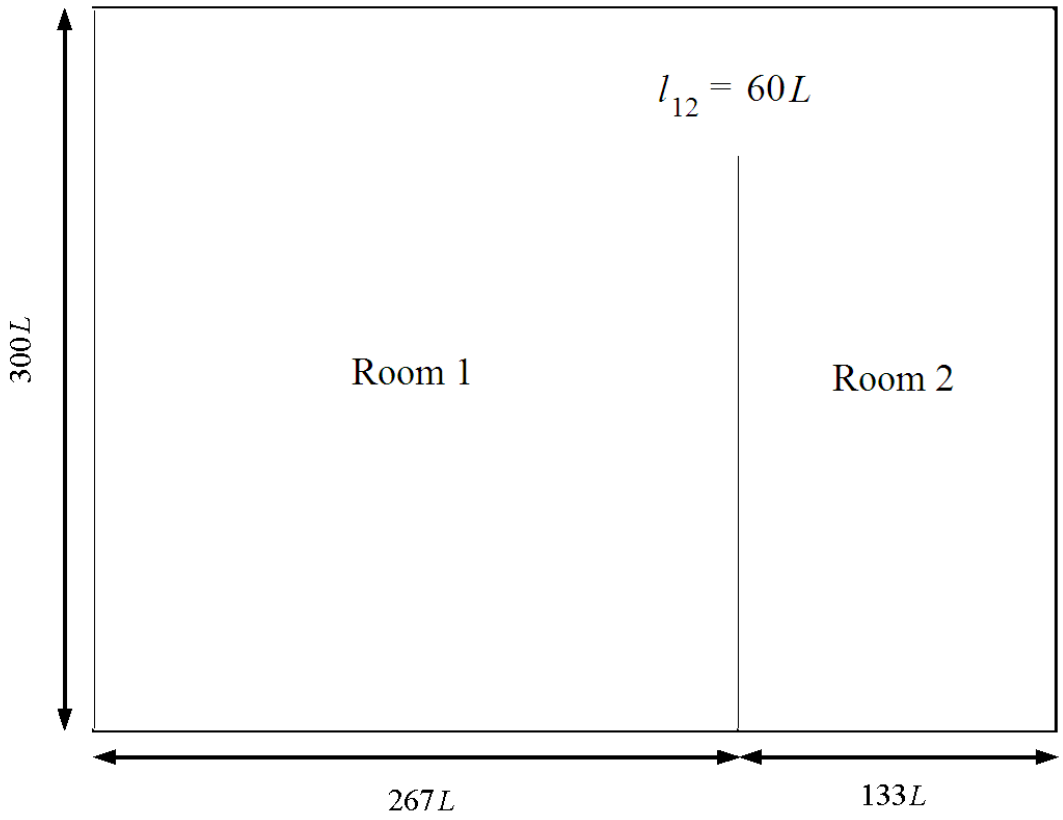

Figure 2.1: Geometry of the two room system described in Section 2.2. The window coupling the two rooms is $l_{12} = 60$ units wide. Units of length are referenced to an arbitrary microscopic length scale L, equal to 1/300 of the room width.

being taken in the usual way (see, e.g., Kittel and Kroemer[52]) are the following:

$$\mathbf{h}_n = \frac{2\pi f}{c^2}(\text{area}_n)\Delta f, \tag{2.18}$$

$$[\mathbf{d}] = \frac{cl_{12}}{\pi}\begin{bmatrix} 1 & -1 \\ -1 & 1 \end{bmatrix} \times \frac{\text{number of modes}}{\text{area}}, \tag{2.19}$$

where c is the velocity of the waves, f is the center frequency of the frequency band, and Δf is the bandwidth. The velocity and frequency are taken here as unity, and the bandwidth is taken as

$1/2\pi$ for the purposes of our artificial simulation. The $\{\psi\}$s thus represent modal energy density, plotted in Fig. 2.2. These parameters result in a first nontrivial eigenvalue of $\lambda_2 = 7.2 \times 10^{-4}$. The

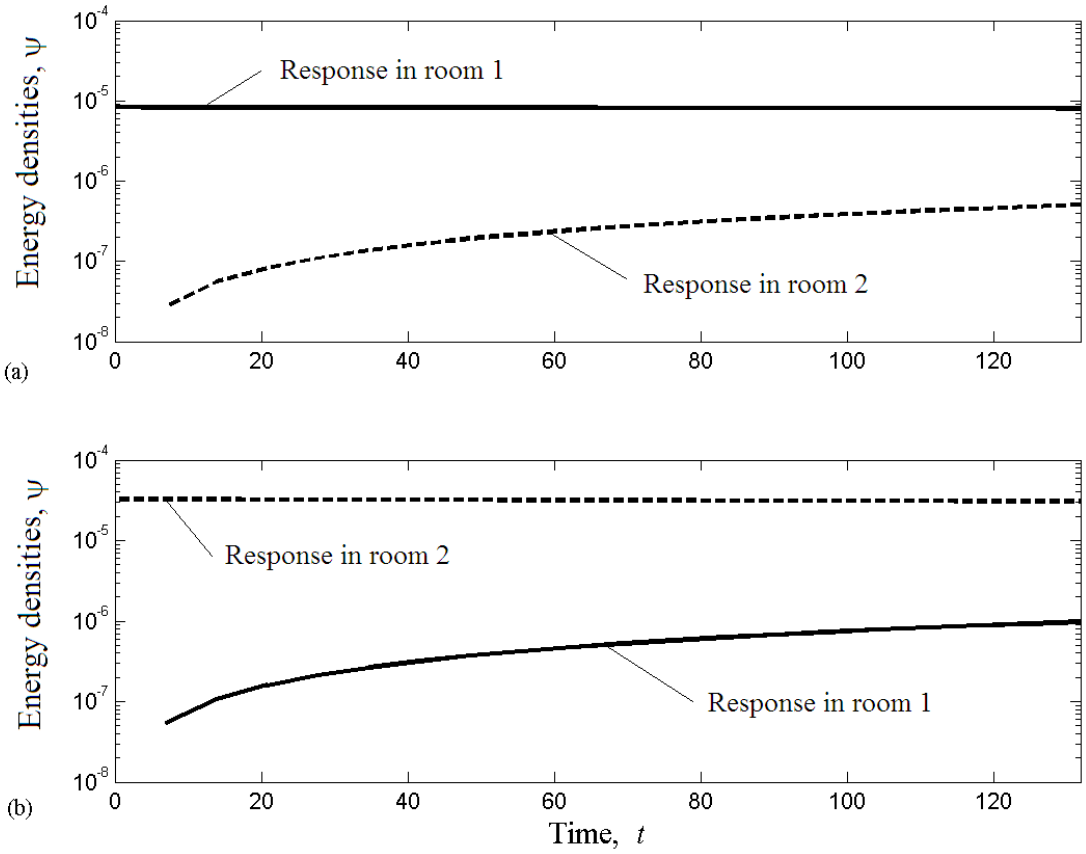

Figure 2.2: The evolution of energy density in each of the two rooms for the period analyzed in Section 2.2. Time is measured in units of L/c. The eigenvalues (in units of c/L) are $\lambda_1 = 0$ and $\lambda_2 = 7.2 \times 10^{-4}$. The eigenvectors are $\{\mathbf{v}\}^1 = \{2.9; 2.9\} \times 10^{-3}$ and $\{\mathbf{v}\}^2 = \{2.0; -4.1\} \times 10^{-3}$. Total time considered was $\frac{1}{10}\frac{1}{\lambda_2}$. (a) A single source in room 1. (b) A single source in room 2.

gains in the $[g]$ matrix were taken from a set of uniformly distributed numbers $[\frac{1}{2}, 2]$.

We considered four data sets, each with a total of 20 receivers, 10 in each room, and took data from two "experiments" corresponding to sources in each of the two rooms. Data were examined out to one-tenth of a decay time, i.e., $t_{\max} = 139$, and 20 data points were constructed for each receiver at evenly spaced times. Fractional fluctuations from the mean energy density were

different in each data set and taken to be $\sigma = 0\%$, $\sigma = 15\%$, $\sigma = 30\%$, and $\sigma = 50\%$.

2.2.2 Fitting procedure

We seek to fit the functional form in Eq. (2.13)

$$\{\Psi(t)\} = [g] \sum_{n=1}^{N} \{\mathbf{v}\}^n \{\mathbf{v}\}^{nT} \{\pi\} e^{-\lambda_n t} \tag{2.20}$$

to the artificial data. Since $\{\mathbf{v}\}^1$ is completely known by Eq. (2.11), and $\{\mathbf{V}\}^1$ is taken as known for the two source locations, elements in the rows of the $[g]$ matrix corresponding to the source locations can be calculated by Eq. (2.14a). The transformation matrix $[g]$ remains unknown for its other 18 elements. One can calculate $\{\mathbf{v}\}^2$ using the two remaining orthogonality conditions:

$$\mathbf{v}_1^1 \mathbf{h}_1 \mathbf{v}_1^2 + \mathbf{v}_2^1 \mathbf{h}_2 \mathbf{v}_2^2 = 0, \tag{2.21a}$$

$$\mathbf{v}_1^2 \mathbf{h}_1 \mathbf{v}_1^2 + \mathbf{v}_2^2 \mathbf{h}_2 \mathbf{v}_2^2 = 1. \tag{2.21b}$$

Solving directly results in

$$\mathbf{v}_1^2 = \frac{\mathbf{v}_2^1 \mathbf{h}_2}{\alpha}, \tag{2.22a}$$

$$\mathbf{v}_2^2 = -\frac{\mathbf{v}_1^1 \mathbf{h}_1}{\alpha}, \tag{2.22b}$$

where

$$\alpha = \sqrt{\left(\mathbf{v}_2^1 \mathbf{h}_2\right)^2 \mathbf{h}_1 + \left(\mathbf{v}_1^1 \mathbf{h}_1\right)^2 \mathbf{h}_2}, \tag{2.23}$$

so that $\{\mathbf{v}\}^2$ is completely known entirely from the specified parameters; the data are not needed to find $\{\mathbf{v}\}^2$. The use of the mapping of Eq. (2.12) may seem to restrict the method only to systems that admit substructuring. However, the substructuring is exploited to reduce the number of fit parameters in the nonlinear fit algorithm that is used and to map directly onto SEA. This apparent need for substructuring could be relaxed simply by fitting all the gains, or, equivalently, fitting all the elements of the eigenvectors $\{\mathbf{V}\}$.

The remaining quantities must be fit by minimizing a χ^2 quantity. The formula for χ^2 can take a few different forms, e.g.,

$$\chi_a^2 = \frac{\sum_t \sum_{r=1}^{R} \sum_{s=1}^{S} \frac{[\mathbf{G}_{rs}(t) - \Psi_{rs}(t)]^2}{[\sigma \mathbf{G}_{rs}(t)]^2}}{N_t RS - \text{d.o.f.}}, \tag{2.24a}$$

$$\chi^2 = \frac{\sum_t \sum_{r=1}^{R} \sum_{s=1}^{S} [\log \mathbf{G}_{rs}(t) - \log \Psi_{rs}(t)]^2}{\sigma^2 (N_t RS - \text{d.o.f.})}, \tag{2.24b}$$

where d.o.f. is the number of fitting parameters, and σ^2 (defined by Eq. (A.4)) is the fractional variance of the signal about the local underlying mean and is identical for every value of $\Psi_{rs}(t)$. The above two forms are nominally equivalent, such that a good fit should have $\chi^2 \approx$ unity. Equation (2.24b) is particularly convenient because of the relatively simple form of the expression.

The remainder of the fitting process consists of letting a nonlinear least-square fitting algorithm search the degrees of freedom to minimize χ^2. The algorithm used is a MATLAB implementation of a "large scale: trust-region reflexive Newton" method.[53] For this problem the logarithm of the data (i.e., in Eq. (2.24b)) is fit to the log of the functional form of Eq. (2.20) with the adjusted parameters being the eigenvalue λ_2 and the 18 elements in the rows of $[g]$ not associated with

sources.

The above procedure may be contrasted with that of Gregory and Keltie.[28] As discussed in the introduction, they use an ERA,[29] a linearized fit algorithm, to obtain estimates for the eigenvalues. However, an ERA does not perform well in our experience with our time-limited data. Their ERA seems to weigh all data equally without normalizing by the mean value, i.e., using a nonweighted χ^2 such as

$$\chi^2_{\mathrm{nw}} = \frac{\sum_t \sum_{r=1}^{R} \sum_{s=1}^{S} [\mathbf{G}_{rs}(t) - \Psi_{rs}(t)]^2}{N_t RS - \mathrm{d.o.f.}}. \tag{2.25}$$

If $[\mathbf{G}]$ has large dynamic range and fluctuates with a fixed fractional standard deviations σ, Eq. (2.25) is inappropriate.

2.2.3 Results

We evaluate the performance of our algorithm by scrutinizing the best fits to the eigenvalues and the value of χ^2 associated with the best fit. The best fits to the eigenvalues are plotted in Fig. 2.3 for different number of receivers in each room considered and different noise levels. The fit algorithm is seen to find the best fit to the decay time regardless of the number of receivers in the experiment or the noise amplitude.

As shown in Fig. 2.4, the best-fit value of χ^2 was evaluated. It fluctuates about unity as it should. The best fit to data from a receiver in each of the substructures is plotted along with the data in Fig. 2.5. The overall fit was to all 10 receivers in both substructures.

The fitting algorithm in this two room case is successful and robust.

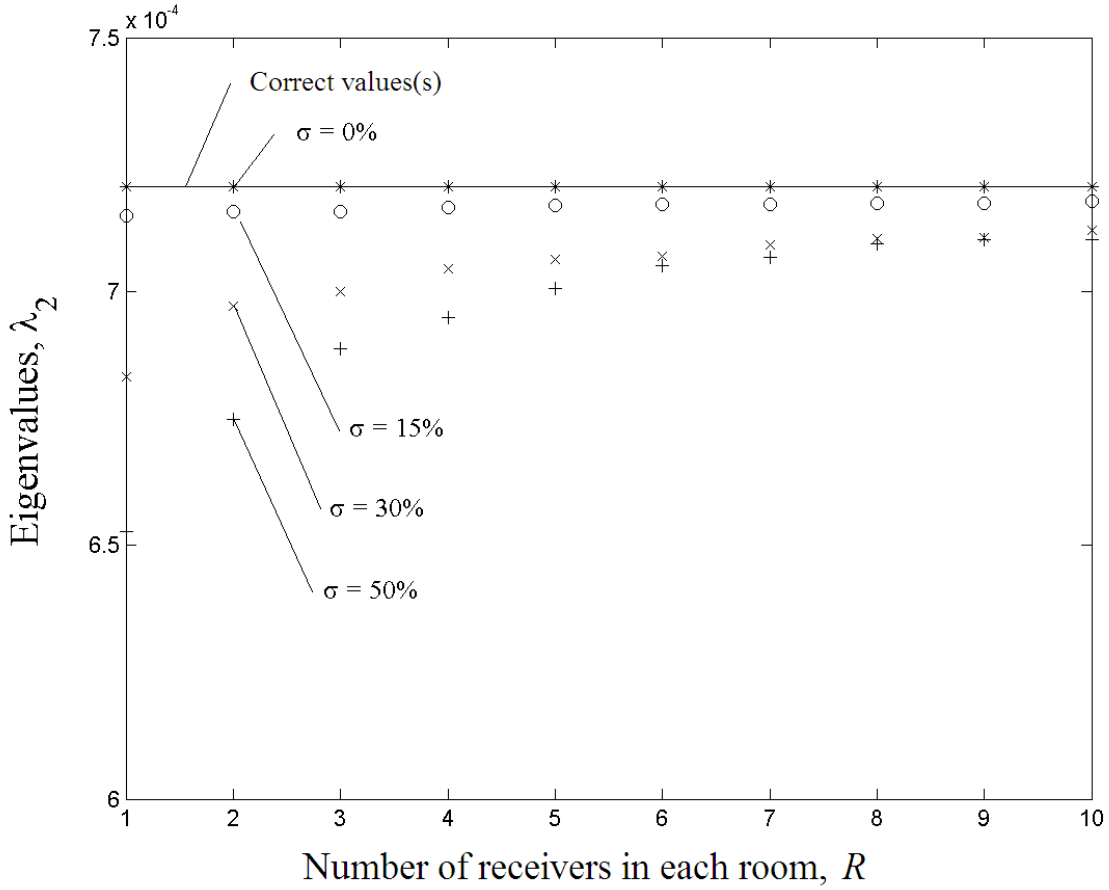

Figure 2.3: The best fit to λ_2 for the two room system for various numbers of receivers in each room and noise levels. The fit is good even with a small number of receivers and large noise amplitude.

2.3 Case study 2: Three-room system with partial coupling

Finally, we extend the class of problems we are considering slightly to a three-room system with no coupling between rooms one and three (i.e., three rooms "in a row").

2.3.1 Description of the data

We consider a structure pictured in Fig. 2.6 of size 400×300, this time with two partitions dividing it into three rooms. The partitions have windows of lengths $l_{12} = 0.20 \times 300 = 60$ and $l_{23} = 0.25 \times$

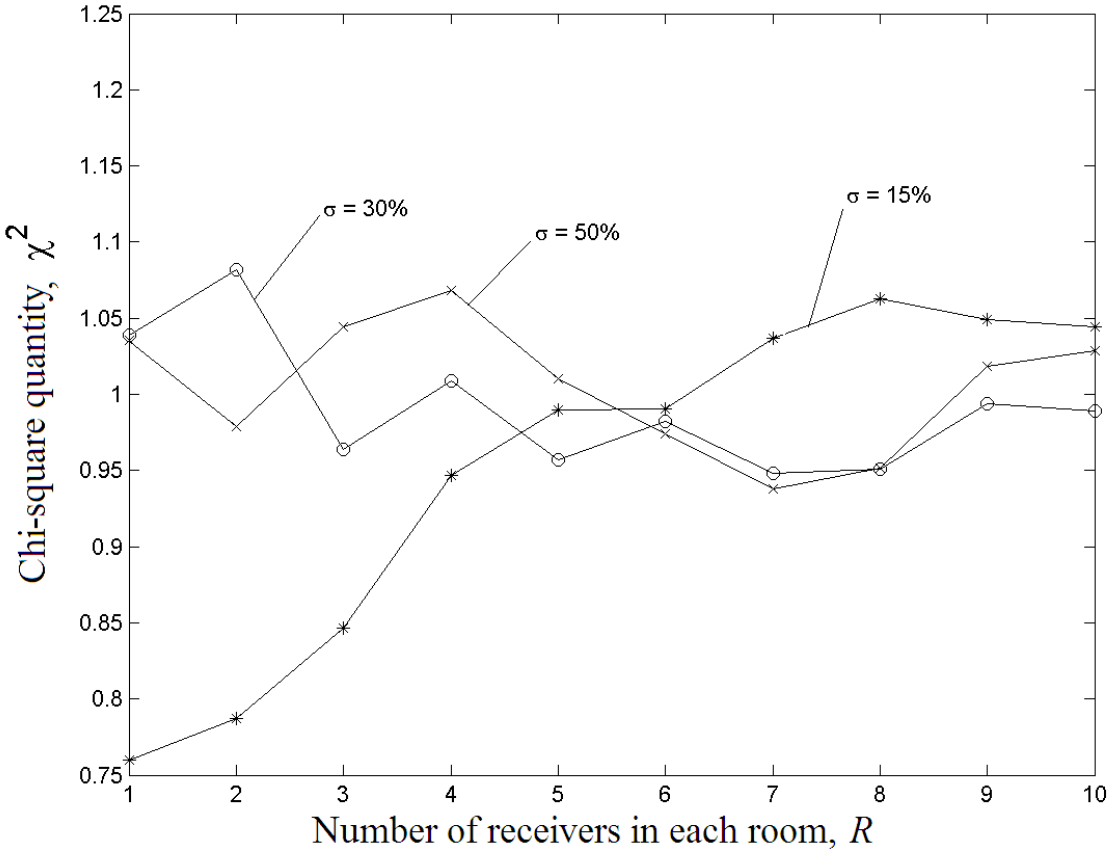

Figure 2.4: The χ^2 value after the fit for various numbers of receivers and noise amplitudes. This value fluctuates randomly about unity as it should. The value of χ^2 shows that the fit is good even for a small number of receivers and large noise amplitudes.

$300 = 75$, allowing energy to flow between the rooms. Therefore, the parameters of Eq. (2.8) with mode counts (with $l_{13} = 0$) approximated by:

$$\mathbf{h}_n = \frac{2\pi f^2}{c^2}(\text{area}_i)\Delta f, \tag{2.26}$$

$$[\mathbf{d}] = \frac{c}{\pi}\begin{bmatrix} l_{12}+l_{13} & -l_{12} & -l_{13} \\ -l_{12} & l_{12}+l_{23} & -l_{23} \\ -l_{13} & -l_{23} & l_{13}+l_{23} \end{bmatrix} \times \frac{\text{number of modes}}{\text{area}}, \tag{2.27}$$

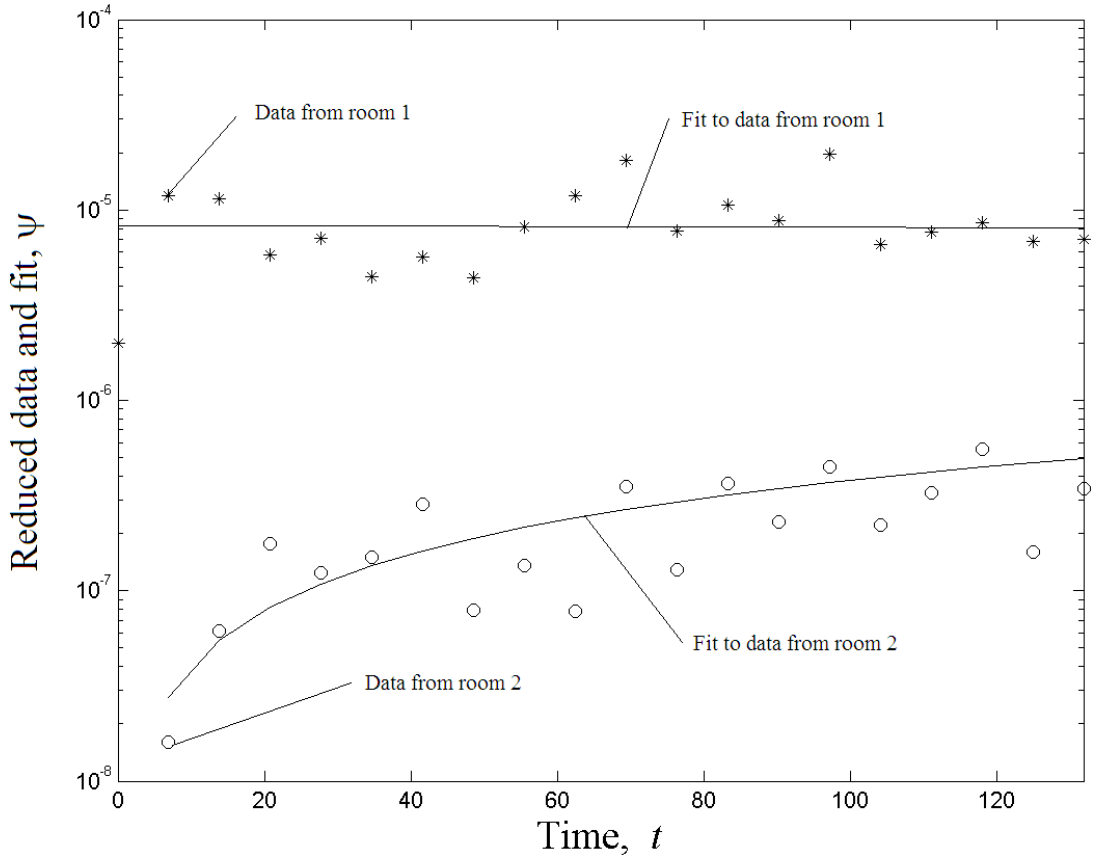

Figure 2.5: An example of the actual fit to the data with noise fluctuations $\sigma = 50\%$. The source in room 1. The overall fit was to data from 10 receivers in each room.

where c is the velocity of the waves, f is the center frequency of the frequency band, and Δf is the bandwidth. The velocity and frequency are taken here to be unity, and the bandwidth is taken to be $1/2\pi$ for the purposes of the artificial simulations. The $\{\psi\}$s thus represent modal energy density, plotted in Fig. 2.7. These parameters result in a first nontrivial eigenvalue of about 4.7×10^{-4} and second nontrivial eigenvalue of about 22.5×10^{-4}. The gains in the $[g]$ matrix were taken from a set of uniformly distributed numbers $[\frac{1}{2}, 2]$.

We consider three data sets, each with a total of 30 receivers, 10 in each room, and took data from three "experiments" corresponding to sources in each of the three rooms. Data were examined

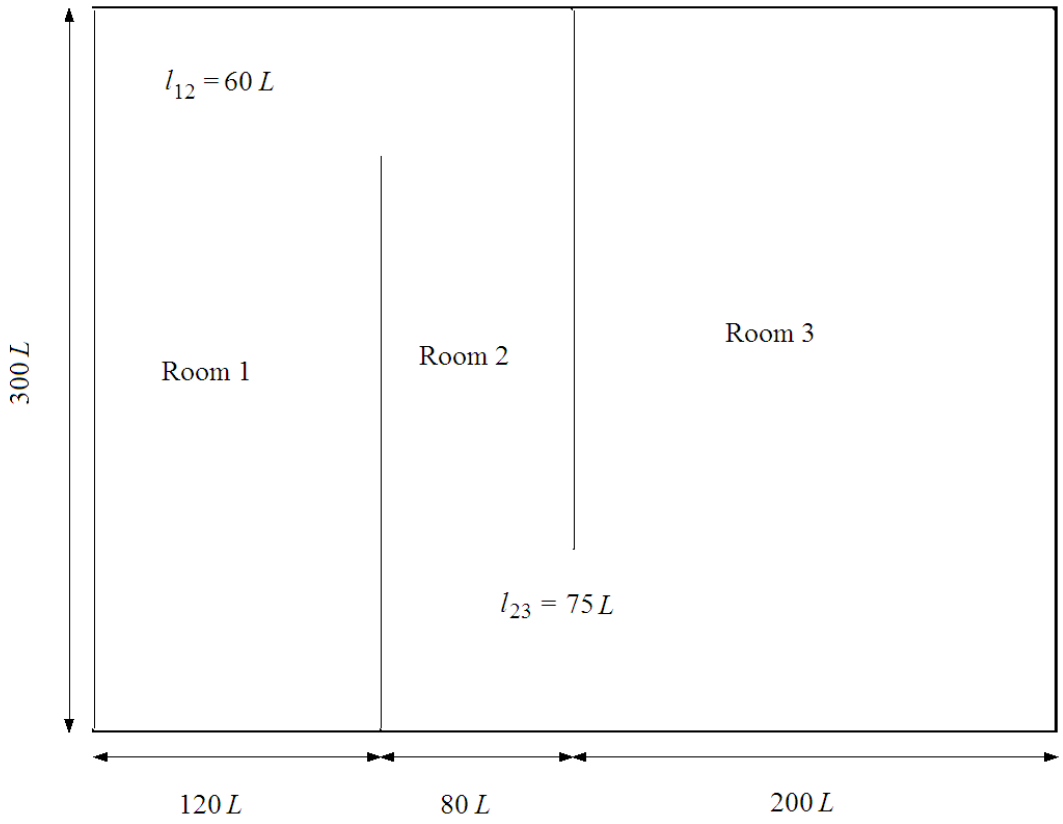

Figure 2.6: Geometry of the system described in Section 2.3. The window coupling rooms 1 and 2 is $l_{12} = 60$ units wide and the window coupling rooms 2 and 3 is $l_{23} = 75$ units wide.

out to one-half of the longer decay time, i.e., $t_{\max} = 1060$, and 20 data points were constructed for each receiver at evenly spaced times. Fractional fluctuations from the mean energy density were different in each data set and taken to be $\sigma = 0\%$, $\sigma = 15\%$, and $\sigma = 30\%$.

2.3.2 Fitting procedure

We seek to fit the form of Eq. (2.20) with $N = 3$ to the data. Since $\{\mathbf{v}\}^1$ is completely known and $\{\mathbf{V}\}^1$ is taken to be known for the three source locations considered, those associated elements of $[g]$ can be calculated completely by Eq. (2.17). One element of one of the higher eigenvectors in

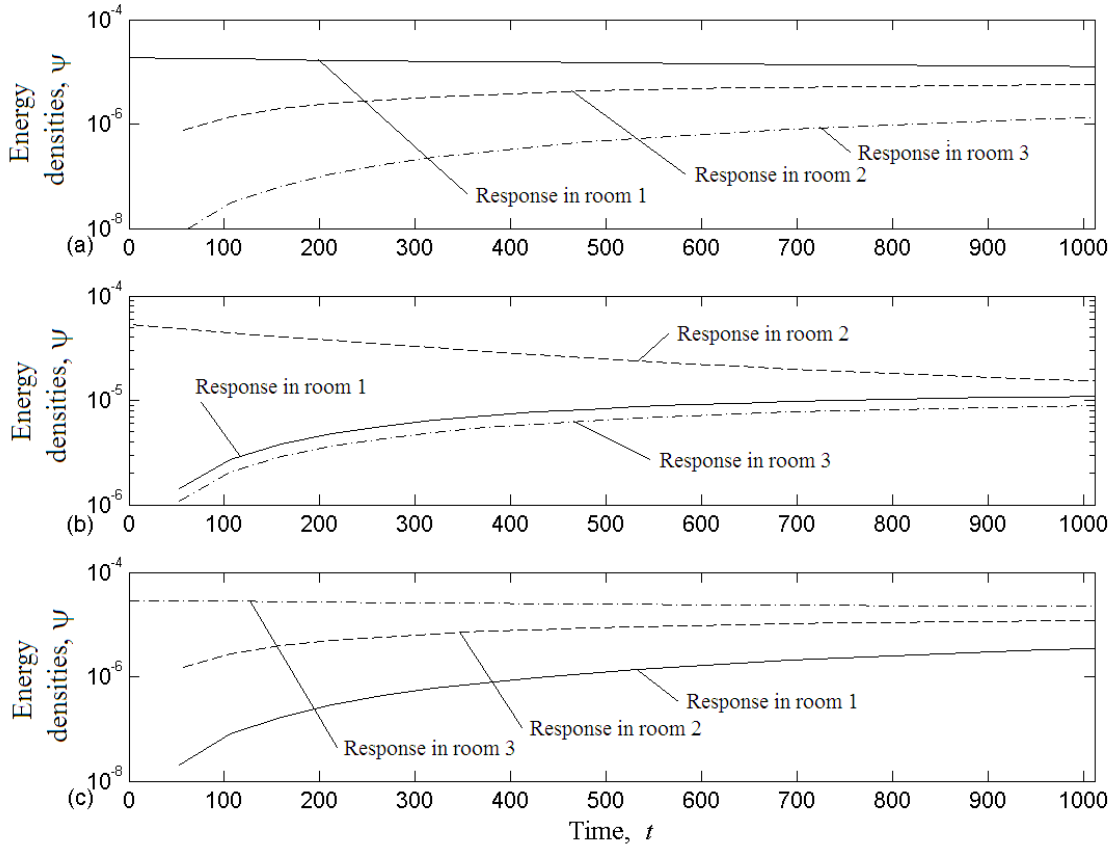

Figure 2.7: The evolution of energy density in each of the three rooms for the period analyzed in Section 2.3. The eigenvalues are $\lambda_1 = 0$, $\lambda_2 = 4.7 \times 10^{-4}$, and $\lambda_3 = 22.5 \times 10^{-4}$. The eigenvectors are $\{\mathbf{v}\}^1 = \{2.9; 2.9; 2.9\} \times 10^{-3}$, $\{\mathbf{v}\}^2 = \{4.0; 0.47; -2.7\} \times 10^{-3}$, and $\{\mathbf{v}\}^3 = \{1.8; -5.8; 1.2\} \times 10^{-3}$. Total time considered was $\frac{1}{2}\frac{1}{\lambda_3}$. (a) A single source in room 1. (b) A single source in room 2. (c) A single source in room 3.

the energy description must be adjusted in the fitting procedure. All that remains is to calculate the remaining elements of $\{\mathbf{v}\}^2$ and $\{\mathbf{v}\}^3$ using the five remaining orthogonality conditions. The solution can be found in Appendix B.

The eigenvalues λ_2 and λ_3, the element $\mathbf{v}_1^2$ of the eigenvectors, and the 27 elements of $[g]$ not already taken to be known are the adjusted parameters.

2.3.3 Results

We evaluate the performance of our algorithm by scrutinizing the best fits to the eigenvalues and the value of χ^2 associated with the best fit. The best fits to the eigenvalues are plotted in Fig. 2.8 for different numbers of receivers in each room and different noise levels. The fit algorithm does

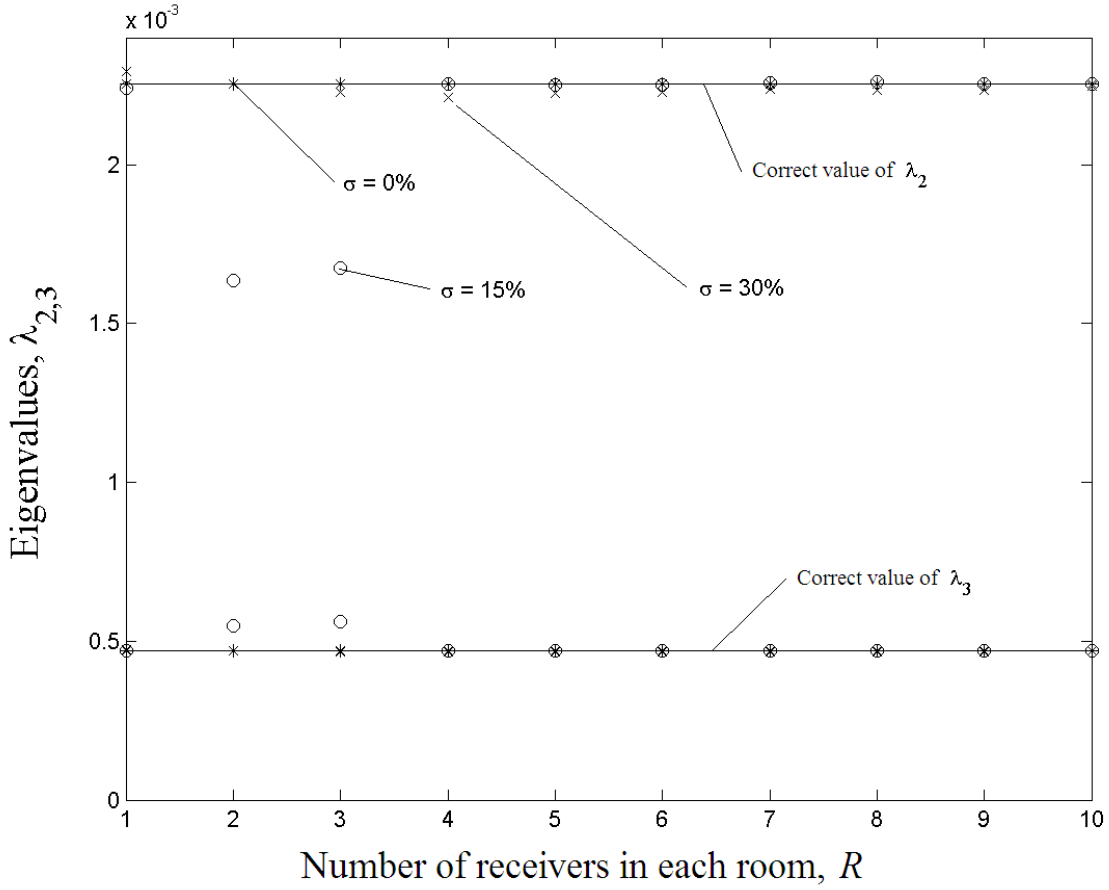

Figure 2.8: The best fit to λ_2 and λ_3 for the three room system for various numbers of receivers in each room and noise levels. The fit is good with enough receivers present. The algorithm does not work well with higher noise amplitudes and/or less time.

find the best fit to the decay times if enough receivers are considered.

If more receivers are considered in the data set (not shown), the fit fails because of the higher number of parameters (gains) that need to be adjusted in the fit procedure. The correct global

minimum χ^2 was not found; instead some other local minimum was found. This failure to find the global minimum may be surprising given that adding an extra receiver adds extra data to which to fit the parameters. It must be noted, however, that the fit in the three-room case is much more difficult overall than the fit in the two-room case because the space that the fit algorithm must explore is much larger. Also, if higher noise amplitudes and/or less time is scrutinized, the fit fails to find the correct eigenvalues.

It is seen (Fig. 2.9) that the χ^2 value is about unity for a sufficient number of receivers and

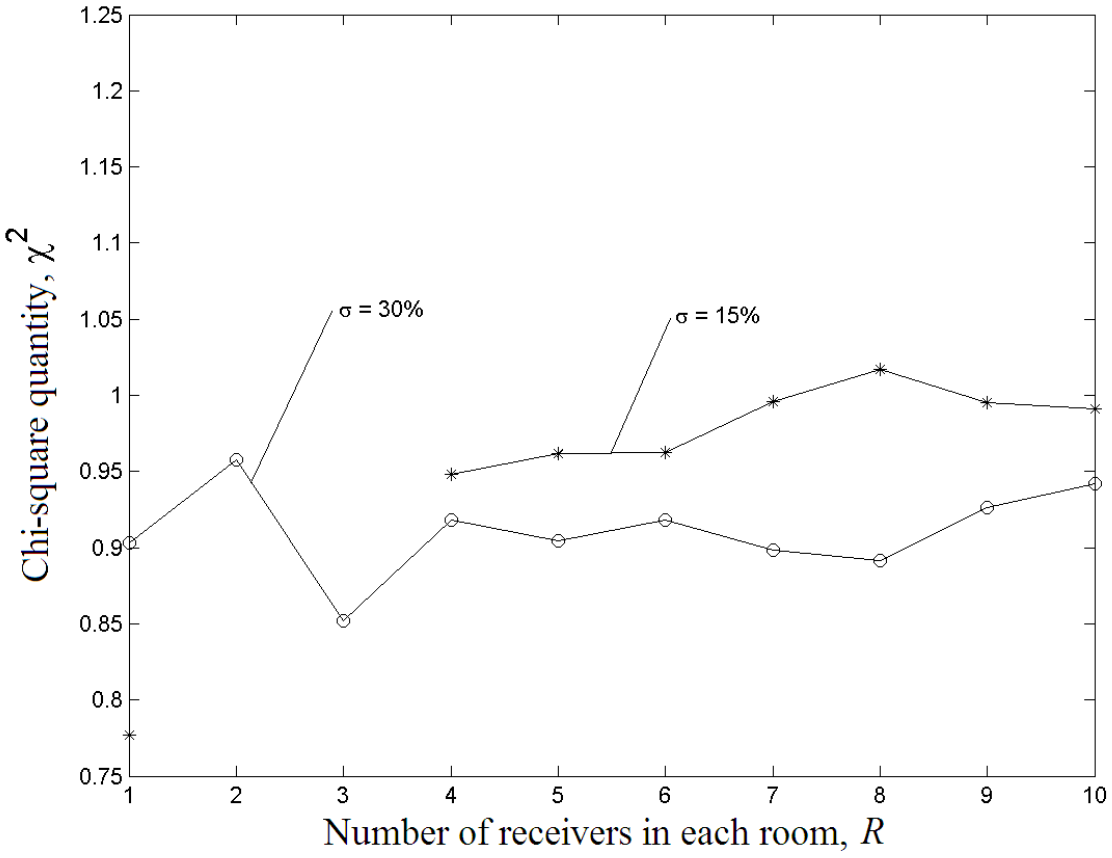

Figure 2.9: The χ^2 value after the fit for various numbers of receivers and noise amplitudes. This value should fluctuate about unity. The large values of χ^2 for few receivers and low noise amplitude (omitted) reflect the lack of good fit. Other values close to unity show that the fit is good in the presence of a sufficient number of receivers.

sufficiently low noise. The value of χ^2 is large (data points not plotted) when only a few receivers in each room are considered for the lower noise level. These large values indicate that the fit failed in those cases; a local, and wrong, minimum was found. The best fit to some of the data is plotted along with the data in Fig. 2.10.

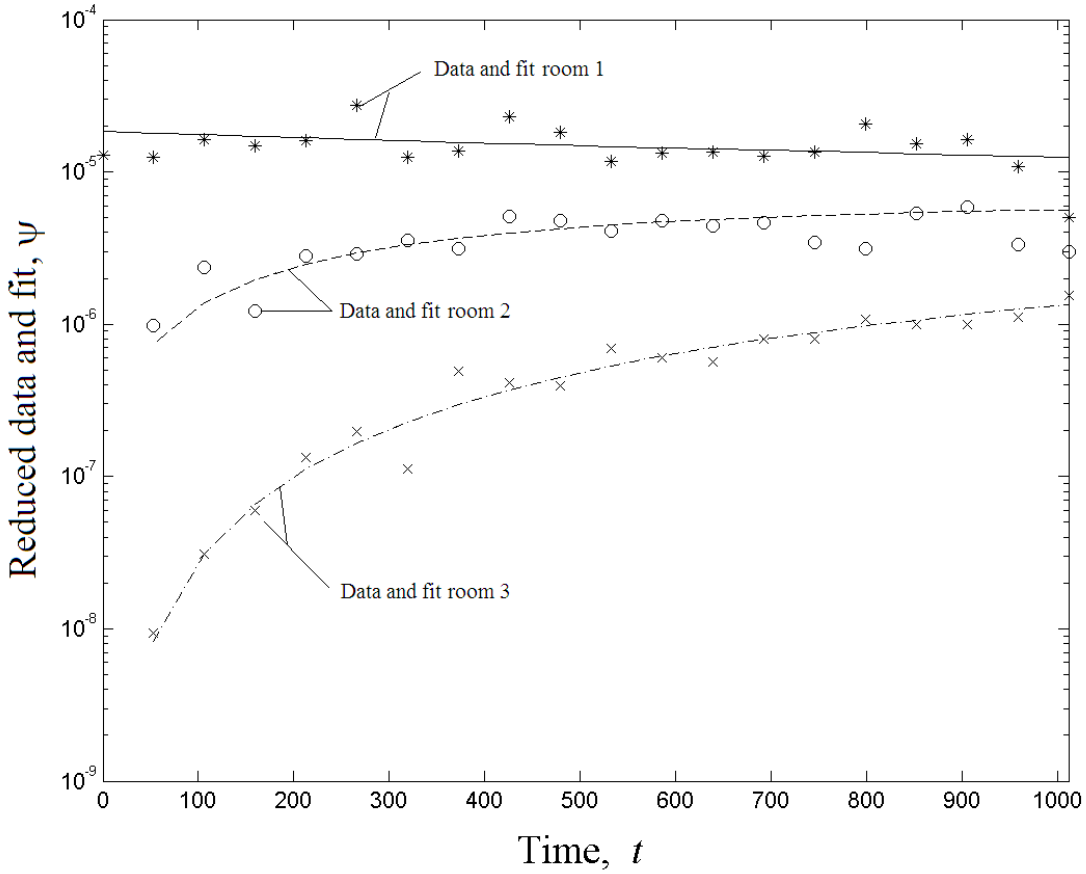

Figure 2.10: An example of the actual fit to the data with noise fluctuations $\sigma = 30\%$. The source in room 1. The overall fit was to data from 10 receivers in each room.

The fitting algorithm in this three-room case is successful, but not as robust as for the two-room case. In particular, the large amount of time needed for a successful fit in the three-room case is disturbing. There is evidence, however, that the lack of robustness is due to the numerical fit algorithm, not the χ^2 formulation. The Newton algorithm finds *a* minimum of Eq. (2.24b), but

does not necessarily find the *global* minimum. When better "first guesses" are used in the Newton algorithm for the eigenvalues and eigenvector element, the fit is successful even when data was examined only out to $t_{\max} = 210$. This better fit under different initial conditions suggests that another numerical minimization algorithm, such as a simplex method or simulated annealing[54] might be preferable.

It is noteworthy that accurate fits (and correct eigenvalues and eigenvectors) can be obtained when only short times are analyzed. This is promising for the ultimate application to DNS data for which long time calculations are expensive. In the next chapter we present a different energy transport theory that does not rely on any fitting procedure or an a priori assumption of diffusive energy transport.

Chapter 3

Concatenation

 Only minor changes have been made in style and organization to fit the context of this thesis. Section II in that paper is Section 3.1 in this thesis.

3.1 A concatenation ansatz

Toward the end of extracting [**H**] and [**D**] in Eq. (2.1), we now present a different model, which we call the "concatenation ansatz."

3.1.1 The model

Consider a set of receivers in an undamped structure, each of which may in principle also act as a source. The intensity Ψ_{rs} at receiver r from a unit band-limited impulsive source at s $\Pi_s(t) =< F^2(t) >= \delta(t)$, i.e., the squared-displacement response smoothed over time, over a frequency band, and possibly over nearby receivers, is denoted as $\widehat{\mathbf{J}}_{rs}$(t). Note that the term "impulsive source" applied to band-limited mean-square forcing is a short-duration tone burst on the inner fast time scale $1/\omega$.

Now consider a version of $\widehat{\mathbf{J}}$ with limited information

$$\widehat{\mathbf{J}}^{\Delta}_{rs}(t) = \widehat{\mathbf{J}}_{rs}(t)e^{-\Delta t}. \tag{3.1}$$

This $\widehat{\mathbf{J}}^{\Delta}$ is sensitive only to transport at short times $t < O(1/\Delta)$. The information in $\widehat{\mathbf{J}}^{\Delta}_{rs}(t)$ may be generated directly in the frequency domain. As an alternative, $e^{-\Delta t}$ might be replaced by a rectangular window $\Theta(1/\Delta - t)$, in which case $\widehat{\mathbf{J}}^{\Delta}_{rs}(t)$ is probably generated most efficiently by a time domain DNS. Either an exponential or a rectangular window emphasizes early times over late times, and $\widehat{\mathbf{J}}^{\Delta}_{rs}$ can be obtained at small computational cost.

The proposed ad hoc concatenation ansatz consists of attempting to construct the intensity at later times by "relaunching" or "bootstrapping"[55] the decayed intensity continuously in time by some weight, $\mathbf{Q}_{rs}$, for each source/receiver. Formally,

$$\widehat{\mathbf{J}}^{\text{concat}}_{rs}(t) = \widehat{\mathbf{J}}^{\Delta}_{rs}(t) + \int_0^t \widehat{\mathbf{J}}^{\Delta}_{r\sigma}(t-\tau)\mathbf{Q}_{\sigma\rho}\widehat{\mathbf{J}}^{\text{concat}}_{\rho s}(\tau)\mathrm{d}\tau. \tag{3.2}$$

Equation (3.2) may be solved by iteration, resulting in

$$\widehat{\mathbf{J}}^{\text{concat}} = \widehat{\mathbf{J}}^{\Delta} + \widehat{\mathbf{J}}^{\Delta} \otimes \mathbf{Q}\widehat{\mathbf{J}}^{\Delta} + \widehat{\mathbf{J}}^{\Delta} \otimes \mathbf{Q}\widehat{\mathbf{J}}^{\Delta} \otimes \mathbf{Q}\widehat{\mathbf{J}}^{\Delta} + \cdots, \tag{3.3}$$

where $\otimes$ represents a convolution. Each term of Eq. (3.3) is a concatenation of short-time propagations, $\widehat{\mathbf{J}}^{\Delta}$. After taking a Fourier transform,

$$\mathbf{J}_{rs}(\Omega) = \int_{-\infty}^{\infty} \widehat{\mathbf{J}}_{rs}(t)e^{-i\Omega t}\mathrm{d}t, \tag{3.4}$$

and shifting to matrix notation, Eq. (3.2) becomes

$$\left[\mathbf{J}^{\text{concat}}(\Omega)\right] = \left[\mathbf{J}^{\Delta}(\Omega)\right] + \left[\mathbf{J}^{\Delta}(\Omega)\right]\left[\mathbf{Q}\right]\left[\mathbf{J}^{\text{concat}}(\Omega)\right]. \tag{3.5}$$

Note that the Fourier transform variable in Eq. (3.4) is the outer frequency Ω of the slow-time energy transport. This is not the inner frequency ω of displacement data obtained in a DNS of the system. The solution of Eq. (3.5) is

$$\left[\mathbf{J}^{\text{concat}}(\Omega)\right] = \left(\left[\mathbf{I}_S\right] - \left[\mathbf{J}^{\Delta}(\Omega)\right]\left[\mathbf{Q}\right]\right)^{-1}\left[\mathbf{J}^{\Delta}(\Omega)\right] = \left(\left[\mathbf{J}^{\Delta}(\Omega)\right]^{-1} - \left[\mathbf{Q}\right]\right)^{-1}, \tag{3.6}$$

where $[\mathbf{I}_S]$ is the $S \times S$ identity matrix, and S is the total number of sources. Thus, $[\mathbf{J}^{\text{concat}}]$ is readily constructed for all times, not only $t < O(1/\Delta)$.

The weights $[\mathbf{Q}]$ of relaunching are determined by solving the equation (details are left to Appendix C)

$$\left(\left[\mathbf{I}_S\right] - \left[\mathbf{J}^{\Delta}(0)\right]\left[\mathbf{Q}\right]\right)\{E\} = 0. \tag{3.7}$$

The array $\{E\}$ contains the admittances given by Eq. (1.18). Equation (3.7) enforces the relative intensity distribution demanded by equipartition[38] in $\left[\widehat{\mathbf{J}}^{\text{concat}}(t \to \infty)\right]$.

Explicit reference to the argument $\Omega = 0$ will be dropped unless needed for clarity. Equation (3.7) has a unique solution for $[\mathbf{Q}]$ if $[\mathbf{Q}]$ is assumed Ω independent and diagonal, implying that the intensity relaunched from receiver r depends only on the intensity observed at receiver r, and only on the intensity observed at the same instant as the relaunching. It is reassuring that large Δ corresponds to small $\mathbf{J}^{\Delta}$ (cf. Eq. (3.1)) and large $[\mathbf{Q}]$ (cf. Eq. (3.2)), thus requiring stronger relaunching to compensate for the rapid decay Δ. Formal solution of Eq. (3.7) for $[\mathbf{Q}]$ is awkward.

One can obtain a column array,

$$\{\mathbf{Q}\} = [E_{\text{inv}}] \left[\mathbf{J}^{\Delta}\right]^{-1} \{E\}\,, \tag{3.8}$$

consisting of the diagonal elements of $[\mathbf{Q}]$, where $[E_{\text{inv}}]$ is a diagonal matrix with elements $1/E_s$.

Requiring the correct relative intensities $\{E\}$ to be reproduced in $\left[\widehat{\mathbf{J}}^{\text{concat}}(t \to \infty)\right]$ leads the condition Eq. (3.7). Requiring the correct absolute intensities Eq. (1.16) leads to (details left to Appendix D)

$$N_D = -\{E\}^T \left[\mathbf{J}^{\Delta}\right]^{-1} \left[\mathbf{J}^{\Delta}\right]' [\mathbf{Q}]\,\{E\}\,, \tag{3.9}$$

where $[\mathbf{J}(\Omega)]' \equiv \frac{\partial}{\partial i\Omega}[\mathbf{J}(\Omega)]$, and i is the imaginary unit. This is a condition on the concatenation ansatz. It is interesting that the right-hand side of Eq. (3.9) may be calculated with no knowledge of the size of the structure, to which N_D is proportional. Thus Eq. (3.9) is a nontrivial condition. Presumably, if all important information is implicit in the limited data $\left[\mathbf{J}^{\Delta}\right]$ and $\{E\}$, then N_D obtained by Eq. (3.9) will be identical to an independently obtained estimate from, e.g., a Weyl series. If not, then some important information has not been accounted for, perhaps by neglecting to place a receiver in some substructure.

3.1.2 Diffusion limit

In the low Ω limit, the solution Eq. (3.6) of Eq. (3.2) may be recognized as the solution of a diffusion equation of the form in Eq. (2.1). We wish to enforce the equality

$$\left[\mathbf{J}^{\text{concat}}(\Omega)\right] = \left(\left[\mathbf{J}^{\Delta}(\Omega)\right]^{-1} - [\mathbf{Q}]\right)^{-1} = (i\Omega[\mathbf{H}] + [\mathbf{D}])^{-1} \tag{3.10}$$

as $\Omega \to 0$. After expanding the left-hand side in $i\Omega$, one identifies

$$[\mathbf{D}] = \left[\mathbf{J}^{\Delta}(0)\right]^{-1} - [\mathbf{Q}]\,, \text{ and} \tag{3.11a}$$

$$[\mathbf{H}] = -\left[\mathbf{J}^{\Delta}(0)\right]^{-1}\left[\mathbf{J}^{\Delta}(0)\right]'\left[\mathbf{J}^{\Delta}(0)\right]^{-1}. \tag{3.11b}$$

Thus the parameters $[\mathbf{H}]$ and $[\mathbf{D}]$ of a diffusion model follow directly from raw data $\left[\mathbf{J}^{\Delta}\right]$. It is interesting that $[\mathbf{H}]$ need not be diagonal, nor must $[\mathbf{D}]$ have support only between physically connected substructures. Recall the previous discussions[2,32] on indirect CLFs.

If raw data $\left[\mathbf{J}^{\Delta}\right]$ happens to be exactly diffusive, i.e., a solution to Eq. (2.1) without fluctuations, one deduces that the parameters $[\mathbf{H}]$ and $[\mathbf{D}]$ are recovered exactly. We take the data to be the solution of Eq. (2.1) with matrices $[\mathbf{d}]$ and diagonal $[\mathbf{h}]$, so

$$\left[\mathbf{J}^{\Delta}(\Omega)\right] = \left((i\Omega + \Delta)\,[\mathbf{h}] + [\mathbf{d}]\right)^{-1}. \tag{3.12}$$

It follows from Eq. (3.11b) that

$$[\mathbf{H}] = -\left[\mathbf{J}^{\Delta}(0)\right]^{-1}\left[\mathbf{J}^{\Delta}(0)\right]'\left[\mathbf{J}^{\Delta}(0)\right]^{-1} = \left(\left[\mathbf{J}^{\Delta}\right]^{-1}\right)'\Big|_{\Omega=0} = [\mathbf{h}]\,, \tag{3.13}$$

which shows that $[\mathbf{H}]$ is correctly recovered by the concatenation ansatz. It also follows from Eq. (3.11a) that

$$[\mathbf{D}] = \left[\mathbf{J}^{\Delta}(0)\right]^{-1} - [\mathbf{Q}] = \Delta\,[\mathbf{h}] + [\mathbf{d}] - [\mathbf{Q}]\,. \tag{3.14}$$

Thus, $[\mathbf{D}] = [\mathbf{d}]$ if $[\mathbf{Q}] = \Delta[\mathbf{h}]$. We confirm that the diagonal matrix $[\mathbf{Q}] = \Delta[\mathbf{h}]$ satisfies Eq. (3.7):

$$([\mathbf{I}_S] - \left[\mathbf{J}^{\Delta}\right] \Delta[\mathbf{h}]) \{E\} = \left([\mathbf{I}_S] - \left[\mathbf{J}^{\Delta}\right] \left(-[\mathbf{d}] + \left[\mathbf{J}^{\Delta}\right]^{-1}\right)\right) \{E\} = -\left[\mathbf{J}^{\Delta}\right] ([\mathbf{D}] \{E\}) = 0. \quad (3.15)$$

That $[\mathbf{D}] \{E\}$ is zero follows from identifying $\{E\}$ with the first eigenvector $\{\mathbf{V}\}^1$.

Finally, the condition Eq. (3.9) is satisfied exactly:

$$N_D = -\{E\}^T \left[\mathbf{J}^{\Delta}\right]^{-1} \left[\mathbf{J}^{\Delta}\right]' [\mathbf{Q}] \{E\} \quad (3.16a)$$

$$= \{E\}^T \left(\left[\mathbf{J}^{\Delta}\right]^{-1}\right)' \left[\mathbf{J}^{\Delta}\right] [\mathbf{Q}] \{E\} \quad (3.16b)$$

$$= \{E\}^T \left(\left[\mathbf{J}^{\Delta}\right]^{-1}\right)' \{E\} \quad (3.16c)$$

$$= \{E\}^T [\mathbf{H}] \{E\} = 1. \quad (3.16d)$$

In summary, closed form expressions for the parameters $[\mathbf{H}]$ and $[\mathbf{D}]$ of a diffusion model have been obtained. They depend on data describing energy flow on short-time scales. If the data are perfectly diffusive, the diffusion parameters the method extracts are exact (and, thus, invariant under Δ, as they ought to be to have meaning and usefulness). Moreover, a generalization to nondiffusive regimes is predicted for Ω away from the low Ω limit.

Weaknesses of the above model include an assumption of diffusion: the model is set up to extract diffusion parameters in the zero Ω limit. If diffusion fails at $\Omega \to 0$ (e.g., in the presence of Anderson localization[11]), the model must fail also. Also, with a view toward DNS simulations where receivers are relatively inexpensive compared to sources, there is a question of how to make use of receivers not allowed to act as sources so that E_r is unknown. One answer may be to use

receivers that are close to sources such that their admittances can be estimated to be the same as those of the sources. Finally, it may be remarked that this concatenation method uses only magnitude information, i.e., the mean squares of the DNS responses. Relative phases are ignored; it is not yet clear what, if any, useful information is thereby neglected.

The present approach is tested in later chapters. In Chapter 4 the model is tested on DNS of two- and three-room systems, systems typically studied with SEA. In Chapter 6 the model is tested on three coupled plates, also typically studied with SEA. Finally, in Chapter 7, we study a hybrid system not typically studied with SEA. In the next section, we develop the concatenation theory for pure diffusion in the absence of substructures.

3.2 Pure diffusion

Section 3.1 contained the development of the concatenation theory inspired by conduction, most appropriate for systems that can be partitioned into substructures. In this section, we develop the concatenation theory in such a way that it can be appropriately applied to systems that do not admit substructures. Such a system will be studied in Chapter 5. Consider a one-dimensional, infinite homogeneous structure with diffusivity constant α. The proper *diffusion* equation governing energy flow in the structure is

$$-\alpha\frac{\partial^2}{\partial x^2}\widehat{\mathbf{J}}_{xy}+\frac{\partial}{\partial t}\widehat{\mathbf{J}}_{xy}=\delta(x-y)\delta(t), \tag{3.17}$$

where $\widehat{\mathbf{J}}_{xy}$ is the intensity of the response at location x and time t due to a source at location y and time zero.

We define the Fourier transform in time as

$$\mathbf{J}_{xy} = \int_{-\infty}^{\infty} \widehat{\mathbf{J}}_{xy} e^{-i\Omega t} \mathrm{d}t \tag{3.18}$$

and the spatial Fourier transform as

$$\overline{\mathbf{J}}_{xy} = \int_{-\infty}^{\infty} \widehat{\mathbf{J}}_{xy} e^{iq(x-y)} \mathrm{d}x. \tag{3.19}$$

Then, the spatial and temporal Fourier transform of $\widehat{\mathbf{J}}_{xy}$ is

$$\overline{\mathbf{J}}_{xy} = \frac{1}{\alpha q^2 + i\Omega}. \tag{3.20}$$

The inverse spatial transform

$$\mathbf{J}_{xy} = \frac{i}{2\alpha} \frac{e^{-i(x-y)\sqrt{-i\Omega/\alpha}}}{\sqrt{-i\Omega/\alpha}} \tag{3.21}$$

can be obtained by evaluating residues. We use the exponential weighting of early-time data $\widehat{\mathbf{J}}^{\Delta}_{xy} = \widehat{\mathbf{J}}_{xy} e^{-\Delta t}$, so that $\mathbf{J}^{\Delta}_{xy} = \mathbf{J}_{xy}(\Omega - i\Delta)$. The last formula with Eq. (3.21) results in

$$\mathbf{J}^{\Delta}_{xy}(0) = \frac{1}{2\sqrt{\Delta/\alpha}} e^{-|x-y|\sqrt{\Delta/\alpha}}, \tag{3.22}$$

and

$$\left(\mathbf{J}^{\Delta}_{xy}\right)'(0) = -\frac{1}{4}\frac{\sqrt{\alpha}}{\Delta^{3/2}} e^{-|x-y|\sqrt{\Delta/\alpha}} \left\{1 + \sqrt{\Delta/\alpha}|x-y|\right\}. \tag{3.23}$$

We note that the dimensionless group $d\sqrt{\Delta/\alpha}$, where d is the receiver spacing, appearing implicitly in Eq. (3.22) is an important parameter in this pure diffusion case. This parameter will be

studied later in Chapter 5. To calculate $\left[\mathbf{J}^{\Delta}\right]^{-1}$, we approximate the matrix product

$$\sum_{z} \mathbf{J}^{\Delta}_{xz} \left(\mathbf{J}^{\Delta}_{zy}\right)^{-1} = \delta_{xy} \tag{3.24}$$

as

$$\frac{1}{d}\int_{-\infty}^{\infty} \mathbf{J}^{\Delta}(x-z) \left(\mathbf{J}^{\Delta}(z-y)\right)^{-1} \mathrm{d}z = d\delta(x-y), \tag{3.25}$$

where $\delta(x)$ is the Dirac delta distribution, and obtain

$$\left(\mathbf{J}^{\Delta}_{xy}\right)^{-1} = d^2 \left(\frac{\Delta}{\alpha}\delta(x-y) - \delta''(x-y)\right). \tag{3.26}$$

The $[\mathbf{Q}]$ matrix is obtained from Eq. (3.7),

$$\left([\mathbf{I}] - \left[\mathbf{J}^{\Delta}\right][\mathbf{Q}]\right)\{E\} = 0, \tag{3.27}$$

where all the the Es are unity, and $[\mathbf{Q}] = Q[\mathbf{I}]$ due to translational invariance. Then we have

$$\int_{-\infty}^{\infty} \left(\delta(x-y) - Q\int_{-\infty}^{\infty} \mathbf{J}^{\Delta}(x-z)\delta(z-y)dz\right)\mathrm{d}y = 0. \tag{3.28}$$

Evaluating the integrals results in $Q = d\Delta$. There is a more complicated formula for Q if d is not assumed small to approximate the matrix sums as integrals.

Finally,

$$[\mathbf{D}] = \left[\mathbf{J}^{\Delta}\right]^{-1} - [\mathbf{Q}]\,, \text{ or} \tag{3.29a}$$

$$\mathbf{D}_{xy} = -d^2\delta''(x-y), \tag{3.29b}$$

and

$$[\mathbf{H}] = -\left[\mathbf{J}^{\Delta}\right]^{-1}\left[\mathbf{J}^{\Delta}\right]'\left[\mathbf{J}^{\Delta}\right]^{-1}, \text{ or} \tag{3.30a}$$

$$\mathbf{H}_{xy} = \frac{d^2}{\alpha}\delta(x-y). \tag{3.30b}$$

The eigenvalue problem

$$\int_{-\infty}^{\infty}\mathbf{D}(x-y)u(y)\mathrm{d}y = \frac{\lambda}{\alpha}\int_{-\infty}^{\infty}\mathbf{H}(x-y)u(y)\mathrm{d}y \tag{3.31}$$

is satisfied by

$$f_\lambda(x,t) = u(x)e^{-\lambda t} = \left(C_{\lambda 1}\cos\left(\sqrt{\frac{\lambda}{\alpha}}x\right) + C_{\lambda 2}\sin\left(\sqrt{\frac{\lambda}{\alpha}}x\right)\right)e^{-\lambda t} \tag{3.32}$$

for $\lambda \geq 0$, which indeed satisfies the diffusion equation. Similarly to Eqs. (3.12–3.16d), this section proves that if data is the solution to the diffusion equation in Eq. (3.17) without fluctuations, then the parameters $[\mathbf{H}]$ and $[\mathbf{D}]$ are recovered exactly. In Chapter 5, we test the concatenation theory on a statistically homogeneous torus without substructures, a system to which SEA cannot be applied.

Instead, in the next chapter, we proceed to apply the concatenation ansatz to systems typically studied using SEA, those of coupled rooms.

Chapter 4

Applications to two and three rooms

4.1 Data with known diffusive character

Our long-range desire is to be able to apply the concatenation ansatz of Chapter 3 to short-time DNS measured data in order to be able to predict transport dynamics over longer times. Toward this end we here consider an easier toy problem. We generate data artificially and attempt to use the equations of Section 3.1 to recover the parameters of diffusion.

We consider a simple case study of the strict substructuring class, which maps well onto SEA. It has two substructures (rooms). For these studies, admittances (i.e., the elements of $\{E\}$) are taken as known, as if they have been evaluated by a procedure such as that in Weaver's paper[38] for sites with a source. Forcing $\{\Pi\}$ is also known as it would be in a DNS.

4.1.1 Description of data

The data are constructed by solving the time-domain SEA equation Eq. (2.1) describing a simple two-substructure system. With a view toward application to data gleaned from a DNS, with inevitable stochastic fluctuations, we then add noise. Appendix A contains the details of the noise construction method. Noise is generated independently at each r, t such that $\{\Psi\}$ has fixed fractional standard deviation σ. Moreover the fractional standard deviation is $\sigma = 1/\sqrt{\Delta f \Delta t}$ in real DNS applications or measurements where Δf is the bandwidth, and Δt is the duration of the time window over which energies are averaged. As discussed in Section 2.2.1, these noise characteristics are typical in stochastic wave systems.

For a sample interesting structure, the diffusion parameters were chosen as

$$[\mathbf{H}] = \begin{bmatrix} 1 & 0 \\ 0 & \frac{1}{2} \end{bmatrix} \qquad \text{and} \qquad [\mathbf{D}] = \begin{bmatrix} 1 & -\frac{1}{2} \\ -\frac{1}{2} & \frac{1}{4} \end{bmatrix}, \tag{4.1}$$

corresponding to a system where one room (room 1) is twice the size of the other room (room 2),

similar to the system in Fig. 2.1. These choices for $[\mathbf{H}]$ and $[\mathbf{D}]$ result in parameters

$$\lambda_1 = 0, \tag{4.2a}$$

$$\lambda_2 = 1.5, \tag{4.2b}$$

$$\{\mathbf{V}\}^1 = \left\{ \begin{array}{c} 1 \\ \\ 2 \end{array} \right\} / \sqrt{3}, \tag{4.2c}$$

$$\{\mathbf{V}\}^2 = \left\{ \begin{array}{c} 1 \\ \\ -1 \end{array} \right\} / \sqrt{1.5}. \tag{4.2d}$$

The array of admittances was taken to be $\{E\} = \{\mathbf{V}\}^1$.

The fundamental solution $\left[\widehat{\mathbf{J}}(t)\right]$ of Eq. (2.1) was constructed for times t out to $T = 100/\lambda_2$, i.e., 100 times the characteristic diffusion time. Data points were spaced by $\delta t = 10^{-2}/\lambda_2$. The information window $e^{-\Delta t}$ was restricted to emphasize time ranges from one time step ($\Delta = 100\lambda_2$) to the full domain ($\Delta = \lambda_2/100$). A few noise amplitudes were considered, in particular $\sigma = 0\%, 10\%, 20\%, 30\%$. Explicitly,

$$\widehat{\mathbf{J}}_{rs}(t) = \left(\mathbf{V}_r^1 \mathbf{V}_s^1 + \mathbf{V}_r^2 \mathbf{V}_s^2 e^{-\lambda_2 t} \right) \times \chi_{rs}(t), \tag{4.3}$$

where χ is a chi-square distributed random number with unity mean and σ standard deviation.

The Fourier transforms needed for Eqs. (3.11a) and (3.11b) are calculated by

$$\left[\mathbf{J}^\Delta(0)\right] = \int_0^T \left[\widehat{\mathbf{J}}(t)\right] e^{(-i\Omega-\Delta)t} \mathrm{d}t \Big|_{\Omega=0} = \int_0^T \left[\widehat{\mathbf{J}}(t)\right] e^{-\Delta t} \mathrm{d}t, \tag{4.4}$$

$$\left[\mathbf{J}^\Delta(0)\right]' = \frac{\partial}{\partial i\Omega} \int_0^T \left[\widehat{\mathbf{J}}(t)\right] e^{(-i\Omega-\Delta)t} \mathrm{d}t \Big|_{\Omega=0} = \int_0^T -t \left[\widehat{\mathbf{J}}(t)\right] e^{-\Delta t} \mathrm{d}t. \tag{4.5}$$

Estimated matrices [**Q**], [**D**], and [**H**] are then obtained from Eqs. (3.8), (3.11a), and (3.11b).

4.1.2 Results and discussion

A plot of the recovered first nontrivial eigenvalue of the estimated [**D**] and [**H**] matrices is shown in Fig. 4.1. The recovered value is accurate except at exceptionally small values of Δ. This inaccuracy

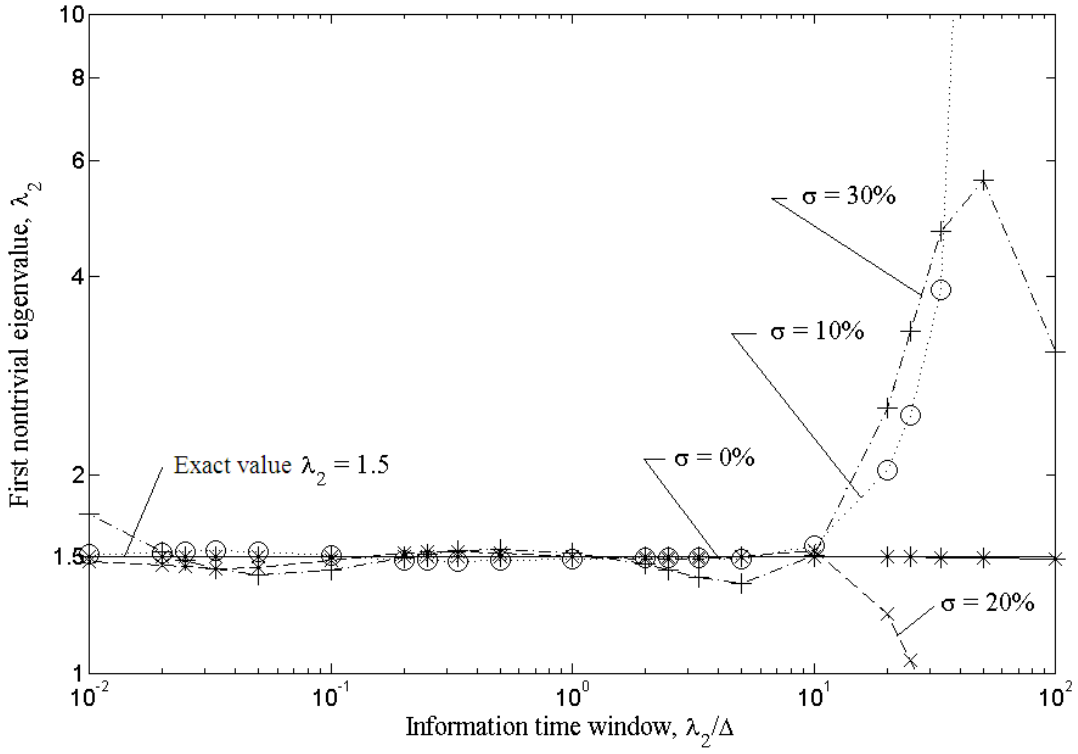

Figure 4.1: First nontrivial eigenvalue for the artificial system is plotted versus a dimensionless measure of the duration of the information window $e^{-\Delta t}$. The extracted eigenvalue is good when sufficient information is retained. The method fails at low Δ (large time window duration) because of an uninteresting cutoff in the numerical integration. Even with large Δ (short time window duration), corresponding to little information retained, the extracted eigenvalue is close to the known value.

at small Δ is related to the cutoff in the numerical time integration. The error stemming from the cutoff is

$$\frac{\int_0^\infty te^{-\Delta t}\mathrm{d}t - \int_0^T te^{-\Delta t}dt}{\int_0^\infty te^{-\Delta t}\mathrm{d}t} = T\Delta e^{-T\Delta} + e^{-T\Delta}, \tag{4.6}$$

which is about 10% when $T\Delta$ is about 3.9. This cutoff explains the low Δ behavior of Fig. 4.1. That said, this error is uninteresting: it simply means that simulations (Eq. (4.3)) need to extend over some minimum multiple of $1/\Delta$ to achieve accuracy in the time integrations in Eqs. (4.4) and (4.5). In any case, small Δ is irrelevant to ultimate applications.

What is more striking is the accuracy for large Δ. As noted above, the largest value of Δ considered corresponds to retaining information in $\left[\mathbf{J}^{\Delta}\right]$ only through times of order $1/100\lambda_2$. Even with so little data effectively being used in the extraction of the diffusion parameters, both in an absolute sense and in a sense relative to how much information there is about the diffusion in the data, the program nevertheless extracts the correct eigenvalue. The implication is that Δ needs be chosen small enough only to capture the earliest stages of diffusive transport.

We consider the condition on the ansatz. The prediction Eq. (3.9) for the denominator Eq. (1.17), is plotted in Fig. 4.2. The quantity N_D should be unity, and the recovered value is close to unity for a broad range of Δ. The uninteresting discrepancy for small Δ is present here as in Fig. 4.1. A discrepancy for large Δ is also observed. The discrepancy's weakness is striking, however, considering how little information is used in the calculations.

Finally, a plot of the prediction $[\mathbf{J}]$ based on the recovered diffusion parameters $[\mathbf{H}]$ and $[\mathbf{D}]$ (that is, the solution to Eq. (2.1) is shown in Fig. 4.3 superimposed on the original noisy data. This figure is for one of the extreme cases suggested by Figs. 4.1 and 4.2 of $\Delta/\lambda_2 = 50$ (corresponding to retention of information through time $1/50\lambda_2$) and $\sigma = 20\%$. The diffusion parameters recovered by the concatenation calculations represent the data well.

With a view toward adding extra receivers in DNS, the above behaviors at large Δ suggest a

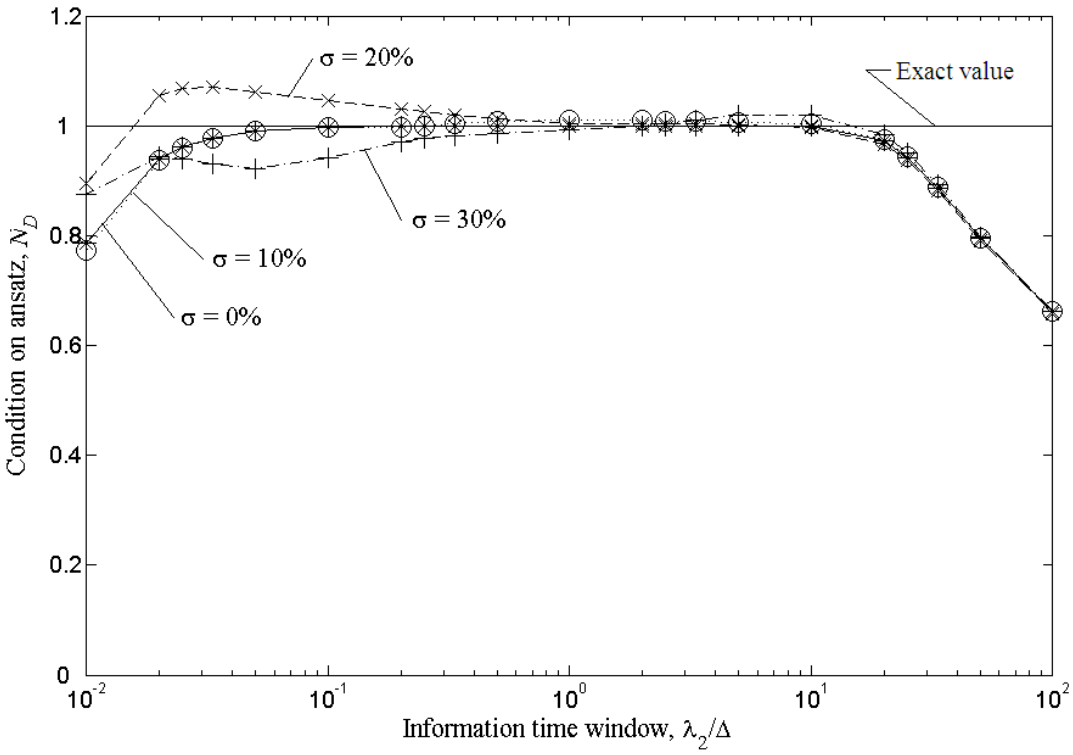

Figure 4.2: Condition of Eq. (3.9). The check fails at low Δ because of the uninteresting cutoff in the numerical integration. It fails at high Δ only when $1/\Delta$ is less than two time steps of data, i.e., 1/50 of a diffusion time $1/\lambda_2$.

figure of merit

$$\text{figure of merit (f.o.m.)} = \frac{1}{\sigma}\sqrt{\frac{R}{S}N_t}, \tag{4.7}$$

where R/S is the number of receivers per source, and $N_t = \frac{1}{\delta t \Delta}$ is the number of uncorrelated time points within the information window. Fluctuations can be effectively reduced by averaging the signal from several nearby receivers. The f.o.m. takes a value of 7.1 with the parameters of Fig. 4.3.

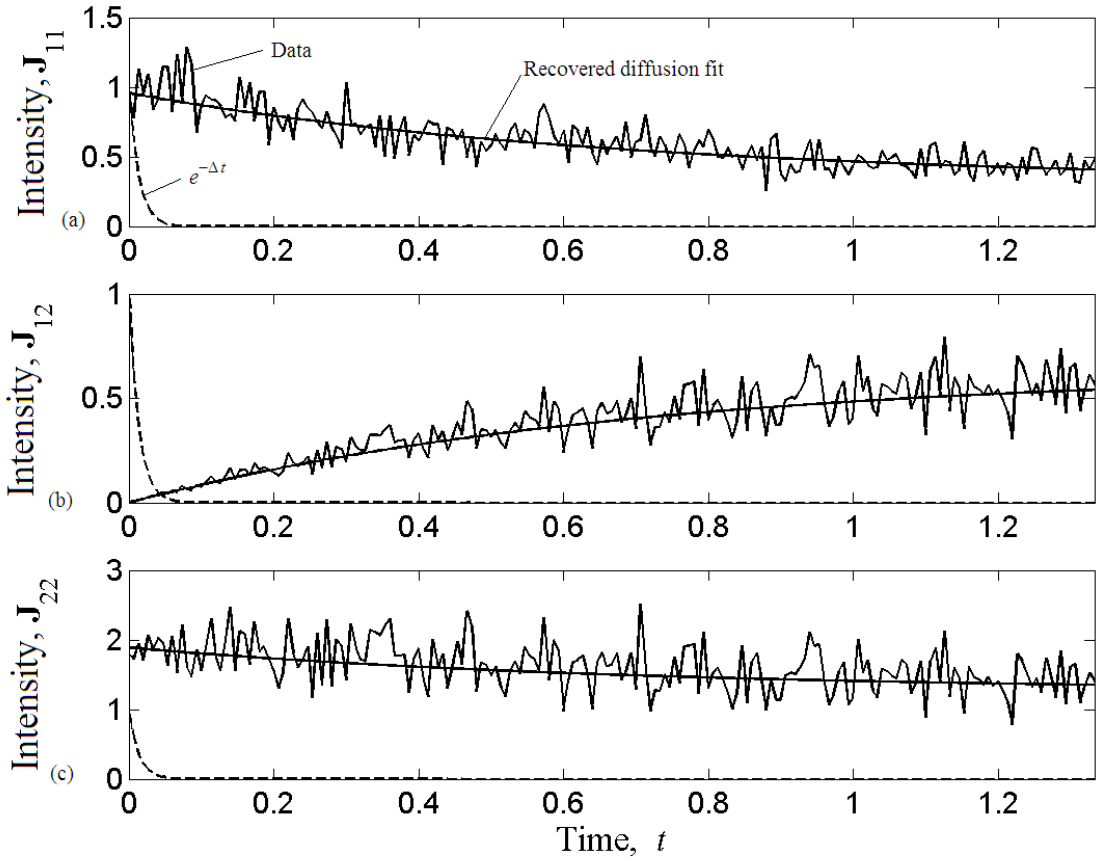

Figure 4.3: Fit of intensity calculated from the recovered diffusion parameters along with original noisy artificial data. Data is plotted out to $t_{\max} = 1.33 = 2/\lambda_2 =$ two diffusion times. Noise amplitude $\sigma = 20\%$; $\Delta/\lambda_2 = 50$. The smooth solid lines represent the solutions based on $[\mathbf{H}]$ and $[\mathbf{D}]$, calculated from $\left[\widehat{\mathbf{J}}^{\Delta}\right]$, equal to data (jagged lines) mulitplied by $e^{-\Delta t}$. The dashed curve shows $e^{-\Delta t}$. (a) receiver in room 1, source in room 1. (b) receiver in room 1, source in room 2. (c) receiver in room 2, source in room 2.

4.2 Application to DNS data

The concatenation ansatz is now applied to imperfectly diffusive data. The analysis here differs from that of Section 4.1 in that the data is generated by DNS; thus, it is not necessarily described by the solution of a diffusion equation such as Eq. (2.1). Also, the noise amplitude cannot be controlled directly; instead, data is smoothed (averaged) over frequency and over nearby receivers where admittances are equal to the admittance at the source. The weak Anderson localization[39] enhanced backscattering effect is first divided out of the intensity at the source site. These nearby receivers thus define a "cloud" of equivalent receivers associated with the source. This smoothing results in noise with fixed fractional standard deviation over the data set. Data is also considered for different center frequencies.

4.2.1 Description of the two-room system

The system considered is pictured in Fig. 4.4. It is based on the two-room toy problem explored in Section 4.1. The system considered here consists of a 400×300 membrane, with nominal wavespeed $c = 1$, divided into two substructures (133×300 and 267×300) coupled by a window of length 60. In practice, this window must be small for the "weak coupling" demanded by SEA but larger than a few wavelengths to avoid localization.[11,38] Scatterers are placed, and the walls are roughened, to scatter the reflecting waves. Placing scatterers enhances randomization and more rapidly establishes a diffuse field in each substructure. In particular, two large rigid (Dirichlet) quarter circles are placed opposite the windows to defocus rays. A total of 50 source/receiver locations are marked in the figure, 25 placed randomly in each room. The two locations acting as

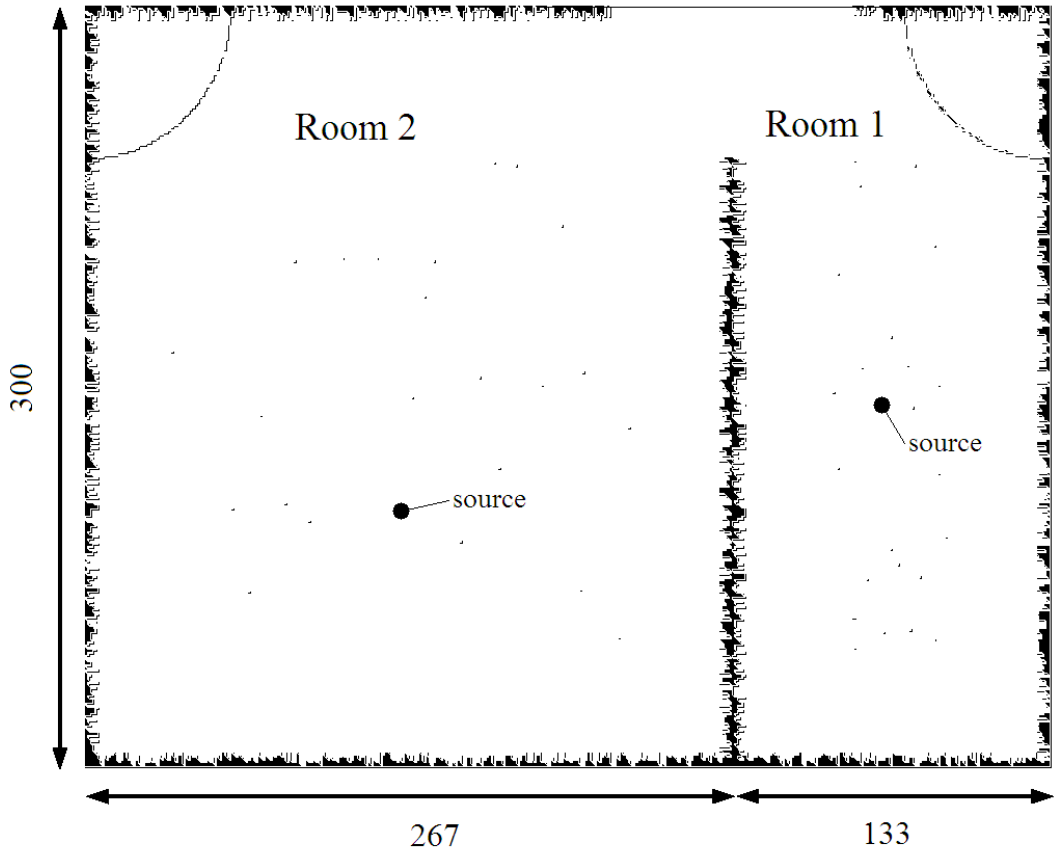

Figure 4.4: Geometry of the system analyzed with DNS. There are two rooms with 25 receivers in each room. Scatters and roughened walls are used to randomize the flow of energy and more rapidly establish a diffuse energy state. The two receivers acting as sources are indicated with heavy dots.

sources are marked with a heavier dot.

The DNS is obtained by solving central-difference equations in space and time. As discussed in Section 1.3.1, the finite-difference equations in space are equivalent to modeling a mesh of unit masses connected by a rectangular grid of strings with unit tension. The time step used is $\delta t = 0.4$. Two solutions are obtained directly, one with an impulsive source at the source site in room one, the other with an impulsive source at the source site in room two. For each source a total of 50 waveforms, one for each receiver, are recorded.

Filtered solutions are obtained by convolving the impulse response with a finite-duration sinusoidal filter

$$B(t) = \begin{cases} 0 & t < -\frac{T_B}{2} \\ B_0 \left(1 + \cos \frac{2\pi t}{T_B}\right) \cos(2\pi f_c t) & -\frac{T_B}{2} < t < \frac{T_B}{2} \\ 0 & t > \frac{T_B}{2}, \end{cases} \tag{4.8}$$

where f_c is the center frequency of the tone burst, $T_B = 60$ is the filter duration, and the coefficient B_0 is such that $\int B^2(t)\mathrm{d}t = 1$. Center frequencies were considered over a range f_c = 0.03–0.20. The full width at half power of $B(t)$, calculated numerically, is $\Delta f = 0.0239$. This bandwidth corresponds to a correlation time in the filtered responses of $\Delta t = 1/\Delta f = 41.8$. These filtered solutions are then squared and averaged over the several (25) nearby receivers in each cloud.

The filter duration was chosen so that there are no reflections from the walls or other scatterers within the duration of the filter; therefore, the admittances $\{E\}$ calculated directly from Eq. (1.18) are identical for each receiver. There is no need to locate a source at each receiver site.

4.2.2 Results and discussion from the two-room system

The nontrivial eigenvalue recovered from the concatenation calculations is shown in Fig. 4.5 as a function of center frequency f_c and for various values of Δ. In Fig. 4.5 and in later plots, the dimensionless representation of of Δ is in terms of the room-acoustics, or, equivalently, the SEA, prediction for the smallest nontrivial eigenvalue. The f.o.m. $= \sqrt{R/S \times \Delta f/\Delta}$ ranges from 14–39 as Δ ranges from $4\lambda_2$ to $0.5\lambda_2$. This estimate of the f.o.m. is perhaps a slight overestimate, as the receivers are not fully independent. The simple theoretical room-acoustics prediction λ_2 is also shown for comparison. The room acoustic prediction is obtained by solving the eigenvalue

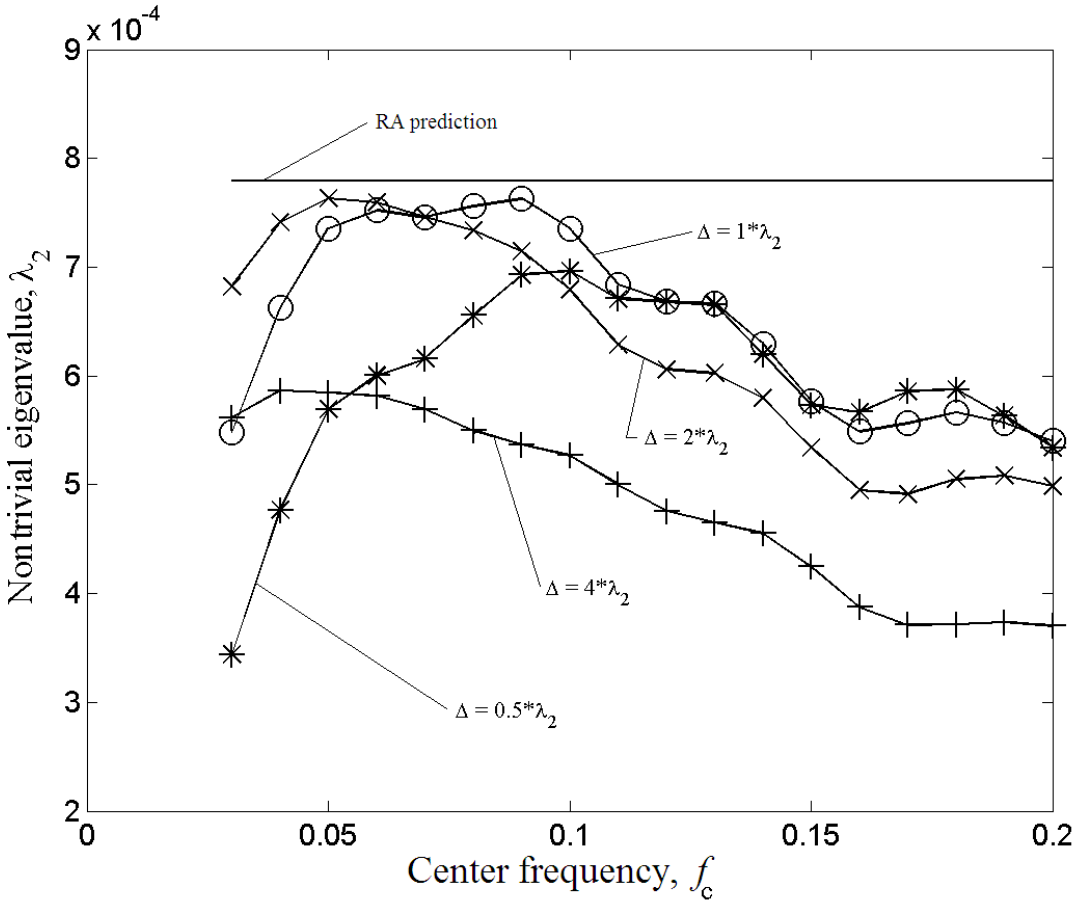

Figure 4.5: First nontrivial eigenvalue obtained from the DNS data for various center frequencies and values of Δ. The Δ is in units of the theoretical room-acoustics (RA) prediction. The smallest $\Delta = 0.5\lambda_2$ corresponds to about 5 information windows in total time. The largest Δ corresponds to about one transit time, before a diffuse field is established.

problem of Eq. (2.3) with

$$[\mathbf{H}] = \begin{bmatrix} A_1 & 0 \\ 0 & A_2 \end{bmatrix} \quad \text{and} \quad [\mathbf{D}] = \frac{cl}{\pi} \begin{bmatrix} 1 & -1 \\ -1 & 1 \end{bmatrix}, \tag{4.9}$$

where A_r is the area of room r, the dimensionless wave speed c is unity, and $l = 60$ is the window width. Corrections to the areas are made for the wall roughness and other scatters. The eigenvalues

are

$$\lambda_1 = 0 \qquad \text{and} \qquad \lambda_2 = \frac{cl}{\pi}\frac{A_1 + A_2}{A_1 A_2} \approx 7.79 \times 10^{-4}. \tag{4.10}$$

The extracted eigenvalue differs from the room-acoustics estimate. The validity of this room-acoustics estimate is in question here: the extracted values of the diffusion parameters represent the data better.

The extracted eigenvalue is independent of Δ over a range of moderate Δ, but differs for either small or large Δ. Deviations can be explained by realizing that the energy in the structure is not fully diffuse at the short times implicit in large Δ. Also, for smaller Δ (not shown), $\left[\mathbf{J}^{\Delta}(0)\right]$ and $\left[\mathbf{J}^{\Delta}(0)\right]'$ are in error because of the uninteresting cutoff in time integration.

Next we consider the condition on the ansatz. Figure 4.6 contains a plot of the prediction Eq. (3.9) for the denominator Eq. (1.17) along with a Weyl-series estimate based on the geometry for comparison. On this scale, all of the curves lie on top of each other and cannot be discerned from each other. The same data on an expanded scale is shown in Fig. 4.7. This Weyl-series estimate was confirmed to be correct by direct comparison to late-time mean-square displacement using the methods in Weaver's paper[38] (not shown). The denominator, N_D, is plotted against frequency for various values of Δ. The recovered value for N_D is reasonably close to the estimate even for the largest value of Δ shown in the figure, but not for small Δ (not shown) due to the required cutoff in numerical integration out to infinite time.

The smooth behavior that underlies the fluctuations is recovered from the extracted diffusion parameters by Eq. (2.6). It represents the filtered, smoothed data well, as shown in Fig. 4.8. The data obtained from DNS fluctuates about the smooth diffusive behavior predicted by the diffu-

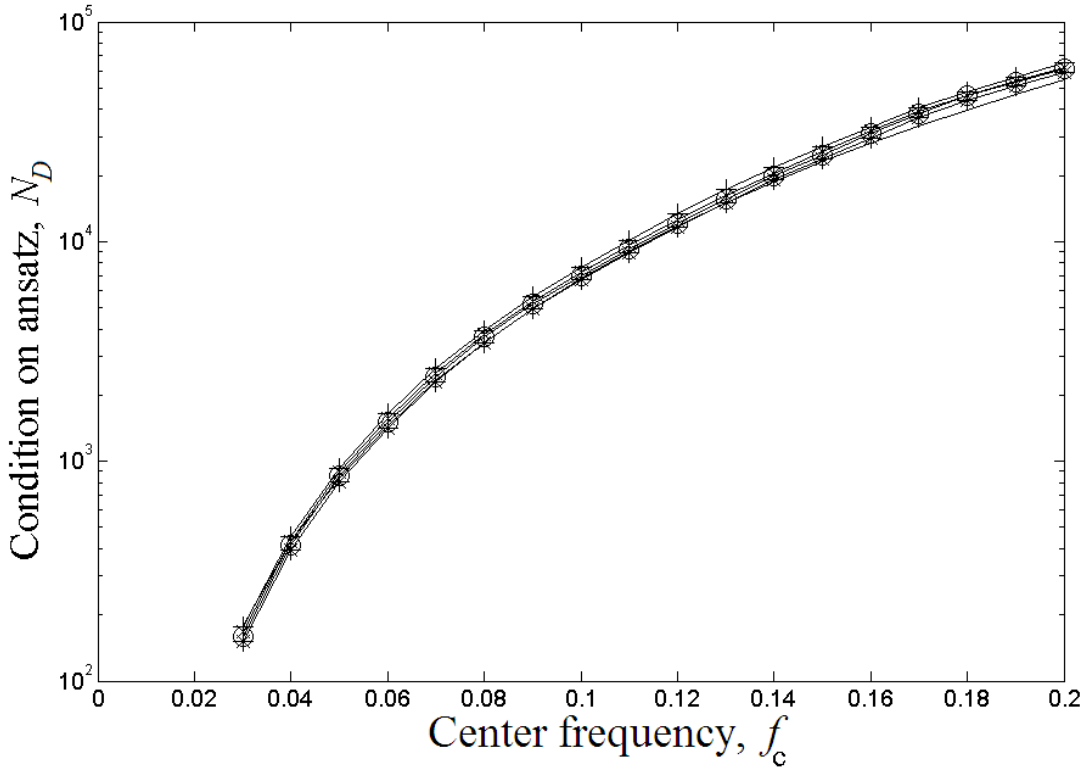

Figure 4.6: Check of Eq. (3.9). The check fails strongly at low Δ (not shown) because of the uninteresting cutoff in the numerical integration, but is reasonable at high Δ in spite of $1/\Delta$ being insufficient time establish a diffuse field. The several lines are the prediction using various values of Δ and a simple theoretical prediction. The same data is plotted in Fig. 4.7 on an expanded scale showing what each line is.

sion limit of the concatenation ansatz. The data shown is for a representative center frequency ($f = 0.150$) and information window ($\Delta = 1 \times \lambda_2$) from within the good range of Δ using in Figs. 4.5-4.7. This data has been smoothed in time over a window of width $T_B/2$ in order to reduce the fluctuations. If the simple room acoustics estimate had been used, the fit would not have represented the data well.

The recovered underlying behavior extracted using a large Δ is plotted against the same filtered, smooth data in Fig. 4.9. The large value used there ($1/\Delta = 321$) corresponds to retention of information over approximately one transit time (time for the first wave front to reach the middle

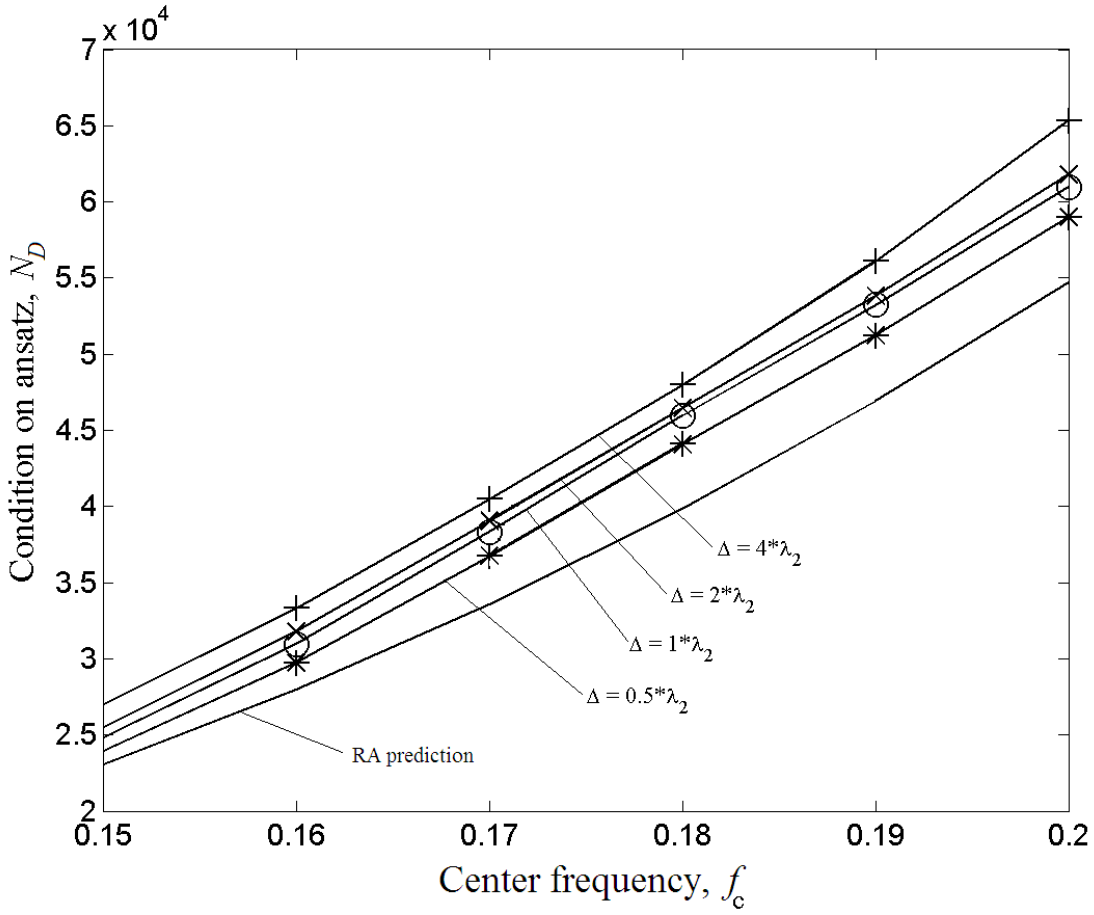

Figure 4.7: Same data as in Fig. 4.6 on an expanded scale.

receiver from the other source ≈ 300). The correct value of the response at late times is predicted, consistent with the reasonable value of N_D seen in Fig. 4.6. However, the rate at which this value is achieved is markedly slow, corresponding to the underprediction of the eigenvalue seen in Fig. 4.5. The discrepancy can be best seen in Fig. 4.9(b), where the smooth diffusion prediction consistently underpredicts the data from DNS at early times, but gradually reaches the actual late-time value.

We ascribe the discrepancy to the imperfectly diffuse character of the wave field at those short times ≈ 300. Indeed, very little signal has yet arrived at distant receivers. It is perhaps surprising that the fits are as good as they are. If Δ had been even slightly larger, $\left[\mathbf{J}^{\Delta}\right]$ would be virtually

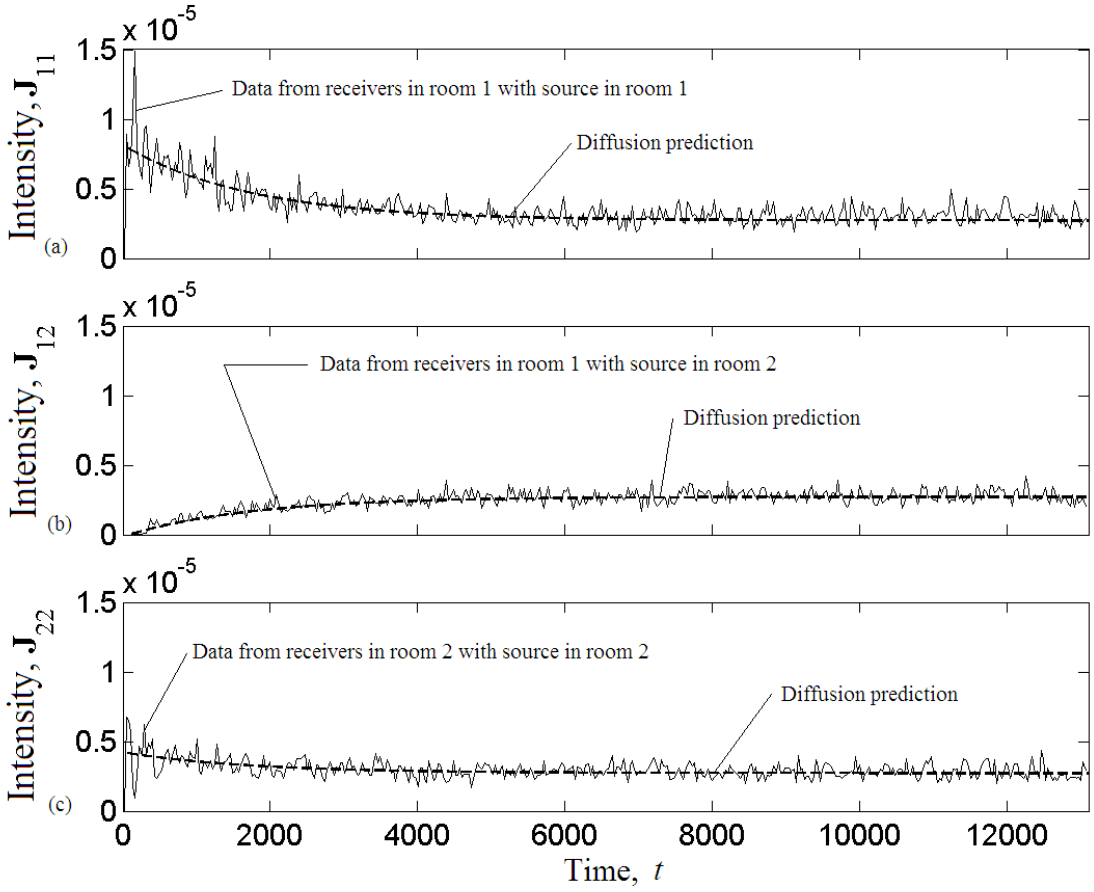

Figure 4.8: Prediction of intensity calculated from the recovered diffusion parameters along with original noisy data (averaged over time and nearby receivers) for a "good" choice of Δ, namely $f_c = 0.15,\ \Delta = 1 \times \lambda_2$. (a) receivers in room 1, source in room 1. (b) receivers in room 1, source in room 2. (c) receivers in room 2, source in room 2.

diagonal, and the ansatz would fail. The f.o.m. for this case is 14, larger than the 7.1 found adequate in Section 4.1.2. A larger f.o.m. is needed here because information is needed covering the early stages of diffusion.

We note that a nondiffusive regime is predicted for early times. The nondiffusive regime is most easily explored by eschewing the $\Omega \to 0$ limit and evaluating the concatenation series for $\widehat{\mathbf{J}}_{22}^{\text{concat}}$ (Eq. (3.3)). Figure 4.10 shows intensity at early times (smoothed in time over a window of width $T_B/2$) as given by a one-term series $\widehat{\mathbf{J}}_{22}^{\Delta}$, a 5-term series, and a 50-term series. We judge

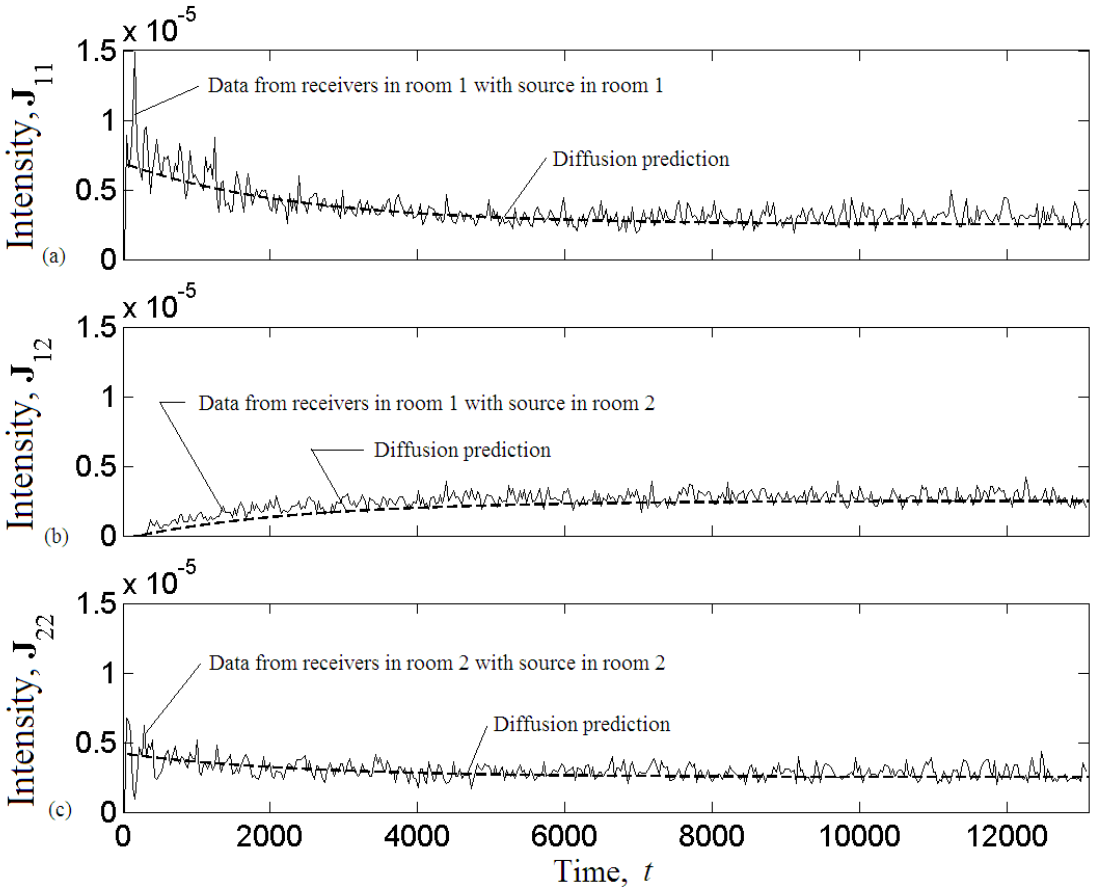

Figure 4.9: Prediction of intensity calculated from the recovered diffusion parameters along with original noisy data (averaged over time and nearby receivers) for a "bad" choice of Δ, namely $f_c = 0.15,\ \Delta = 4 \times \lambda_1$. The late time response is predicted correctly corresponding to a reasonable value of N_D in Fig. 4.6. The diffusion rate is slow, corresponding to the incorrect value in Fig. 4.5. (a) receivers in room 1, source in room 1. (b) receivers in room 1, source in room 2. (c) receivers in room 2, source in room 2.

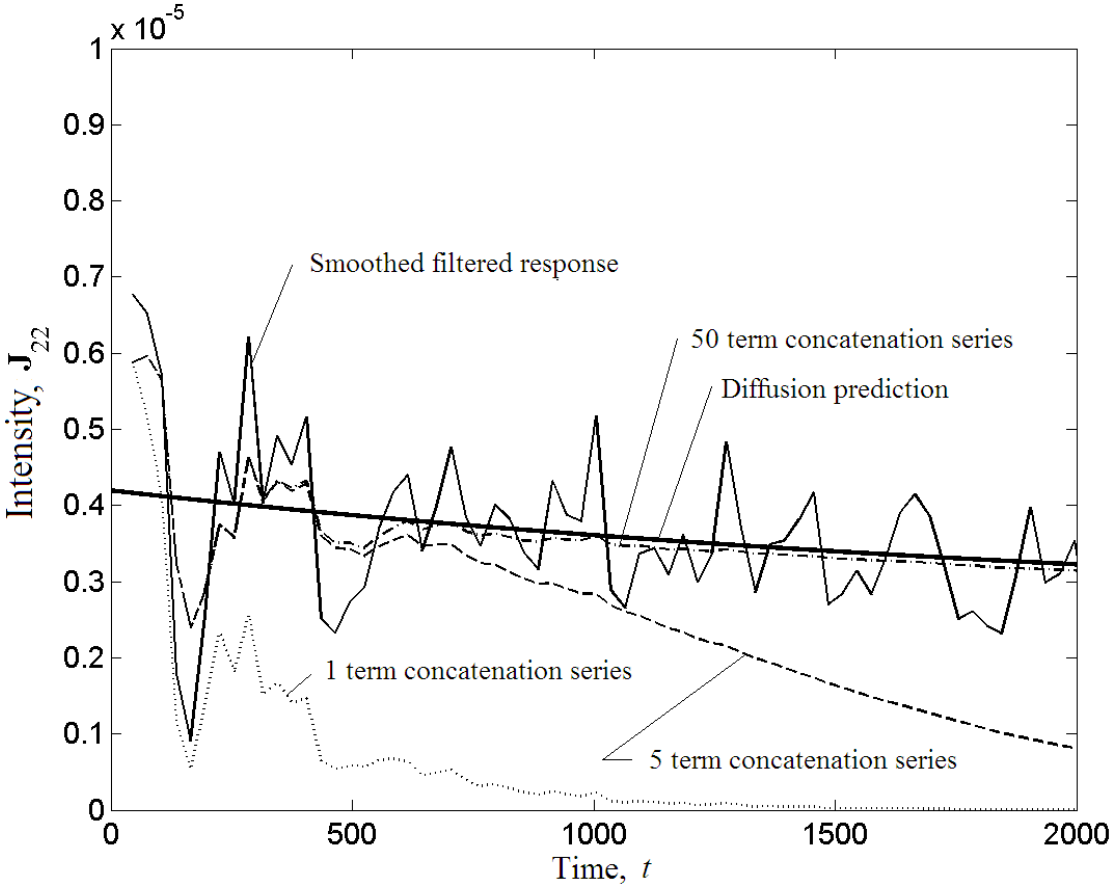

Figure 4.10: Prediction from the concatenation series of Eq. (3.3) at early times with receivers in room 2 and source in room 2. The parameters are $f_c = 0.15$ and $\Delta = 4\lambda_2$. The solid jagged line is the smoothed filtered response at receivers in room 2 from the source in room 2, $\widehat{\mathbf{J}}_{22}$; the lowest data (dotted line) are a one term concatenation series, $\widehat{\mathbf{J}}^{\Delta}_{22}$; and the smooth solid line is the diffusion prediction from $[\mathbf{H}]$ and $[\mathbf{D}]$. The concatenation series represents the data well during the early time, nondiffusive, regime; the diffusion prediction represents the data well after a sufficient time has passed to establish a diffusive field.

by visual inspection that the series in Eq. (3.3) has converged over the time range shown. The diffusion prediction is also plotted. The concatenation series represents the response at early times $t < 600$ better than the diffusion prediction. In particular, it captures the undulations of period ≈ 150 due to reverberations off the walls. After this early time, the direct concatenation prediction represents the data well.

One might object that the substructuring is being used explicitly in the selection of source/receiver sites. We have carried out similar analysis with receivers more closely spaced, eschewing knowledge of substructuring. In particular, the receivers were placed in one cloud—in each room close to the respective source—each a five by five array with receivers spaced 15 grid spacing apart. Results (not shown) were almost as good. In particular, the denominator, N_D, was somewhat underpredicted for large Δ. This underprediction of N_D led to an overshooting of the prediction for late-time response, suggesting that the method was seeing the structure as smaller than it really was. The more random placement of receivers leads to a better sampling of energy density throughout the structure.

4.3 Redundant sources

Here we take an additional step toward not requiring knowledge of substructures in a large system. The advantage of such a program that does not require a partitioning of a system into substructures will become clear in Chapter 5, containing a single homogeneous structure. For now, we consider as a toy problem the same room geometry described in Section 4.2.1, with two sources in the room 1 on the right (sources 1 and 2) and one source (source 3) in the room 2 on the left. Each source

has a cloud of 25 receivers associated with it.

Nominally, the average response at cloud 2 due to a source at source 1 should be the same as the response at cloud 1 due to a source at source 1 leading to a singular $\left[\mathbf{J}^{\Delta}\right]$ matrix that cannot be inverted to construct $[\mathbf{Q}]$, $[\mathbf{H}]$, and $[\mathbf{D}]$. However, normal random fluctuations and slight space between clouds 1 and 2 break the singularity and lead to a $\left[\mathbf{J}^{\Delta}\right]$ matrix that is (usually) well-conditioned or (sometimes) ill-conditioned for certain choices of Δ and center frequency of the filter, f_c, in this two-room example. For the rare cases in this example, and the more common cases in Chapter 5, that $\left[\mathbf{J}^{\Delta}\right]$ is ill-conditioned, it is necessary to have an automatic algorithm built into the concatenation ansatz to cast the matrix into a more robust form.

We consider the same frequency interval from $f = 0.03$–0.2 and five values of $\Delta = 0.01\lambda_2$, $0.5\lambda_2$, $1.0\lambda_2$, $2.0\lambda_2$, and $4.0\lambda_2$, where λ_2 is the second eigenvalue as predicted from room acoustics.

The program to handle an ill-conditioned $\left[\mathbf{J}^{\Delta}\right]$ matrix is a "guess and check" approach. We calculate the eigenvalues of $[\mathbf{H}]$ and $[\mathbf{D}]$ keeping all $S = 3$ singular values[56] of $\left[\mathbf{J}^{\Delta}\right]$. If any of the eigenvalues do not make sense on physical grounds (i.e., if any of them are negative beyond machine precision or have a nonzero imaginary part), we recalculate the eigenvalues of $[\mathbf{H}]$ and $[\mathbf{D}]$ after eliminating the smallest singular value of $\left[\mathbf{J}^{\Delta}\right]$. This procedure is repeated until all the singular values have been eliminated (failure of the program) or all the resulting eigenvalues make sense.

After a direct numerical simulation of the two-room structure with a redundant source, the program typically finds three physical eigenvalues, one close to zero, one close to the room acoustics prediction, and one large. For eleven isolated (Δ, f_c) combinations, the program originally finds

either a large negative eigenvalue or complex eigenvalues. For these eleven isolated cases, elimination of one singular value leads to two physical eigenvalues, one close to zero, the other close to the room acoustics prediction. The third eigenvalue then becomes $+\infty$.

The first eigenvalue is plotted in Fig. 4.11. This first eigenvalue should be trivial, that is $\lambda_1 = 0$.

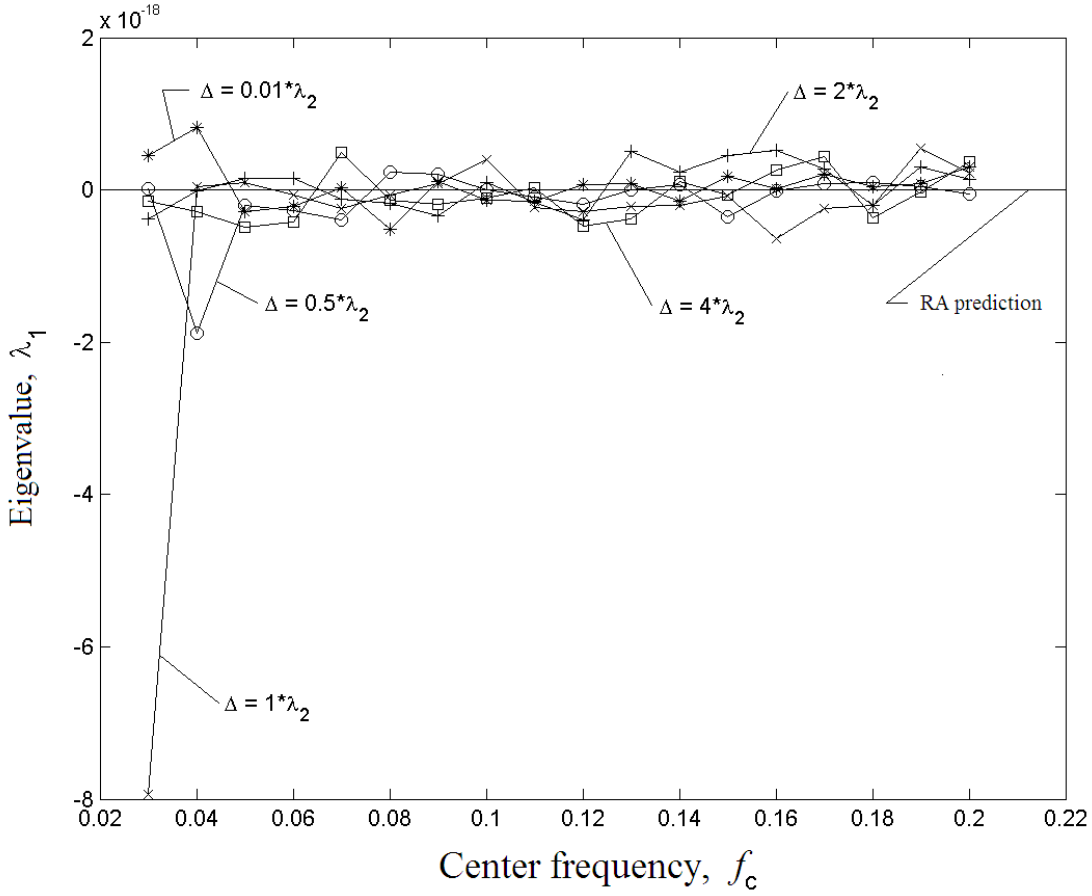

Figure 4.11: First, nominally trivial, eigenvalue for redundant source in the two-room structure. It is 13 orders of magnitude smaller than typical values of λ_2 in Fig. 4.12 below.

The eigenvector associated with this trivial eigenvalue is the vector containing the admittances (Es) and, thus, information about the late-time averages that the responses take. The late-time averages neither grow nor decay, so the eigenvalue associated with them ought to be zero. Due to issues of machine precision, one cannot expect a numerical program to extract exactly zero. The first

eigenvalue actually extracted by the concatenation ansatz diffusion limit fluctuates around zero with typical values of 1×10^{-18}, or 13 orders of magnitude smaller than typical values of λ_2. This order of magnitude is, indeed, on the order of double-digit machine precision. Similar plots could have been constructed for the two-room systems considered earlier in this thesis.

The second eigenvalue λ_2 is plotted in Fig. 4.12. Figure 4.12 can be compared to Fig. 4.5

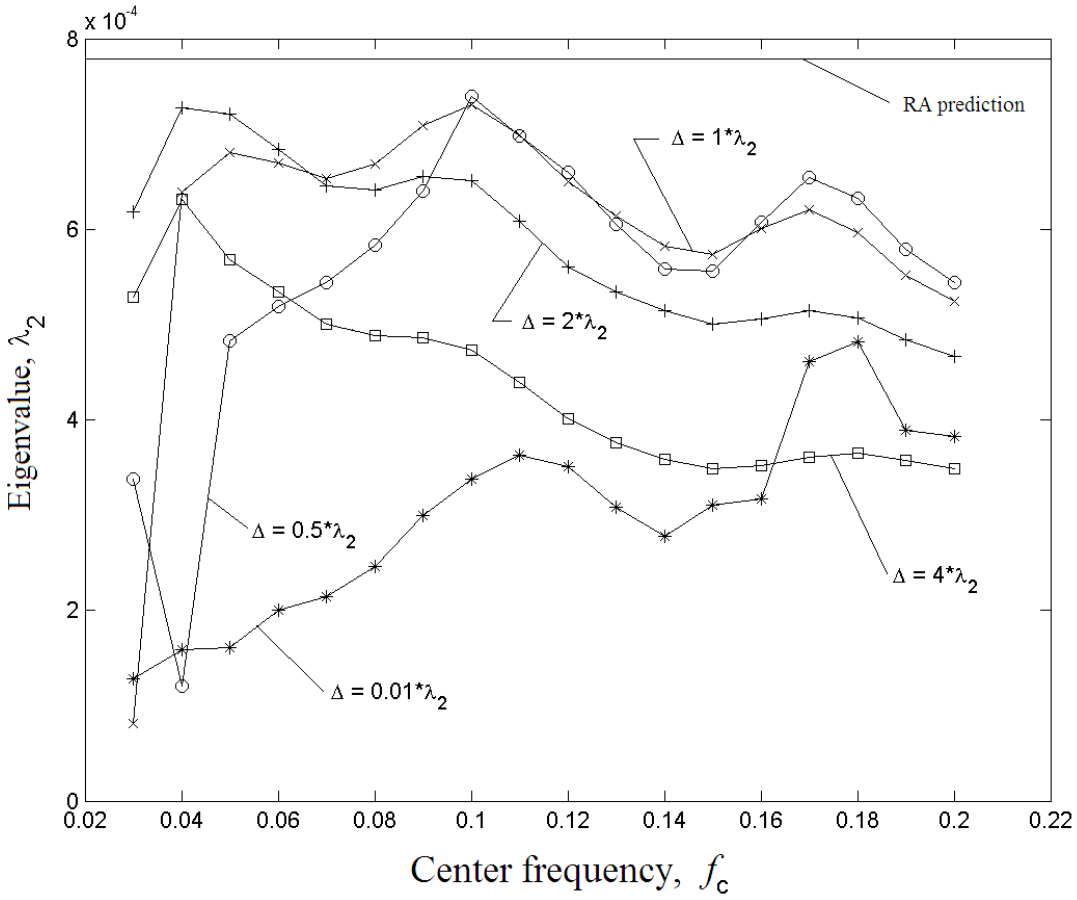

Figure 4.12: Second eigenvalue for redundant source in the two-room structure. The room-acoustics (RA) prediction for this eigenvalue is the same as in Fig. 4.5, as it is the same physical system. The diffusion limit of the concatenation ansatz extracts the same eigenvalue in the system with redundant sources as it does without redundant sources.

containing a plot of the second eigenvalue in the case of no redundance source. As we are still studying the same physical system, the eigenvalues specifying the leak rate of energy between

rooms 1 and 2 should be the same. Indeed, the room-acoustic prediction is the same by construction. The diffusion limit of the concatenation ansatz also extracts leak rates in the system with redundant sources comparable to those extracted in the system with only one source and cloud of receivers in each room.

The curves in Fig. 4.12 that diverge the most with the others are the ones plotting the eigenvalues extracted with the smallest value of Δ and the largest value of Δ. The one associated with the smallest value of Δ does not agree because of the uninteresting cutoff in numerical integration, and this curve was omitted in Fig. 4.5. The one associated with the largest value of Δ was extracted by the concatenation ansatz diffusion limit using the least amount of data (one-fourth of a diffusion time), so it may be surprising that this curve agrees as well as it does.

The third eigenvalue ($\lambda_3 \to \infty$) is plotted in Fig. 4.13. The missing data points in Fig. 4.13 represent the rare situations when a singular value was eliminated in the course of the guess-and-check portion of the program described above. The eigenvalue solver had found either a complex eigenvalue or a negative eigenvalue (beyond machine precision). In these cases, the third eigenvalue λ_3 was effectively set to $+\infty$.

It may be interesting to note that a complex eigenvalue would result in a prediction oscillating about behavior governed by a diffusion process. The oscillating part would have a period given by the imaginary part of the eigenvalue, while it would decay at a rate given by the real part of the eigenvalue. Though not extensively studied, it was found that the oscillating part did, indeed, fit some of the early fluctuations well when the program was modified to not eliminate the smallest singular value in the case of complex eigenvalues. In the case of negative eigenvalues, the associate eigenvector grows, and this case must be rejected on physical ground.

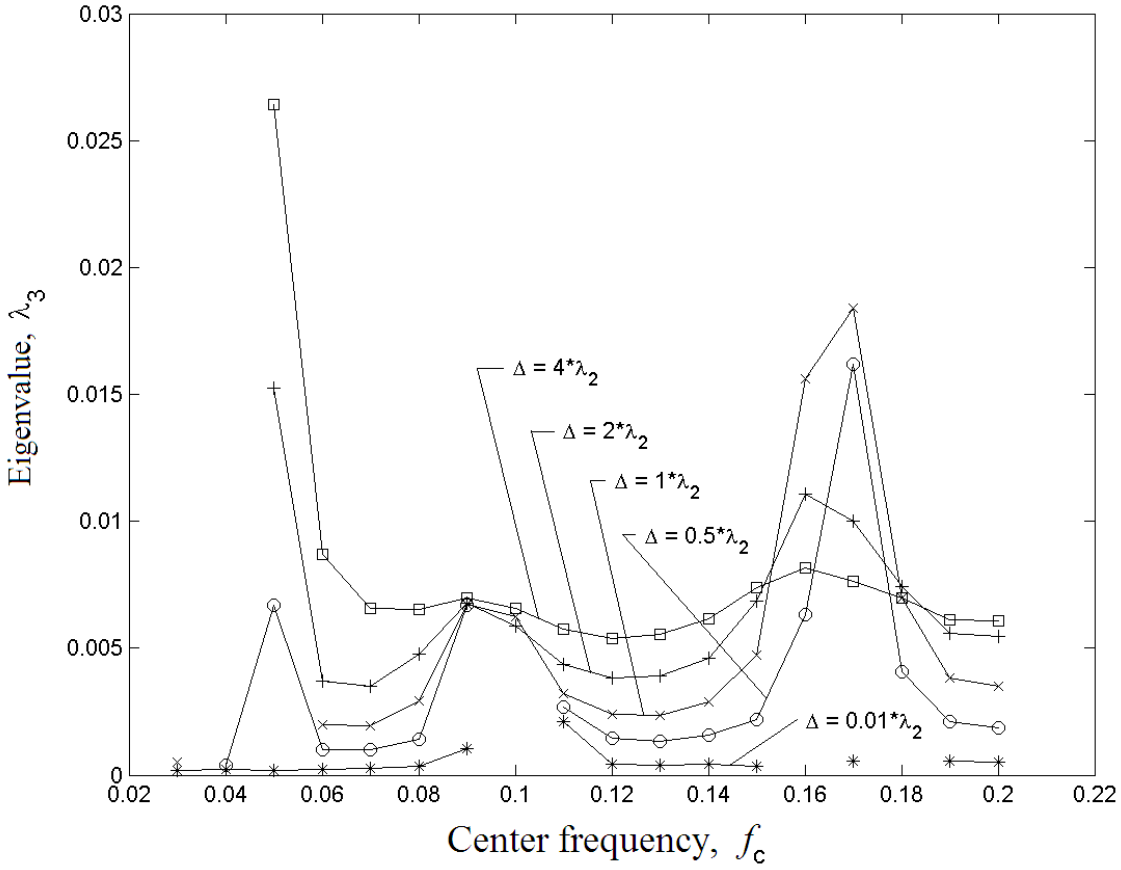

Figure 4.13: Third eigenvalue for redundant source in the two-room structure. Missing data points correspond to infinite values. The RA prediction is $\lambda_3 = \infty$. The values of λ_3 are, indeed, some two orders of magnitude larger than the extracted values of λ_2, indicating that any higher order eigenvectors decay in the diffusion limit solution quickly.

Table 4.1 contains the eleven isolated cases and the reason why a singular value had to be eliminated. Most of these cases were in the low end of the frequency range across all values of Δ. Three were of the possibly interesting case of a complex eigenvalue and oscillating "diffusion" prediction. The other eight were of the clearly nonphysical case of a growing diffusion solution with a negative eigenvalue.

The denominator N_D is plotted in Fig. 4.14. This figure can be compared to Fig. 4.6. The room-acoustics prediction is the same in both figures by construction as, again, the systems are

f_c	Δ	reason
0.03	$0.5\lambda_2$	complex
0.03	$2.0\lambda_2$	negative
0.03	$4.0\lambda_2$	negative
0.04	$1.0\lambda_2$	negative
0.04	$2.0\lambda_2$	negative
0.04	$4.0\lambda_2$	negative
0.05	$1.0\lambda_2$	negative
0.10	$0.01\lambda_2$	negative
0.10	$0.5\lambda_2$	negative
0.16	$0.01\lambda_2$	complex
0.18	$0.01\lambda_2$	complex

Table 4.1: Summary of the reason (negative or complex third eigenvalue) why one singular value of the matrix $\left[\mathbf{J}^{\Delta}\right]$ was eliminated by the concatenation ansatz in the rare cases that it was.

physically identical. The values of N_D extracted by the concatenation ansatz are also similar in the two figures. The values found using the smallest value of $\Delta = 0.01\lambda_2$ was not included in Fig. 4.6, but it is included in Fig. 4.14 to show that the uninteresting cutoff in numerical integration has a large effect. The numerical integration does not result in as large as a value as it should, making the system smaller than it really is to the concatenation ansatz.

One of the more interesting comparisons of the diffusion limit of the concatenation prediction to raw data is in Fig. 4.15. In this case, there is a redundant source and a spurious third eigenvalue extracted. In the SEA prediction, the intensity at clouds 1 and 2, both in room 1, due to a source in room 1 at either cloud would be identical functions of time. Both intensities would be maximum at $t = 0$ and decay to a steady-state value at late time, as though energy immediately spread across the entire room. However, it takes finite time for information to travel from one cloud of receivers to another cloud, even in the same substructure. It take some time for the room with the source to equilibrate internally, though this time is shorter than the time for the entire system to equilibrate. With a redundant source and finite third eigenvalue, the third eigenvalue helps predict the initial

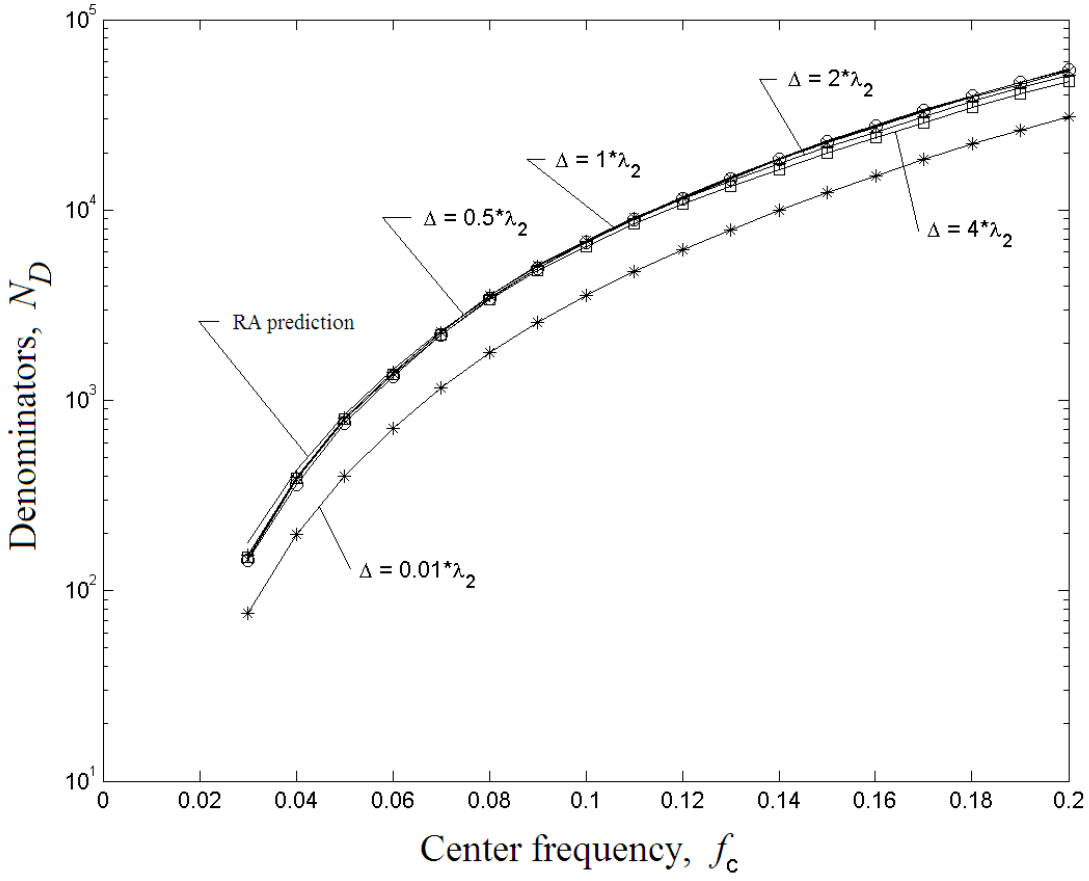

Figure 4.14: The “denominator” check for redundant source in two-room structure. The values extracted in the redundant source case are comparable to those in Fig. 4.6.

condition for the source 1 to cloud 2 combination.

A second interesting comparison of the prediction to raw data is in Fig. 4.16, where one can explicitly see localization for a low frequency. In particular, Figs. 4.16(b) and 4.16(c) show the energy flow from room 2 to room 1. In both of these plots, the diffusion limit of the concatenation ansatz overshoots the late-time average of the actual DNS data. The flow of energy has stopped before diffusion could carry the system to a state of equipartition. The energy has localized on room 2. In addition, the concatenation ansatz diffusion limit was unable to identify the correct initial condition of having no energy in room 1.

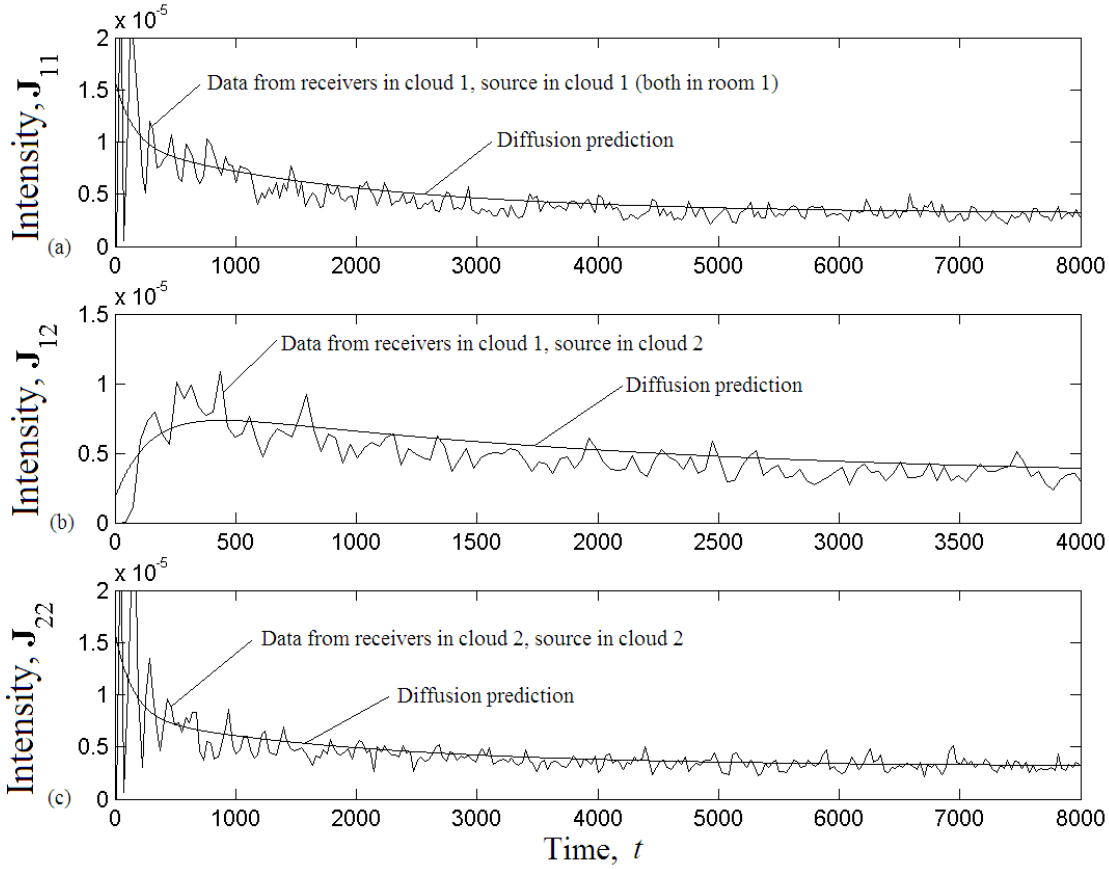

Figure 4.15: Prediction including three eigenvalues for redundant source in the two-room structure. Here, the frequency is $f_c = 0.15$, and $\Delta = 2 \times \lambda_2$. All data is from receivers from the two clouds in room 1 with the source also in room 1. (a) receivers in cloud 1, source in cloud 1. (b) receivers in cloud 1, source in cloud 2. (c) receivers in cloud 2, source in cloud 2.

We have shown in this section that the diffusion limit of the concatenation ansatz is readily extended to systems with more than two sets of receivers in a substructure, even if two sets of receivers collect substantially the same data. Indeed, if two sets of receivers collected identically the same data, the requisite matrix inversions would be impossible. The difference between "sub-structures" defined by a user of the program may not be discerned by the concatenation ansatz. The program's ability to eliminate higher order singular values may give direction to a program that automatically identifies substructures if an analyst has defined more than are needed.

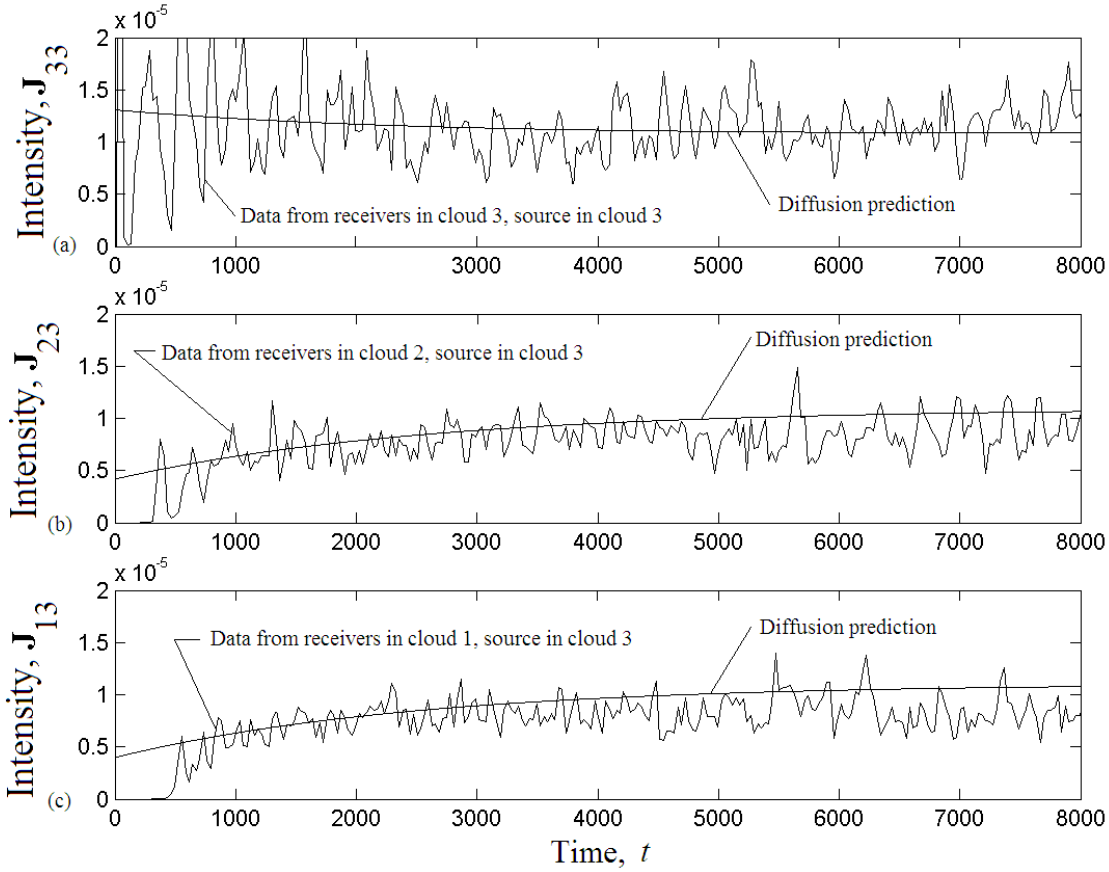

Figure 4.16: Prediction including three eigenvalues for redundant source in the two-room structure at low frequency illustrating Anderson localization. Here, the frequency is $f_c = 0.04$, and $\Delta = 0.5 \times \lambda_2$. (a) receivers in cloud 3 (in room 2), source in room 2. (b) receivers in cloud 2 (in room 1), source in room 2. (c) receiver in cloud 1 (in room 1), source in room 2. The localization can bee seen in plots (b) and (c).

4.4 Three rooms

Next we consider a DNS of the dynamics of a three-room system. This is a second system that is typically studied using SEA. It is only slightly more complicated than the two-room system just studied, and there are few new physical issues to discuss other than that we now expect one trivial (zero) eigenvalue and two other eigenvalues defining leak rates.

4.4.1 Description of the three-room system

The room geometry is in Figs. 4.17 along with a snapshot of the wavefield at an early time

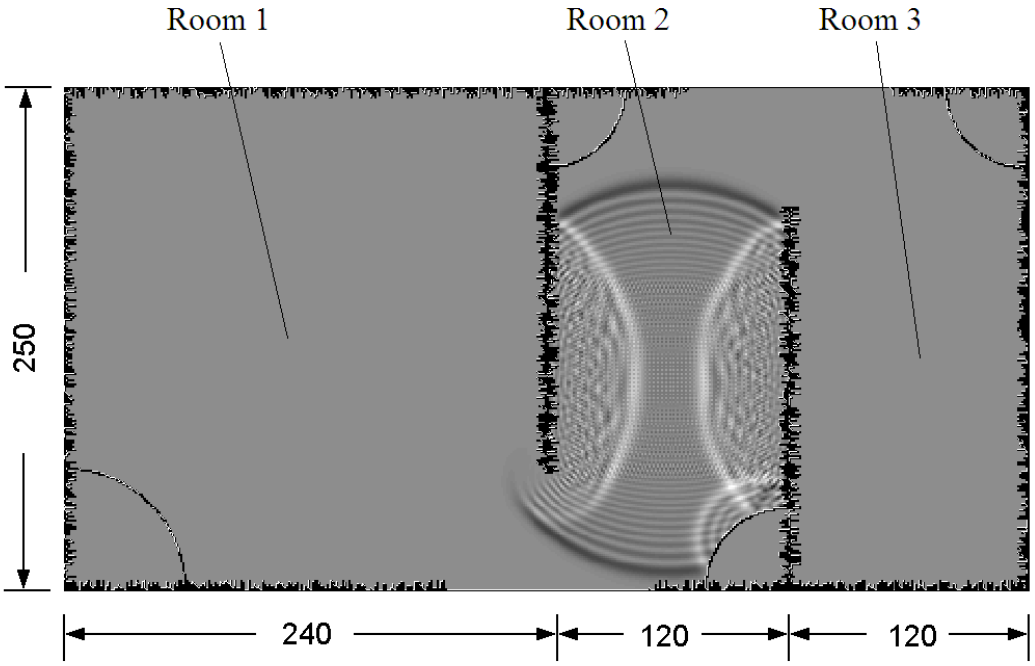

Figure 4.17: Three-room geometry and wavefield at early time $(t_1 = 100)$. The cloud positions are essentially in the centers of the left and right rooms. The radius of the quarter circle in the lower left is 60; the radii of the other circles are 40. The smooth portions of the walls are each 100 long. The width of the windows are both $l_{12} = l_{23} = 60$. Rooms 1 and 3 are not directly coupled. The concentric circles and reflections are consistent with the designed wavespeed of unity and rigid boundary conditions.

$(t_1 = 100)$. The system has overall dimensions of 250×480. Room 1 on the left has dimensions 250×240; room 2 in the middle has dimensions 250×120; and room 3 on the right also has dimensions 250×120. Rooms 1 and 2 are directly coupled by a window with width $l_{12} = 60$, and rooms 2 and 3 are also directly coupled with a window of width $l_{23} = 60$. The walls are roughed, and quarter-circle scatters are placed opposite the windows to encourage the establishment of dif-

fuse energy fields, as in Section 4.2.1. The other system parameters (unit masses, strings with unit length and unit tension, and filter duration) are also unchanged from Section 4.2.1.

Rooms 1 and 3 are not directly coupled. From the standpoint of traditional SEA, one can see how indirect coupling loss factors[2,32] may be important. A ray could travel from room 1 to room 3 through the two windows without reflecting off of any scatterers and spending much time reverberating in room 2. Energy will seem as though it has traveled directly from room 1 to room 3 if it is not well detected by a cloud of receivers in room 2. The system would behave as though rooms 1 and 3 were directly coupled. Our concatenation ansatz does not depend on any foreknowledge of direct or indirect coupling.

4.4.2 Results and discussion from the three-room system

Figure 4.17 also contains a snapshot of the displacement field at an early time $(t_1 = 100)$ after a broadband impulsive source in room 2. These wavefields are particular interesting to see in this three-room case. One can see the typical coherent circular ripples spreading out from the point source before they have reflected off of any scatterers, as expected. The leading edge of the wavefront is a distance of about 100 from the source, consistent with a nominal wavespeed of unity. The wavefront can still be clearly seen after only one reflection off of the walls. There is a change of sign after reflection off of the rigid boundaries. Finally, the energy has started to leak into room 1 from room 2.

A second snapshot of the wavefield at a somewhat later time $(t_2 = 225)$ is in Fig. 4.18. At this moderate time, the wave front is still propagating into rooms 1 and 3 without a lot of reflection off of walls or scattering. The reflections in room 2, however, are becoming intractable, and the field

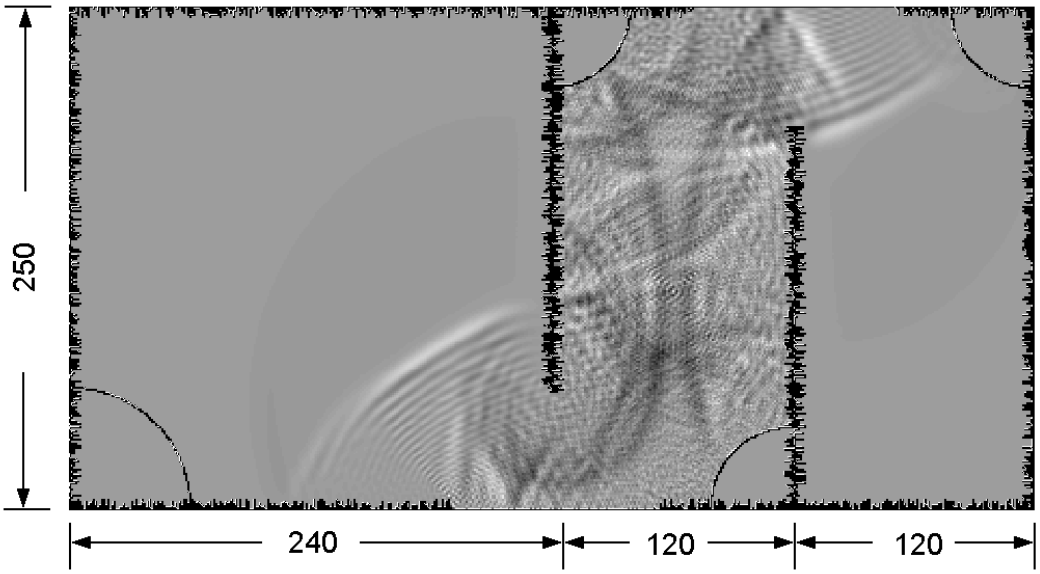

Figure 4.18: Wavefield in the three-room system at moderate time $(t_2 = 225)$. A diffuse field is being established in room 2, while the wavefronts (seen only faintly) have traveled about halfway through rooms 1 and 3.

is starting to become diffuse with wavefronts coming from all directions at any given point.

Finally, a snapshot of the wavefield at late time $(t_3 = 13\,107)$ corresponding to the end of the simulation, or 2^{14} time steps, is in Fig. 4.19. Though this wavefield is broadband, the energy fields in rooms 1 and 3 look fully diffuse. Detailed analysis of the distribution of energy is most appropriate on band-limited data, which is unavailable in such snapshots in Figures 4.17-4.19, but one may still comment on the distribution qualitatively. There is no longer any signs of any wavefronts propagating through the system and reflecting at the various scatterers. The average intensity, or square amplitude of displacement, is about the same in rooms 1 and 3. The apparent enhanced intensity in room 2 can be ascribed to Anderson localization in the low frequency content. We do not expect our concatenation ansatz to perform well in the presence of localization, and SEA

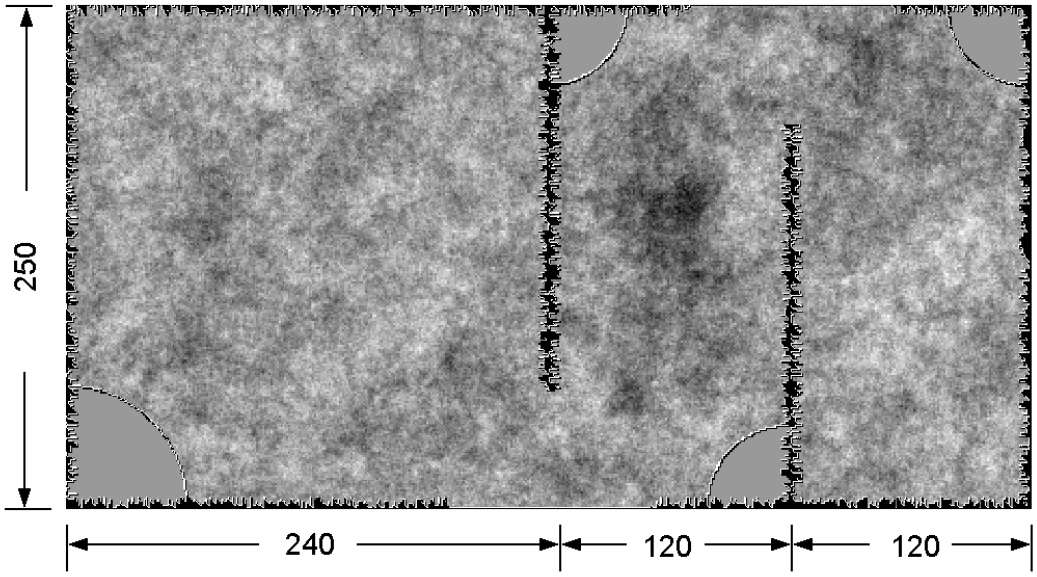

Figure 4.19: Wavefield in the three-room system at late time ($t_3 = 13\,107$). By inspection, the wavefield has become diffuse. The somewhat higher intensity in room 2 is not inconsistent with localization for low frequencies.

would fail as well.

The room-acoustics predictions for the eigenvalues governing the rate of flow of energy between the three rooms at all frequencies are $\lambda_1 = 0$, $\lambda_2 = 5.196 \times 10^{-4}$, and $\lambda_3 = 21.06 \times 10^{-4}$. These eigenvalues were found using an analysis similar to that in Section 4.2.2. For all (f_c, Δ) pairs, the program uses all three singular values to find three physical eigenvalues (plausibly) close to the room-acoustics prediction. The extracted eigenvalue of the nominally trivial eigenvalue λ_1 is plotted in Figs. 4.20. This figure can be compared to Fig. 4.11 for the two-room case (with a redundant source). The typical magnitude of the first eigenvalue is 1×10^{-19}, or about 15 orders of magnitude smaller than the extracted values of λ_2 shown below. The difference is on the order

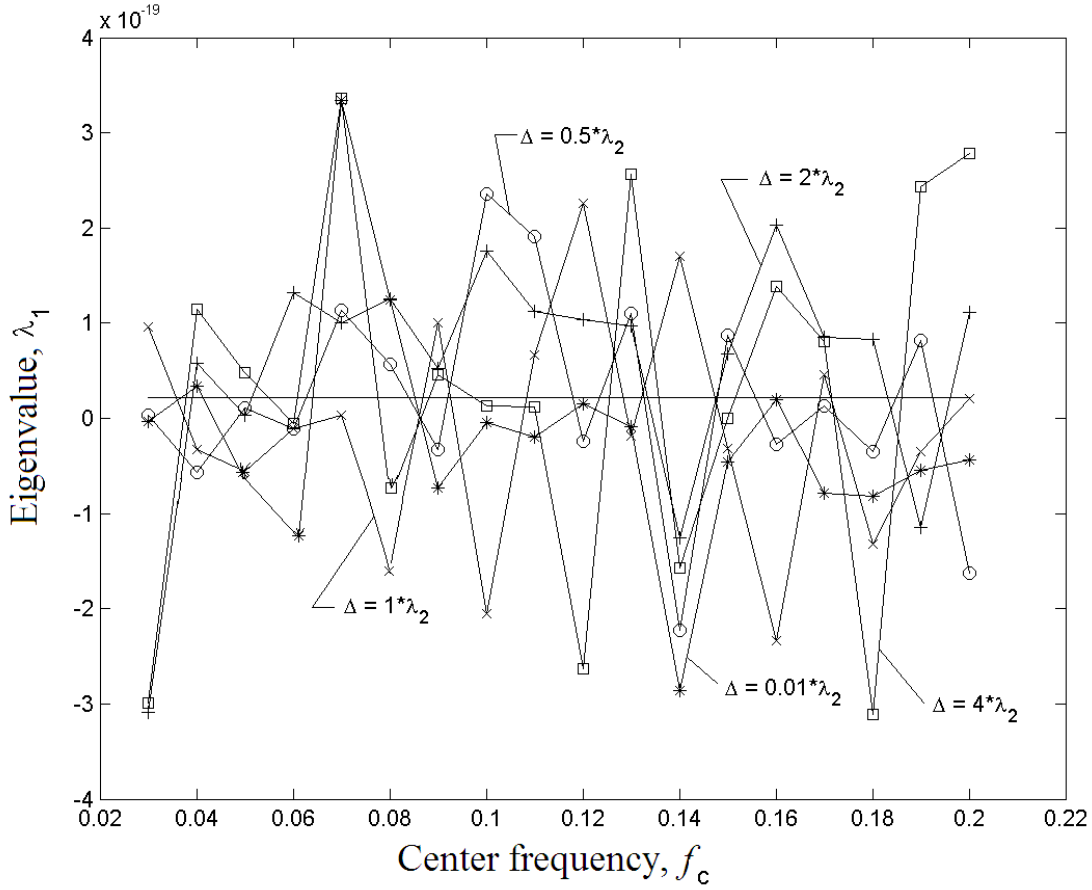

Figure 4.20: The trivial eigenvalue of the three-room system over the frequency range and for various values of Δ.

of machine precision, and any growth or decay associated with these eigenvalues not being exactly zero is insignificant compared to the evolution due to the larger eigenvalues.

The extracted values of λ_2 are plotted in Fig. 4.21. This figure is qualitatively comparable to Figs. 4.5 and 4.12. We do not expect to find the same leak rate, since the system is qualitatively different having three rooms instead of two. However, we do expect to find *some* leak rate that can be compared to the room-acoustics prediction for the three room system.

The only curve that does not agree with the others is the one plotting the eigenvalues extracted with the smallest value of Δ used. It does not agree because of the uninteresting cutoff in numerical

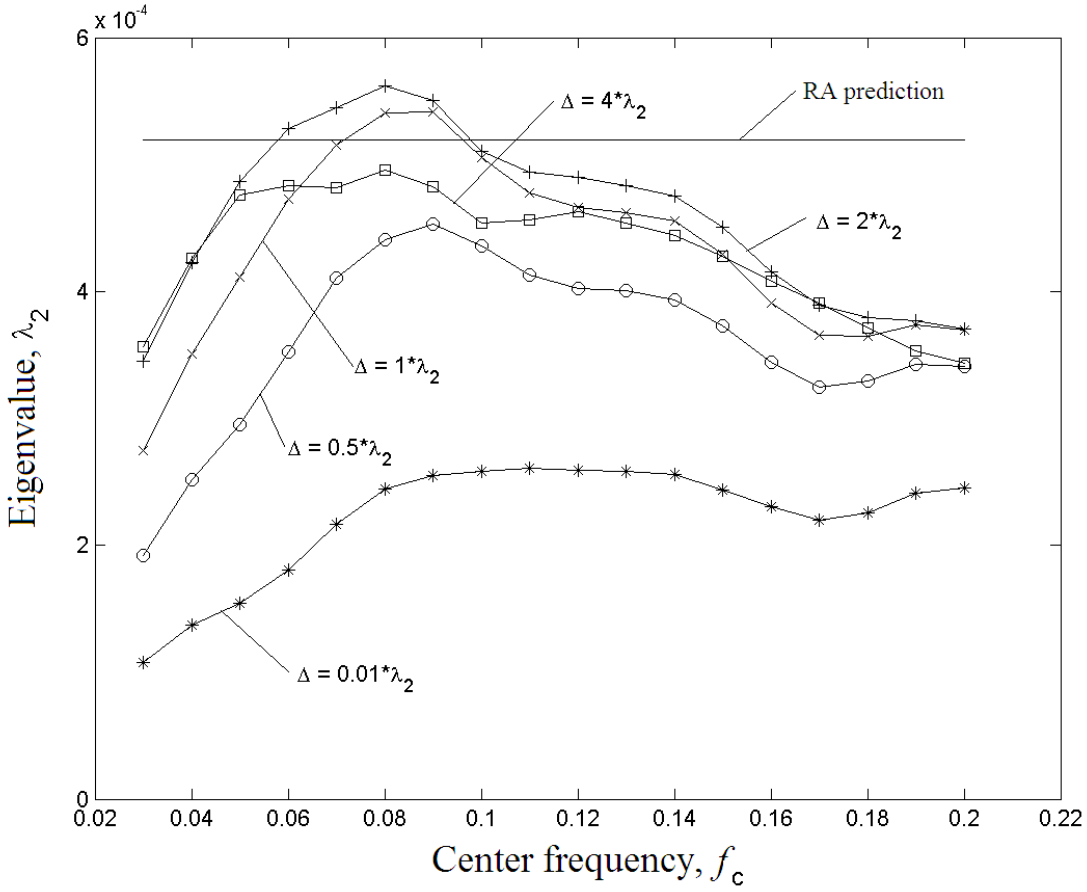

Figure 4.21: Second eigenvalue of the three-room system over the frequency range and for various values of Δ. The room-acoustics (RA) prediction is $\lambda_2 = 5.196 \times 10^{-4}$.

integration, and this curve was omitted in Fig. 4.5. Generally, the eigenvalues extracted using the other four values of Δ agree with each other, as they did in Fig. 4.5. They also agree with the room-acoustic prediction in the lower end of the frequency range considered and then predict a somewhat lower value at higher frequencies. Again, it is the RA prediction that is suspect here. If we were to use the RA prediction, diffusion fits to the DNS data would be worse than those using the concatenation ansatz prediction.

The values of λ_3 extracted by the concatenation ansatz are plotted in Fig. 4.22. Figure 4.22 is not even qualitatively comparable to Fig. 4.13. In the system with redundant sources, we expect

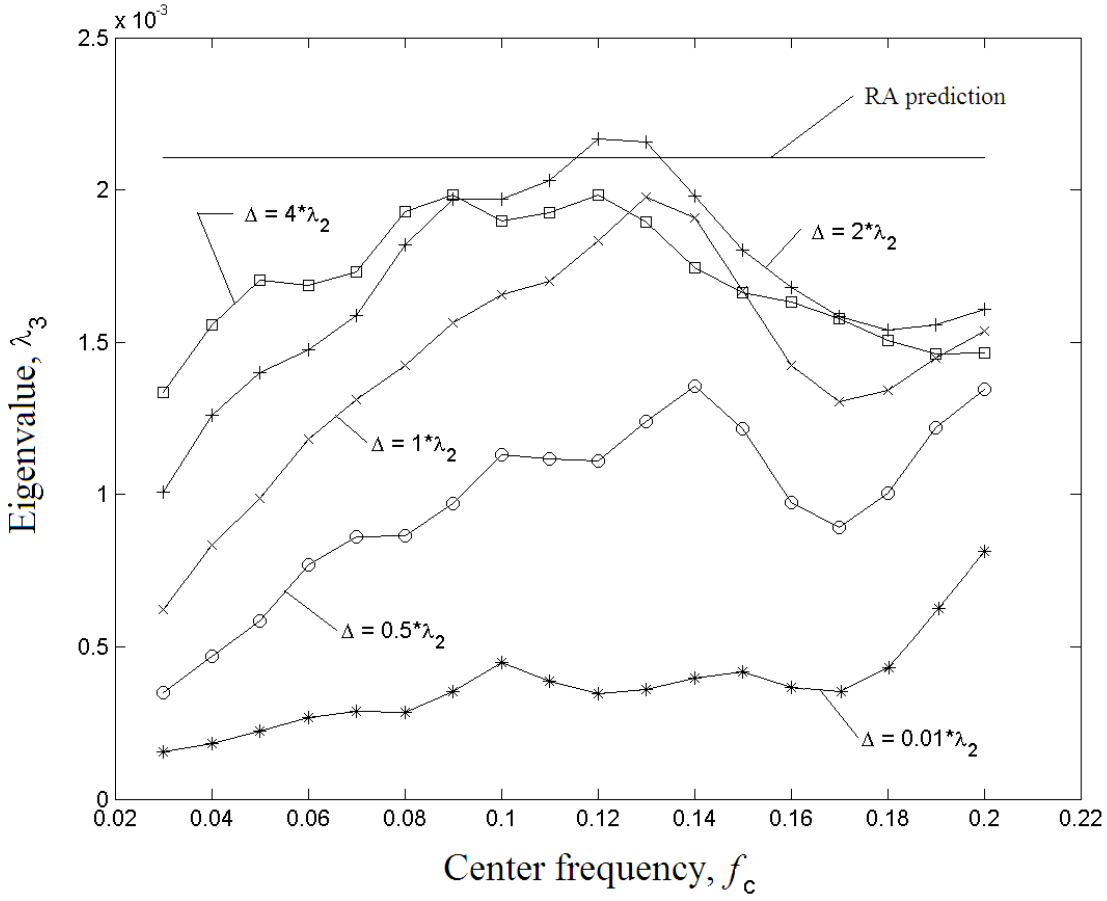

Figure 4.22: Third eigenvalue of the three-room system over the frequency range and for various values of Δ. The room-acoustics (RA) prediction is $\lambda_3 = 21.06 \times 10^{-4}$.

the third eigenvalue to be infinite or, at least, very large. In the current three-room case, we expect to find all three eigenvalues to be finite because the system was constructed to have three subsystems. The behavior of the extracted values of λ_3 is qualitatively similar to that of λ_2. The values extracted using the two smallest values of Δ diverge from the values extracted using larger values of Δ. The diffusion limit predictions of λ_3 agree with the room-acoustics prediction in the middle of the frequency range considered, but a somewhat lower value is extracted at the lower and upper regions of the frequency range.

Finally, the denominator N_D is plotted in Fig. 4.23 as a function of frequency for various values

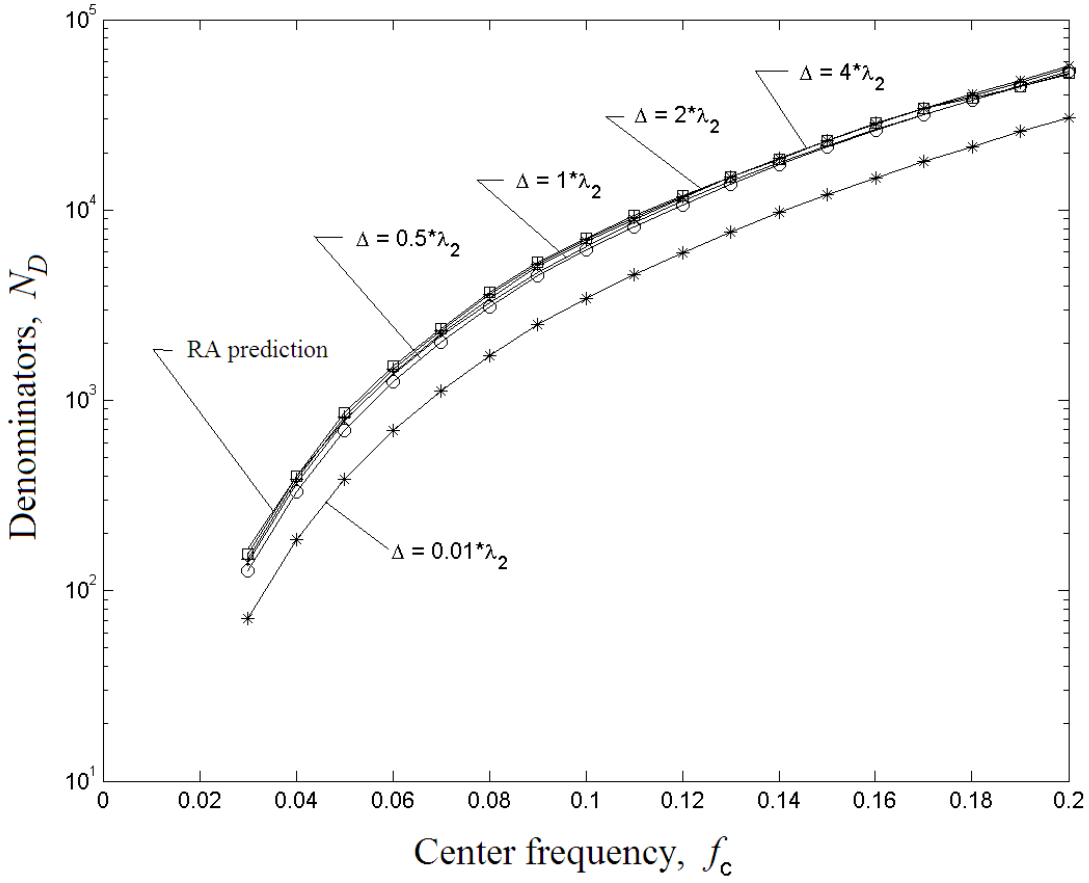

Figure 4.23: The "denominator" check of the three-room system over the frequency range and for various values of Δ.

of Δ. As in Fig. 4.6, the values of N_D extracted by the concatenation ansatz all lie on top of the value required by the room-acoustics prediction except for the very smallest value of Δ used.

The overall results for the three-room system are as encouraging as they are for the two-room system. The diffusion parameters extracted by the concatenation routine represent the original data well over the range of frequency and Δ considered. Though the three-room system is not much more complicated physically than the two-room system, it does three eigenvalues to be extracted instead of two. This slight increase in complexity, along with the procedure in Section 4.3 to consider systems with more sources than subsystems, gives us some confidence to consider the

even more complicated systems with many eigenvalues that may or may not be able to be extracted in later chapters.

4.5 Conclusion

In this chapter, we have been able to successfully apply our concatenation ansatz to two relatively simple structures typically studied by SEA. The structures had two or three obvious substructures, making the framework easily comparable to SEA. The flow rates extracted by the diffusion limit of the concatenation ansatz better represent the data then the flow rates predicted by SEA. The nondiffusive regime of the concatenation ansatz can be used to provide more information at early times than what can be provided by SEA.

In the next chapter, we apply the concatenation ansatz to a single statistically homogenous structure, a structure to which the SEA framework cannot be applied.

Chapter 5

Application to pure diffusion

We discussed the applicability of concatenation to diffusion in Section 3.2 as opposed to conduction. As discussed in Section 1.2.2, applications of diffusion in mechanics include scattered wave propagation in polycrystals,[15] water,[16–18] and granular materials.[19] Room acoustics[20] is also based on assumptions of diffuse wave fields. In this chapter, we perform a numerical simulation in a purely diffusive (vs conductive) structure and apply the concatenation routine.

5.1 Description of the system

A cartoon of the diffusive system is in Fig. 5.1. The system being studied is a 60×600 mesh of unit masses and unit length strings under unit tension. Each mass is indexed by i and j, where $i \in \{1 \dots 60\}$, and $j \in \{1 \dots 600\}$. As discussed in Section 1.3.1, such a mesh can be thought of a model of a membrane, but reproducing the membrane model is not necessary.

Each mass is connected to a linear spring in the out-of-plane direction, constituting a springy base. The spring constants are chosen from a uniform distribution $\kappa \in [0, 1]$. The springs constituting the elastic base act as scatterers at every node. Wavefronts cannot propagate coherently through the structure, and, instead, we imagine vibrational energy spreading out diffusively.

The boundary conditions are periodic across both the width and the length. The structure

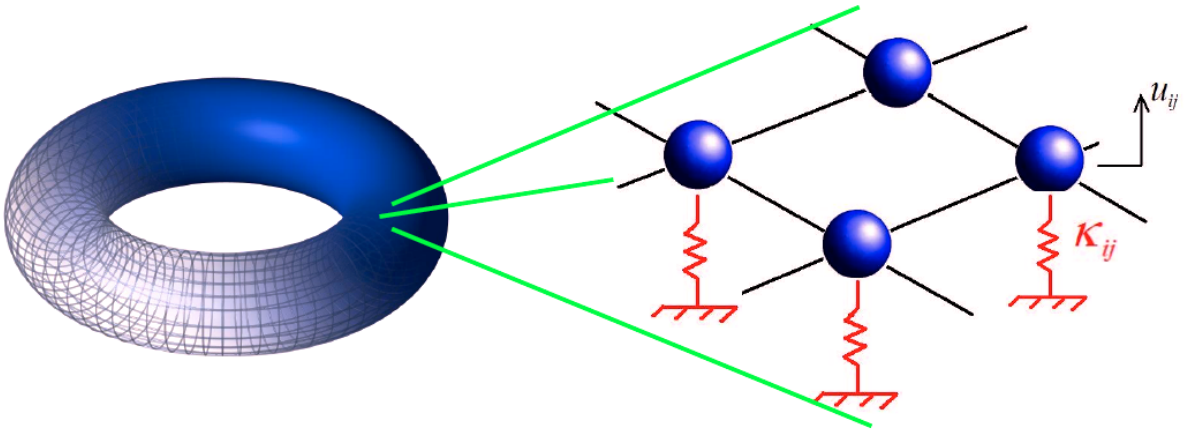

Figure 5.1: (Color in the electronic version.) A cartoon of the diffusing system. It is a rectangular strip (membrane or, alternatively, a mesh of masses and strings). The strip has periodic boundary conditions in both directions, so it can (abstractly) be thought of as a torus. The strip lies on a random elastic foundation to provide scattering.

can, thus, be thought of as a torus. The torus model is abstract. There is no stretching of the coordinates, so they remain on a rectangular mesh. The purpose of enforcing periodic boundary conditions is so that there are no reflections from boundaries, and the structure is statistically homogeneous. Statistical homogeneity implies that there is a single diffusivity constant—analogous to α in Eq. (1.7)—that describes the energy flow in the structure.

Applying Newton's second law to each mass in the mesh results in the governing differential equation

$$\left(4+\kappa_{ij}\right) u_{i,j}(t) - u_{i-1,j}(t) - u_{i+1,j}(t) - u_{i,j-1}(t) - u_{i,j+1}(t) + \frac{\mathrm{d}^2}{\mathrm{d}t^2} u_{i,j}(t) = B_{ij}(t), \qquad (5.1)$$

for the displacement $u_{i,j}$ of the mass at location i, j. In Eq. (5.1), B_{ij} is a source on the mass at location i, j. Using the three-step centered scheme in Eq. (1.11) to approximate the time derivatives and specifying quiescent initial conditions as in Eq. (1.9) results in a well posed algebra problem

that can be solved by a computer implementation.

Ten sources are placed equal distances (60 mesh spacings) apart from each other along the centerline of the mesh. A cloud of receivers is constructed around each of these nominal sites by placing eight receivers in a circle of radius of ten mesh spacings around each source, for a total of nine receivers in each cloud. The clouds are labeled $\rho \in \{1,2,3,\ldots,N_\rho\}$, with $N_\rho = 10$. The individual sites in each cloud are labeled $r \in \{1,2,3,\ldots,R\}$, with $R = 9$. The center site with the source is labeled $r = 1$, while the labeling for the other 8 sites is never particular used.

5.2 Results

Using $\delta t = 0.4$, the admittances E of Eq. (1.18) were calculated explicitly for all 90 receiver sites. They are plotted for a relatively low frequency $f_c = 0.11$ in Figs. 5.2. The admittances from DNS were not studied in detail in the two- and three-room problems in Chapter 4, but it is important to study them in the present problem. The reason they were not studied carefully in Chapter 4 is because there, the admittances were all the same at every source and receiver location. Every site was in the same environment. In particular, there were no reflections from boundaries or scatterers arriving back at the source site before T_B, the duration of the filter in time. It is evident from Eq. (1.18) that if there are no reflections arriving back at the source site before the end of the duration of the source, and the environment of the source site is the same amongst the several source sites, then the admittances E must be identical at all sites. In the present problem of pure diffusion there are no boundaries off which wavefronts can reflect. However, waves are continually being scattered off of the random elastic base.

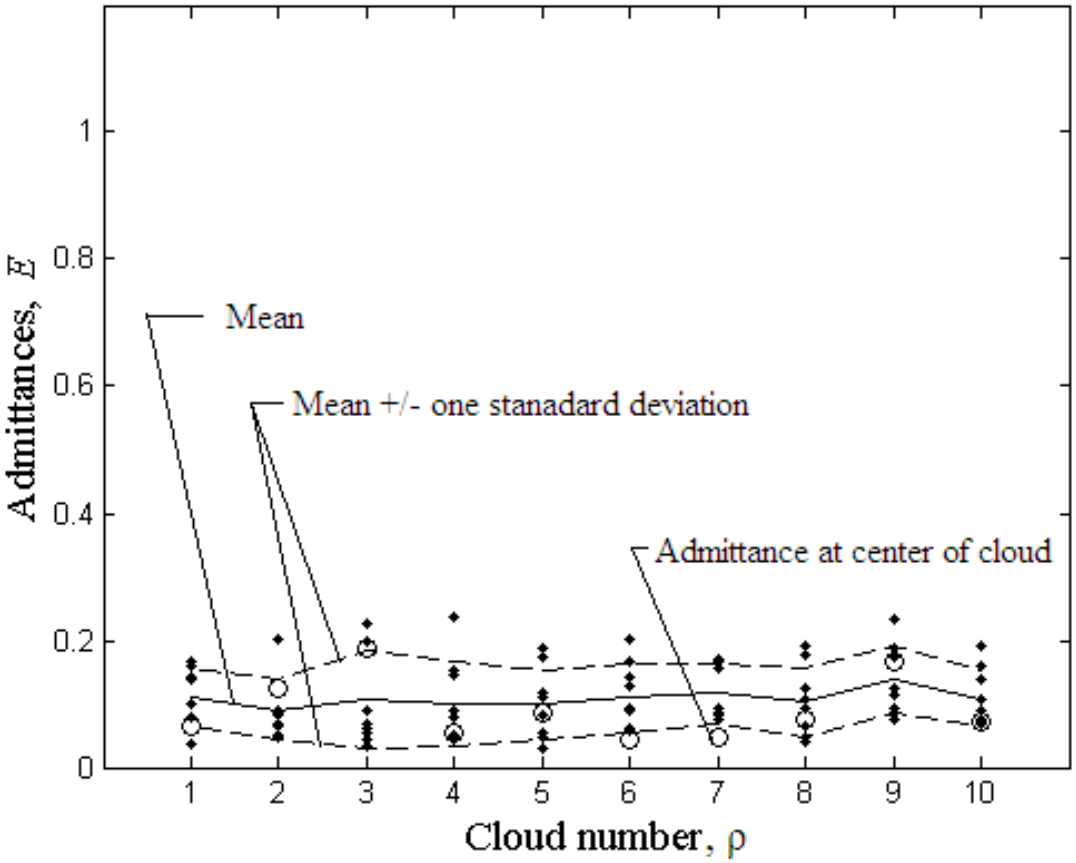

Figure 5.2: Admittances E at the various sites with a filter centered at $f_c = 0.11$

We expect the admittances E to be different at different sites, so that the late-time mean-square displacement at the various sites are expected to be different. The differences in the admittances can be seen in Fig. 5.2. The E associated with the nominal site in the center of each cloud ρ is marked with a circle while other Es in each cloud are marked with a dot. A solid line indicates the mean, while dashed lines mark intervals of one standard deviation. There is some spread in the data. The fluctuations away from the mean are around 100%, meaning that the energy deposited at one site is a bad estimate for the energy deposited at the other sites. The mean is used as an effective $E_{\text{eff}}(f) = \langle E \rangle_{\rho r}$, where the angled brackets denote average, below. The effective admittance E_{eff} is

a function of frequency, as are the individual admittances, but functional notation will be dropped for simplicity.

The admittances E are plotted for frequency $f_c = 0.20$ in Fig. 5.3 on the same scale as in

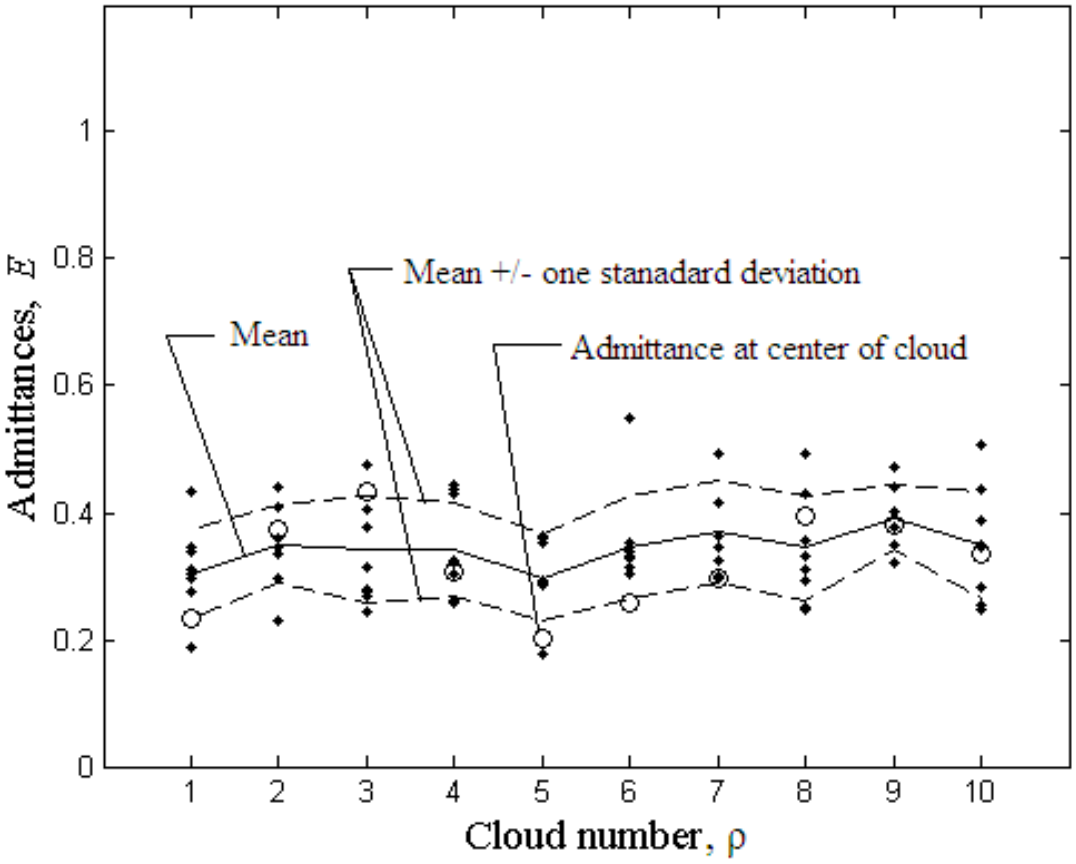

Figure 5.3: Admittances E at the various sites with a filter centered at $f_c = 0.20$

Fig. 5.2 for the lower frequency. The average admittance is higher at higher frequency. Increasing admittance with increasing frequency is expected, as the modes are more closely spaced. The variability across the various sites in the Es from the mean is still large. The typical fractional fluctuations are about 50% of the average, while the absolute fluctuations are only slightly larger than they were at the lower frequency.

The admittances E are plotted for frequency $f_c = 0.25$ in Fig. 5.4 again on the same scale as

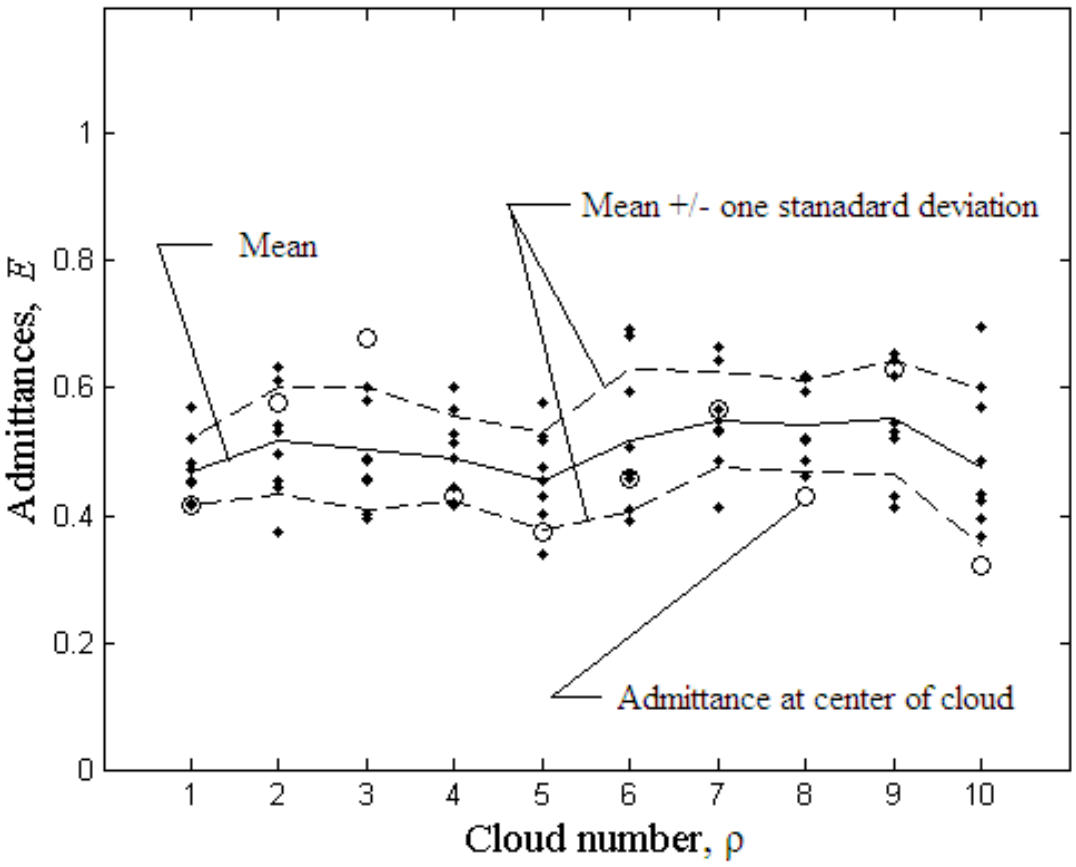

Figure 5.4: Admittances E at the various sites with a filter centered at $f_c = 0.25$

in Fig. 5.2 for ease of comparison. The admittances continue to increase with frequency. The fractional fluctuations across the 90 sites is smaller than it was at the two lower frequencies, but it is still too large to estimate the all of the Es using the admittance from the site in the center of the cloud.

Finally, in Fig. 5.5, the admittances E are plotted for a relatively large frequency $f_c = 0.30$ in the range considered in this chapter. The E generally increase again with frequency, and the typical spread is larger.

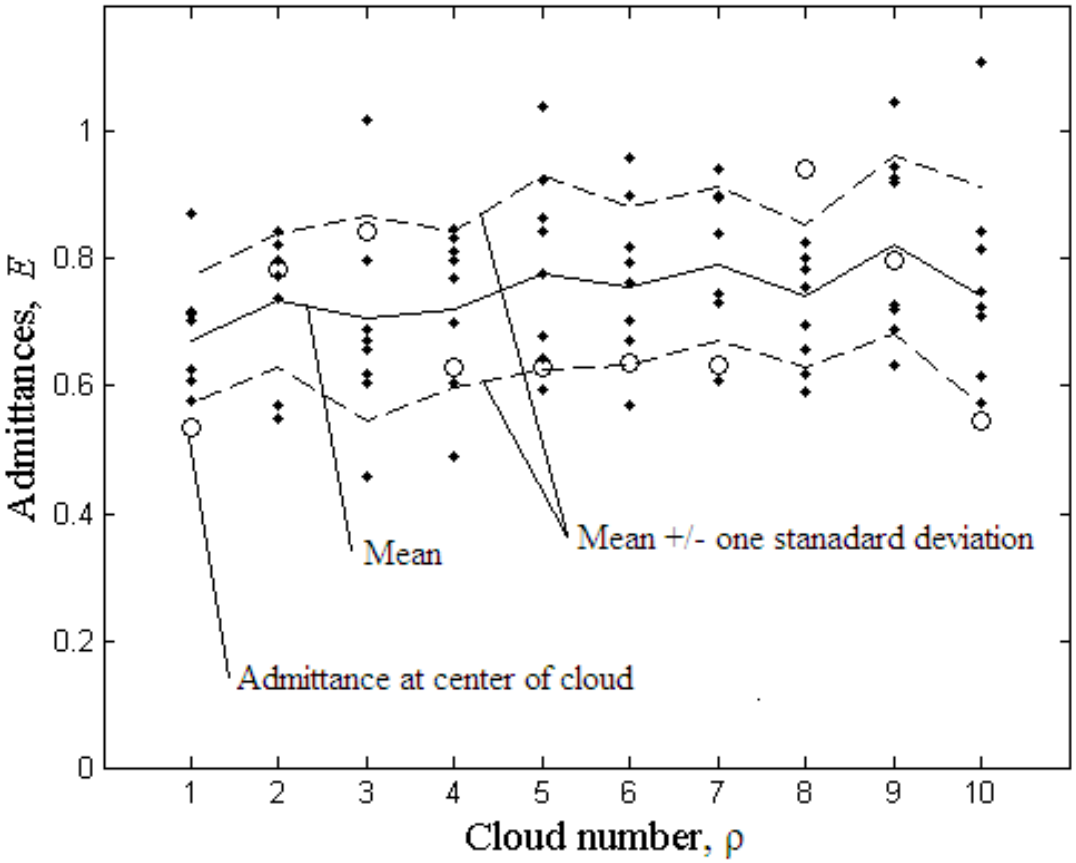

Figure 5.5: Admittances E at the various sites with a filter centered at $f_c = 0.30$

These values for E calculated from Eq. (1.18) were compared to a different calculation. The numerical simulation was run using the filter as a source, and the energy in the structure was calculated by finite-difference version of energy in Eq. (1.15) when the source had ceased at the end of the filter duration. The results (not shown) were identical up to machine precision, as they should be.

The dependence of admittance E on δt (also not shown) was also explored. The Es were found after running the DNS with the smaller time step $\delta t = 0.1$ to solve the ODEs more accurately compared to the time step $\delta t = 0.4$ used to produce Figs. 5.2-5.5. At frequency $f = 0.2$, the Es

were $\approx 10\%$ lower with $\delta t = 0.4$ than with $\delta t = 0.1$, and at frequency $f = 0.3$, the Es were $\approx 20\%$ lower with $\delta t = 0.4$ than with $\delta t = 0.1$. This dependence on the time step makes sense in light of Eq. (1.14). At the time step is increased at fixed frequency, the modes being investigated under the filter in the frequency domain are lower modes (with lower frequencies) of the exact ODEs. As we have already seen from Figs. 5.2-5.5, the admittances decrease with decreasing frequency, so they should also decrease with increasing time step.

The smoothed, squared, filtered response is found similarly to how it was found in the conduction two- and three-room cases in Chapter 4. The energy density, or intensity, quantity in cloud ρ due to a source in cloud $\sigma = 5$ being plotted in Fig. 5.6 is

$$\mathbf{J}_{\rho\sigma} = \left\langle \frac{\mathbf{J}_{\rho r\sigma 1}}{E_{\rho r} E_{\sigma 1}} \right\rangle_r E_{\text{eff}}^2, \tag{5.2}$$

where $\mathbf{J}_{\rho r\sigma 1}$ is the intensity at site r in cloud ρ due a source in cloud σ (at site 1 in the center of the cloud). Since the Es were different at each site, some care was taken in the averaging over the nine receivers in each cloud. Each squared, filtered response was divided by its own E and the E associated with the source site, and then each was multiplied by the effective (average) E for the structure. This averaging ensures that the *predicted* late-time averages for each site are identical, and the fluctuations decrease more rapidly with increasing the number of receivers in the average. This averaging required a short-time DNS at each of the $R \times N_\rho = 9 \times 10 = 90$ sites, but a long-time DNS at only $1 \times N_\rho = 10$ of the sites. An example of such a smoothed, squared, filtered response to a source at a site 5 in the "middle" of the strip in at frequency $f_c = 0.20$ is shown in Fig. 5.6.

The intensity quantity $\mathbf{J}_{\rho\sigma}$ does not exhibit reciprocity, i.e., $\mathbf{J}_{\rho\sigma} \neq \mathbf{J}_{\rho\sigma}$; however, the DNS does

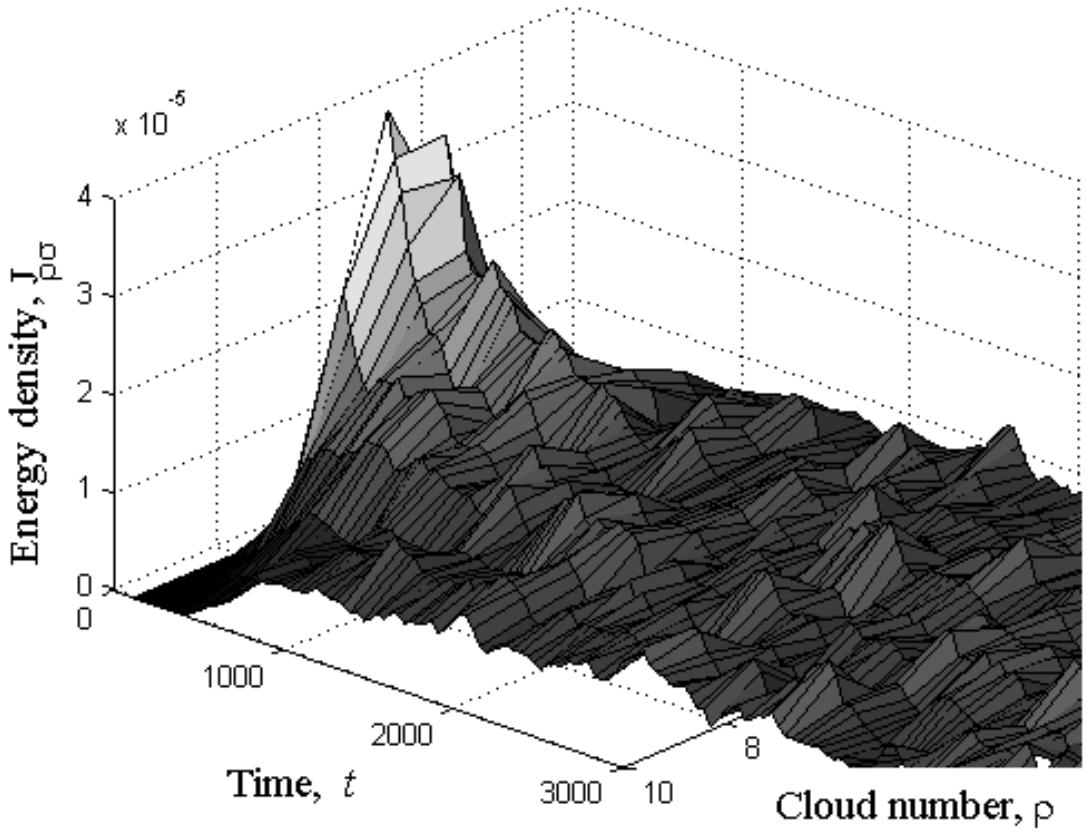

Figure 5.6: Smoothed, squared, filtered response from a source at the center of cloud number $\sigma = 5$ in a frequency band with $f_c = 0.20$.

such that $\mathbf{J}_{\rho r \sigma s} = \mathbf{J}_{\sigma s \rho r}$. The intensity $\mathbf{J}_{\rho\sigma}$ is close to symmetric. In order for it to be identically symmetric, averaging would have to be performed over sources acting through all nine sites in each of the ten clouds.

The intensity in Fig. 5.6 can be compared to the solution to the one-dimensional diffusion equation Eq. (1.7) (with a normalized impulsive source term at time $t = 0$ and location $x = 0$). It is

$$\mathbf{J}(x,t) = \frac{1}{\sqrt{4\pi\alpha t}} e^{-\frac{x^2}{4\alpha t}}, \tag{5.3}$$

or a spreading Gaussian centered at the source location. The solution at the source location decays like $1/\sqrt{t}$. The spreading Gaussian nature of the response is evident in Fig. 5.6, with a peak at $t = 0$ and $\sigma = \rho = 5$. There are some minor differences. In the DNS, the system in periodic, so one must imagine other spreading Gaussian distributions extending in both directions. Related to the periodicity of the system, the single spreading Gaussian decays to zero everywhere, as the energy density (energy per unit length) is zero. In contrast, the solution by DNS goes to the quantity given by Eq. (1.16), as the energy density is finite. Finally, energy does not travel instantly across the entire structure as in diffusion. The DNS solution does not behave like a spreading Gaussian until diffusion has set in after some short finite time.

We next attempt to extract eigenvalues and eigenvectors using the concatenation ansatz diffusion limit. We must choose a Δ. We choose $\Delta = 1/300, 0.5/300, 0.25/300, 0.1/300$. The reference time 300 was chosen because it takes roughly $t = 300$ for the excitation from a given source to explore the entire structure and for diffusion to set in, by inspection of plots of energy density. The extracted eigenvalues are shown in Fig. 5.7. The meaning of the dimensionless values of Δ_{1-4} in the figure is discussed below after defining a diffusion constant α for the system. The concatenation diffusion limit finds reasonable values for 7 eigenvalues for the largest two values of Δ, but fewer for the lower two values of Δ. Nonetheless, the eigenvectors associated with the higher eigenvalues decay quickly, so they are important only at relatively early times before diffusion sets in. Eigenvalues predicted by a diffusion theory would not describe the DNS solution well, anyway, as such early times because diffusion has not yet set in. The first two nontrivial eigenvalues come in pairs, as they should. The second pair of eigenvalues, particularly for the largest value of Δ, are approximately four times greater than the first pair, as they should be. The first pair of eigenvalues

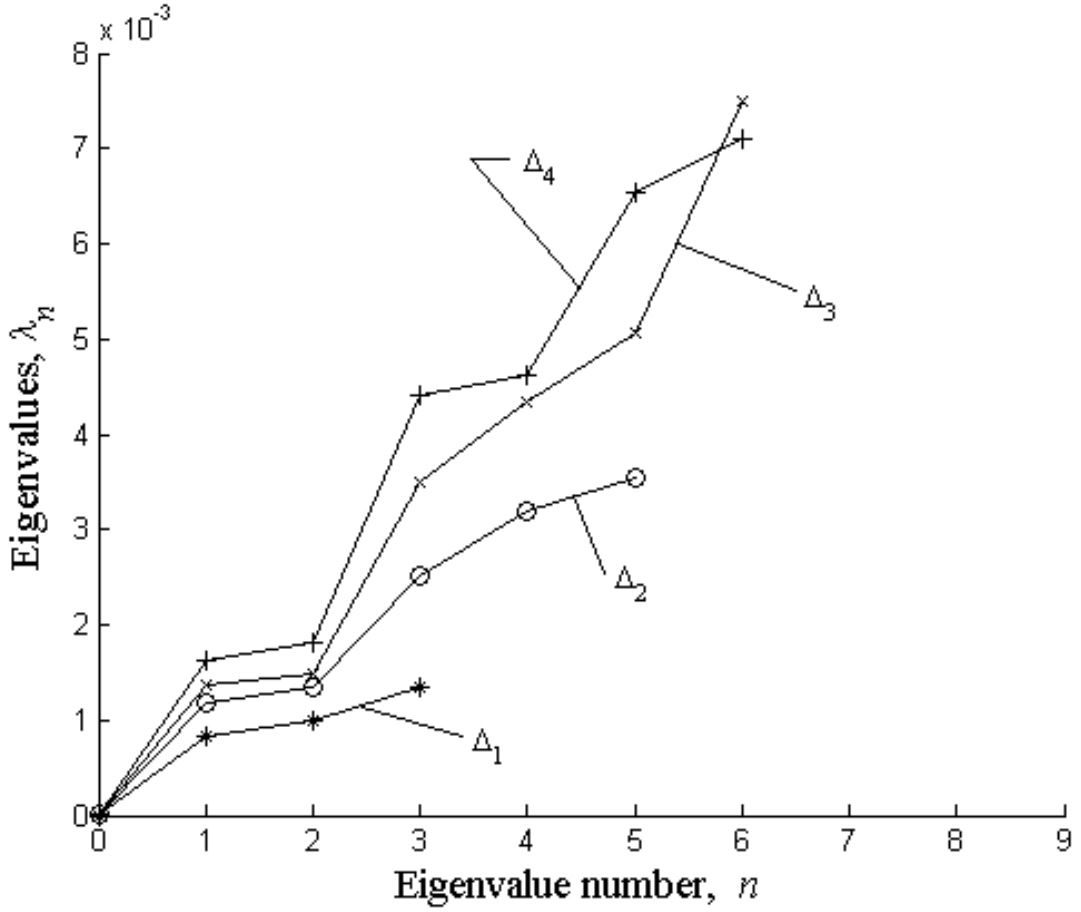

Figure 5.7: Eigenvalues extracted by concatenation using data in Fig. 5.6.

have a value of about 0.0013, yielding a diffusion time of $1/\lambda_2 = 770$. The smallest time information window $(1/\Delta)$ used was somewhat more than one-third of this diffusion time, and the longest time information window used was somewhat less than four times this diffusion time.

Using the first two nontrivial eigenvalues, we can estimate a diffusion coefficient α for the structure

$$\alpha = \frac{1}{(2\pi)^2}\frac{\lambda_2+\lambda_3}{2}L^2, \tag{5.4}$$

where $L = 600$ is the length of the structure. The retrieved diffusion coefficient is plotted against frequency and Δ in Fig. 5.8. The behavior of α is an interesting function of frequency. Though

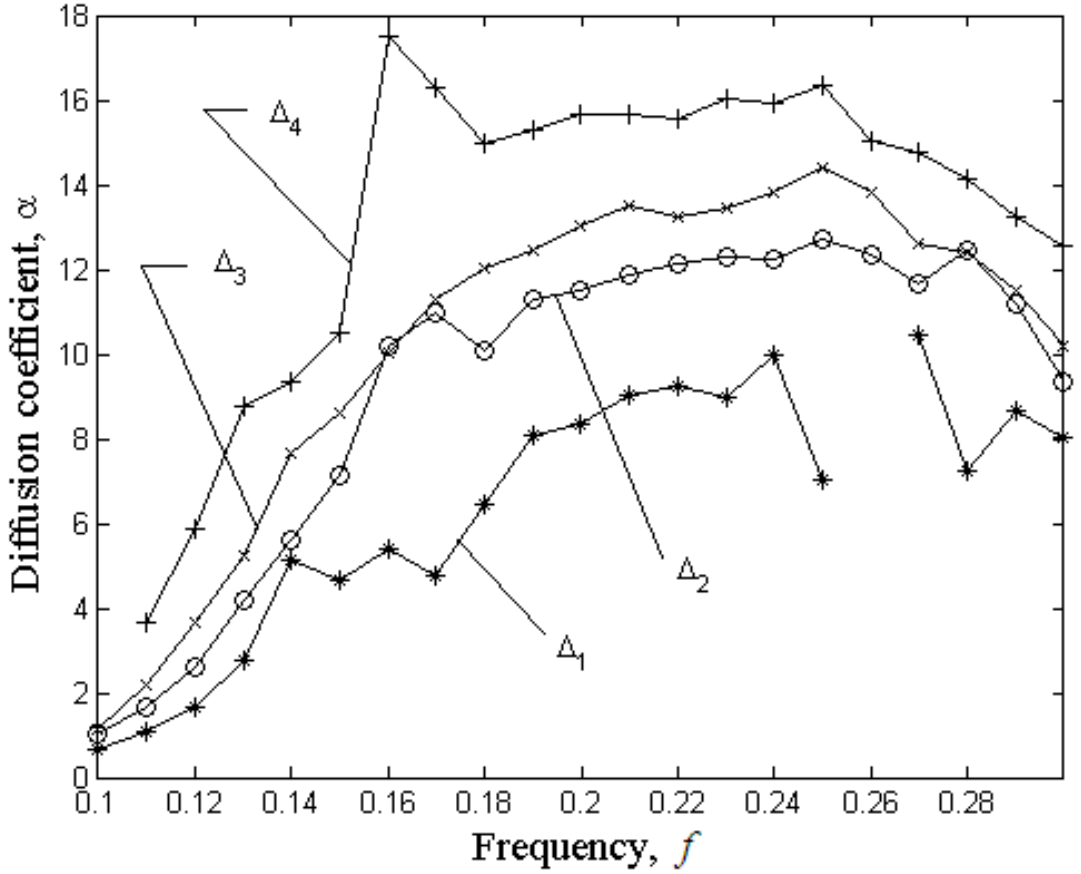

Figure 5.8: Diffusion constants α calculated by the formula in Eq. (5.4) and eigenvalues in Fig. 5.7.

the exact value of α extract by the diffusion limit of the concatenation ansatz depends on the value of Δ used, the trend is the same, and they are all in the same order of magnitude. The diffusivity of the structure increases with frequency to some maximum in the middle of the frequency range considered here, then decreases again. They system spreads energy across the structure most efficiently in the middle of the frequency range.

The values of the dimensionless Δ_{1-4} were then constructed as $\Delta d^2/\alpha$ with Δ being the dimensional values of $\Delta = 1/300, 0.5/300, 0.25/300, 0.1/300$. One can see the importance of this dimensionless Δ be recognizing it as (the square of) the exponent appearing in Eq. (3.22) for two adjacent

sites. The dimensionless values of Δ are plotted in Fig. 5.9. Since Δ and d are constants for each of

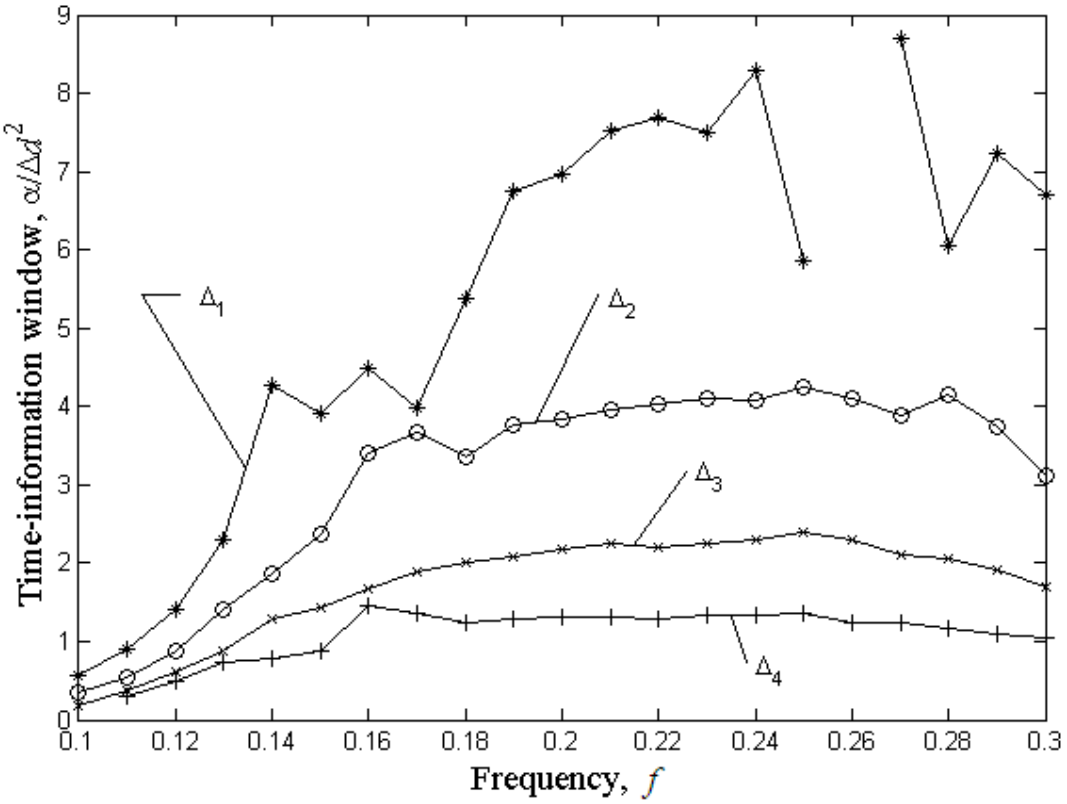

Figure 5.9: Dimensionless version of the information-time window $1/\Delta$.

the four curves in Fig. 5.9, they have the same functional form as α corresponding to each curve. As expected, the smallest Δ retains information for the longest amount of time, while the largest Δ retains information for the shortest amount of time.

In Fig. 5.8, the values for α agree for the middle two values of Δ. The discrepancies for the two extreme values of Δ can be explained as follows. For the largest value of Δ, $\Delta_4 = \Delta d^2/\alpha \approx 1$, so that the energy does not have time to spread over nearby receivers. That is, there is not enough information in the data to retrieve accurate diffusion parameters. For the smallest value of Δ, the numerical integrals of Eq. (4.5) do not converge with the limited data obtained from the DNS. This

explanation for the error for small Δ was confirmed with a convergence study of partial integrals.

To show how well the concatenation ansatz performs, we show the prediction constructed from the eigenvalues and eigenvectors extracted by concatenation (for $\Delta = 0.5/300$) in Fig. 5.10 for the a source in cloud $\sigma = 5$ and $f_c = 0.20$, that is the same conditions for the DNS plotted

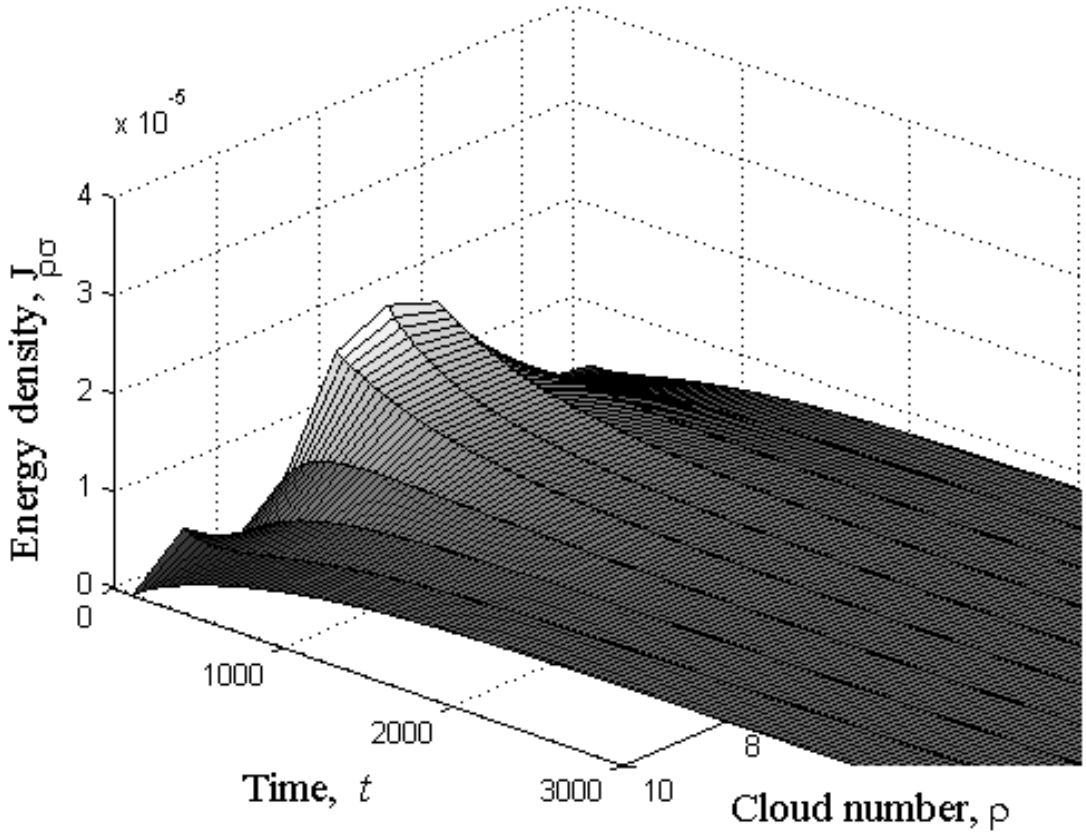

Figure 5.10: Prediction from the concatenation ansatz diffusion limit with a source in the center of cloud $\sigma = 5$. The value of $\Delta = 1/600$ used here corresponds to a time information window somewhat less than a full diffusion time.

in Fig. 5.6. Both the overall shape is captured correctly, and the overall magnitude is captured correctly, at least at late times where we expect the diffusion limit of the concatenation to extract a good first correction to the late-time steady-state values in Eq. (1.16). The overall shape is a

property related to the eigenvalues, while the over magnitude is a property related to modal density. Early-time behavior is not predicted as well, as expected. Only a maximum of 10 eigenvalues are available, as there are only ten clouds of receivers. Mathematically, one cannot capture a the sharp peaked Gaussian of Eq. (5.3) at early times well with only ten eigenvalues. In addition, and more physically important, diffusion has not yet set in at such early times when the diffusion limit of the concatenation ansatz fails to represent DNS well. Using the convolution integrals in Eq. (3.3) to construct the concatenation solution directly outside of the diffusion limit would predict the early-time behavior well.

5.3 Conclusion

This chapter emphasizes a powerful advantage our concatenation ansatz has over SEA. Any implementation of SEA for a complex system requires that it be broken up into various substructures with modal densities that can be estimated. Such a partitioning into substructures can be problematic. It may be difficult to know if part of the structure is sufficiently homogenized to be able to consider it a single substructure. Different mode types may have to be separated. A small substructure may not be sufficiently large for the necessary modal averaging to be valid. The example of a single homogeneous system in this chapter illustrates that there is no such need for substructures in the concatenation ansatz framework.

Chapter 6

Three coupled plates

So far, we have established the usefulness of using our concatenation theory in some simple two- and three-room systems typically studied with SEA in Chapter 4 and a single system without substructures in Chapter 5. In this chapter we study a system more of interest to the structural mechanics community. The system consists of three parallel simply-supported plates coupled by a number of identical springs. A cartoon of the system is in Fig. 6.1. Before describing our problem in detail in Section 6.2, we review plate theory and the statistics of wave energy transfer between plates.

6.1 Mathematical preliminaries

6.1.1 Plate theory

To define terms, we briefly review Kirchhoff plate theory for the dynamics of the plates[57] before describing the statistical energy flow between the plates through the springs. The governing differential equation for the out-of-plane displacement w of a plate in the xy plane as a function of time t is

$$D\nabla^4 w(x,y,t) + \rho h \partial_t^2 w(x,y,t) = q(x,y,t), \tag{6.1}$$

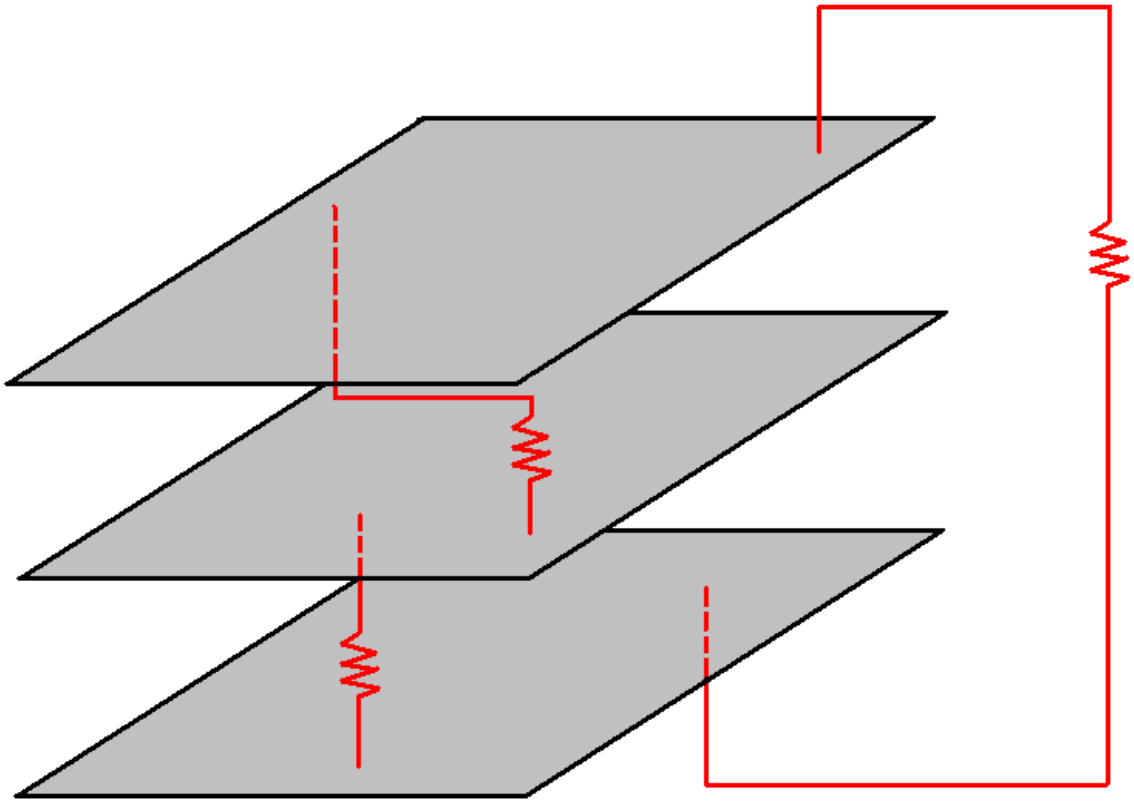

Figure 6.1: (Color in the electronic version.) A cartoon of a system of three plates coupled by springs.

where D is the plate rigidity, ρ is the volumetric mass density, h is the plate thickness, and q is a force per unit area perpendicular to the plate. The plate rigidity is

$$D = \frac{Eh^3}{12\,(1-\nu^2)} \tag{6.2}$$

in terms of the Young's modulus E and Poisson's ratio ν.

In the next section, we derive a characteristic spring stiffness and expressions for the rate of energy flow between two plates coupled with a number of springs with that characteristic stiffness. The development in the next section is the SEA formulation to which our concatenation results

will be compared.

6.1.2 Statistics of wave energy transfer between plates

The spring stiffness used in our DNS was taken to be a characteristic spring stiffness, derived in this section, obtained from energy flow considerations. Consider the two plates connected by a spring with stiffness κ in Fig. 6.2. The two plates have thickness h_{up} and h_{low}, area A_{up} and A_{low},

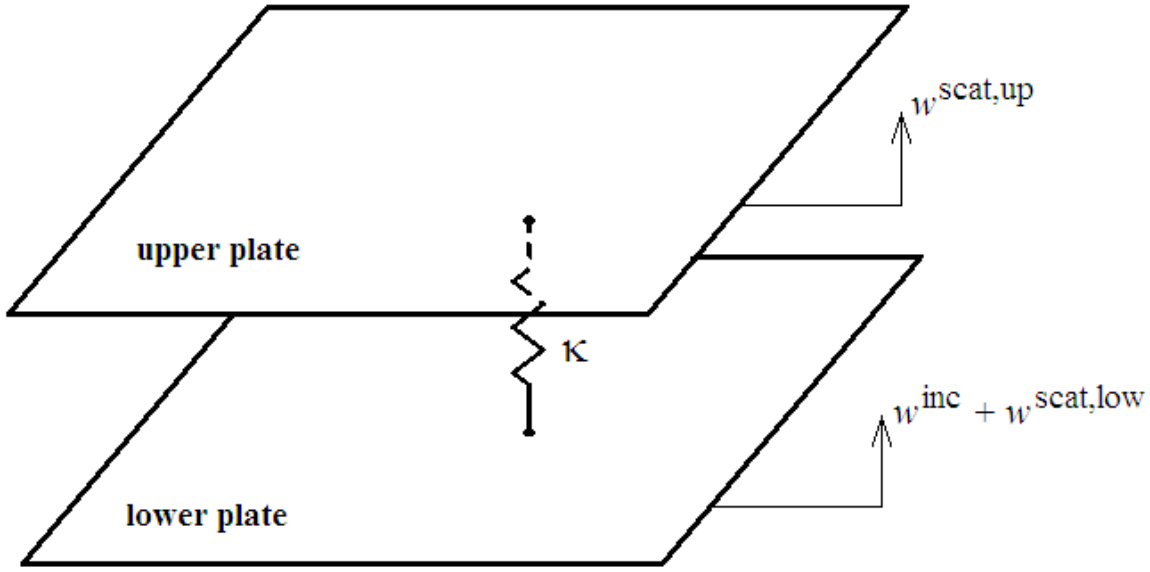

Figure 6.2: A cartoon of a system of two plates, a lower plate and an upper plate, coupled by a spring of stiffness κ. The field in the lower plate is an incident wave w^{inc} plus a scattered wave $w^{scat,low}$ from the spring. The field in the upper plate is only a scattered wave $w^{scat,up}$ from the spring.

density ρ_{up} and ρ_{low}, stiffness D_{up} and D_{low}, and Green's function G_{up} and G_{low} in the upper and lower plate, respectively. The incident displacement w^{inc} in the lower plate is a diffuse (random) wave field. The upper plate is initially quiescent.

Invoking Hooke's law, the upward force from the spring onto the upper plate is

$$f = \kappa\left(w^{\text{inc}} + w^{\text{scat,low}} - w^{\text{scat,up}}\right), \tag{6.3}$$

where $w^{\text{scat,low}}$ is the scattered field reflected back into the lower plate and $w^{\text{scat,up}}$ is the scattered field radiated into the upper plate. All functions over space in Eq. (6.3) and in what follows are evaluated at the location where the spring is connected to the upper plate. Substituting

$$w^{\text{scat,low}} = -G_{\text{low}} f \tag{6.4}$$

and

$$w^{\text{scat,up}} = G_{\text{up}} f \tag{6.5}$$

into Eq. (6.3) and rearranging, we find that the force in the spring is

$$f = \frac{\kappa w^{\text{inc}}}{1 + \kappa\left(G_{\text{up}} + G_{\text{low}}\right)}. \tag{6.6}$$

The initial energy in the lower plate in a narrow frequency band centered at ω is twice the kinetic energy, so

$$E_{\text{low}} = 2 \times \frac{1}{2}\rho_{\text{low}} h_{\text{low}} A_{\text{low}} \left\langle \left(w^{\text{inc}}\right)^2 \right\rangle \omega^2, \tag{6.7}$$

where the angle brackets denote spatial average. The power flow into the upper plate is the dot product of the force that the spring exerts on the upper plate with the velocity of the upper plate

evaluated at the point the spring is connected, or

$$\Pi = f\frac{\partial w^{\text{scat,up}}}{\partial t}. \tag{6.8}$$

We now invoke the narrow band nature of the spring force and wavefields to write

$$f = \left(Fe^{i\omega t} + F^* e^{-i\omega t}\right)/\sqrt{2}, \tag{6.9a}$$

$$w^{\text{inc}} = \left(We^{i\omega t} + W^* e^{-i\omega t}\right)/\sqrt{2}, \tag{6.9b}$$

$$w^{\text{scat,up}} = \left(Ve^{i\omega t} + V^* e^{-i\omega t}\right)/\sqrt{2}, \tag{6.9c}$$

where the superscript $*$ denotes complex conjugate. Substitution into Eqs. (6.6), (6.5), (6.7), and (6.8) results in

$$F = \frac{\kappa W}{1+\kappa\left(G_{\text{up}} + G_{\text{low}}\right)}, \tag{6.10a}$$

$$V = G_{\text{up}} F, \tag{6.10b}$$

$$E_{\text{low}} = \rho_{\text{low}}\left(WW^*\right)\omega^2 A_l, \tag{6.10c}$$

$$\Pi = \left(FV^* i\omega - F^* V i\omega\right)/2, \tag{6.10d}$$

respectively, where i is the imaginary unit. The characteristic leaking time into the upper plate is defined as the initial energy in the lower plate divided by the initial power flow into the upper plate. That is,

$$T_{\text{L}} = \frac{E_{\text{low}}}{\Pi} = -\frac{1}{\omega}\frac{\left|1+\kappa\left(G_{\text{up}} + G_{\text{low}}\right)\right|^2}{\kappa^2 \Im G_{\text{up}}}\rho_{\text{low}} A_{\text{low}}\omega^2. \tag{6.11}$$

Evaluation of the leaking time in Eq. (6.11) requires the Green's function,

$$G = \frac{-i}{8\sqrt{\rho h D}\omega}, \tag{6.12}$$

of the plate at the excitation point, found by standard methods such as that found in Graff's textbook.[57] Substituting into Eq. (6.11) shows that the leak time,

$$T_{\mathrm{L}} = \frac{1+\frac{\kappa^2}{64\omega^2}\left(\frac{1}{\sqrt{\rho_{\mathrm{up}}h_{\mathrm{up}}D_{\mathrm{up}}}}+\frac{1}{\sqrt{\rho_{\mathrm{low}}h_{\mathrm{low}}D_{\mathrm{low}}}}\right)^2}{\kappa^2/8\omega^2\sqrt{\rho_{\mathrm{up}}h_{\mathrm{up}}D_{\mathrm{up}}\rho_{\mathrm{low}}h_{\mathrm{low}}D_{\mathrm{low}}}} A_{\mathrm{low}}\sqrt{\rho_{\mathrm{low}}h_{\mathrm{low}}/D_{\mathrm{low}}}, \tag{6.13}$$

is proportional to what is essentially the Heisenberg time, or modal density, in the lower plate,

$$T_{\mathrm{H,low}} = 2\pi\frac{\partial N}{\partial\omega} = \frac{1}{2}A_{\mathrm{low}}\sqrt{\rho_{\mathrm{low}}h_{\mathrm{low}}/D_{\mathrm{low}}}, \tag{6.14}$$

and inversely proportional to a symmetric coupling loss factor,

$$\eta(\kappa) = \frac{\kappa^2/8\omega^2\sqrt{\rho_{\mathrm{up}}h_{\mathrm{up}}D_{\mathrm{up}}\rho_{\mathrm{low}}h_{\mathrm{low}}D_{\mathrm{low}}}}{1+\frac{\kappa^2}{64\omega^2}\left(\frac{1}{\sqrt{\rho_{\mathrm{up}}h_{\mathrm{up}}D_{\mathrm{up}}}}+\frac{1}{\sqrt{\rho_{\mathrm{low}}h_{\mathrm{low}}D_{\mathrm{low}}}}\right)^2}. \tag{6.15}$$

The coupling loss factor is symmetric in plate labeling, i.e., $\eta_{\mathrm{up,down}} = \eta_{\mathrm{down,up}}$. If the upper and lower plates have identical thicknesses and material properties, the leak time reduces to

$$T_{\mathrm{L}} = \frac{2+\left(\kappa^2/8\omega^2\rho h D\right)}{\left(\kappa^2/8\omega^2\rho h D\right)}T_{\mathrm{H,low}}, \tag{6.16}$$

and we can define a characteristic spring stiffness

$$\kappa_{\mathrm{ch}} = \sqrt{8\omega^2\rho h D}. \tag{6.17}$$

Note that if the spring has the characteristic stiffness $\kappa = \kappa_{\text{ch}}$, the leak time is $T_{\text{L}} = 3T_{\text{H,low}}$. For infinite stiffness $\kappa = \infty$, that is, rigidly attached plates, the leak time is $T_{\text{L}} = T_{\text{H,low}}$.

Naturally, with more springs, energy leaks from the lower plate into the upper plate faster. If there are N_{sp} springs between the pair of plates, and the attachment points of the springs are far enough apart (say, a quarter wavelength), the springs act independently of each other. If the springs act independently of each other, the coupling loss factor

$$\eta_{N_{\text{sp}}}(\kappa) = N_{\text{sp}}\eta(\kappa) \tag{6.18}$$

is proportional to the number of springs between the pair of plates, and the leak time

$$T_{\text{L}} = \frac{1}{N_{\text{sp}}}\frac{2 + \left(\kappa^2/8\omega^2\rho hD\right)}{\left(\kappa^2/8\omega^2\rho hD\right)}T_{\text{H,low}} \tag{6.19}$$

is inversely proportional to the number of springs between the plates.

Now consider three plates with identical material properties and thickness, but with possibly different areas A_i, $i = 1,\ 2,\ 3$, with the same number of independent, identical springs coupling each pair of plates. Define the energy density in plate i as

$$\mathcal{E}_i = \frac{E_i}{A_i\sqrt{\rho h/D}}. \tag{6.20}$$

The power balance between the three plates becomes

$$\sqrt{\frac{\rho h}{D}}\begin{bmatrix} A_1 & 0 & 0 \\ 0 & A_2 & 0 \\ 0 & 0 & A_3 \end{bmatrix}\frac{\partial}{\partial t}\begin{Bmatrix} \mathcal{E}_1 \\ \mathcal{E}_2 \\ \mathcal{E}_3 \end{Bmatrix} = \{\Pi\}^{\text{ext}} - N_{\text{sp}}\eta\begin{bmatrix} 2 & -1 & -1 \\ -1 & 2 & -1 \\ -1 & -1 & 2 \end{bmatrix}\begin{Bmatrix} \mathcal{E}_1 \\ \mathcal{E}_2 \\ \mathcal{E}_3 \end{Bmatrix}, \tag{6.21}$$

where $\{\Pi\}^{\text{ext}}$ is the externally deposited power. Diffusion times can be estimated from the eigenvalue problem suggested by Eq. (6.21), that is,

$$N_{\text{sp}}\eta\begin{bmatrix} 2 & -1 & -1 \\ -1 & 2 & -1 \\ -1 & -1 & 2 \end{bmatrix}\{u\} = \lambda\sqrt{\frac{\rho h}{D}}\begin{bmatrix} A_1 & 0 & 0 \\ 0 & A_2 & 0 \\ 0 & 0 & A_3 \end{bmatrix}\{u\}. \tag{6.22}$$

Now that we have described the SEA formulation for plates couple with springs, we go on to describe our three-plate system in detail and the results of applying concatenation to DNS of the dynamics of the system.

6.2 Description of the system

Our three plate system (Fig. 6.1) was designed to have about 10 wavelengths per edge at some target frequency. We meshed the plates on a rectangular grid such that there were four nodes per nominal wavelength ($\lambda_c = 4$) at the (yet to be determined) target frequency with unit spacing between the nodes, so that the length units are in quarter-wavelengths at the target frequency.

The details of the meshing were determined by considering a $L_x \times L_y$ rectangular plate meshed on a regular grid with nodes located at (x_i, y_j), with $x_i = i$ for $i = 1,\ 2,\ 3 \ldots (L_x - 1)$, and $y_j =$

j for $j = 1,\ 2,\ 3 \ldots (L_y - 1)$. The displacement at position $\left(x_i, y_j\right)$ and time t_k is denoted by $w\left(x_i, y_j, t_k\right) = w_{i,j}\left(t_k\right)$. The derivatives in space at $\left(x_i, y_j\right)$ and time t_k are approximated by

$$\nabla^4 w\left(x_i, y_j, t_k\right) \approx \frac{1}{\Delta x^4}\left(20 w_{ij}\left(t_k\right) - 8 \sum_{\substack{\text{nearest} \\ \text{neighbors}}} w\left(t_k\right) + \sum_{\substack{\text{next} \\ \text{nearest} \\ \text{neighbors}}} w\left(t_k\right) + 2 \sum_{\substack{\text{diagonal} \\ \text{nearest} \\ \text{neighbors}}} w\left(t_k\right)\right), \quad (6.23)$$

where $\Delta x = x_{i+1} - x_i = y_{j+1} - y_j = 1$ is the spacing between nodes, equal in both directions. The time derivatives are approximated the same way as they were in Section 1.3.1.

Consider a spring connected to the plate at location $\left(x_i, y_j\right)$. The force density from this spring is

$$q_{ij} = \kappa\left(w_0 - w_{ij}\right), \quad (6.24)$$

where κ is the spring constant, and w_0 is the displacement of the plate to which the other end of the spring is attached at its attachment point.

The material properties of the plates were identical, with Young's modulus $E = 1$, density $\rho = 1$, and Poisson's ratio $\nu = 0.3$. The thickness of the plates were taken to be unity. The dimensions of the plates are 40×40 for plate one, 35×45 for plate two, and 30×55 for plate three, so that they all have about the same area A and, therefore, modal density by Eq. (6.14). These parameter choices result in a target frequency of

$$\omega_c = \sqrt{\frac{D}{\rho h}}\left(\frac{2\pi}{\lambda_c}\right)^2 = 2\pi \times 0.0750. \quad (6.25)$$

There are a set of identical springs of stiffness $\kappa = \kappa_{\text{ch}}\left(\omega_c\right)$ calculated from Eq. (6.17) between each pair of plates so that the plates are in a ring, and their ordering is unambiguous because every

one of the three plates is directly coupled to the other two plates by the same number N_{sp} springs. The locations of the ends of the springs on each plate were chosen independently using a random number generator, so the springs need to be thought of as having kinks in them. We studied three different realizations of the system with N_{sp} = 5, 10, and 35.

Boundary conditions of zero displacement at the edges and zero second derivative of displacement in the direction normal to the edges were enforced. The initial conditions were impulsive sources at each of 10 source/receiver sites in each of the three plates. The locations of the sites are chosen with a random number generator.

6.2.1 Results

In this section we discuss the results of the concatenation prediction algorithm and its diffusion limit. Most of the results are for the realization of the system with $N_{sp} = 10$ springs. We start with concatenation directly, i.e., the iterative convolution formula in Eq. (3.3). In Fig. 6.3, we have plotted the concatenation prediction vs time for various numbers of terms kept in Eq. (3.3). In Fig. 6.3, and later figures, the mean-square displacement (intensity) quantity being plotted is similar as that in Section 5.2. That is,

$$\mathbf{J}_{\rho\sigma} = \left\langle \frac{\mathbf{J}_{\rho r\sigma 1}}{E_{\rho r} E_{\sigma s}} \right\rangle_{rs} E_{\text{eff}}^2, \tag{6.26}$$

where ρ and σ range over 1 to 3, corresponding to the three plates, and *rrsub* and *sssub* range over 1 to 10, corresponding to the 10 sites in each plate. In contrast to the pure diffusion problem in Chapter 5, we have performed a long-time DNS with a source at each of the 10 sites in the three plates for a total of 30 simulations. In the pure diffusion problem, we would have needed

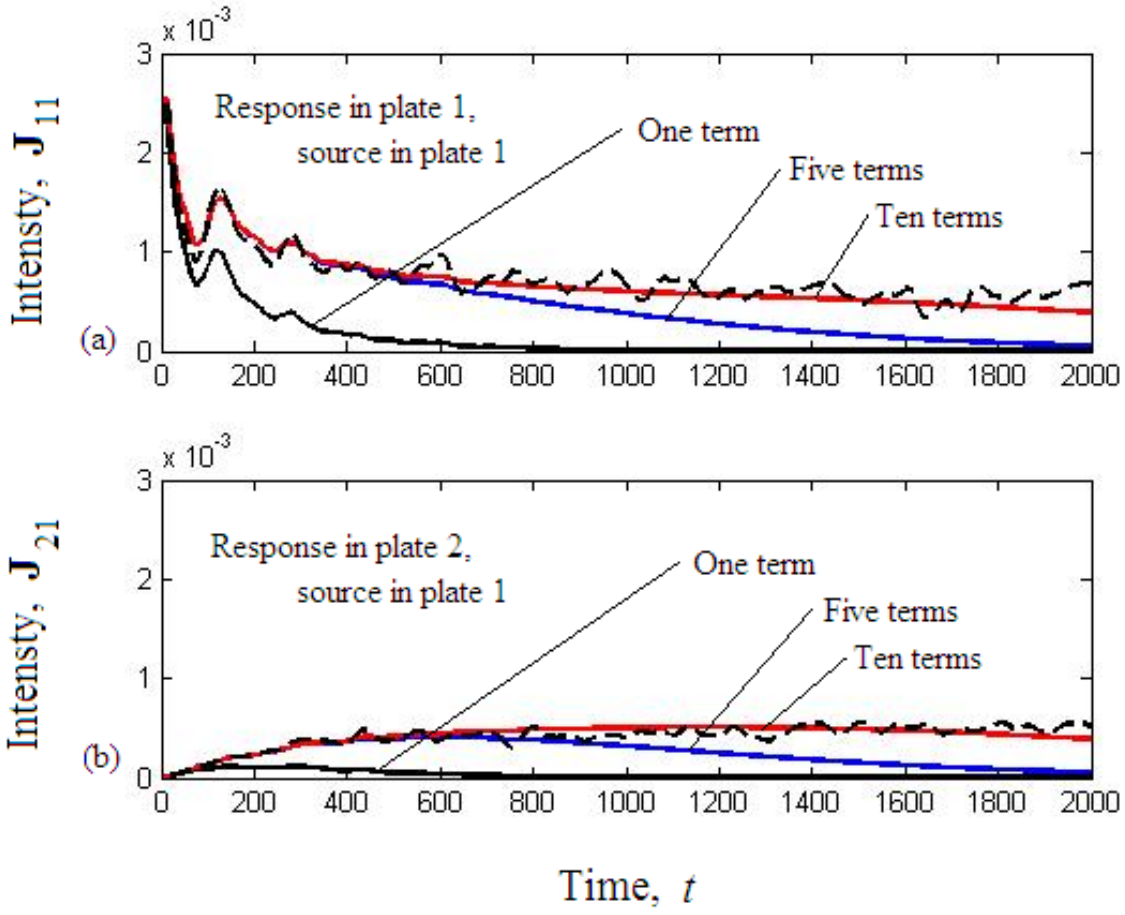

Figure 6.3: (Color in the electronic version.) Concatenation prediction for various number of terms kept in Eq. (3.3). The broken curves in each plot are the (mean squared bandlimited) response from DNS. The bottom one-term curves are $\widehat{\mathbf{J}}^{\Delta}$. (a) sources and receivers both in plate one. (b) sources in plate one, receivers in plate two.

$R \times N_{\rho} = 9 \times 10 = 90$ simulations to do the same amount of averaging as done for the present three-plate system.

Figure 6.3(a) contains results for the sources and receivers both in plate one, while Fig. 6.3(b) contains results for the sources in plate one and receivers in plate two. The broken curve in both plots is the (mean squared bandlimited) response from DNS. The bottom curve in both plots is the prediction retaining only one term, so it is precisely $\widehat{\mathbf{J}}^{\Delta}$. One can see how much data is

being kept from the one-term curve. The value of Δ being used is approximately equal to the first nontrivial eigenvalue predicted by SEA at the target frequency of $f_c = 0.0750$. We have assigned $\lambda_2 = 1/250$ for simplicity. The late time behavior is captured well if enough terms are kept, but, more impressively, the fluctuations at early times are also captured well in a very natural way, unlike in SEA.

There are four other independent plate-plate combinations. Both the response in plate two due to a source in plate two as well as the response in plate three due to a source in plate three look similar to Fig. 6.3(a). Similarly, both the response in plate three due to a source in plate one as well as the response in plate three due to a source in plate two look similar to Fig. 6.3(b). Two other combinations are not independent due to reciprocity, which holds because averaging is conducted over sources acting through every receiver. In particular, $\mathbf{J}_{12} = \mathbf{J}_{21}$, $\mathbf{J}_{13} = \mathbf{J}_{31}$, and $\mathbf{J}_{23} = \mathbf{J}_{32}$.

Here we discuss the validity condition Eq. (3.9) on the concatenation program. In Fig. 6.4 , we have plotted the extracted values of the modal density from the concatenation program for various values of Δ vs frequency. The straight horizontal curve is the known simple approximate constant value

$$\mathcal{N} = \frac{\mathrm{d}N}{\mathrm{d}f} = \frac{1}{2} A_{\mathrm{p}} \left(\frac{\rho_{\mathrm{p}} h}{D} \right)^{\frac{1}{2}} \tag{6.27}$$

from continuum mechanics. The value of Δ used to create Fig. 6.3 is one of the intermediate values used to create Fig. 6.4. The smaller value of Δ used to create the top curve retains data over more time, while the two larger values of Δ used to create the two bottom curves retain less time. There is a factor of eight difference between the smallest and largest values of Δ, and the various curves are in reasonably good agreement with each other.

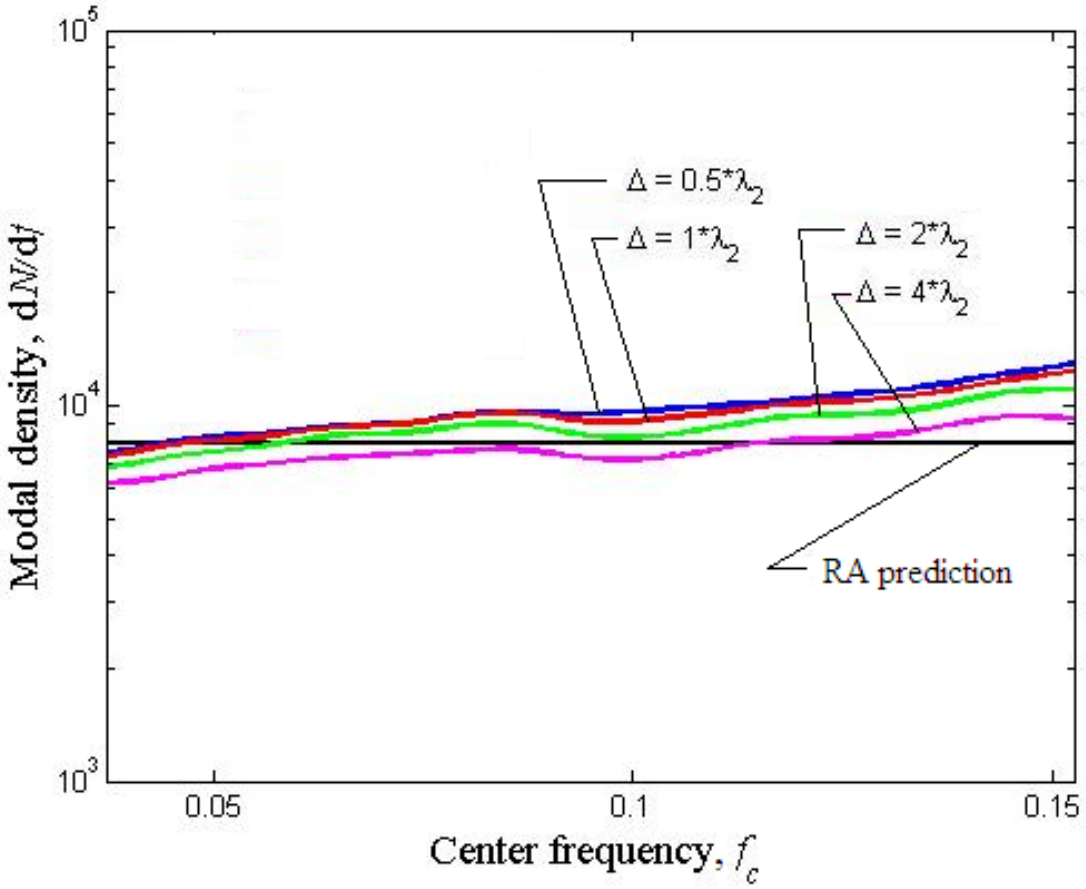

Figure 6.4: (Color in the electronic version.) The concatenation prediction of modal density. The predicted value of modal density from room acoustics (RA) is the straight horizontal line. For the dimensionless representation of Δ labeling the curves in the plots, we have assigned $\lambda_2 = 1/250$, which is approximately the leak rate predicted by room acoustics at the target frequency $f_c = 0.0750$.

We move on to some results of the diffusion limit of the concatenation program. In Fig. 6.5 we have the leak rate, defined as the first nontrivial eigenvalue of the [**H**] and [**D**] matrices, for the same values of Δ as in Fig. 6.4 vs frequency. In Eq. (6.22), the [**H**] matrix is on the right, and the [**D**] matrix is on the left. The smooth solid curve is the SEA prediction. The curves agree with each other, particularly at higher frequencies, which is not very surprising. Our curves deviate from the SEA prediction over part of the frequency range, especially the lower frequency range, but that is

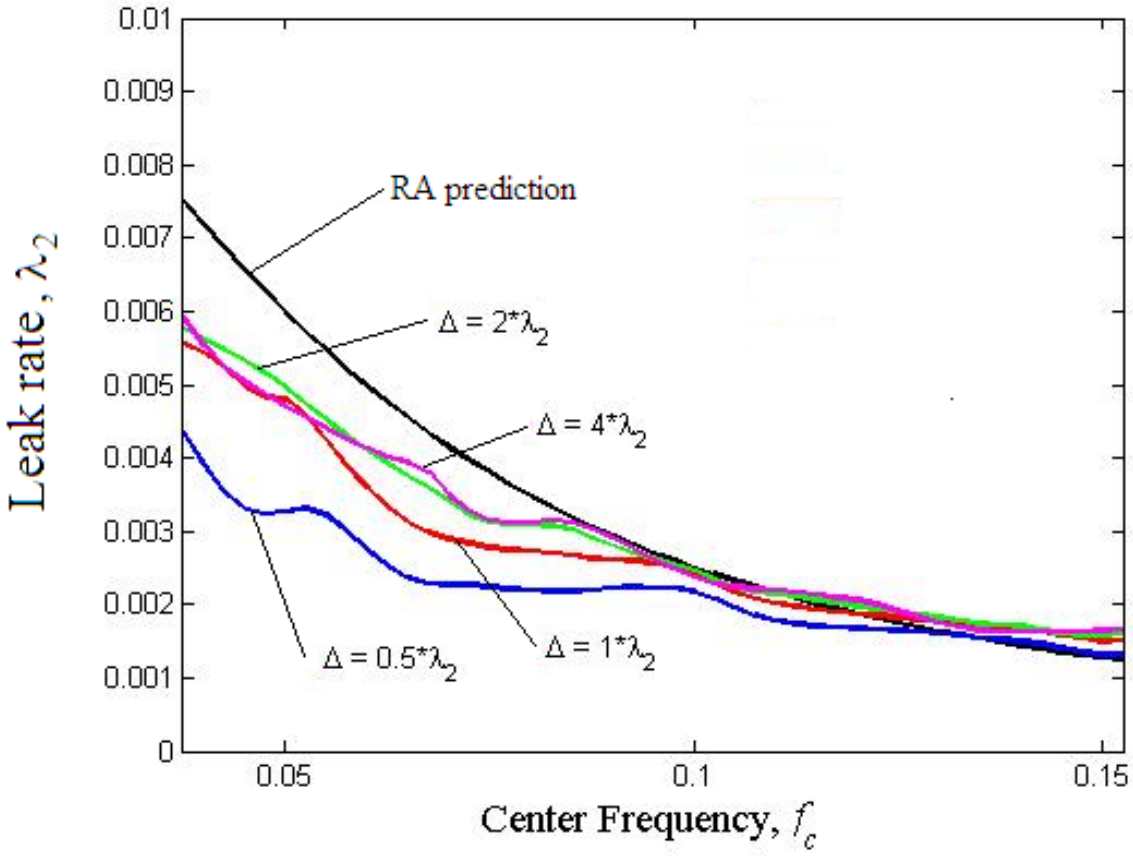

Figure 6.5: (Color in the electronic version.) Leak rate for various values of Δ compared to the SEA prediction. The meaning of the representation of Δ labeling the curves is given in the caption of Fig. 6.4.

not terribly surprising, either. The diffusion limit concatenation predictions for the leak rate agree with each other better than they agree with the SEA prediction. The SEA prediction does not well approximate the physics at lower frequencies.

We extend the diffusion limit prediction in Figs. 6.6 and 6.7. In these two figures, the smooth curves are the diffusion limit predictions vs time for the same values of Δ as in the previous figures, while the fluctuating curve in each plot is the DNS response. Figure 6.6 contains the response in plate one when the sources are also in plate one, while Fig. 6.7 contains the response in plate two

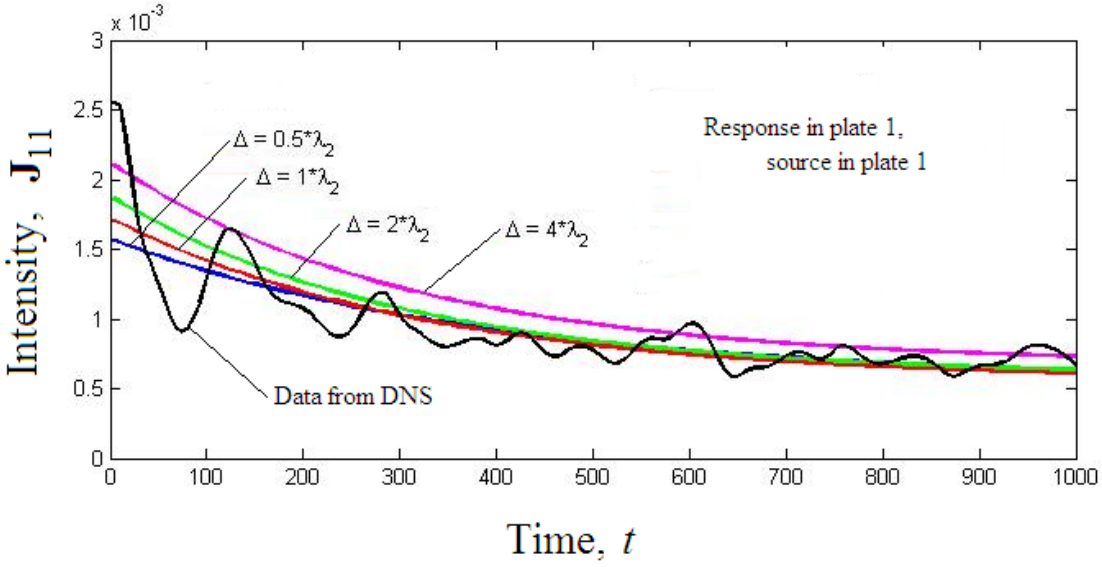

Figure 6.6: (Color in the electronic version.) The diffusion limit of the concatenation prediction to the DNS response for various values of Δ. The jagged curve is the DNS response in plate one when the sources are also in plate one.

when the sources are in plate one.

The smooth trend at late time is still captured well, though the early time trend is not captured as well. One cannot expect the fluctuates at early times to be captured by the diffusion limit of the concatenation program. The fluctuations are captured only by the convolutions of Eq. (3.3) directly. The diffusion limit is only a correction to the constant late time prediction. It is not surprising that the method works best using a relatively large value of Δ, keeping a full diffusion time or more of data. It may be surprising, however, how well the method works with the largest value of Δ considered, keeping DNS data only only one-fourth of a diffusion time.

Finally, we also explore the effect of changing the coupling strength between the plates by changing the number of springs between each pair of plates. The results of different coupling strengths are in Figs. 6.8 and 6.9. Figure 6.8 contains the response in plate one when the sources

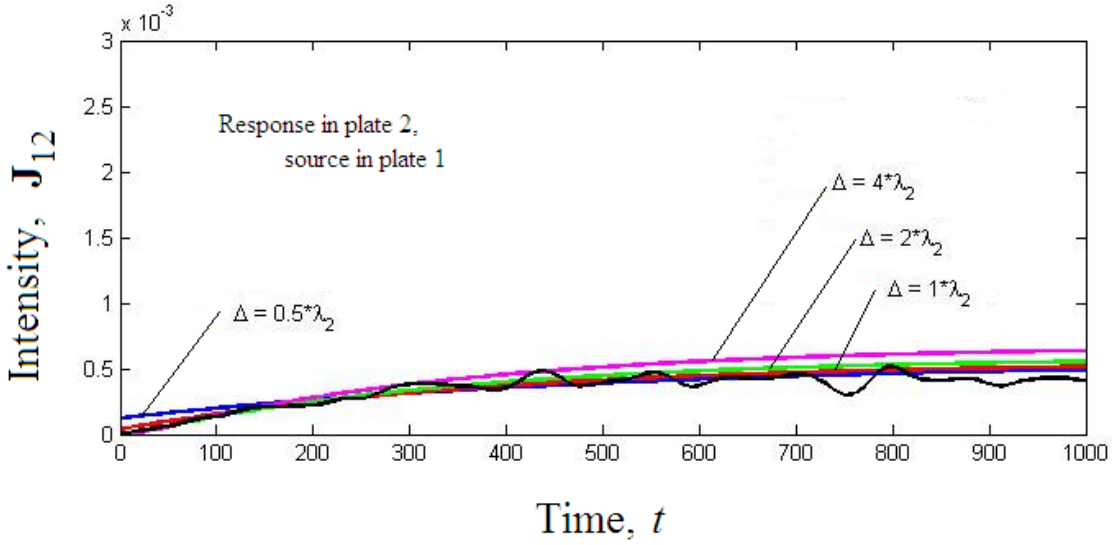

Figure 6.7: (Color in the electronic version.) Same as Fig. 6.6 with the response in plate one when the sources are in plate two.

are in plate one, while Fig. 6.9 contains the response in plate two when the sources are in plate one. Both figures contain subplots with results for 5, 10, and 35 springs. In each plot the smooth curves are the diffusion limit predictions vs time for the same values of Δ relative to the leak time predicted by SEA as in the previous figures. When $N_{\text{sp}} = 5$, we assigned $\lambda_2 = 1/500$, and when $N_{\text{sp}} = 35$, we assigned $\lambda_2 = 1/72$. The noisy curve in each plot is the DNS response.

For most of ranges plotted in these two figures at the resolution at which they are presented, the curves lie on top of each other. It is difficult to differentiate the curves, but this is unimportant. One can see that with five springs, the plates are less strongly coupled, and energy flows between the plates at slower time scales. With 35 springs, the plates are more strongly coupled, and energy flows between the plates at faster times scales. The maximum times for the different coupling strengths was scaled so that the smooth diffusion limit approximation would look the same for all coupling strengths, assuming that the SEA prediction was correct. They do, indeed, look similar.

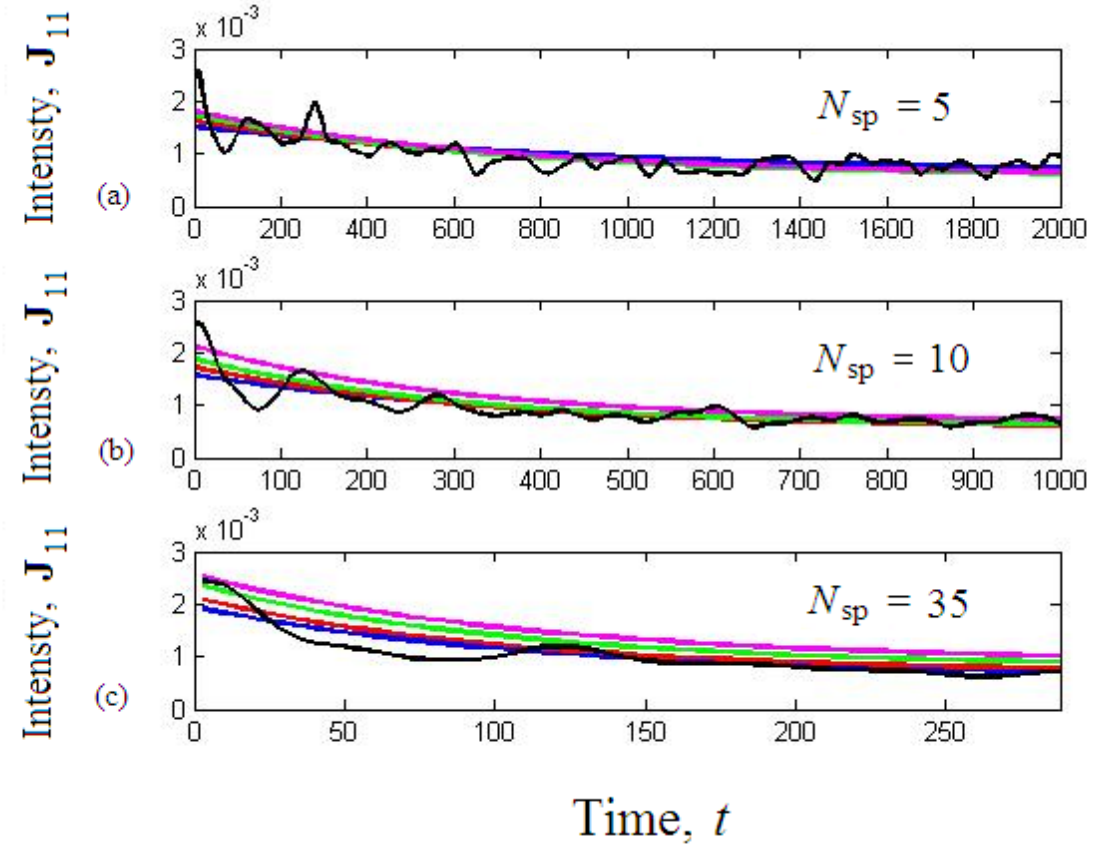

Figure 6.8: (Color in the electronic version.) The diffusion limit of the concatenation prediction to the DNS response for various values of Δ and coupling strength. The jagged curve is the DNS response in plate one when the sources are also in plate one. The (color) key is the same as in Figs. 6.4-6.7, though it is not very illuminating as the curves mostly lie on top of each other. (a) The number of springs is $N_{\text{sp}} = 5$. (b) $N_{\text{sp}} = 10$. (c) $N_{\text{sp}} = 35$.

When the system has the weakest coupling with only five springs, we see some localization where we expect both SEA and our concatenation program to fail. With 35 springs, the transport time of wave energy between plates is on the same order as the filter duration, so those time scales cannot be resolved well.

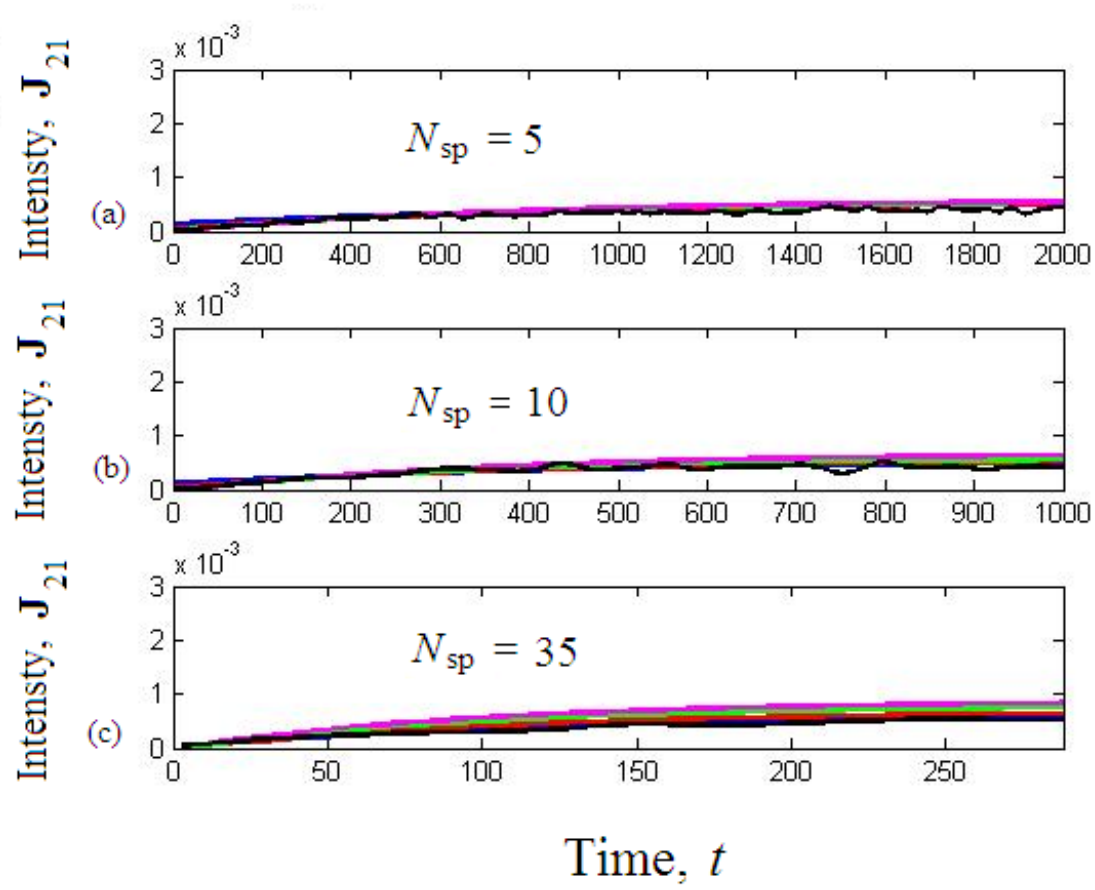

Figure 6.9: (Color in the electronic version.) Same as Fig. 6.8 with the response in plate one when the sources are in plate two. (a) The number of springs is $N_{\text{sp}} = 5$. (b) $N_{\text{sp}} = 10$. (c) $N_{\text{sp}} = 35$.

6.3 Conclusion

We have expanded our range of systems to which we can apply our concatenation ansatz to beyond simple membranes to somewhat more complex assemblages of plates and springs that are of interest to the structures community. The springs coupling the plates allow energy to be transferred between them diffusively. Both the concatenation ansatz and its diffusion limit serve their purposes well. The diffusion limit predicts the time scale on which energy transfer occurs. The direct concatenation ansatz captures the early-time fluctuations in particular systems which SEA cannot

capture. For our final example of systems to which to apply our concatenation ansatz in the next chapter, we consider a “hybrid” system. It has one structure that would normally be treated deterministically in DNS coupled to another structure that would normally be treated in a statistical framework such as SEA.

Chapter 7

A hybrid problem

7.1 Background and motivation

So far we have considered structures that are statistical in nature. In this chapter, we further extend the range of systems to which the concatenation ansatz is applied. We wish to model the dynamics of a system such as that pictured in Fig. 7.1 consisting of two substructures using

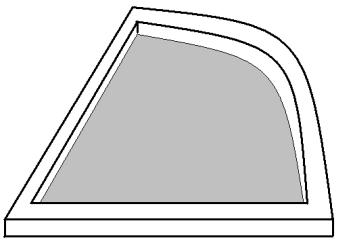

Figure 7.1: A cartoon of a hybrid system consisting of a stiff beam frame and a compliant plate interior.

the finite-element method (FEM). This type of structure is inspired by Langley and Bremner[25] and Shorter and Langley.[58] They have developed what they call the "hybrid method" which they would apply to a system such as the one in Fig. 7.1. Their hybrid method combines both deterministic and statistical frameworks. We adopt the language and refer to a "hybrid system" as a system with some internal structure that can would normally be described in a deterministic framework and some other internal structure that would normally be considered statistically.

In the sections that follow we will describe several such hybrid systems in detail. They share

some general characteristics. The outside frame is stiff, consisting of beams with a few wavelengths per side at the target frequency of interest, making it deterministic. The interior is compliant, consisting of a plate with several wavelengths per side at the target frequency of interest, making it statistical. The wavelengths in the beams are typically ten times the wavelengths in the plate.

This problem is interesting to the structural mechanics industry because the interior can be modeled using statistical models, such as statistical energy analysis, while the stiff frame cannot. As mentioned above, others[25,58] have developed a theoretical framework that they call the hybrid approach in vibroacoustics in which one can analyze such hybrid systems. In this chapter we apply the concatenation approach that we have applied to several different purely statistical systems in previous chapters.

The finite-element (FE) models we construct in this chapter range from fairly small with a few thousand degrees of freedom to significantly large with nearly a quarter of a million degrees of freedom. We use MSC.Patran[59] as a preprocessor to define mesh geometry and implement the finite-element program in Matlab.[60] We use standard textbook[61] formulas using a cubic-interpolation formulation for the beams, a discrete Kirchhoff-triangle[61] (DKT) formulation for the plate stiffness matrices, and quartic integration using area coordinates of quadratic shape functions[62] for the plate mass matrices. Finally, we (sometimes) use the ad hoc HRZ lumping procedure[61] to obtain diagonal element mass matrices before assembly of the global mass matrix, although the last step to obtain a diagonal mass matrix is not necessary for all elements as noted below.

Since we perform explicit time-domain numerical simulations, we would like to suppress frequency content significantly larger than our target frequency. That is, we wish to have a typical

mesh size larger in the beam frame than in the plate interior to model the longer wavelengths in the beam. We require a coarse mesh in the beams and a fine mesh in the plate. We can model the frame and interior separately in a standard way, but the graceful transition from the beam mesh to the plate mesh is more subtle. As mathematical preliminaries, we describe the procedure we use to join the FE models of the beam and the plate in the next section. We also derive the leak time for energy used in SEA analysis in the next section.

7.2 Mathematical preliminaries

In this section we develop the mathematical modeling preliminaries for two issues concerning our hybrid system. The first is the method for joining the course mesh in the stiff beam frame and the fine mesh in the compliant plate interior of our hybrid system. The second subsection contains the analysis related to SEA and diffusion.

7.2.1 Reduced matrices

In this section we describe how to construct and use a reduced stiffness matrix based on Guyan reduction[61] of a finite-element model of a beam consisting of several “master” degrees of freedom and many “slave” degrees of freedom. The slave degrees of freedom are necessary to rigidly connect the stiff beam with long target wavelengths to a more compliant structure with shorter target wavelengths. To evaluate the efficacy of the reduced FE model, the eigenfrequencies of the reduced model are compared to those of two benchmark models and to theory. One benchmark model is large with a fine mesh. The other benchmark model is small with a coarse mesh.

The toy problem and theory

We wish to model the vibrational dynamics of the beam pictured in Fig. 7.2. The beam is simply

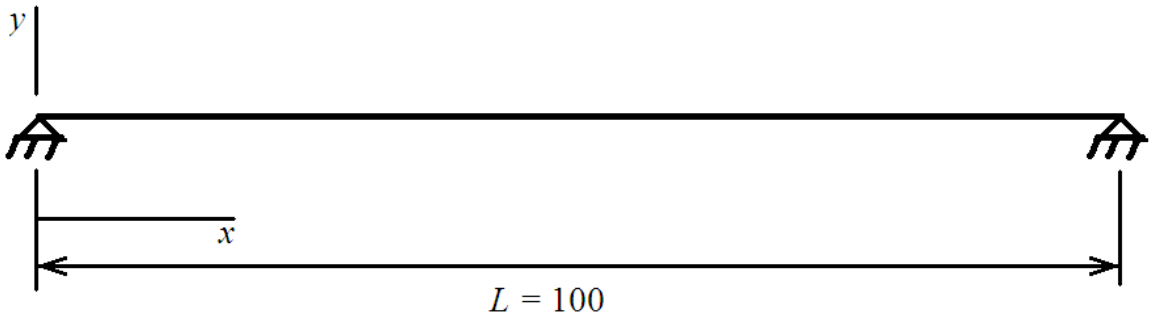

Figure 7.2: A cartoon of a simply supported beam with length $L = 100$, with its neutral axis coinciding with the x axis, and with vibrational degrees of freedom in the y direction.

supported, has its neutral axis coincident with the x axis, and has vibrational degrees of freedom in the y direction. It has material properties of Young's modulus $E = 10\ 000$ and linear density $\rho = 1$, and geometric properties of length $L = 100$, cross sectional area $A = 1$, and cross sectional second moment of area $I = 1$.

The eigenfrequencies predicted by theory are

$$\omega_n = 4\pi^2 \left(\frac{EI}{\rho A}\right)^{1/2} \frac{1}{\lambda_n^2}, \tag{7.1}$$

for $n = 1, 2, 3, \ldots$, where λ_n is the wavelength associated with frequency ω_n. Since the beam is simply supported, $\lambda_n = 2L/n$. The eigenfrequencies are

$$\omega_n = \pi^2 \left(\frac{EI}{\rho A}\right)^{1/2} \frac{n^2}{L^2} = \frac{\pi^2 n^2}{100}. \tag{7.2}$$

In the following three subsections we compare three FE models to this beam theory. We

describe a large benchmark model of the beam with a fine FE mesh and a small benchmark model of the beam with a course FE mesh. These two FE models constitute two benchmark models to which we compare the reduced FE model.

Large benchmark model

We mesh the beam in Fig. 7.2 into 100 elements with 101 nodes located at $x = i$ with $i = 0, 1, 2, \ldots 100$. Each node has two degrees of freedom, one translational in the y direction and the other rotational about the z axis, specifying slope. The deflection in the interior of any beam element is given by a cubic interpolation implied by the deflection and slope degrees of freedom at the nodes at either end of the element. The FE model consists of mass and stiffness matrices $[M]$ and $[K]$, respectively, derived in a textbook[61] fashion.

The eigenvalue problem

$$[K]\{u\}_n = \omega_n^2 [M]\{u\}_n \tag{7.3}$$

is solved for the eigenfrequencies. The "stairstep" function $N(\omega)$ indicating the number of frequencies in the system at or below frequency ω is in Fig. 7.3 along with the prediction from theory (Eq. (7.2)). The FE model and theory predictions agree well for lower frequencies, then diverge at higher frequencies, as expected. Theory and the FE model agree well up to a frequency of about 500, corresponding to a wavelength of about 2.8 by Eq. (7.1), indicating that we need at least three elements per wavelength to accurately model the frequencies of interest.

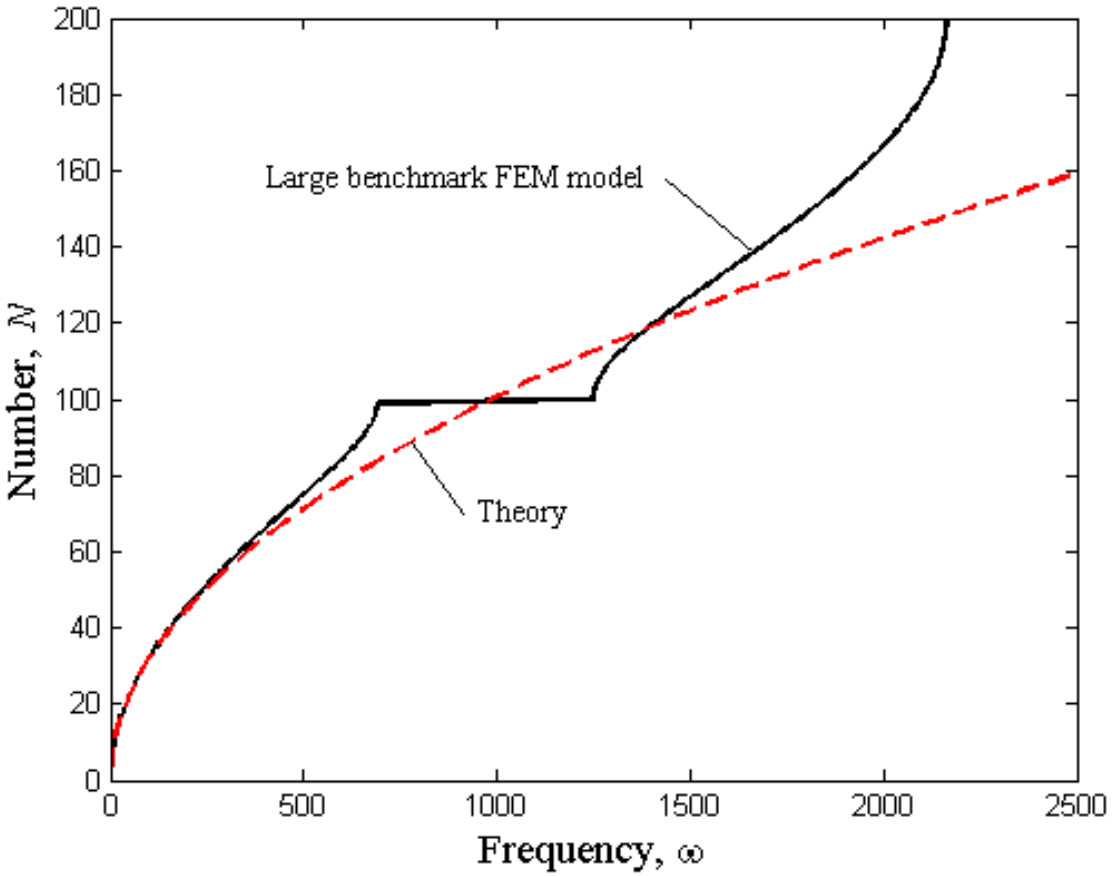

Figure 7.3: The "stairstep" function $N(\omega)$ for the large benchmark FE model. The solid line is the results from the FE model eigenvalue problem. The broken line is the results from theory (Eq. (7.2)). The FE model and theory agree well over an expected range of frequency. The apparent "kinks" in the solid curve are a consequence of a band gap, or a jump in the natural frequency, in the discrete model of the beam.

Small benchmark model

Using the same node numbering as for the large benchmark model, we mesh the beam into 10 elements with nodes at $x = i$, with $i = 0, 10, 20, \ldots, 100$. The mass and stiffness matrices are evaluated on the course mesh, and the eigenvalue problem is solved for the eigenfrequencies.

The "stairstep" function $N(\omega)$ indicating the number of frequencies in the system at or below frequency ω is in Fig. 7.4 along with the prediction from theory (Eq. (7.2)). The FE model and

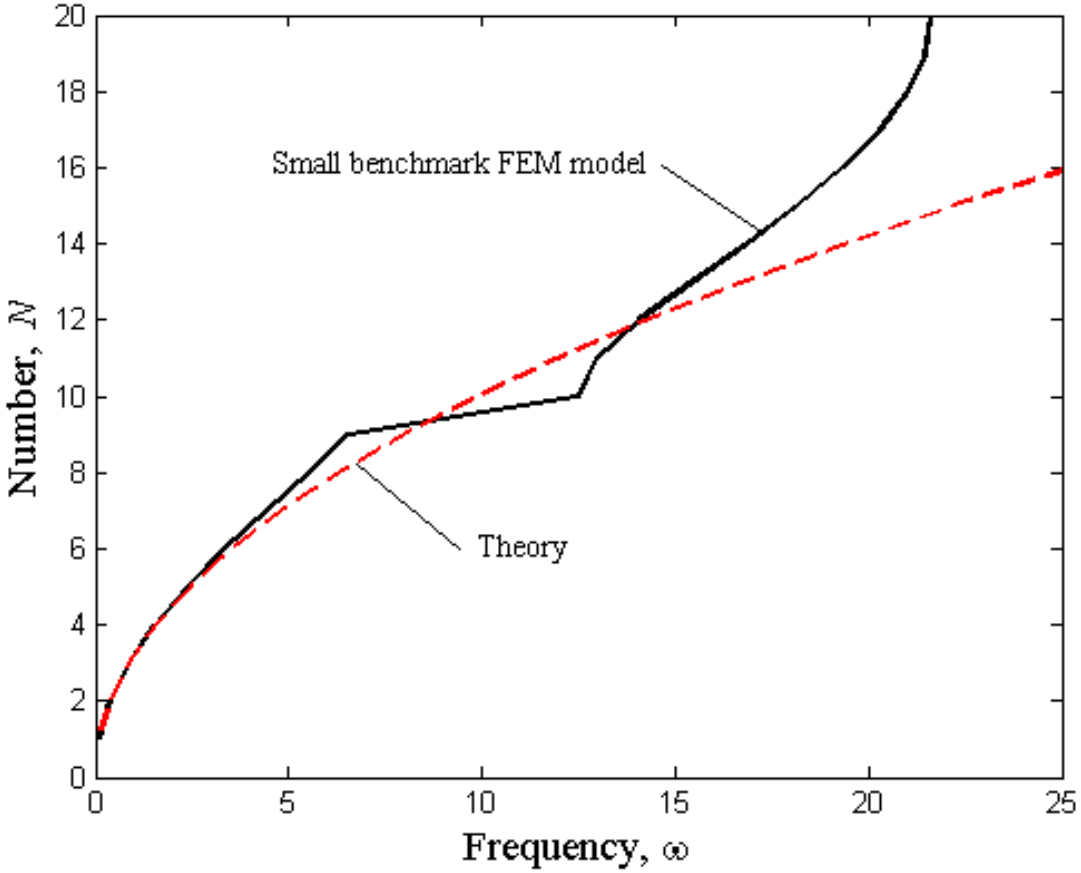

Figure 7.4: The "stairstep" function $N(\omega)$ for the small benchmark FE model. The solid line is the results from the FE model eigenvalue problem. The broken line is the results from theory (Eq. (7.2)). The FE model and theory agree well over an expected range of frequency, small than that for the large benchmark model. The apparent "kinks" in the solid curve are a consequence of a band gap in the discrete model of the beam.

theory predictions again agree well for lower frequencies, then diverge, as expected. However, they agree over a smaller range of frequency compared to the large benchmark model, also as expected.

Indeed, Fig. 7.4 can be compared to Fig. 7.3. To plotting precision it looks like the stairstep function in Fig. 7.3 could be simply scaled in frequency and number of modes to produce the stairstep function in Fig. 7.4. However, there are more data point in Fig. 7.3 corresponding to the

larger number of degrees of freedom in the large benchmark model.

The reduced FE model

Now we derive and use a reduced FE model based on Guyan reduction.[61] The beam is meshed into elements as for the large benchmark model, but now the various degrees of freedom are partitioned into "master" degrees of freedom $\{d_{\mathrm{m}}\}$ and "slave" degrees of freedom $\{d_{\mathrm{s}}\}$. In this toy example, we assign the master degrees of freedom to the nodes of the small benchmark model. The slave degrees of freedom are all the other nodes. The stiffness matrix is partitioned as well and written as

$$[K] = \begin{bmatrix} K_{\mathrm{mm}} & K_{\mathrm{ms}} \\ K_{\mathrm{sm}} & K_{\mathrm{ss}} \end{bmatrix}. \tag{7.4}$$

Cubic interpolation is used between the nodes of the small benchmark problem to relate the slave degrees of freedom to the master degrees of freedom. The relationship can be written as

$$\{d_{\mathrm{s}}\} = [T]\{d_{\mathrm{m}}\}, \tag{7.5}$$

where the interpolation matrix $[T]$ is sparse. In general, when elements can have any orientation in space, each element interpolation matrix must be transformed from a local coordinate system to a global coordinate system. Then, the element interpolation matrices must be assembled into a global interpolation matrix, as for the mass and stiffness matrices.

The reduced stiffness matrix $[K_{\mathrm{red}}]$ is derived by enforcing an equality of potential energies

using all of the degrees of freedom and only the master degrees of freedom. Explicitly,

$$\text{Potential energy} = \frac{1}{2}\begin{Bmatrix} d_{\mathrm{m}} \\ d_{\mathrm{s}} \end{Bmatrix}^{T}\begin{bmatrix} K_{\mathrm{mm}} & K_{\mathrm{ms}} \\ K_{\mathrm{sm}} & K_{\mathrm{ss}} \end{bmatrix}\begin{Bmatrix} d_{\mathrm{m}} \\ d_{\mathrm{s}} \end{Bmatrix} = \frac{1}{2}\{d_{\mathrm{m}}\}^{T}[K_{\mathrm{red}}]\{d_{\mathrm{m}}\}, \qquad (7.6)$$

where a superscript T indicates transpose. After substituting Eq. (7.5), the reduced stiffness matrix is found to be

$$[K_{\mathrm{red}}] = [K_{\mathrm{mm}}] + [K_{\mathrm{ms}}][T] + [T]^{T}[K_{\mathrm{sm}}] + [T]^{T}[K_{\mathrm{ss}}][T]. \qquad (7.7)$$

There is a reduced mass matrix of the same form as $[K_{\mathrm{red}}]$ in Eq. (7.7). However, the mass matrix based on Eq. (7.7) is nondiagonal and inconvenient for explicit time domain simulations that require the inverse of the mass matrix. There are two methods of handling this problem, and both are used in the examples below. The first is to use the same mass matrix as that used in the small benchmark model for $[M_{\mathrm{red}}]$. With this method, we lump all of the mass of the beams at master degrees of freedom on the beam to obtain the mass matrix in the small benchmark model, and we ignore the small amount of the mass of the plate associated with slave degrees of freedom.

The second method is to use the nondiagonal $[M_{\mathrm{red}}]$ calculated using Eq. (7.7) (with K replaced by M). This matrix is block diagonal. With a convenient ordering of master degrees of freedom, There is a relatively small, but essentially full, matrix of rank equal to the number of master degrees of freedom around the frame which is relatively easy to invert by brute force. There is a second relatively large, but strictly diagonal, matrix that is also easy to invert. The mass matrix has to be inverted only once to perform all of the time-domain simulations. If we allow nondiagonal $[M_{\mathrm{red}}]$ matrices, there is no reason to perform HRZ lumping in the beam elements; however, HRZ

lumping is still used on the plate elements to maintain a diagonal mass matrix constructed using the master degrees of freedom in the interior of the plate. This part of the mass matrix remains diagonal after the transformations by inspections of Eqs. (7.5) and (7.7).

The results of the eigenvalue problem are in Fig. 7.5. The results from the reduced FE model

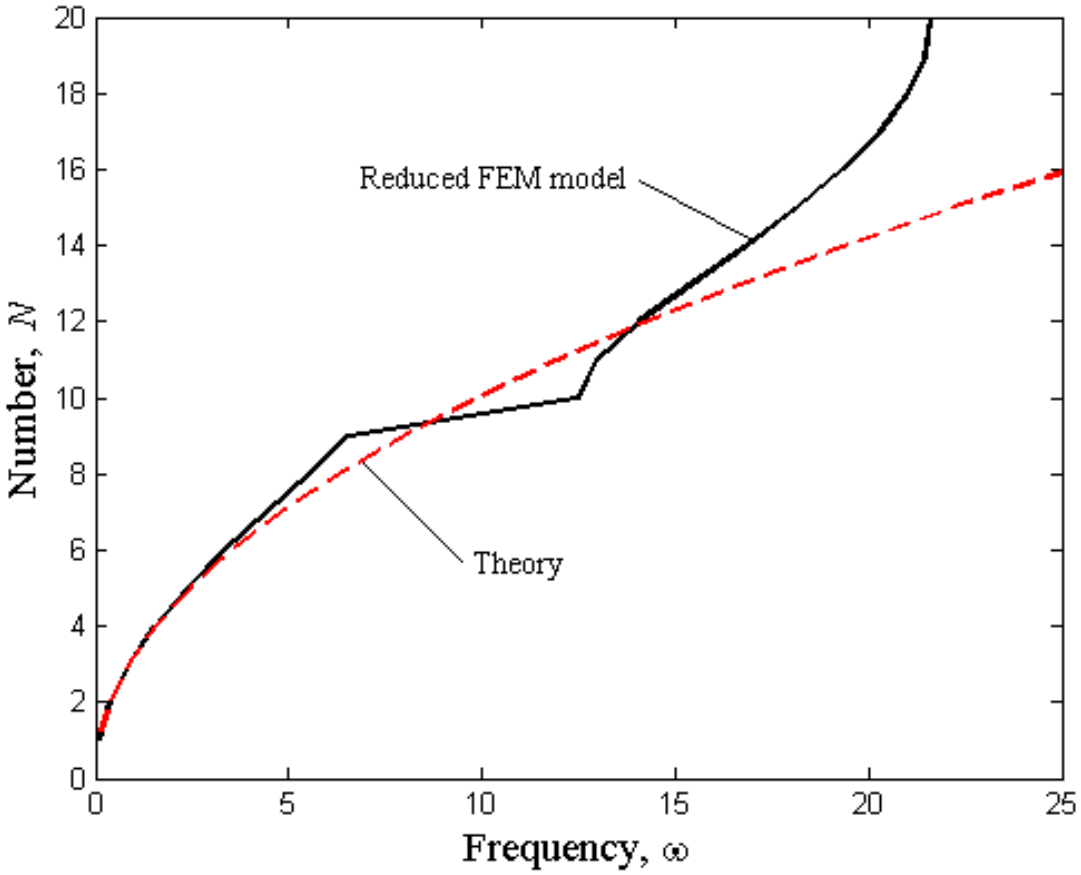

Figure 7.5: The "stairstep" function $N(\omega)$ for the reduced FE model. The solid line is the results from the FE model eigenvalue problem. The broken line is the results from theory (Eq. (7.2)). The reduced FE model are identical to the small benchmark model.

the small benchmark model seem to be identical. We now have a way of modeling only the low frequency content of the stiff beams while correctly accounting for the interaction of the compliant interior and stiff frame of our hybrid system between master degrees of freedom that are along the

frame.

7.2.2 Statistics of wave energy transfer

In this section we derive the characteristic leak time of energy transfer from a beam into a plate. First, recall some general theory.

Review of general theory

A cartoon of a semi-infinite plate lying in the xy-plane with its free edge attached to an infinite beam parallel to the y-axis is in Fig. 7.6. The deflection $w(y;t)$ in the z-direction in the beam must

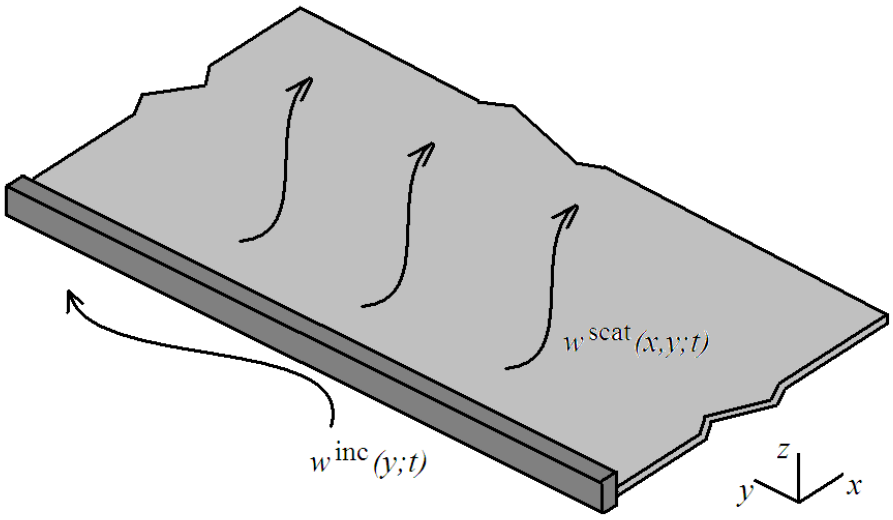

Figure 7.6: A cartoon of wave energy in an infinite dark-gray beam leaking into a semi-infinite light-gray plate.

satisfy the governing PDE

$$EI\partial_y^4 w + \rho_b A_b \partial_t^2 w = 0, \tag{7.8}$$

where EI is the flexural rigidity of the beam, and $\rho_b A_b$ is the lineal mass density of the beam. Substituting the solution for a traveling wave in the $+y$-direction, $w = e^{i(\gamma_b y - \omega t)}$, where $\gamma_b = 2\pi/\lambda_b$

is the wavenumber in the beam, λ_b is the wavelength in the beam, and ω is the frequency of oscillation, one obtains the dispersion relationship

$$\omega = \left(\frac{EI}{\rho_b A_b}\right)^{\frac{1}{2}} \gamma_b^2 \tag{7.9}$$

in the beam. The deflection $w(x,y;t)$ in the z-direction in the plate must satisfy the governing PDE

$$D\nabla^4 w + \rho_p h \partial_t^2 w = 0, \tag{7.10}$$

where, as in Eq. (6.1), D is the plate rigidity, and $\rho_p h$ is the areal mass density of the plate. The dispersion relationship between ω and the wavenumber γ_p in the plate is

$$\omega = \left(\frac{D}{\rho_p h}\right)^{\frac{1}{2}} \gamma_p^2, \tag{7.11}$$

where $\gamma_p = 2\pi/\lambda_p$, and λ_p is the wavelength in the plate.

The beam experiences an incident wave with wavenumber γ_b and frequency ω of deflection in the z-direction of $w^{\text{inc}}(y;t) = Ae^{i(\gamma_b y - \omega t)}$, and the plate experiences a scattered wave field of deflection in the z-direction of $w^{\text{scat}}(x,y;t) = Be^{i(\gamma_b y - \omega t)} f(x)$.

The scattered wave field must satisfy Eq. (7.10), so $f(x) = e^{i\gamma_x x}$, where

$$\gamma_x^2 = -\gamma_b^2 \pm \gamma_p^2, \tag{7.12}$$

where we have used Eq. (7.11). We interest ourselves in a regime for which γ_x^2 takes on a positive value in Eq. (7.12) so that γ_x takes on a real value and w^{scat} is a traveling wave, not an evanescent

wave. It follows that $\gamma_p > \gamma_b$, i.e., $\lambda_b > \lambda_p$. The wavenumber γ_x can then take on the two real values

$$\gamma_{xr} = \pm\gamma_b \sqrt{-1 + \left(\gamma_p/\gamma_b\right)^2} \tag{7.13}$$

and the two imaginary values $\gamma_x = i\gamma_{xi}$ with

$$\gamma_{xi} = \pm\gamma_b \sqrt{1 + \left(\gamma_p/\gamma_b\right)^2}. \tag{7.14}$$

For a traveling wave in the $+x$-direction, we keep the positive real root in Eq. (7.13) and reject the minus real root on physical grounds. Similarly, for a wave that does not grow to infinity, we keep the imaginary root with the positive sign in Eq. (7.14) and reject the minus sign on physical grounds. Finally, the scattered wavefield in the plate is

$$w^{\text{scat}}(x,y;t) = B_1 e^{i(\gamma_b y + \gamma_{xr} x - \omega t)} + B_2 e^{i(\gamma_b y - \omega t) - \gamma_{xi} x}, \tag{7.15}$$

where the coefficients B_1 and B_2 are to be determined by satisfying boundary conditions.

We consider hinged boundary conditions such that the deflection of the plate at the boundary equals the deflection of the beam, and the bending moment in the plate about the axis of the beam (i.e., the bending moment acting on the cross section in the plate perpendicular to the x-axis at the beam) vanishes. The bending moment (per unit length) of interest is[57,61]

$$M_x = -D\partial_x^2 w^{\text{scat}} - \nu D\partial_y^2 w^{\text{scat}}, \tag{7.16}$$

where ν is the Poisson's ratio of the material of the plate; therefore,

$$w^{\text{scat}}(0,y;t) = w^{\text{inc}}(y;t) \text{ and} \tag{7.17a}$$

$$D\partial_x^2 w^{\text{scat}}(0,y;t) + \nu D\partial_y^2 w^{\text{scat}}(0,y;t) = 0 \tag{7.17b}$$

must hold. After substitution and differentiation, the above two equations become

$$B_1 + \qquad\qquad B_2 = A, \tag{7.18a}$$

$$\left(\gamma_{\text{xr}}^2 + \nu\gamma_{\text{b}}^2\right)B_1 + \left(-\gamma_{\text{xi}}^2 + \nu\gamma_{\text{b}}^2\right)B_2 = 0, \tag{7.18b}$$

so

$$B_1 = \frac{\left(\gamma_{\text{p}}/\gamma_{\text{b}}\right)^2 + 1 - \nu}{2\left(\gamma_{\text{p}}/\gamma_{\text{b}}\right)}A. \tag{7.19}$$

In the limit of long wavelengths in the beam,

$$B_1 \approx \frac{\gamma_{\text{p}}}{2\gamma_{\text{b}}}A \gg A. \tag{7.20}$$

In the following, we will consider only the traveling wave portion of Eq. (7.15), and not the evanescent portion, so we do not solve for B_2.

The leak time

Now we start to consider energy transfer from the beam to the plate. Consider the kinetic energy in a differential cross section of the beam,

$$\mathrm{d}T = \frac{1}{2}\mathrm{d}m\left(\Re\partial_t w^{\text{inc}}\right)^2. \tag{7.21}$$

The differential mass is $\mathrm{d}m = \rho_\mathrm{b} A_\mathrm{b} \mathrm{d}y$, and the (complex) material velocity is given by $\partial_t w^\mathrm{inc} = -i\omega w^\mathrm{inc}$. The total energy per wavelength in the beam is twice the kinetic energy per wavelength, so

$$E = 2T = \frac{\pi}{\gamma_\mathrm{b}} \rho_\mathrm{b} A_\mathrm{b} \omega^2 A^2. \tag{7.22}$$

The power density, or rate at which the energy in Eq. (7.22) leaks into the plate per unit length in the y-direction, at a point is the internal net force in the z-direction (per unit width) acting on a plane perpendicular to the x-axis dotted with the velocity of the plate at that point, or

$$\mathrm{d}\Pi = \Re\left(V_x\right) \Re\left(\partial_t w^\mathrm{scat}\right), \tag{7.23}$$

where, according to Graff,[57]

$$V_x = Q_x + \partial_y M_{xy}, \tag{7.24a}$$

$$Q_x = \partial_x M_x + \partial_y M_{xy}, \text{ and} \tag{7.24b}$$

$$M_{xy} = D(1-\nu)\partial_x \partial_y w^\mathrm{scat}. \tag{7.24c}$$

In Eq. (7.24b), Q_x is the internal shear force, and M_{xy} is the internal twisting moment acting on the plane of interest. Substituting,

$$V_x = D\left(\partial_x^3 + (2-\nu)\partial_y^2 \partial_x\right) w^\mathrm{scat} \tag{7.25a}$$

$$= -iD\left(\gamma_\mathrm{xr}^3 + (2-\nu)\gamma_\mathrm{xr}\gamma_\mathrm{b}^2\right) B_1 e^{i(\gamma_\mathrm{b} y + \gamma_\mathrm{xr} x - \omega t)}. \tag{7.25b}$$

Taking the derivative $\partial_t w^\mathrm{scat} = -i\omega B_1 e^{i(\gamma_\mathrm{b} y + \gamma_\mathrm{xr} x - \omega t)}$ and averaging over one wavelength in the

beam, the power at which energy is being deposited into the plate per beam wavelength is

$$\Pi = \frac{\pi}{\gamma_b} B_1^2 D \left(\gamma_{xr}^3 + (2-\nu)\gamma_{xr}\gamma_b^2\right) \omega. \tag{7.26}$$

Finally, the leak time from the beam to the plate is defined as

$$T_L^{b-p} \equiv \frac{E}{\Pi} \tag{7.27a}$$

$$= \frac{4\rho_b A_b \omega}{D\gamma_p^3} \frac{\left(\gamma_p/\gamma_b\right)^7}{\left[\left(\gamma_p/\gamma_b\right)^2 - 1\right]^{1/2} \left\{\left[\left(\gamma_p/\gamma_b\right)^2 - 1\right] + (2-\nu)\right\}^3}, \tag{7.27b}$$

which goes to

$$T_L^{b-p\,\infty} = T_L^{b-p}\left(\lambda_b/\lambda_p \to \infty\right) = \frac{4\rho_b A_b \omega}{D\gamma_p^3} \tag{7.28}$$

in the limit of long wavelengths in the beam. This leak time is infinity when the wavelengths in the beam equal wavelengths in the plate as expected.

The normalized leak time $T_L^{b-p}/T_L^{b-p\,\infty}$ is plotted in Fig. 7.7 vs a normalized wavelength in the beam $\left(\left(\lambda_b/\lambda_p\right)^2 - 1\right)$ for various values of Poisson's ratio ν. The leak time "blows-up" slowly as the beam wavelength is reduced to the plate wavelength. The leak time does asymptotically reach the simple limit in Eq. (7.28) for beam wavelengths of about 10 times the plate wavelengths. The beam radiates into the plate most efficiently when $\lambda_b \approx \sqrt{2}\lambda_p$ so that the scattered wave is traveling in a direction about 45° from the beam.

The leak time in Eq. (7.27b) needs to be used with some care. First, there was a semi-infinite plate on one one side of the beam in the geometry. It is not obvious what the leak time would be if the geometry were different with a beam coupled to an infinite plate extending from both sides

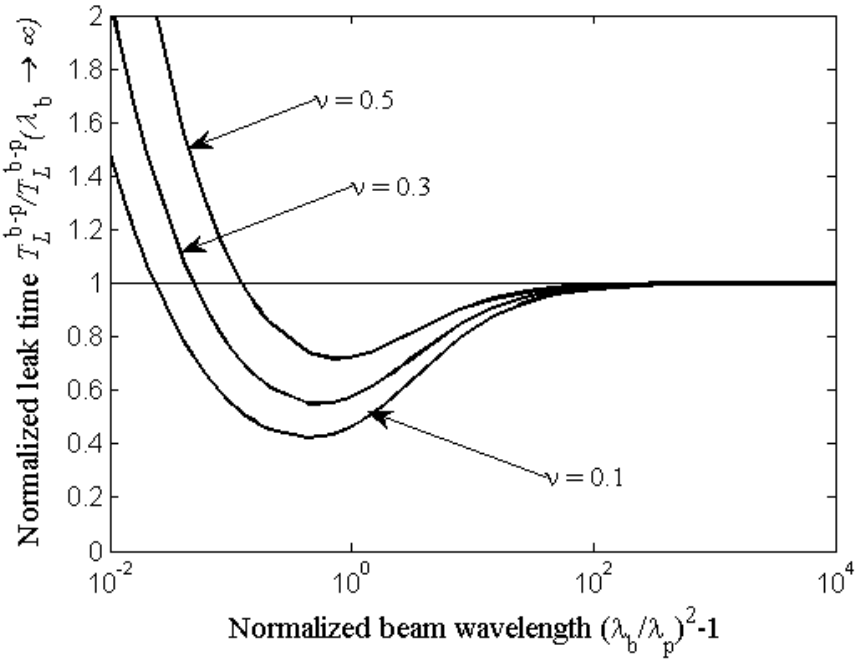

Figure 7.7: The leak time of Eq. (7.27b) vs beam wavelength for various values of Poisson's ratio ν. The time for energy to leak from the beam to the plate is infinite when the beam wavelength is as small as the plate wavelength. The leak time asymptotically reaches a constant from the bottom for large beam wavelengths.

of the beam. Second, the hinged boundary condition between the beam and the plate means that there is no coupling between twisting of the beam (torsion) and bending of the plate.

The diffusion time

The modal densities ($\mathcal{N} = \mathrm{d}N/\mathrm{d}\omega$, where N is the number of modes below frequency ω) in a beam of length L and plate of area A_p are

$$\mathcal{N}_\mathrm{b} = \frac{1}{4\pi} L \left(\frac{\rho_\mathrm{b} A_\mathrm{b}}{EI}\right)^{\frac{1}{4}} \frac{1}{\sqrt{\omega}}, \text{ and} \tag{7.29a}$$

$$\mathcal{N}_\mathrm{p} = \frac{1}{4\pi} A_\mathrm{p} \left(\frac{\rho_\mathrm{p} h}{D}\right)^{\frac{1}{2}}, \tag{7.29b}$$

respectively. The total energy in a substructure is the modal density times energy per mode, or $E = \mathcal{N}\mathcal{E}$, where $\mathcal{E}$ is the energy density, i.e., energy per mode. At late-time quasi-equilibrium when the energy density in the beam equals the modal density in the plate $\mathcal{E}_{\mathrm{b}}(t \to \infty) = \mathcal{E}_{\mathrm{p}}(t \to \infty)$, the power from the plate to the beam is equal to the power from the beam to the plate. That is,

$$\Pi = \frac{\mathcal{N}_{\mathrm{b}}\mathcal{E}_{\mathrm{b}}(t \to \infty)}{T_{\mathrm{L}}^{\mathrm{b-p}}} = \frac{\mathcal{N}_{\mathrm{p}}\mathcal{E}_{\mathrm{p}}(t \to \infty)}{T_{\mathrm{L}}^{\mathrm{p-b}}}, \tag{7.30}$$

and we conclude that the leak time from the plate to the beam is

$$T_{\mathrm{L}}^{\mathrm{p-b}} = \frac{\mathcal{N}_{\mathrm{p}}}{\mathcal{N}_{\mathrm{b}}} T_{\mathrm{L}}^{\mathrm{b-p}}, \tag{7.31}$$

which is a reciprocal relationship that holds for any two substructures. Note that

$$T_{\mathrm{L}}^{\mathrm{p-b}} \gg T_{\mathrm{L}}^{\mathrm{b-p}} \tag{7.32}$$

if the modal density in the plate is large compared to the modal density in the beam $\mathcal{N}_{\mathrm{p}} \gg \mathcal{N}_{\mathrm{b}}$, as we expect it to be.

The SEA dynamics of energy flow (without sources) between the beam and the plate is governed by

$$\frac{\mathrm{d}}{\mathrm{d}t}\begin{bmatrix} \mathcal{N}_{\mathrm{b}} & 0 \\ 0 & \mathcal{N}_{\mathrm{p}} \end{bmatrix}\begin{Bmatrix} \mathcal{E}_{\mathrm{b}} \\ \mathcal{E}_{\mathrm{p}} \end{Bmatrix} = -\begin{bmatrix} \frac{\mathcal{N}_{\mathrm{b}}}{T_{\mathrm{L}}^{\mathrm{b-p}}} & -\frac{\mathcal{N}_{\mathrm{b}}}{T_{\mathrm{L}}^{\mathrm{b-p}}} \\ -\frac{\mathcal{N}_{\mathrm{p}}}{T_{\mathrm{L}}^{\mathrm{p-b}}} & \frac{\mathcal{N}_{\mathrm{p}}}{T_{\mathrm{L}}^{\mathrm{p-b}}} \end{bmatrix}\begin{Bmatrix} \mathcal{E}_{\mathrm{b}} \\ \mathcal{E}_{\mathrm{p}} \end{Bmatrix}. \tag{7.33}$$

The matrix on the right-hand side is symmetric in light of Eq. (7.31). We define the diffusion rate (= 1/diffusion time) as the smallest nontrivial eigenvalue of the matrices in Eq. (7.33). The

eigenvalue problem to be solved is

$$\begin{bmatrix} \mathcal{N}_\mathrm{b} & 0 \\ 0 & \mathcal{N}_\mathrm{p} \end{bmatrix} \begin{Bmatrix} \mathcal{E}_\mathrm{b} \\ \mathcal{E}_\mathrm{p} \end{Bmatrix}^i = \lambda_i \frac{\mathcal{N}_\mathrm{b}}{T_\mathrm{L}^{\mathrm{b-p}}} \begin{bmatrix} 1 & -1 \\ -1 & 1 \end{bmatrix} \begin{Bmatrix} \mathcal{E}_\mathrm{b} \\ \mathcal{E}_\mathrm{p} \end{Bmatrix}^i . \tag{7.34}$$

The eigenvalues are $\lambda_0 = 0$ and

$$\lambda_1 = \frac{\mathcal{N}_\mathrm{b} + \mathcal{N}_\mathrm{p}}{\mathcal{N}_\mathrm{p} T_\mathrm{L}^{\mathrm{b-p}}}, \tag{7.35}$$

so the diffusion time is

$$T_\mathrm{D} \equiv \frac{1}{\lambda_1} = \frac{\mathcal{N}_\mathrm{p} T_\mathrm{L}^{\mathrm{b-p}}}{\mathcal{N}_\mathrm{b} + \mathcal{N}_\mathrm{p}} \tag{7.36a}$$

$$= \frac{\mathcal{N}_\mathrm{b} T_\mathrm{L}^{\mathrm{p-b}}}{\mathcal{N}_\mathrm{b} + \mathcal{N}_\mathrm{p}}. \tag{7.36b}$$

By Eq. (7.36a), the diffusion time is approximately equal to the leak time from the beam to the plate

$$T_\mathrm{D} \approx T_\mathrm{L}^{\mathrm{b-p}} \tag{7.37}$$

if the modal density in the plate is large compared to the modal density in the beam $\mathcal{N}_\mathrm{p} \gg \mathcal{N}_\mathrm{b}$.

In the next section, we describe the details of our first hybrid system and attempt to extract the diffusion parameters describing the slow-time energy flow using the diffusion limit of the concatenation ansatz. The attempt generally fails, as the parameters were chosen rather naïvely; however, we do learn from the experience and discuss some of the physics governing the system. We go on to develop guidelines for a better choice of system parameters which are used in the final sections of this chapter.

7.3 A naïve hybrid system

7.3.1 Description

A cartoon of our hybrid system used for our first attempt is in Fig. 7.8. It is based on a quarter

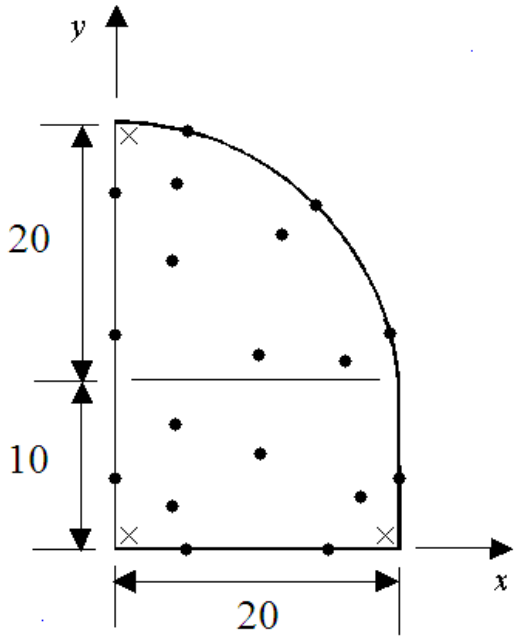

Figure 7.8: A cartoon of the hybrid system. The lengths are in units of the wavelengths in the plate at the target frequency. The curved portion is a quarter circle. The source/receiver sites (•) are positioned as uniformly as possible around the frame and pseudo-randomly in the plate interior. The pinned (ball-and-socket) boundary conditions (×) are positioned one plate wavelength at the target frequency away from the frame.

stadium. The periphery is a stiff beam frame, and the interior is a compliant plate. The lengths are in units of nominal wavelengths in the plate at the target frequency. The boundary conditions are ball-and-socket joints near the three corners. Deflections are constrained to be zero, but slopes are unconstrained at the locations of the boundary conditions. The geometric and material properties of the beams and plate are such that the wavelengths in the beams are ten times longer than the wavelengths in the plate at the target frequency. This constraint on the relative wavelengths in

the plate and beam can be realized with different sets of parameters. We choose, more-or-less randomly, in the plate, $D = 0.5066 \times 10^{-3}$, $\rho_p = 0.09905$, $h = 0.1$, and, in the beams, $E = 511.4$, $I = \rho_b A_b = 1$, so the target frequency is

$$f_T = \frac{\omega}{2\pi} = 2\pi \left(\frac{D}{\rho_p h} \right)^{\frac{1}{2}} \frac{1}{\lambda_p^2} = 2\pi \left(\frac{EI}{\rho_b A_b} \right)^{\frac{1}{2}} \frac{1}{\lambda_b^2} = 1.421. \tag{7.38}$$

We mesh the system, placing nodes at about every quarter-wavelength in both the beams and the plate. The mesh fully resolves both the beam and the plate. The mesh has 36 beam elements, 18 400 plate elements, and 27 168 degrees of freedom. The highest natural frequency in the system is about ten times the target frequency, or $f_{\max} = 12.40$. For time stepping in the numerical simulation, we use $\delta t = 0.1028 \approx 1/\omega_{\max}$ and carry simulation out to 2^{16} time steps, or $T_{\max} = 839$. The time duration of the filter was $T_B = 14.1$.

The system parameters were also designed so that there are about 10 leak times in the total simulation. The leak time, from Eq. (7.28) is about $T_L^{b-p} \approx 280$ at the target frequency. This leak time is short compared to the break time estimated from the modal density of the plate alone. In particular,

$$T_{\text{Heisenberg}} = \frac{1}{2} (\text{Area of the plate}) \sqrt{\frac{\rho_p h}{D}} = 1137, \tag{7.39}$$

which is approximately equal over the entire frequency range.

For reference, the modal density in the frame, considering it to be a loop, is

$$\frac{\partial N}{\partial f} = \frac{1}{2} (\text{Perimeter}) \left(\frac{\rho_b A_b}{EI} \right)^{\frac{1}{4}} \frac{1}{\sqrt{\omega}} = 3.167 \tag{7.40}$$

at the target frequency.

Though torsion was not studied in the analysis above in Section 7.2.2, we include it here for a physically realistic system. The plate is fixed to the beam along the frame so that the twisting modes of the various sections of beams are coupled to the bending modes of the plate. For the stiffness matrices, we are using Poisson's ratio $\nu = 0.3$ and

$$GJ = \frac{E}{2(1+\nu)} * 2I = 393.4, \tag{7.41}$$

and for the mass matrices, we are using $\kappa = 1$ for the radius of gyration of the cross section. These parameters were designed so that the torsion frequencies were about the same as the bending frequencies on the same mesh. In later sections we will not use any torsion at all, and the reason why will become clear as we discuss the results from this particular hybrid system.

We investigate the nine source/receiver sites in each of the beam frame and plate interior pictured in Fig. 7.8. A source acts through each receiver for a total of 18 simulations, and we average over every source/receiver combination treating the frame and interior as two substructures.

7.3.2 Results

We perform time domain simulations of the responses due to impulsive sources out to a time required for about 100 reflections in the plate. The time for one reflection was taken to be 20 plate wavelengths divided by the plate group velocity. This total simulation time is equivalent to about 200 round trips around the frame of waves in the frame.

The intensity quantities plotted in Fig. 7.9 and for other figures in this section are a hybrid of those defined in Sections 5.2 and 6.2.1. We denote mean-square band-limited displacements by $\mathbf{J}_{\rho r \sigma s}$, where ρ ranges over $\rho \in \{\text{beam}, \text{plate}\}$ for the subsystem the receiver is located, and r ranges

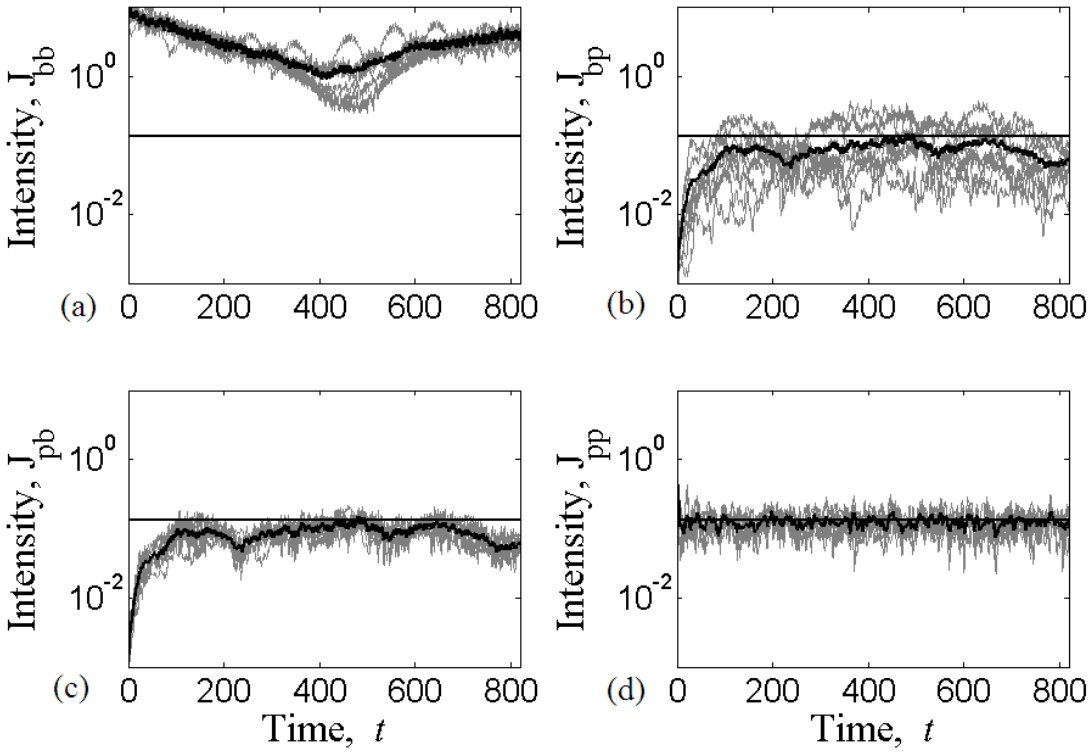

Figure 7.9: Responses at half the target frequency $\frac{1}{2} f_{\mathrm{T}}$. The straight horizontal line is the prediction at late times. The gray lines are from the nine individual sources in each of the frame and the interior. (a) receivers in beam, sources in beam. (b) receivers in beam, sources in plate. (c) receivers in plate, sources in beam. (d) receivers in plate, sources in plate.

over $r \in \{1 \ldots 9\}$ for the receiver in that subsystem. Similarly, σ ranges over $\sigma \in \{\text{beam}, \text{plate}\}$, and s ranges over $s \in \{1 \ldots 9\}$ for the sources. The gray curves are the average among the various receivers in a substructure due to a single source normalized by admittance at each site, then multiplied by square of the effective admittance $E_{\text{eff}} = \langle E \rangle_{\rho r}$ averaged over all of the receiver sites, or, more precisely,

$$\mathbf{J}_{\rho\sigma s} = \left\langle \frac{\mathbf{J}_{\rho r\sigma s}}{E_{\rho r} E_{\sigma s}} \right\rangle_r \times E_{\text{eff}}^2. \tag{7.42}$$

The black noisy curve is the average among the various receivers and sources, or

$$\mathbf{J}_{\rho\sigma} = \left\langle \frac{\mathbf{J}_{\rho r \sigma s}}{E_{\rho r} E_{\sigma s}} \right\rangle_{rs} \times E_{\text{eff}}^2. \tag{7.43}$$

Each of the gray lines is an average of nine responses, while the black noisy line is an average of those nine averages of nine. There is no reciprocity in $\mathbf{J}_{\rho\sigma s}$ but there is in $\mathbf{J}_{\rho\sigma}$, as discussed in Section 5.2.

For comparison, the (average) late-time prediction in Eq. (1.16) is also plotted as a solid horizontal line. The DNS response should asymptote to the late-time prediction. The modal density used for the denominator N_D in the late-time prediction calculation is the modal density of the plate plus the modal density of the bending modes in the beam,

$$\frac{\partial N}{\partial \omega} = \frac{1}{4\pi} (\text{Area of the plate}) \sqrt{\frac{\rho_p h}{D}} + \frac{1}{4\pi} (\text{Perimeter}) \left(\frac{\rho_b A_b}{EI} \right)^{\frac{1}{4}} \frac{1}{\sqrt{\omega}}. \tag{7.44}$$

The above formula should include the contribution from torsion, too, but the term for the modal density in the plate already dominates the term for the beams. We could just as well discard the modal density for the beams altogether when estimating the modal density of the entire system.

The data plotted in Fig. 7.9 are for a low frequency, half that of the target frequency $\frac{1}{2} f_T$. The discrepancies between the data and the predictions are disturbingly large, particularly in the response with both sources and receivers in the beam in Fig. 7.9(a). The response first decays exponentially, as expected in a diffusion model. The, the response then "bounces" back upwards at a time around $t \approx 450$, a time scale that has not been identified in the discussion above. It bounces back up by about a factor of three in the simulation time shown here. Later, the response does not

reach its late-time value in the manner that it should. This bounce is a localization phenomenon, but one that we have not seen before. Typically in a localizing system, a response will initially decay in a diffusive process, but then the diffusive behavior will stop at a characteristic Heisenberg time given by the model density of the system.

The (reciprocal) beam-plate responses and the plate-plate response behave more as expected. It should be noted that the plate-plate response is nearly trivial. Since the modal density of the plate is so much larger than the modal density of the beam, any energy that is deposited in the plate tends to stay in the plate without leaking into the beams. That theory agrees with the DNS data only confirms that the estimate for plate modal density is approximately correct.

The intensities for the target frequency f_{T} are plotted in Fig. 7.10. We see an even larger bounce in the beam-beam response here. The bounce now occurs at a time $t \approx 350$, again a time not seen in the analysis above. The bounce is nearly a factor of 10, and the response nearly regains its original value at the initial time. The two beam-plate and plate-plate represent a diffuse process better. These two sets of simulations do not represent the system well because the modal density of the plate dominates the character responses.

The intensities for the twice the target frequency $2f_{\mathrm{T}}$ are plotted in Fig. 7.10. There is no large bounce as there was for the two lower frequencies in this hybrid system. However, localization is clearly evident. The average intensities were constructed such that the predicted late-time values are identical for all source/receiver combinations. However, the actual late-time beam-beam response is about 50 times greater than the late-time responses in plate. It is also clear from Fig. 7.10(d) that the late-time prediction itself is wrong, but this is not very surprising. At twice the target frequency, there are fewer than three elements per wavelength in the plate, but we had

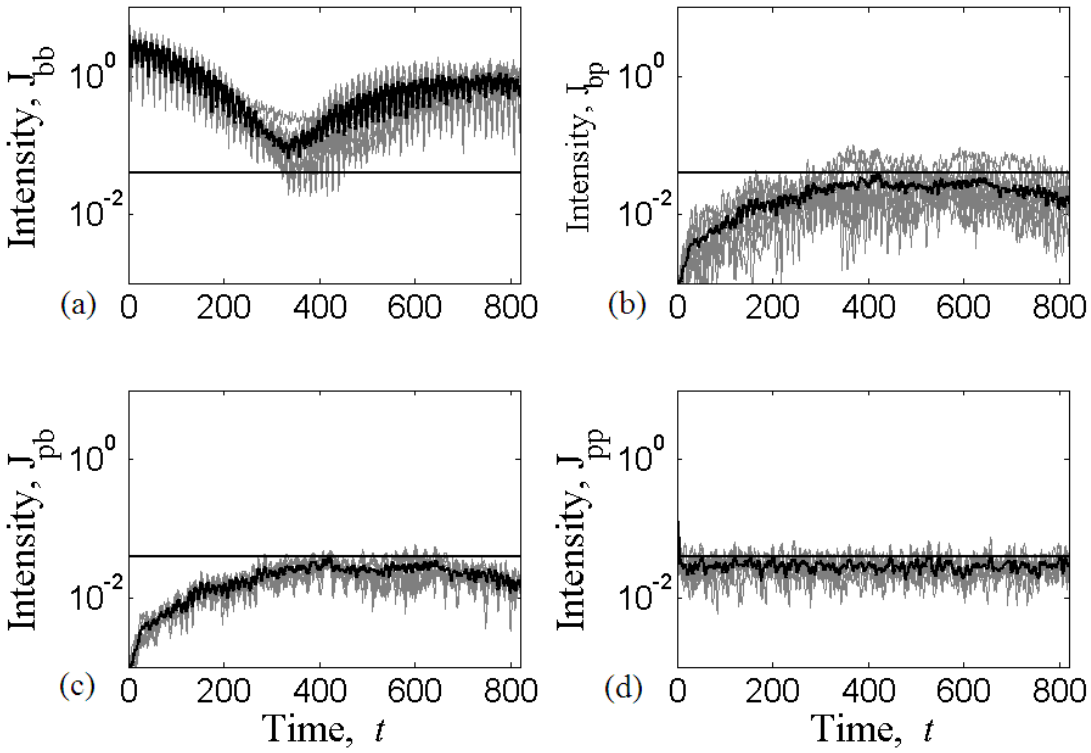

Figure 7.10: Responses at the target frequency f_T. The straight line is the prediction at late times. The gray lines are from the nine individual sources in each of the frame and the interior. (a) receivers in beam, sources in beam. (b) receivers in beam, sources in plate. (c) receivers in plate, sources in beam. (d) receivers in plate, sources in plate.

found earlier that we needed about four elements per wavelength for accuracy.

Explaining in detail the bounces that we see in the response of this hybrid system is beyond the scope of this thesis. The goal of this thesis is to explore the concatenation of early-time diffusive data, with fluctuations inherent in DNS, to predict late-time diffusive behavior.

We briefly offer some possible explains for such large deviations from expected diffusive behavior. The first is that the bounces could be a resonance effect. Two modes vibrating at slightly different frequencies will exhibit beats in the time domain. This beating phenomenon would be immediately understood by a musician familiar with listening to two slightly out-of-tune

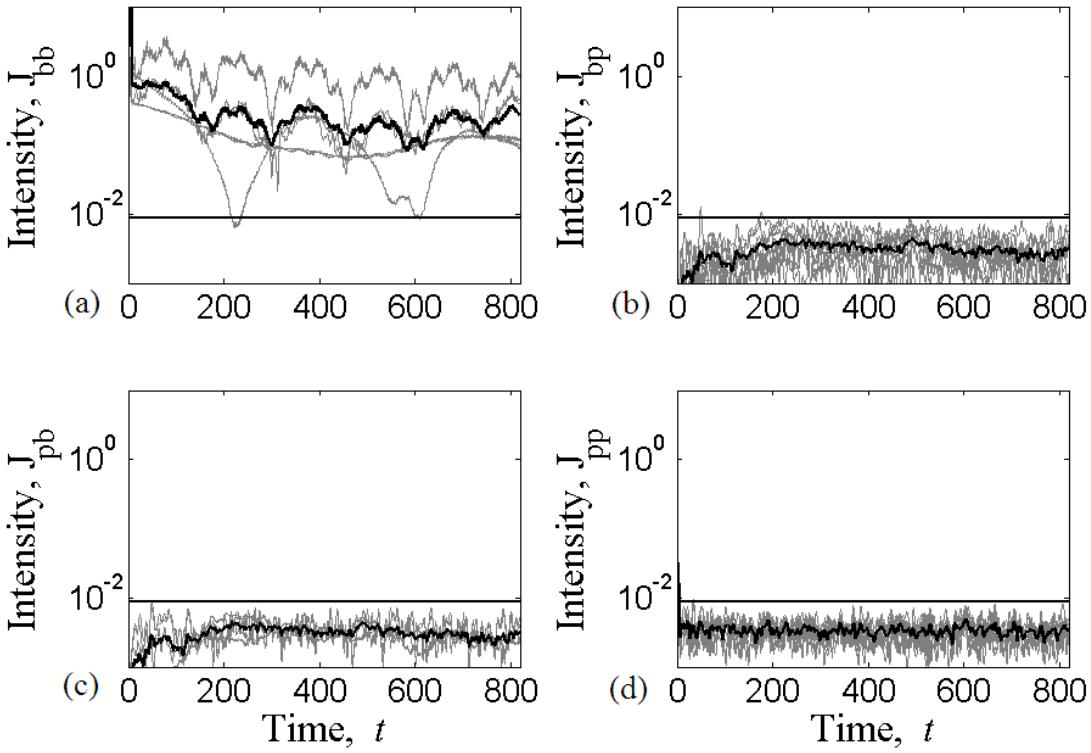

Figure 7.11: Responses at twice the target frequency $2f_T$. The straight line is the prediction at late times. The gray lines are from the nine individual sources in each of the frame and the interior. (a) receivers in beam, sources in beam. (b) receivers in beam, sources in plate. (c) receivers in plate, sources in beam. (d) receivers in plate, sources in plate.

instruments. We investigated the modes and natural frequencies of the beam frame in isolation, uncoupled to the plate, and found no two frequencies appropriately spaced to explain the bounces we see in Figs. 7.9(a) and 7.10(a). However, we did find that the modes strongly localize in each side of the beam frame.

Attributing the localization in the entire structure to the localization in the uncoupled beam frame would be naïve. Localization in one-dimensional structures, such as the isolated frame, is common, but once coupled again to the frame, the system is not one-dimensional. In particular, vibrational energy should be able to leak out of any portion of the frame into the plate, then back

into the beam frame.

A final, and more likely, explanation we can offer regards the modal density of the frame. Modes in the beam are sparse. The width of any given mode in frequency in the beam is on the order of the inverse of the leak time ($\approx 1/300$), while modal spacing, the width between modes, in frequency is on the order of the inverse of modal density ($\approx 1/3$). Energy is deposited into the beams through a source only in narrow frequency bins corresponding to the modes of the beam, and only a small fraction of the modes in the plate overlap with the beam modes. Only a small fraction of the energy deposited in the beams can leak into the plate through these narrow frequency windows. Moreover, the bandwidth of the filter is about $\frac{2}{T_B} \approx 1/7$, so statistically there are not many modes under the filter.

Since the system localizes, we do not expect concatenation to extract reasonable diffusion parameters and do not attempt to do so. We have found that there are more constraints on the hybrid system than having longer wavelengths in the beams than in the plate so that there is, indeed, any energy transfer at all. We need to find a better parameter regime where it is plausible that we will find diffusive behave in the beam-plate system. We formally explore where this good parameter regime lies in the next section on dimensional analysis and constraints.

In addition, we find that our system contains too many complications obscuring the physics we wish to study. To the end of simplifying the system to better uncover the physics being studied in this thesis, we eliminate torsion from the problem. Setting the torsional rigidity and the radius of gyration of the cross sectional area equal to zero is equivalent to the hinged boundary conditions considered in Section 7.2.2.

7.4 Dimensional analysis and constraints

In this section, we identify the important parameters involved in a beam-plate structure and explore several important conditions between these parameters that must be imposed if we are to explore the parameter regime of interest. We reduce all of the material properties and dynamic parameters to only three important non-trivial adjustable quantities. We impose conditions such that the system does not localize, that the beam wavelengths are longer than the plate wavelengths, that we can resolve the diffusive behavior between the beam and the plate in time, and that each substructure homogenizes before energy leaks out of it.

7.4.1 Dimensional analysis

The five parameters that we have control over are the ratios of the plate stiffness to the areal density of the plate $D/\rho_p h$, the bending stiffness of the beam to the lineal density of the beam $EI/\rho_b A_b$, and the plate stiffness to the lineal density of the beam $D/\rho_b A_b$, as well as a length scale of the system L and the target frequency of interest ω_T. The dimensions of these five parameters are

$$\left[\frac{D}{\rho_p h}\right] = \frac{1}{L^4 T^2}, \tag{7.45a}$$

$$\left[\frac{EI}{\rho_b A_b}\right] = \frac{1}{L^4 T^2}, \tag{7.45b}$$

$$\left[\frac{D}{\rho_b A_b}\right] = \frac{1}{L^3 T^2}, \tag{7.45c}$$

$$[L] = L, \text{ and} \tag{7.45d}$$

$$[\omega_T] = \frac{1}{T}. \tag{7.45e}$$

Note that mass is completely scaled out of the problem. We can use the last two dimensional L and ω_{T} parameters to define the three dimensionless quantities

$$\left(\frac{D}{\rho_{\mathrm{p}} h}\right)^{*} = \left(\frac{D}{\rho_{\mathrm{p}} h}\right) \frac{1}{L^4 \omega_{\mathrm{T}}^2}, \tag{7.46a}$$

$$\left(\frac{EI}{\rho_{\mathrm{b}} A_{\mathrm{b}}}\right)^{*} = \left(\frac{EI}{\rho_{\mathrm{b}} A_{\mathrm{b}}}\right) \frac{1}{L^4 \omega_{\mathrm{T}}^2}, \text{ and} \tag{7.46b}$$

$$\left(\frac{D}{\rho_{\mathrm{b}} A_{\mathrm{b}}}\right)^{*} = D \frac{1}{L^3 \omega_{\mathrm{T}}^2} \tag{7.46c}$$

over which we have meaningful control. In the following, we drop the asterisk for brevity as we will always mean the dimensionless quantity.

7.4.2 Constraints on the dimensionless parameters

There are several constraints on the dimensionless parameters defined in section Section 7.4.1, some of which are more important than others.

Localization

We require that there be enough modal overlap so that energy localizes in neither the beam nor the plate. First, consider energy initially deposited into the beam leaking into the plate. We wish to enforce that local modes in the beam leak into the plate fast enough that they overlap each other. Taking the width of a mode in the frequency domain to be $T_{\mathrm{L}}^{\mathrm{b-p}}\left(\lambda_{\mathrm{b}}/\lambda_{\mathrm{p}} \to \infty\right)$ for clarity, this condition is

$$\frac{\mathcal{N}_{\mathrm{b}}}{T_{\mathrm{L}}^{\mathrm{b-p}}\left(\lambda_{\mathrm{b}}/\lambda_{\mathrm{p}} \to \infty\right)} = \frac{1}{4\pi} \frac{\left(\frac{D}{\rho_{\mathrm{b}} A_{\mathrm{b}}}\right)}{\left(\frac{EI}{\rho_{\mathrm{b}} A_{\mathrm{b}}}\right)^{\frac{1}{4}} \left(\frac{D}{\rho_{\mathrm{p}} h}\right)^{\frac{3}{4}}} > 1. \tag{7.47}$$

To derive Eq. (7.47), we took our structure to be a square with sides of length L and substituted $L \to 4L$ in Eq. (7.29a). As the ratio $\frac{\mathcal{N}_\mathrm{b}}{T_\mathrm{L}^{\mathrm{b}-\mathrm{p}}} = \frac{\mathcal{N}_\mathrm{p}}{T_\mathrm{L}^{\mathrm{p}-\mathrm{b}}}$, there is no separate condition for localization in the plate.

In the "naïve" hybrid system considered so far above, we have $\frac{1}{4\pi}\frac{\left(\frac{D}{\rho_\mathrm{b}A_\mathrm{b}}\right)}{\left(\frac{EI}{\rho_\mathrm{b}A_\mathrm{b}}\right)^{\frac{1}{4}}\left(\frac{D}{\rho_\mathrm{p}h}\right)^{\frac{3}{4}}} \approx 0.002 \ll 1$, so that system is clearly localizing by this condition.

Wavelengths in the beam and plate

We require that typical length scales in the beam be long compared to a wavelength in the beam. This condition is

$$\frac{\gamma_\mathrm{b}L}{2\pi} = \frac{1}{2\pi}\frac{1}{\left(\frac{EI}{\rho_\mathrm{b}A_\mathrm{b}}\right)^{\frac{1}{4}}} > 1. \tag{7.48}$$

We also require that the wavelengths in the beam be long compared to wavelengths in the plate so that waves propagating into the plate from the beams are not evanescent. This condition is

$$\frac{\gamma_\mathrm{p}L}{2\pi} = \frac{1}{2\pi}\frac{1}{\left(\frac{D}{\rho_\mathrm{p}h}\right)^{\frac{1}{4}}} > \frac{\gamma_\mathrm{b}L}{2\pi} = \frac{1}{2\pi}\frac{1}{\left(\frac{EI}{\rho_\mathrm{b}A_\mathrm{b}}\right)^{\frac{1}{4}}}, \tag{7.49}$$

which is equivalent to

$$\frac{\left(\frac{EI}{\rho_\mathrm{b}A_\mathrm{b}}\right)}{\left(\frac{D}{\rho_\mathrm{p}h}\right)} > 1. \tag{7.50}$$

Resolution in time

We would like for there to be several periods at frequency ω_T in a diffusion time so that the transfer of energy between the plate and the beam can be captured in a numerical simulation. Again using

the leak time $T_{\mathrm{L}}^{\mathrm{b-p}}\left(\lambda_{\mathrm{b}}/\lambda_{\mathrm{p}} \to \infty\right) \approx T_{\mathrm{D}}$ for simplicity, this condition is

$$\frac{\omega_{\mathrm{T}} T_{\mathrm{D}}}{2\pi} = \frac{\omega_{\mathrm{T}} T_{\mathrm{L}}^{\mathrm{b-p}}\left(\lambda_{\mathrm{b}}/\lambda_{\mathrm{p}} \to \infty\right)}{2\pi} = \frac{2}{\pi} \frac{\left(\frac{D}{\rho_{\mathrm{p}} h}\right)^{\frac{3}{4}}}{\left(\frac{D}{\rho_{\mathrm{b}} A_{\mathrm{b}}}\right)} \gg 1. \tag{7.51}$$

If this condition cannot be satisfied, it can be remedied by ensemble averaging.

Transit times

We would also like the transit time across the structure to be less than the leak time, particularly in the plate, so that the energy field inside the plate reaches a homogenous state before the interesting dynamics of energy transfer from the plate to the beam stops. If one defines one transit time across the plate as

$$T_{\mathrm{Tp}} \equiv \frac{L}{c_{\mathrm{gp}}}, \tag{7.52}$$

where, from Eq. (7.11),

$$c_{\mathrm{gp}} = \frac{\partial \omega}{\partial \gamma_{\mathrm{p}}} = 2L\omega_{\mathrm{T}} \left(\frac{D}{\rho_{\mathrm{p}} h}\right) \tag{7.53}$$

is the group velocity of waves in the plate, then the relevant constraint is

$$\frac{T_{\mathrm{L}}^{\mathrm{p-b}} c_{\mathrm{gp}}}{L} = \frac{\mathcal{N}_{\mathrm{p}}}{\mathcal{N}_{\mathrm{b}}} \frac{T_{\mathrm{L}}^{\mathrm{b-p}}\left(\lambda_{\mathrm{b}}/\lambda_{\mathrm{p}} \to \infty\right) c_{\mathrm{gp}}}{L} = 2 \frac{\left(\frac{D}{\rho_{\mathrm{p}} h}\right)^{\frac{1}{2}} \left(\frac{EI}{\rho_{\mathrm{b}} A_{\mathrm{b}}}\right)^{\frac{1}{4}}}{\left(\frac{D}{\rho_{\mathrm{b}} A_{\mathrm{b}}}\right)} > 1, \tag{7.54}$$

where we have used $A_{\mathrm{p}} = L^2$ in Eq. (7.29b). A more restrictive constraint is to use the diffusion time $T_{\mathrm{D}} \approx T_{\mathrm{L}}^{\mathrm{b-p}}$ instead of the leak time, i.e.,

$$\frac{T_{\mathrm{D}} c_{\mathrm{gp}}}{L} \approx \frac{T_{\mathrm{L}}^{\mathrm{b-p}}\left(\lambda_{\mathrm{b}}/\lambda_{\mathrm{p}} \to \infty\right) c_{\mathrm{gp}}}{L} = 8 \frac{\left(\frac{D}{\rho_{\mathrm{p}} h}\right)}{\left(\frac{D}{\rho_{\mathrm{b}} A_{\mathrm{b}}}\right)} > 1, \tag{7.55}$$

so that the energy field inside the plate reaches a homogenous state on the time scale over which diffusion between the frame and the interior occurs. For completeness, one may also consider the condition that the leak time from the beam to the plate is large compared to a transit time across a beam segment. This condition is

$$\frac{T_{\mathrm{L}}^{\mathrm{b-p}}\left(\lambda_{\mathrm{b}}/\lambda_{\mathrm{p}}\to\infty\right)c_{\mathrm{gb}}}{L}=8\frac{\left(\frac{D}{\rho_{\mathrm{p}}h}\right)^{\frac{3}{4}}\left(\frac{EI}{\rho_{\mathrm{b}}A_{\mathrm{b}}}\right)^{\frac{1}{4}}}{\left(\frac{D}{\rho_{\mathrm{b}}A_{\mathrm{b}}}\right)}>1, \tag{7.56}$$

where we have used

$$c_{\mathrm{gb}}=\frac{\partial\omega}{\partial\gamma_{\mathrm{b}}}=2L\omega_{\mathrm{T}}\left(\frac{EI}{\rho_{\mathrm{b}}A_{\mathrm{b}}}\right) \tag{7.57}$$

from Eq. (7.9).

Discussion

It is evident that the conditions in Eqs. (7.47) and (7.56) cannot be met simultaneously: a fraction cannot be both large and small at the same time. However, the latter condition is unimportant, as any energy in the beam immediately leaks into the plate without having to travel through the beam to the plate first.

Ignoring numerical coefficients, from Eqs. (7.48), (7.50), and (7.55),

$$\left(\frac{D}{\rho_{\mathrm{b}}A_{\mathrm{b}}}\right)<\left(\frac{D}{\rho_{\mathrm{p}}h}\right)<\left(\frac{EI}{\rho_{\mathrm{b}}A_{\mathrm{b}}}\right)<1 \tag{7.58}$$

must hold. If the above inequalities do hold, then Eq. (7.47) is impossible. Since Eqs. (7.47), (7.48), and (7.50) are required, we must abandon Eq. (7.55), the condition that the energy density in the plate reaches a (quasi-)equilibrium before a diffusion time. The consequence of abandoning

Eq. (7.55) is that the average square displacement at a small number of receivers in the plate will not be a good approximation to the energy density in the plate during the first critical diffusion time. The same will be true in the beam, as well, since Eq. (7.56) has been abandoned. We may be able to compensate by ignoring data at early enough times when the plate has net yet homogenized and energy is still concentrated around the source site.

If we instead try to satisfy Eqs. (7.48), (7.50), and (7.51),

$$\left(\frac{D}{\rho_b A_b}\right) < \left(\frac{D}{\rho_p h}\right)^{\frac{3}{4}} < \left(\frac{EI}{\rho_b A_b}\right)^{\frac{3}{4}} < 1 \tag{7.59}$$

must hold, again ignoring numerical coefficients. Under the above inequalities, the condition in Eq. (7.54) is automatically satisfied. It should not be surprising that Eq. (7.54) is easily satisfied, as T_L^{p-b} is, presumably, very long.

It can be shown that we can satisfy the only remaining condition (i.e., Eq. (7.47)) by using the following recipe. Choose dimensionless parameters $\left(\frac{D}{\rho_p h}\right)$ and $\left(\frac{D}{\rho_b A_b}\right)$ such that the inequality of Eq. (7.51) is satisfied. Now, from Eq. (7.47), $\left(\frac{EI}{\rho_b A_b}\right)^{(1/4)} < (1/2\pi)\left(\frac{D}{\rho_b A_b}\right) / \left(\frac{D}{\rho_p h}\right)^{(3/4)}$ must hold, so a value of $\left(\frac{EI}{\rho_b A_b}\right)$ can be set. Now these values of the dimensionless parameters will not necessarily satisfy the inequalities of Eq. (7.59) because of the condition of Eq. (7.50). So, we can reset $\left(\frac{D}{\rho_p h}\right)$ so that there are any desired number of plate wavelengths per beam wavelength. Finally, to maintain the same ratio in Eq. (7.51), reset $\left(\frac{D}{\rho_b A_b}\right)$.

After setting the values of all three dimensionless paramters, one can calculate the number wavelengths in the plate per side of the structure. If the structure is too small (say, fewer than 10 wavelengths per side of the structure) to be considered statistical, one may always adjust the

parameter values downward so that the structure is somewhat larger and still satisfy all of the conditions.

7.5 Three examples

We present three examples of the responses to hybrid systems in this section. A cartoon of the geometry on which the systems are based is in Fig. 7.12. We discuss the properties of the system

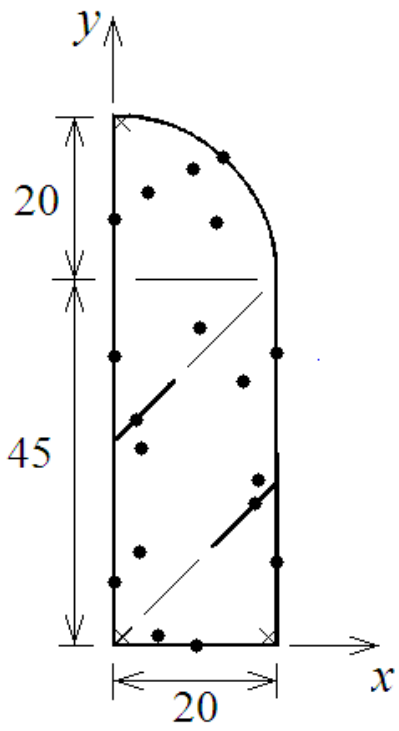

Figure 7.12: A cartoon of the hybrid system geometry. The curved portion is a quarter circle. The source/receiver sites (•) are given for the first example. The ball-and-socket boundary conditions (×) are positioned one plate wavelength at the target frequency away from the frame.

common to all three examples here and how they are different in their respective sections below. The systems are based on a quarter stadium, like the original geometry pictured in Fig. 7.8. The structure was given a larger aspect ratio so that the perimeter could be increased without increasing

the area of the plate as quickly as it would be by just scaling up the system size (in units of plate wavelengths). Increasing the perimeter will help satisfy the localization condition Eq. (7.47), but increasing the area of the plate increases the computational burden.

As before, the periphery is a stiff beam frame, and the interior is a compliant plate. For all three examples the boundary conditions are ball-and-socket joints near the three corners, and the plate is hinged to the beams so that torsion does not enter into the problem. The material properties are such that there are five plate wavelengths per beam wavelength at the target frequency.

For the first example only, there are "extra" portions of beam of length 10 extending into the plate. The extra lengths of beam also slightly increase the modal density of the beam frame without increasing the area of the plate. Adding these lengths of beam adds its own problems, discussed in the results section for example 1.

For each of the three examples detailed more fully below there is some problem. The problems are different for each example, but they can be explained. No one example is completely satisfying, but they all show encouraging improvements over the first hybrid problem studied in Section 7.3.

For all three examples, the target frequency is $\omega_{\mathrm{T}} = 8.929$. The system length scale can be defined two different ways. One-fourth of the perimeter is $L = 40.35$, while the square root of the area of the plate, $L = 34.84$, is similar. The values of the frequency of interest and the size of the system are not particularly important in light of the discussion of the meaningful dimensionless parameters in Section 7.4.1. These particular numbers were chosen simply to be comparable to those found in the first attempt above.

7.5.1 Example 1

Setup and response

The system parameters are $EI = 1.4385$, $D = 5.066 \times 10^{-4}$, $\rho_b A_b = 0.045$, and $\rho_p h = 9.905 \times 10^{-3}$. The wavelengths in the beam and in the plate are $\lambda_b = 5$ and $\lambda_p = 1$, respectively, so the length scale in Fig. 7.12 can be thought of being in terms of plate wavelengths. We mesh the system by placing nodes at every quarter-wavelength in both the beams and the plate. The mesh fully resolves both the beam and the plate. The mesh has 144 beam elements, 52 750 plate elements, and 78 357 degrees of freedom. The highest natural frequency in the system is about twenty times the target frequency.

The leak time calculated from Eq. (7.28) is $T_L^{p-b} = 12.8$; however, there is evidence, discussed below, that suggests that this estimate of the leak time is wrong. The relevant condition on resolution in time, Eq. (7.51) reads $18 \gg 1$, so it is generously satisfied.

The modal densities of the beam (Eq. (7.29a)) and the plate (Eq. (7.29b)) are $\mathcal{N}_b = 1.97$ and $\mathcal{N}_p = 427$, respectively. The modal density of the beam is still significantly less than the leak time, but the disparity is significantly improved over the first attempt. The condition of Eq. (7.47), using L = Perimeter/4 and ignoring the extra lengths of beam extending into the center of the area, reads $0.14 > 1$, so it is satisfied significantly better than it is in the first attempt.

The time duration of the filter (tone burst in time domain under a cosine envelope) constructed as in Section 4.2.1 is $T_B = 7$. Its half power bandwidth in the frequency domain is approximately $\frac{2}{T_B} \approx 0.3$. The time duration of the filter here is half of what what used in the first attempt at studying the hybrid system. The shorter filter has a wider bandwidth in frequency, averaging

more modes, particularly in the beams. The shorter filter also resolves the diffusion times better, though the time domain filter itself is less resolved by the number of oscillations in the filter. The filter duration was chosen such that the correlation time (about half the filter duration) was approximately the geometric mean of the period of oscillation and the leak time. This choice for the filter duration means that the filter is resolved by the fast oscillations of the dynamics approximately as well as the diffusion time is resolved by the filter.

We obtained displacements by carrying out time domain simulations for $N_t = 2^{14}$ time steps with time step $\delta t = 0.005 \approx 1/\omega_{\max}$, or out to a total time of approximately $N_t \delta t = 82$, or approximately $7T_{\mathrm{L}}^{\mathrm{b-p}}\left(\lambda_{\mathrm{b}}/\lambda_{\mathrm{p}} \to \infty\right)$ (7 diffusion times) as determined by Eq. (7.28).

We investigate the nine source/receiver sites in each of the beam frame and plate interior pictured in Fig. 7.12. A source acts through each receiver for a total of 18 simulations, and we average over every source/receiver combination treating the frame and interior as two substructures.

The energy densities are plotted in Fig. 7.13. Similarly to what was done in the first hybrid system attempt and earlier chapters, we denote mean-squared, filtered displacements (intensity) by $\mathbf{J}_{\rho r \sigma s}$, where ρ ranges over $\rho \in \{\text{beam}, \text{plate}\}$ for the subsystem in which the receiver is located, and r ranges over $r \in \{1 \ldots 9\}$ for the receiver in that subsystem. Similarly, σ ranges over $\sigma \in \{\text{beam}, \text{plate}\}$, and s ranges over $s \in \{1 \ldots 9\}$ for the sources.

The gray lines are the average among the various receivers in a substructure due to a single source normalized by the late-time prediction by Weaver,[38] or, more precisely,

$$\mathbf{J}_{\rho\sigma s} = \left\langle \frac{\mathbf{J}_{\rho r \sigma s}}{\mathbf{J}_{\rho r \sigma s}(t \to \infty)} \right\rangle_r . \tag{7.60}$$

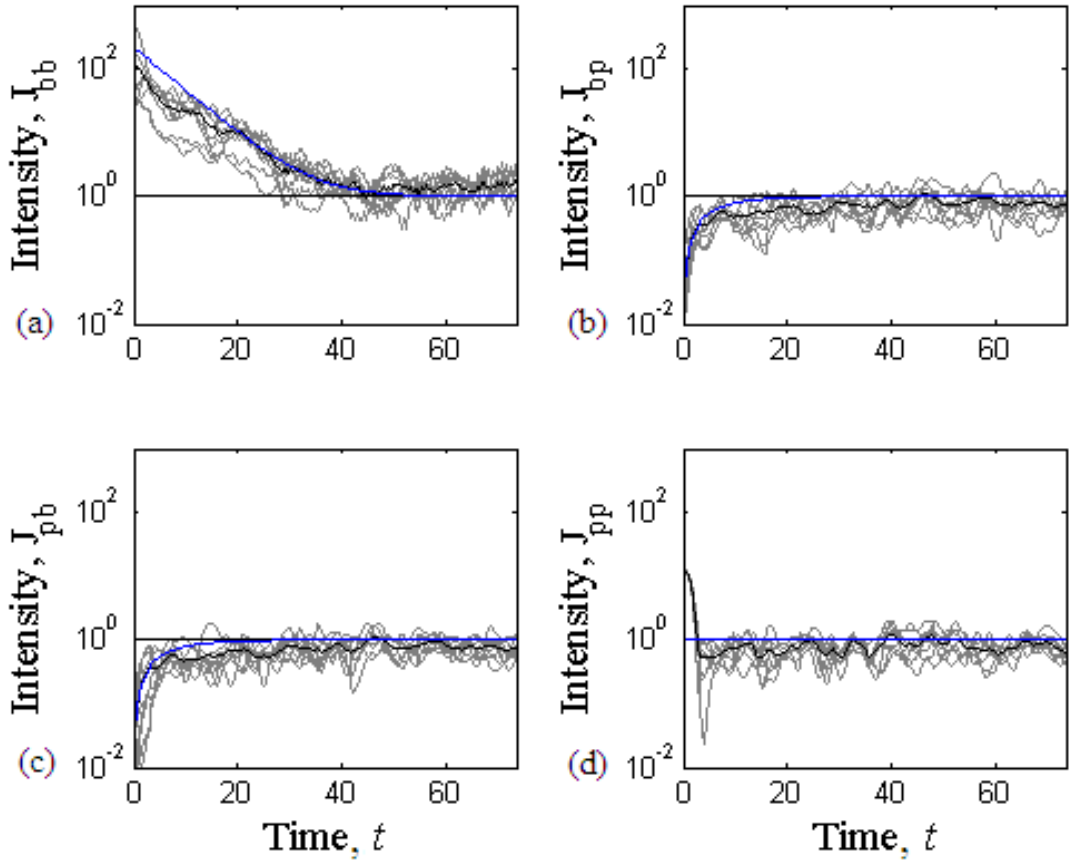

Figure 7.13: (Color in electronic version.) Responses at the target frequency ω_T for example 1. The straight line is the prediction at late times. The gray lines are from the nine individual sources in each of the frame and the interior. (a) receivers in beam, sources in beam. (b) receivers in beam, sources in plate. (c) receivers in plate, sources in beam. (d) receivers in plate, sources in plate.

The black noisy curve is the average among the various receivers and sources, or

$$\mathbf{J}_{\rho\sigma} = \left\langle \frac{\mathbf{J}_{\rho r\sigma s}}{\mathbf{J}_{\rho r\sigma s}(t \to \infty)} \right\rangle_{rs} . \tag{7.61}$$

Both of these average intensities were constructed to have a (predicted) late-time value of unity for easy comparison. Finally, the smooth curve (color in electronic version) is the theoretical prediction (Eq. (7.33)) using initial conditions such that either all of the energy is initially deposited in the beams or all of the energy is initially deposited in the plate.

The solid curve represents the data from the simulation well, apparently without localization, indicating that the underlying behavior is well represented by a diffusion process. In the next section, we will use the diffusion limit of the concatenation ansatz to extract diffusion parameters for the system. However, two notes about the response need to be made first.

First, there is a large, nonphysical response at early times in the plate-plate response. This character of the early response is a trivial statistical artifact due to having only nine receivers in the substructure. The receiver through which the source acts is over-weighted at such early times. Due to the high relative modal density of the plate compared to the beams, we know that the response in the plate essentially takes on its late-time value. This problem is only a minor annoyance, and it could be alleviated by adding (perhaps many) more receivers in the plate at the cost of additional computational burden.

Second, and more interestingly, the leak time used to produce the smooth black curve is half of that calculated when using Eq. (7.28). The stronger coupling is apparently due to the beams extending into the interior of the plate. Since the leak time is only half of what we thought it was, the condition in Eq. (7.47) actually reads $0.28 < 1$. It is still unsatisfied, but it is satisfied better than what we though it was.

Concatenation results and discussion

We apply the diffusion limit of the concatenation routine to the data of example 1 to extract the diffusion parameters. We plot the underlying behavior of the data constructed from the diffusion parameters extracted by the concatenation program along with the responses in Fig. 7.14. The four values of Δ used were based on the theoretical value of the leak time from the beam to the

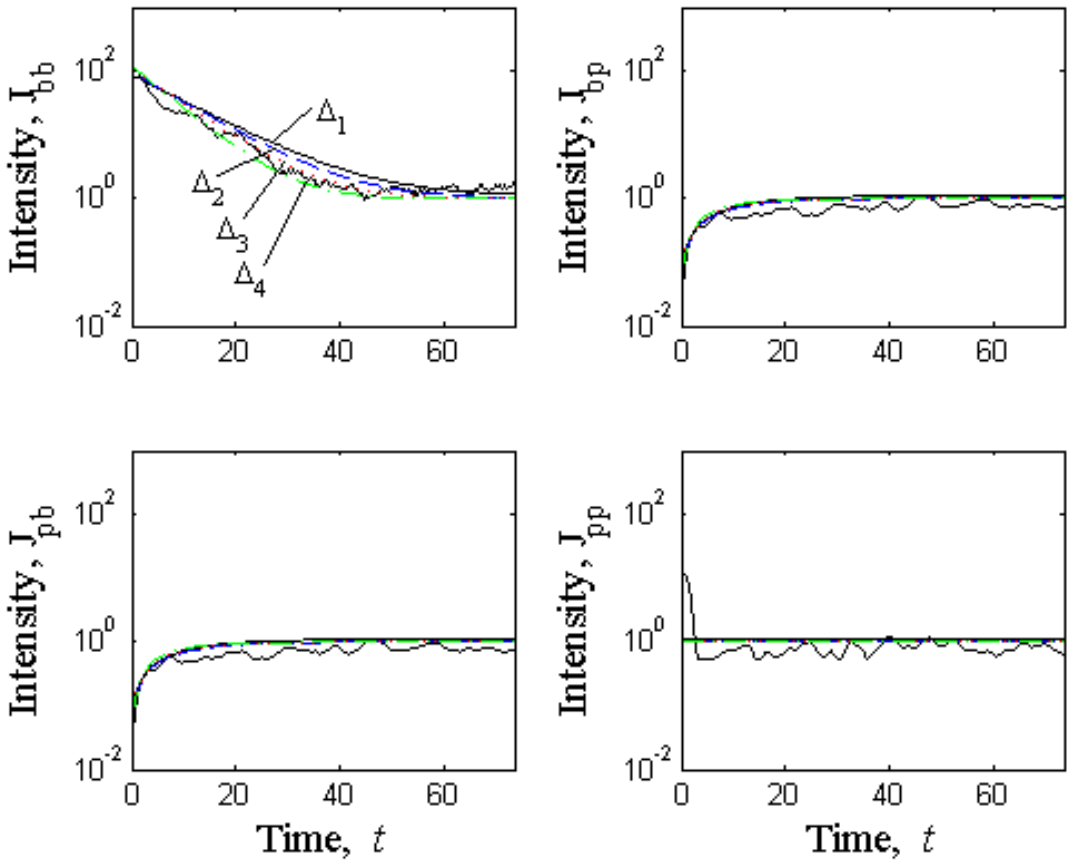

Figure 7.14: (Color in electronic version.) Comparison of the concatenation prediction with response for example 1 for various values of Δ. (a) receivers in beam, sources in beam. (b) receivers in beam, sources in plate. (c) receivers in plate, sources in beam. (d) receivers in plate, sources in plate.

plate as given by Eq. (7.28). In particular, $\Delta_1 = 0.5/T_{\mathrm{L}}^{\mathrm{b-p}\,\infty}$ retains the most data, $\Delta_2 = 1/T_{\mathrm{L}}^{\mathrm{b-p}\,\infty}$, $\Delta_3 = 2/T_{\mathrm{L}}^{\mathrm{b-p}\,\infty}$, and $\Delta_4 = 4/T_{\mathrm{L}}^{\mathrm{b-p}\,\infty}$ retains the least amount of data.

All four curves represent the data well. In Fig. 7.14(a), the concatenation diffusion predictions agree with each other well enough that the four curves are difficult to discern from each other. Indeed, in Figs. 7.14(b)-(d), the four curves lie on top of each other. One caveat, which equally applies to examples 2 and 3 below, should be noted. The plate-plate response was replaced with the late-time prediction given by Weaver[38] (i.e., unity) for all times to avoid problems associated

with the nonphysical statistical artifact mentioned above.

In conclusion for example 1, we are encouraged by the apparent smooth diffusive behavior of the system, even if the localization condition in Eq. (7.47) is not satisfied. However, the leak time seems to be wrong, approximately twice of what it was expected to be. Energy is leaking into the plate at twice the rate of what we expected. The idea now is to remove the extra lengths of beam extending into the area, as they do not strictly satisfy the assumptions used to derive the approximation for the leak time.

7.5.2 Example 2

For example 2, the only change in the physical setup is to eliminate the two extra beams extending into the plate. Though the modal density of the beam will be lowered slightly, the assumptions in the derivation of the leak time will be satisfied, and the new extracted leak time should now be the value estimated by Eq. (7.28).

Setup and response

We repeat the numerical experiment of Section 7.5.1 with identical system parameters $EI = 1.4385$, $D = 5.066 \times 10^{-4}$, $\rho_b A_b = 0.045$, and $\rho_p h = 9.905 \times 10^{-3}$, but without the extra lengths of beam. It was therefore necessary to move some of the source/receiver sites from their positions as indicated in Fig. 7.12 in the beams. Some sites were also moved in the plate to better represent a uniform distribution over the area. The wavelengths in the beam and the plate are $\lambda_b = 5$ and $\lambda_p = 1$, respectively, so the length scales in Fig. 7.12 can be thought of as being in terms of plate wavelengths, as in example 1. The new mesh has 128 beam elements, 40 800 plate elements, and

60 624 degrees of freedom. The highest natural frequency in the system is again about twenty times the target frequency.

The only parameter related to energy flow that is different from example 1 is the modal density in the beams, now that the total length of beams in the system is shorter. The leak time calculated from Eq. (7.28) is $T_{\mathrm{L}}^{\mathrm{p-b}} = 12.8$. The modal densities of the beam (Eq. (7.29a)) and the plate (Eq. (7.29b)) are $\mathcal{N}_{\mathrm{b}} = 1.81$ and $\mathcal{N}_{\mathrm{p}} = 427$, respectively. The localization condition in Eq. (7.47) reads $0.14 > 1$. It is not satisfied, but it is formally the same as in example 1. Since we expect the leak time to be twice as long here in example 2, we might expect to see more localization than in exmaple 1.

We change some of the parameters related to resolving the energy flow. The time duration of the filter is $T_B = 4.22$. Its half power bandwidth in the frequency domain is approximately $\frac{2}{T_B} \approx 0.5$.

We obtained displacements by carrying out time domain simulations for $N_t = 2^{15}$ time steps with time step $\delta t = 0.005 \approx 1/\omega_{\max}$, or out to a total time of approximately $N_t \delta t = 160$, or approximately $13 T_{\mathrm{L}}^{\mathrm{p-b}}$ (13 diffusion times). We carry out the simulations for twice the time as in example 1 because we expect the diffusion time to be twice as long.

We again investigate the nine source/receiver sites in each of the beam frame and plate interior. A source acts through each receiver for a total of 18 simulations, and we average over every source/receiver combination treating the frame and interior as two substructures.

The energy densities are plotted in Fig. 7.15. We denote intensity by $\mathbf{J}_{\rho r \sigma s}$, with the same notation used in example 1. The gray lines are the average among the various receivers in a substructure due to a single source normalized by the late-time prediction by Weaver,[38] and the

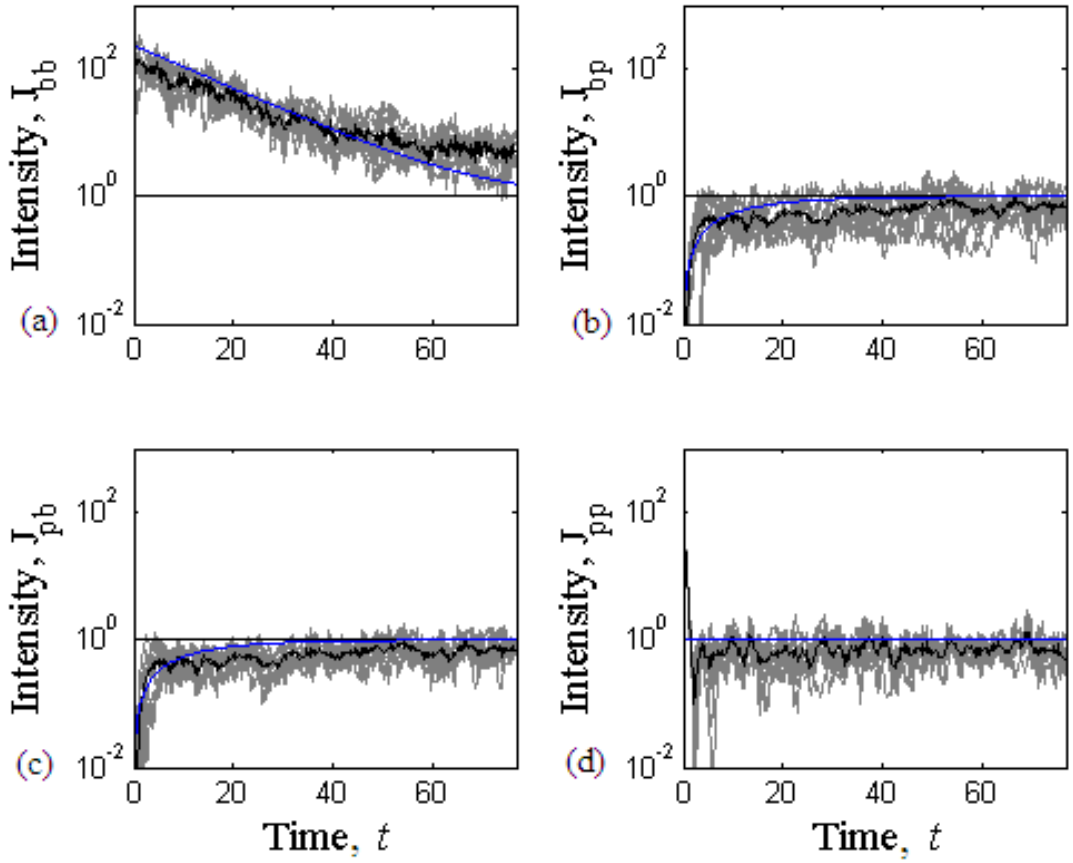

Figure 7.15: (Color in electronic version.) Responses at the target frequency ω_T for example 2. The straight line is the prediction at late times. The gray lines are from the nine individual sources in each of the frame and the interior. (a) receivers in beam, sources in beam. (b) receivers in beam, sources in plate. (c) receivers in plate, sources in beam. (d) receivers in plate, sources in plate.

black noisy curve is the average among the various receivers and sources. The late-time prediction for this average is unity. Finally, the black smooth curve is the theoretical prediction (Eq. (7.33)) using initial conditions such that either all of the energy is initially deposited in the beams or all of the energy is initially deposited in the plate.

The solid curve represents the data from the simulation well, at least at early times, indicating that the underlying behavior is well represented by a diffusion process. At first glance at the beam-beam response in particular, it may seem like the structure localizes. The response does not

reach the late-time prediction quickly. However, upon closer inspection, one may notice that the response (on the log scale) up to time $t \approx 40$ is linear at the expected rate for a few leak times, then becomes nearly linear at a different, slower, rate after a few leak times. There is a second, slower, leak rate associated with a larger leak time that we do not fully understand.

Localization is still plausible, however. The condition in Eq. (7.47) is, indeed, still not satisfied. It is difficult to understand how the physics will carry the system out to later times without conducting further DNS studies. Understanding the other time scales apparent in Fig. 7.15 is beyond the scope of this thesis. We are encouraged by the presence of the time scale predicted by Eq. (7.28) and attempt to extract it using the concatenation ansatz diffusion limit in the next section.

One may also note that in Fig. 7.15, and in example 3 below, there is an offset at early time when the predicted beam-beam response is greater than the actual data. This early-time offset is easily explained. When the source is nominally on the beam frame structure, not all of the energy is deposited into the beam. Some energy is deposited into the plate. However, the solution to Eq. (7.33) used to construct the theoretical prediction was obtained with the simpler initial conditions of placing all of the energy in either the beam or in the plate.

Concatenation results and discussion

We apply the diffusion limit of the concatenation routine to the data of example 2 to extract the diffusion parameters. We plot the underlying behavior of the data constructed from the diffusion parameters extracted by the concatenation program along with the responses in Fig. 7.16. The four values of Δ used were based on the theoretical value of the leak time from the beam to the plate as given by Eq. (7.28). In particular, $\Delta_1 = 0.5/T_{\mathrm{L}}^{\mathrm{b-p}\ \infty}$ retains the most data, $\Delta_2 = 1/T_{\mathrm{L}}^{\mathrm{b-p}\ \infty}$,

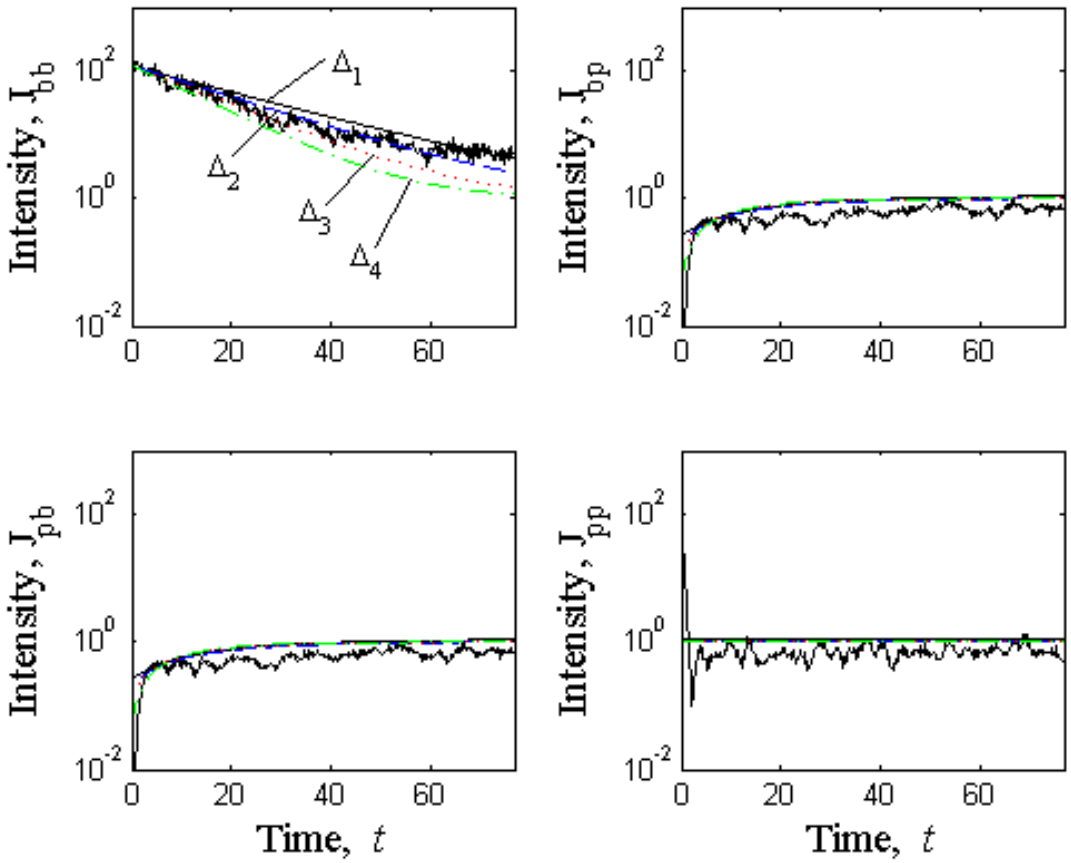

Figure 7.16: (Color in electronic version.) Comparison of the concatenation prediction with response for example 2 for various values of Δ. (a) receivers in beam, sources in beam. (b) receivers in beam, sources in plate. (c) receivers in plate, sources in beam. (d) receivers in plate, sources in plate.

$\Delta_3 = 2/T_{\mathrm{L}}^{\mathrm{b-p}\,\infty}$, and $\Delta_4 = 4/T_{\mathrm{L}}^{\mathrm{b-p}\,\infty}$ retains the least amount of data.

As in example 1, all four curves represent the data well. In Fig. 7.16(a), the concatenation diffusion predictions agree with each other well enough that the four curves are difficult to discern from each other. Also, in Figs. 7.16(b)-(d), the four curves lie on top of each other. Even though there is more interesting behavior at moderate to late times, the amplitude is low enough that it does not contribute strongly in the concatenation calculations.

The problem in example 1 of predicting a leak time half that of what was expected has appar-

ently been solved by removing the extra beams extending into the interior of the plate. However, this doubling of the leak time while keeping the modal density of the beam essentially constant has apparently introduced localization or, at least, some other longer time scale into the system. In the final example we change the system parameters holding the leak time constant but doubling the modal density of the beam frame.

7.5.3 Example 3

The purpose of example 3 is to attempt to reproduce the smooth diffuse behavior found in Figs. 7.13 and 7.14, but with the expected leak time evident in Figs. 7.15 and 7.16.

Setup and response

We repeat the numerical experiment of Section 7.5.2 with new system parameters $EI = (1.4385)/16$, $D = (5.066 \times 10^{-4})/8$, $\rho_b A_b = 0.045$, and $\rho_p h = 2 \times 9.905 \times 10^{-3}$, again without the extra lengths of beam extending into the interior of the plate. The wavelengths in the beam and the plate are $\lambda_b = 2.5$ and $\lambda_p = 0.5$, respectively, so the length scales in Fig. 7.12 can be thought of as being in terms of the more awkward double plate wavelengths, in contrast to examples 1 and 2. The new set of parameters was designed to double the modal density in the beams, leaving the leak time the same. The source/receiver sites were in the same nominal position as in Section 7.5.2, but were moved slightly so that they coincide with a node. The new mesh has 256 beam elements, 163 200 plate elements, and 243 646 degrees of freedom. The highest natural frequency in the system is again about twenty times the target frequency.

The only parameters related to energy flow that is different from example 2 are the modal

densities. The leak time calculated from Eq. (7.28) is $T_{\mathrm{L}}^{\mathrm{p-b}} = 12.8$. The modal densities of the beam (Eq. (7.29a)) and the plate (Eq. (7.29b)) are $\mathcal{N}_{\mathrm{b}} = 2 \times 1.81$ and $\mathcal{N}_{\mathrm{p}} = 4 \times 427$, respectively. The parameters related to resolving the energy flow are the same as in Section 7.5.2. The time duration of the filter is 4.22. Its half power bandwidth in the frequency domain is approximately 0.5.

We obtained displacements by carrying out time domain simulations for 2^{15} time steps with time step $\delta t = 0.005 \approx 1/\omega_{\max}$, or out to a total time of approximately 160, or approximately 13 diffusion times, as determined by Eq. (7.28). We carried out the simulation for the same number of time steps and total time as in example 2, as expect the diffusion time to be the same. However, wall clock time was quadrupled, as the area of the plate (in units of plate wavelengths) and, therefore, the number of degrees of freedom was quadrupled. The simulation took approximately three days on a desktop computer.

We again investigate the nine source/receiver sites in each of the beam frame and plate interior. A source acts through each receiver for a total of 18 simulations, and we average over every source/receiver combination treating the frame and interior as two substructures.

The energy densities are plotted in Fig. 7.17. As before, we denote intensity by $\mathbf{J}_{\rho r \sigma s}$, using the same notation as in examples 1 and 2. In Fig. 7.17, the gray lines are the average among the various receivers in a substructure due to a single source normalized by the late-time prediction by Weaver,[38] and the black noisy curve is the average among the various receivers and sources. Finally, the black smooth curve is the theoretical prediction (Eq. (7.33)) using initial conditions such that either all of the energy is initially deposited in the beams or all of the energy is initially deposited in the plate.

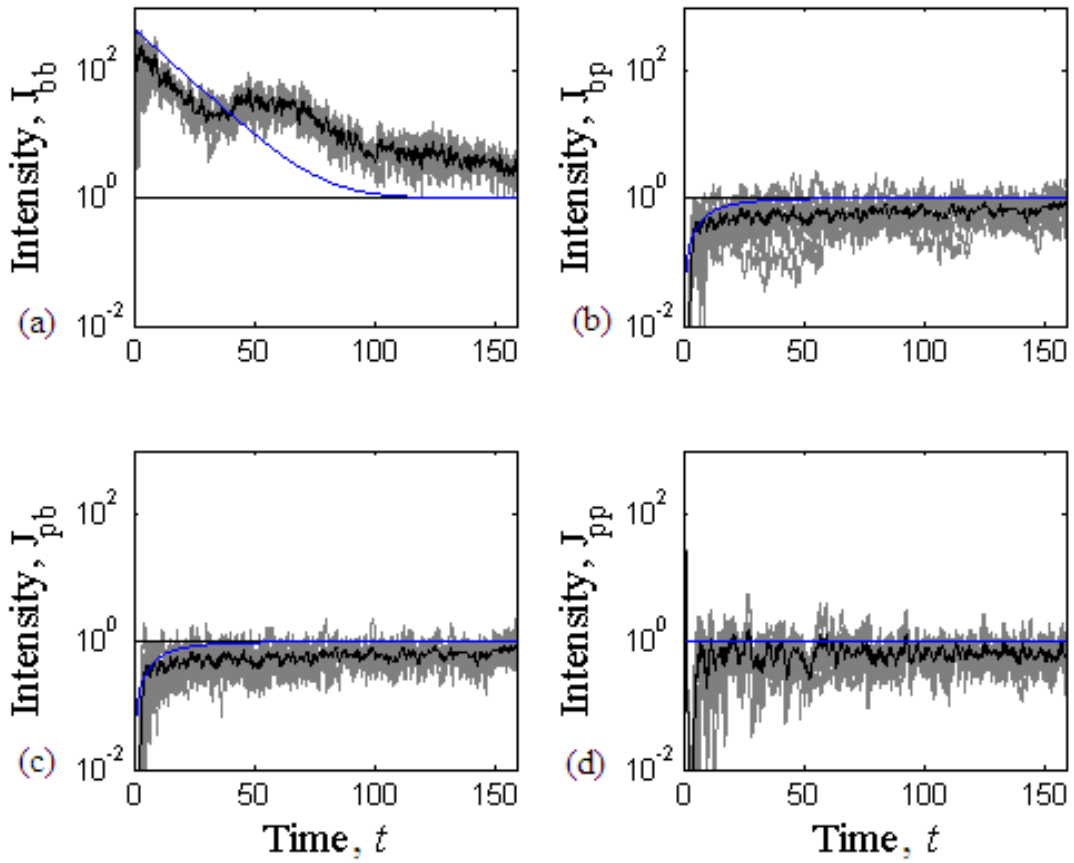

Figure 7.17: (Color in electronic version.) Responses at the target frequency ω_T for example 3. The straight line is the prediction at late times. The gray lines are from the nine individual sources in each of the frame and the interior. (a) receivers in beam, sources in beam. (b) receivers in beam, sources in plate. (c) receivers in plate, sources in beam. (d) receivers in plate, sources in plate.

The initial slope of the prediction up to time $t \approx 30$ matches the initial slope of the data well. However, the change in behavior at some moderate time is more pronounced in this example than as in example 2, at it occurs at an earlier time. Even though we did not see localization in example 1, it is still plausible, as the condition against localization in Eq. (7.47) is not satisfied. The "bounce" in the response at around $t = 40$ is indeed, remarkable. We expect energy transfer to simply slow down from the rate given by diffusing and cease short of the late-time prediction (Eq. (1.16)) in a localizing system. However, the bounce in the response in this example is not as

pronounced as that seen in the first hybrid system attempt seen in Fig. 7.10(a).

At alternative explanation to “localization” may be that energy originally deposited into the plate at time zero may be leaking into the beam. This leak rate is at a time scale longer than the expected diffusion time and may physically be the same time scale more cleanly observed in the results for example 2.

Although the time over which we see the expected leaking rate is shorter in example 3 than it was in example 2, we proceed with the diffusion limit concatenation ansatz in the next section to attempt to extract the diffusion parameters. The program was successful to the degree one could expect it to be in example 2. It may extract the correct diffusion time here, as well.

Concatenation results and discussion

We apply the diffusion limit of the concatenation routine to the data of example 3 to extract the diffusion parameters. We plot the underlying behavior of the data constructed from the diffusion parameters extracted by the concatenation program along with the responses in Fig. 7.18. The four values of Δ used were based on the theoretical value of the leak time from the beam to the plate as given by Eq. (7.28). In particular, $\Delta_1 = 0.5/T_{\mathrm{L}}^{\mathrm{b-p}\,\infty}$ retains the most data, $\Delta_2 = 1/T_{\mathrm{L}}^{\mathrm{b-p}\,\infty}$, $\Delta_3 = 2/T_{\mathrm{L}}^{\mathrm{b-p}\,\infty}$, and $\Delta_4 = 4/T_{\mathrm{L}}^{\mathrm{b-p}\,\infty}$ retains the least amount of data.

The curves do not represent the data well. The diffusion time extracted by the concatenation ansatz does not agree with the initial leak rate at early times, as it did in example 2. The interesting behavior at moderate to late times has a large enough amplitude that it contributes strongly in the concatenation calculations.

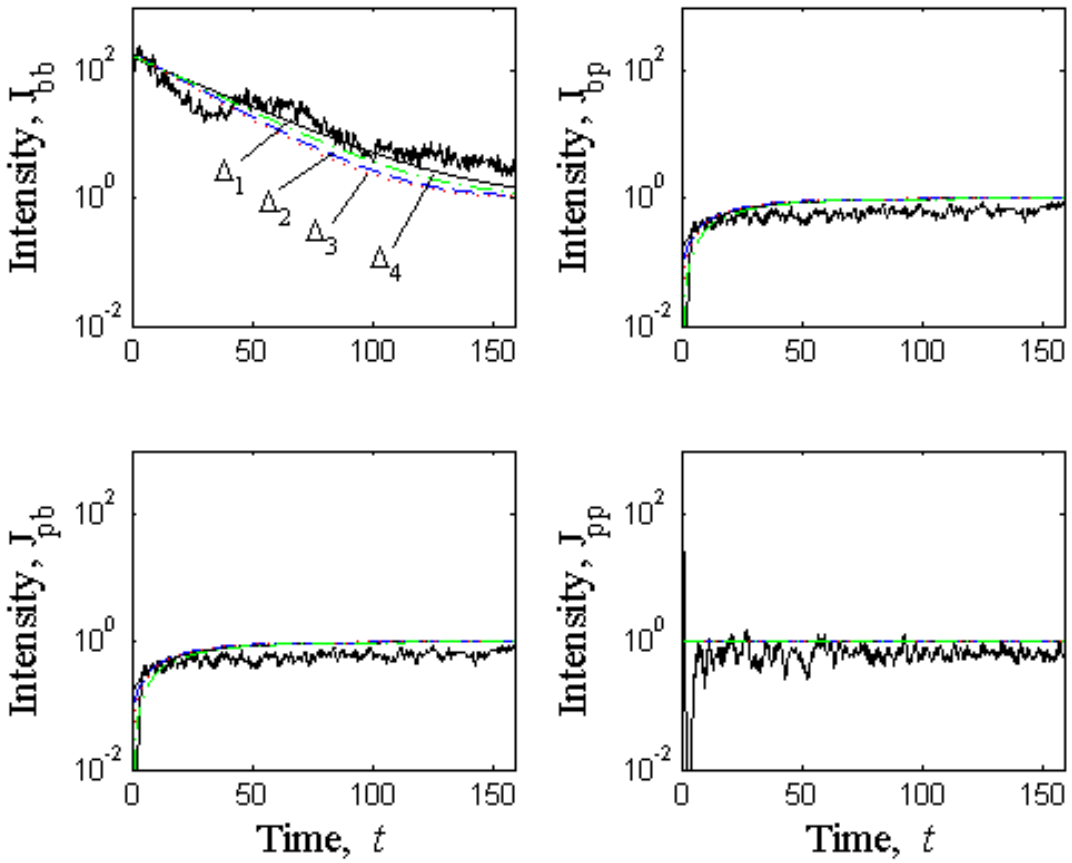

Figure 7.18: (Color in electronic version.) Comparison of the concatenation prediction with response for example 3 for various values of Δ. (a) receivers in beam, sources in beam. (b) receivers in beam, sources in plate. (c) receivers in plate, sources in beam. (d) receivers in plate, sources in plate.

7.6 Conclusion

We have applied our concatenation ansatz diffusion limit to several hybrid systems combining deterministic structures and statistical structures. We have not had enough success describing these systems as we did earlier with two- and three-room systems, a torus, and three plates coupled with springs. However, we have had success with different aspects of the theory in different realizations of the hybrid system. We were able to obtain a system with apparently completely

diffusive underlying behavior in example 1 and extract the correct value of the leak rate; however, the leak rate twice that predicted by theory. We were able to observe the leak rate predicted by theory in examples 2 and 3, but both examples exhibited a second time scale that was not accounted for in the theory. Even though there was a second time scale present, the correct initial leak rate was extracted by the concatenation theory in example 2.

There is good direction to conduct further DNS to attempt to find a system that exhibits the single diffusion time predicted by theory. However, the cost is not worth the benefit. In order to completely satisfy the condition in Eq. (7.47) to avoid localization, the system size would have to continue to increase, as from example 2 in Section 7.5.2 to example 3 in Section 7.5.3. The modal density of the beam would have to be quadrupled, increasing the length scales by a factor of four and increasing the area of the plate by a factor of 16. A DNS of that size would take approximately one-and-a-half months to complete with our current technology, considering only CPU time and not memory requirements. The only benefit to this thesis would be to obtain more visually appealing figures. Learning more about the character of the localization apparent in examples 2 and 3 would, indeed, be interesting, but it is beyond the scope of this thesis. Localization violates the assumptions in the development of Eq. (1.16) and, therefore, the development of the concatenation ansatz. We understand well the behavior of our concatenation theory as it stands.

It is more interesting to propose to move on to other aspects of the concatenation theory, some of which are briefly explored in our concluding chapter.

Chapter 8

Conclusions

8.1 Summary

We have shown that a concatenation ansatz of energy flow in large, irregular structures well predicts smooth late-time behavior of square band-limited displacement variables. Statistical energy analysis has been used for several decades to make such predictions, but it is not without problems. The particular problems addressed in this thesis include the reliance on an assumption of diffusive transfer of vibrational and acoustic energy in SEA. It also requires a division of a large structure into smaller substructures. It requires an estimate of coupling loss factors that govern the energy flow. There is no way to account for local variations of admittances within a substructure. Finally, the dynamic variables in SEA are global energy-density variables that cannot be measured directly in physical or numerical experiments.

Before developing the concatenation ansatz, we explored brute-force fits of diffusion equations to noisy diffusion data. The purpose was to determine how much data was needed to reasonably extract diffusion parameters. We found that the number of fit parameters rises too quickly with the number of sources and receivers involved for brute-force fitting to be efficient.

We then developed the concatenation formulation, based on the idea of relaunching early-time DNS or experimental data continuously in time. It requires no partitioning into substructures,

and local fluctuations in measurable quantities are taken into account. Though it is not strictly based on diffusion, there is a diffusion limit readily comparable to SEA. In the diffusion limit, the parameters governing energy flow are automatically calculated from measured data emphasizing early times.

The framework was tested on several systems, some typically studied with SEA, others not. The first were a two- and three-room system that easily admits substructures. These consisted of rooms coupled by a window wide enough to avoid Anderson localization but narrow enough to satisfy the condition of weak coupling. The concatenation program was able to correctly identify the energy flow parameters between the rooms. The identified parameters were compared to those predicted by room acoustics.

We moved on to a system that does not admit substructures, that of a single statistically homogeneous periodic strip on a random springy base, or a torus. Although the concatenation diffusion limit could not extract all eigenvalues, it did consistently extract the smallest eigenvalues associated with the slowest flow rates and long diffusion times. The large eigenvalues are associated with energy transfer on short, early time scales, so not being able to resolve them is not surprising or disturbing. The diffusion limit can be expected only to be a correction to the late-time steady-state values of mean-squared field variables.

A system of interest to the structures community we studied is a system of three plates connected by springs. We derived SEA coupling loss factors by considering energy deposited into one plate from another plate with a random vibration field. We favorably compared the leak rates implied by the SEA CLFs with the leak rates extracted by the diffusion limit of the concatenation ansatz. We adjusted the coupling strength by changing the number of springs between each pair of

plates.

Finally, we studied a hybrid system composed of a stiff frame normally described deterministically and a compliant plate normally described statistically as with SEA. A leak rate from an infinite beam supporting a traveling wave radiating into a semi-infinite plate was derived. The parameter range in which this rate could be discerned in DNS data was narrow, but the concatenation ansatz was able to predict behavior at moderate times from early-time DNS. The discrepancies can be attributed to localization or an evident leak rate at a longer-time scale than that predicted by theory.

8.2 Future study

All formulations of the concatenation ansatz in this thesis have been in the time domain. There is a formulation in the frequency domain. Such a frequency-domain formulation has the advantage that numerical codes for solving the underlying wave equation are often written in the frequency domain. Also, the numerical integrations of Eqs. (4.4) and (4.5) no longer have to be considered. In addition, attenuation is often defined in the frequency domain. However, preliminary studies suggest that there is no savings of computation time in the frequency domain, while only early-time DNS is needed in the time domain.

One can explore the way early-time data is emphasized in the formulation. Multiplying by a decaying exponential time window as in this work is straightforward analytically, but using a rectangular time window would result in additional computational time savings. The derivation of the formulas for $[\mathbf{H}]$ and $[\mathbf{D}]$ using the power series expansion in Ω on the left-hand side of

Eq. (3.10) would have to be revisited.

One objection to using a diffusion model is that the diffusion equation is an elliptic PDE where information travels with infinite speed, which is profoundly wrong. In reality, vibrations and acoustics are described by the wave equation, a hyperbolic PDE where information travels with finite speed. Though the transit time is typically smaller than the diffusion time, making the issue relatively unimportant, it may be interesting to explore. One can construct a diffusion model—with information traveling at finite speed—by adding a second time derivative to the usual diffusion Eq. (1.7) or Eq. (2.1). Such an equation and the properties of its solution are discussed by Buckingham.[63] There would be another parameter, namely the coefficient to the second time derivative term, that would have to be calculated from the early-time data. Again, the derivation of the formulas for $[\mathbf{H}]$ and $[\mathbf{D}]$ using the power series expansion in $\boldsymbol{\Omega}$ on the right-hand side of Eq. (3.10) would have to be revisited.

In the time-domain, the concatenation ansatz described in this thesis well predicts transport to late-time steady-state values from short-time DNS.

Appendix A

Generation of noise

In this section the procedure used to construct noise artificially is explained.

We begin by constructing centered Gaussian distributed noise with unity standard deviation using the Box-Muller method.[54] Consider a pair of uniformly distributed numbers $\xi_1, \xi_2 \in [0,1]$. By performing the transformation

$$\eta_1 = \sqrt{-2\ln\xi_1}\cos 2\pi\xi_2 \tag{A.1a}$$

$$\eta_2 = \sqrt{-2\ln\xi_1}\sin 2\pi\xi_2 \tag{A.1b}$$

one obtains a pair of quantities η_1, η_2 with the normal (Gaussian) distribution

$$f(\eta) = \frac{1}{\sqrt{2\pi}} e^{-\eta^2/2}. \tag{A.2}$$

That is, η_1, η_2 are two independent Gaussian distributed numbers with a mean of zero and standard deviation of unity.

Then, for each r and t, one constructs

$$\chi_{rt} = \frac{\sum_{i=1}^{n_\eta} \eta_i^2}{n_\eta}, \tag{A.3}$$

a chi-square distribution of positive random numbers with mean unity and standard deviation

$$\sigma = \sqrt{2/n_\eta}. \tag{A.4}$$

Therefore, the number of smoothing points n_η to be used in the construction of χ should be $2/\sigma^2$, and Eq. (A.4) defines σ. Finally, noisy data $\mathbf{G}$ is constructed by multiplying the original underlying smooth mean square response Ψ by this χ and a gain g, i.e., $\mathbf{G}_r(t) = g_{rn}\psi_n\chi_{rt}$.

Appendix B

Solution for the three-room problem

The problem is, given $\{\mathbf{v}\}^1$, $[\mathbf{h}]$, and $\mathbf{v}_1^2$, solve for the remaining elements of $\{\mathbf{v}\}^2$ and $\{\mathbf{v}\}^3$ in

$$\mathbf{v}_1^1\mathbf{h}_1\mathbf{v}_1^2+\mathbf{v}_2^1\mathbf{h}_2\mathbf{v}_2^2+\mathbf{v}_3^1\mathbf{h}_3\mathbf{v}_3^2=0 \tag{B.1a}$$

$$\mathbf{v}_1^1\mathbf{h}_1\mathbf{v}_1^3+\mathbf{v}_2^1\mathbf{h}_2\mathbf{v}_2^3+\mathbf{v}_3^1\mathbf{h}_3\mathbf{v}_3^3=0 \tag{B.1b}$$

$$\mathbf{v}_1^2\mathbf{h}_1\mathbf{v}_1^3+\mathbf{v}_2^2\mathbf{h}_2\mathbf{v}_2^3+\mathbf{v}_3^2\mathbf{h}_3\mathbf{v}_3^3=0 \tag{B.1c}$$

$$\mathbf{v}_1^2\mathbf{h}_1\mathbf{v}_1^2+\mathbf{v}_2^2\mathbf{h}_2\mathbf{v}_2^2+\mathbf{v}_3^2\mathbf{h}_3\mathbf{v}_3^2=1 \tag{B.1d}$$

$$\mathbf{v}_1^3\mathbf{h}_1\mathbf{v}_1^3+\mathbf{v}_2^3\mathbf{h}_2\mathbf{v}_2^3+\mathbf{v}_3^3\mathbf{h}_3\mathbf{v}_3^3=1. \tag{B.1e}$$

Physically, we know the subspace that $\{\mathbf{v}\}^2$ and $\{\mathbf{v}\}^3$ span and that all three vectors satisfy mutual orthogonality, so there is only one free parameter (say, an angle) to completely specify the two higher eigenvectors. Mathematically, there are five remaining orthogonality conditions after $\{\mathbf{v}\}^1$ has been normalized and six elements of the other two higher eigenvectors, so one element must be specified in order to be able to solve for everything.

If we make the following definitions

$$a = \mathbf{v}_2^1 \mathbf{h}_2 \tag{B.2a}$$

$$b = \mathbf{v}_3^1 \mathbf{h}_3 \tag{B.2b}$$

$$c = -\mathbf{v}_1^1 \mathbf{h}_1 \mathbf{v}_1^2 \tag{B.2c}$$

$$d = \mathbf{h}_2 \tag{B.2d}$$

$$e = \mathbf{h}_3 \tag{B.2e}$$

$$f = 1 - \mathbf{h}_1 \left(\mathbf{v}_1^2\right)^2, \tag{B.2f}$$

then

$$\mathbf{v}_2^2 = \frac{\frac{ace}{b^2} \pm \sqrt{\frac{a^2c^2e^2}{b^4} - \left(d + \frac{a^2e}{b^2}\right)\left(\frac{c^2e}{b^2} - f\right)}}{\left(d + \frac{a^2e}{b^2}\right)}, \text{ and} \tag{B.3a}$$

$$\mathbf{v}_3^2 = -\frac{a}{b}\mathbf{v}_2^2 + \frac{c}{b}. \tag{B.3b}$$

The $\pm$ ambiguity in Eq. (B.3a) is a labeling issue. It is impossible to know *a priori* which of the higher eigenvectors is $\{\mathbf{v}\}^2$ and which is $\{\mathbf{v}\}^3$. In our implementation, the + sign is taken.

Furthermore, if we define

$$\beta = \frac{-\mathbf{v}_2^2\mathbf{h}_2\left(\mathbf{v}_1^2\mathbf{v}_3^1\mathbf{h}_3 - \mathbf{v}_1^1\mathbf{v}_3^2\mathbf{h}_3\right) + \mathbf{v}_3^2\mathbf{h}_3\left(\mathbf{v}_1^2\mathbf{v}_2^1\mathbf{h}_2 - \mathbf{v}_1^1\mathbf{v}_2^2\mathbf{h}_2\right)}{\mathbf{v}_1^2\mathbf{h}_1}, \tag{B.4a}$$

$$\gamma = \mathbf{v}_1^2\mathbf{v}_3^1\mathbf{h}_3 - \mathbf{v}_1^1\mathbf{v}_3^2\mathbf{h}_3, \text{ and} \tag{B.4b}$$

$$\delta = -\left(\mathbf{v}_1^2\mathbf{v}_2^1\mathbf{h}_2 - \mathbf{v}_1^1\mathbf{v}_2^2\mathbf{h}_2\right) \tag{B.4c}$$

$$\alpha^2 = \beta^2\mathbf{h}_1 + \gamma^2\mathbf{h}_2 + \delta^2\mathbf{h}_3 \tag{B.4d}$$

then

$$\mathbf{v}_1^3 = \frac{\beta}{\alpha} \tag{B.5a}$$

$$\mathbf{v}_2^3 = \frac{\gamma}{\alpha} \tag{B.5b}$$

$$\mathbf{v}_3^3 = \frac{\delta}{\alpha}. \tag{B.5c}$$

Existence of a solution is governed by the discriminant in Eq. (B.3a). Depending on the values of $[\mathbf{h}]$ and $\{\mathbf{v}\}^1$, there may be a well defined upper bound on the magnitude of $\mathbf{v}_1^2$ in order for there to be a solution. Otherwise, $\mathbf{v}_1^2$ can be any nonzero number. In our implementation $\mathbf{v}_1^2$ is taken to be positive to enforce uniqueness of the solution.

Appendix C

Derivation of $[\mathbf{Q}]$ formula

To obtain $[\mathbf{Q}]$ we constrain $\widehat{\mathbf{J}}^{\text{concat}}$ to have a specified steady-state (late-time) value. So,

$$\widehat{\mathbf{J}}_{rs}^{\text{concat}}(t) = \widehat{\mathbf{J}}_{rs}^{\text{steady-state}}(t) + \widehat{\mathbf{J}}_{rs}^{\text{trans}}(t) \tag{C.1a}$$

$$= \frac{E_r E_s}{N_D}\Theta(t) + \widehat{\mathbf{J}}_{rs}^{\text{trans}}(t), \tag{C.1b}$$

where $\widehat{\mathbf{J}}_{rs}^{\text{steady-state}}$ is the late-time steady-state response which can be predicted accurately by Eq. (1.16), and $\widehat{\mathbf{J}}_{rs}^{\text{trans}}$ is the transient response (which vanishes at $t \to \infty$). It is this transient response which this thesis is attempting to recover. This transient response is an extension of the theory in Weaver's paper.[38]

Taking a Fourier transform and considering the zero frequency limit results in

$$\lim_{\Omega \to 0} \mathbf{J}_{rs}^{\text{concat}}(\Omega) = \frac{E_r E_s}{N_D i\Omega} + \mathbf{J}_{rs}^{\text{trans}}(\Omega = 0), \tag{C.2}$$

where i is the imaginary unit, and the second term on the right hand side is bounded. Shifting to matrix notation and substituting from Eq. (3.6),

$$\lim_{\Omega \to 0} ([\mathbf{I}_S] - \left[\mathbf{J}^{\Delta}\right][\mathbf{Q}])^{-1} \left[\mathbf{J}^{\Delta}\right] = \frac{\{E\}\{E\}^T}{N_D i\Omega} + \left[\mathbf{J}^{\text{trans}}\right]. \tag{C.3}$$

So,

$$\lim_{\Omega\to 0}\left[\mathbf{J}^{\Delta}(\Omega)\right] = ([\mathbf{I}_S] - \left[\mathbf{J}^{\Delta}\right][\mathbf{Q}])\frac{\{E\}\{E\}^T}{N_D i\Omega} + ([\mathbf{I}_S] - \left[\mathbf{J}^{\Delta}\right][\mathbf{Q}])\left[\mathbf{J}^{\text{trans}}\right], \tag{C.4}$$

and, clearly,

$$\lim_{\Omega\to 0}([\mathbf{I}_S] - \left[\mathbf{J}^{\Delta}\right][\mathbf{Q}])\{E\} = \{\mathbf{A}\}\, i\Omega \tag{C.5}$$

for some vector $\{\mathbf{A}\}$. So, defining $[\mathbf{J}(\Omega)]' \equiv \frac{\partial}{\partial i\Omega}[\mathbf{J}(\Omega)]$,

$$([\mathbf{I}_S] - \left[\mathbf{J}^{\Delta}(0)\right][\mathbf{Q}])\{E\} = 0 \tag{C.6a}$$

$$\left[\mathbf{J}^{\Delta}(0)\right]'[\mathbf{Q}]\{E\} = -\{\mathbf{A}\} \tag{C.6b}$$

are conditions on $[\mathbf{Q}]$ and $\{\mathbf{A}\}$. Equation (3.7) is thus derived as Eq. (C.6a), and Eq. (C.6b) will be used in subsequent analysis.

Appendix D

Derivation of N_D condition

Substituting Eq. (C.6b) into Eq. (C.4) results in

$$\left[\mathbf{J}^{\Delta}\right] = -\frac{\left[\mathbf{J}^{\Delta}\right]'[\mathbf{Q}]\{E\}\{E\}^T}{N_D} + ([\mathbf{I}_S] - \left[\mathbf{J}^{\Delta}\right][\mathbf{Q}])\left[\mathbf{J}^{\text{trans}}\right]. \tag{D.1}$$

Multiplying on the left by $\left[\mathbf{J}^{\Delta}(0)\right]^{-1}$ gives

$$[\mathbf{I}_S] = -\frac{\left[\mathbf{J}^{\Delta}\right]^{-1}\left[\mathbf{J}^{\Delta}\right]'[\mathbf{Q}]\{E\}\{E\}^T}{N_D} + (\left[\mathbf{J}^{\Delta}\right]^{-1})\left[\mathbf{J}^{\text{trans}}\right]. \tag{D.2}$$

Multiplying on the left by $\{E\}^T$, the second term vanishes by Eq. (3.7), and one obtains

$$\{E\}^T = \frac{\left(-\{E\}^T\left[\mathbf{J}^{\Delta}\right]^{-1}\left[\mathbf{J}^{\Delta}\right]'[\mathbf{Q}]\{E\}\right)\{E\}^T}{N_D}. \tag{D.3}$$

The term in parentheses is, evidently, N_D:

$$N_D = -\{E\}^T\left[\mathbf{J}^{\Delta}\right]^{-1}\left[\mathbf{J}^{\Delta}\right]'[\mathbf{Q}]\{E\}, \tag{D.4}$$

and Eq. (3.9) is derived as Eq. (D.4).

References

[1] R. H. Lyon and R. G. DeJong. *Theory and Application of Statistical Energy Analysis*. Butterworth-Heimann, Boston, second edition, 1995.

[2] Frank J. Fahy. Statistical energy analysis: a critical overview. *Phil. Trans. R. Soc. London Ser. A*, 346:431–447, 1994.

[3] C. H. Hodges and J. Woodhouse. Theories of noise and vibration transmission in complex structures. *Reports Prog. Phys.*, 49:107–170, 1986.

[4] J. Woodhouse. An introduction to statistical energy analysis of structural vibration. *Appl. Acoust.*, 14:455–469, 1981.

[5] Murty S. Kompella and Robert J. Bernhard. Measurement of the statistical variation of structural-acoustic characteristics of automotive vehicles. In *Proceedings of the Society of Automotive Engineers Noise and Vibration Conference*, Warrendale, PA, USA, 1993.

[6] Frank P. Incropera and David P. DeWitt. *Introduction to Heat Transfer*. John Wiley & Sons, New York, third edition, 1996.

[7] J. Woodhouse. An approach to the theoretical background of statistical energy analysys applied to structural vibration. *Journal of the Acoustical Society of America*, 69(6):1695–1709, 1981.

[8] R. H. Lyon and G. Maidanik. Power flow between linearly coupled oscillators. *Journal of the Acoustical Society of America*, 34(5):623–639, 1962.

[9] Terry D. Scharton and Richard H. Lyon. Power flow and energy sharing in random vibration. *Journal of the Acoustical Society of America*, 43(6):1332–1343, 1968.

[10] E. H. Dowell and Yuji Kubota. Asymptotic modal analysis and SEA of dynamical systems. *Journal of Applied Mechanics*, 52:949–957, 1985.

[11] Richard L. Weaver and Oleg I. Lobkis. Anderson localization in coupled reverberation rooms. *Journal of Sound and Vibration*, 231(4):1111–1134, 2000.

[12] R. S. Langley, J. R. D. Smith, and F. J. Fahy. Statistical energy analysis of periodically stiffened damped plate structures. *Journal of Sound and Vibration*, 208(3):407–426, 1997.

[13] R. S. Langley and P. J. Shorter. The wave transmission coefficients and coupling loss factors of point connected structures. *Journal of the Acoustical Society of America*, 113(4):1947–1964, 2003.

[14] A. Le Bot. Energy transfer for high frequencies in built-up structures. *Journal of Sound and Vibration*, 250(2):247–275, 2002.

[15] Richard L. Weaver. Diffusivity of ultrasound in polycrystals. *Journal of the Mechanics and Physics of Solids*, 38(1):55–86, 1990.

[16] Arnoud Tourin, Arnaud Derode, Philippe Roux, Bart A. Tiggelen, and Mathias Fink. Time-dependent coherent backscattering of acoustic waves. *Phys. Rev. Lett.*, 79(19):3637–3639, 1997.

[17] Arnoud Tourin, Arnaud Derode, Aymeric Peyre, and Mathias Fink. Transport parameters for an ultrasonic pulsed wave propagating in a multiple scattering medium. *Journal of the Acoustical Society of America*, 108(2):503–512, 2000.

[18] Richard L. Weaver and Wolfgang Sachse. Diffusion of ultrasound in a glass bead slurry. *Journal of the Acoustical Society of America*, 97(4):2094–2102, 1995.

[19] X. Jia, C. Caroli, and B. Velicky. Ultrasound propagation in externally stressed granular media. *Phys. Rev. Lett.*, 82(9):1863–1866, 1999.

[20] Vern O. Knudsen and Cyril M. Harris. *Acoustical Designing in Architecture*. John Wiley & Sons, Inc., New York, 1950.

[21] Alexis Billon, Cédric Foy, Judicaël Picaut, Vincent Valeau, and Anas Sakout. Modeling the sound transmission between rooms coupled through partition walls by using a diffusion model. *Journal of the Acoustical Society of America*, 123(6):4261–4271, 2008.

[22] Takayuki Hidaka and Noriko Nishihara. Objective evaluation of chamber-music halls in Europe and Japan. *Journal of the Acoustical Society of America*, 116(1):357–372, 2004.

[23] M. L. Lai and A. Soom. Prediction of transient vibration envelopes using statistical energy analysis techniques. *J. Vib. Acoust.*, 122:127–137, 1990.

[24] R. J. Pinnington and D. Lednik. Transient SEA of an impulsively excited two oscillator system. *Journal of Sound and Vibration*, 189:249–264, 1996.

[25] R. S. Langley and P. G. Bremner. A hybrid method for the vibrational analysis of complex structural-acoustic systems. *Journal of the Acoustical Society of America*, 105:1657–1671, 1999.

[26] V. Catoni, R. S. Langley, and M. R. F. Kidner. Numerical and experimental validation of variance prediction in the statistical energy analysis of built-up systems. *Journal of Sound and Vibration*, 288(3):701–728, 2005.

[27] M. L. Mehta. *Random Matrices*. Elsevier, Amsterdam, third edition, 2004.

[28] Joseph W. Gregory and Richard F. Keltie. SEA system identification using transient vibration data. In *Proceedings of the Second International AutoSEA Users Conference*, Detroit-Troy Marriott—Troy, Michigan, USA, 2002.

[29] Jer-Nan Juang and Richard S. Pappa. An eigensystem realization algorithm for modal parameter identification and model reduction. *Journal of Guidance,* 8(5):620–627, 1985.

[30] C. Simmons. Structure-borne sound transmission through plate junctions and estimates of SEA coupling loss factors using the finite element method. *Journal of Sound and Vibration,* 144:215–227, 1991.

[31] J. A. Steel and R. J. M. Craik. Statistical energy analysis of structure-borne sound transmission by FEM. *Journal of Sound and Vibration,* 178(4):553–561, 1994.

[32] K. Shankar and A. J. Keane. A study of the vibrational energies of two coupled beams by FEM and receptance methods. *Journal of Sound and Vibration,* 181(5):801–838, 1995.

[33] K. Shankar and A. J. Keane. Energy flow predictions in a structure of rigidly joined beams using receptance theory. *Journal of Sound and Vibration,* 185(5):867–890, 1995.

[34] K. Shankar and A. J. Keane. Vibrational energy flow analysis using a substructure approach: the application of receptance theory to FEA and SEA. *Journal of Sound and Vibration,* 201(4):491–513, 1997.

[35] C. R. Fredö. SEA-like approach for the derivation of energy flow coefficients with a finite element model. *Journal of Sound and Vibration,* 199:645–666, 1997.

[36] B. R. Mace and P. J. Shorter. Energy flow models from finite element analysis. *Journal of Sound and Vibration,* 233:369–389, 2000.

[37] M. C. M. Wright. A short history of bad acoustics. *Journal of the Acoustical Society of America,* 120(4):1807–1815, 2006.

[38] Richard L. Weaver. Equipartition and mean-square responses in large undamped structures. *Journal of the Acoustical Society of America,* 110(2):894–903, 2001.

[39] Richard L. Weaver and John Burkhardt. Weak Anderson localization and enhanced backscatter in reverberation rooms and quantum dots. *Journal of the Acoustical Society of America,* 96(5):3186–3190, 1994.

[40] Nicholas L. Wolff and Richard L. Weaver. Towards a diffusion model of acoustic energy flow in large undamped structures. *Journal of Sound and Vibration,* 288(3):729–749, 2005.

[41] Richard L. Weaver. Spectral statistics in elastodynamics. *Journal of the Acoustical Society of America,* 85(3):1005–1013, 1989.

[42] Richard L. Weaver. On the ensemble variance of reverberation room transmission function, the effect of spectral rigidity. *Journal of Sound and Vibration,* 130(3):487–491, 1989.

[43] D. E. Newland. *An Introduction to Random Vibrations and Spectral Analysis*. Longman House, New York, second edition, 1984.

[44] J. L. Davy. The ensemble variance of random noise in a reverberation room. *Journal of Sound and Vibration*, 107(3):361–373, 1986.

[45] R. H. Lyon. Statistical analysis of power injection and response in structures and rooms. *Journal of the Acoustical Society of America*, 45(3):545–565, 1967.

[46] J. L. Davy. The relative variance of the transmission funcion of a reverberation room. *Journal of Sound and Vibration*, 77(4):455–479, 1981.

[47] J. L. Davy. Improvements to formulae for the ensemble relative variance of random noise in a reverberation room. *Journal of Sound and Vibration*, 115(1):145–161, 1987.

[48] Oleg I. Lobkis, Richard L. Weaver, and Igor Rozhkov. Power variances and decay curvature in a reverberant system. *Journal of Sound and Vibration*, 237(2):281–302, 2000.

[49] Robin S. Langley and Vincent Cotoni. Response varience prediction in the statistical energy analysis of built-up structures. *Journal of the Acoustical Society of America*, 115(2):706–718, 2004.

[50] R. S. Langley and A. W. M. Brown. The ensemble statistics of the energy of a random system subjected to harmonic excitation. *Journal of Sound and Vibration*, 275:823–846, 2004.

[51] R. S. Langley and A. W. M. Brown. The ensemble statistics of the band-averaged energy of a random system. *Journal of Sound and Vibration*, 275:847–857, 2004.

[52] Charles Kittel and Herbert Kroemer. *Thermal Physics*. W. H. Freeman and Company, New York, second edition, 1980.

[53] The MathWorks, Inc., Natick, MA 01760-2098. *Optimization Toolbox 4, User's Guide*, 1990–2008.

[54] William H. Press, Saul A. Teukolsky, William T. Vetterling, and Brian P. Flannery. *Numerical Recipes: The Art of Scientific Computing*. Cambridge University Press, Cambridge, second edition, 1992.

[55] L. Kaplan. Correlation function bootstrapping in quantum chaotic systems. *Physical Reveiw E*, 71:056212–1–056212–12, 2005.

[56] Thomas S. Shores. *Applied Linear Algebra and Matrix Analysis*. McGraw-Hill, New York, revised second edition, 2000.

[57] Karl F. Graff. *Wave Motion in Elastic Solids*. Oxford University Press, New York, 1975.

[58] P. J. Shorter and R. S. Langley. Vibro-acoustic analysis of complex systems. *Journal of Sound and Vibration*, 288(3):669–699, 2005.

[59] MSC Software, http://www.mscsoftware.com. *MSC.Patran User's Guide*.

[60] The MathWorks, Inc., Natick, MA 01760-2098. *MATLAB 7 Getting Started Guide*, 1984–2008.

[61] Robert D. Cook, David S. Malkus, Michael E. Plesha, and Robert J. Witt. *Concepts and Applications of Finite Element Analysis*. John Wiley & Sons, New York, fourth edition, 2002.

[62] K. Sham Sunder and R. A. Cookson. Integration points for triangles and tetrahedrons obtained from the Gaussian quadrature points for a line. *Computers & Structures*, 21(5):881–885, 1985.

[63] Michael J. Buckingham. On the transient solutions of three acoustic wave equations: van Wijngaarden's equation, Stoke's equation, and the time-dependant diffusion equation. *Journal of the Acoustical Society of America*, 124(4):1909–1920, 2008.

Author's Biography

Nicholas Wolff attended high school at Wakefield Community Schools in rural northeast Nebraska. He earned his B.S. in Mechanical Engineering from the University of Nebraska-Lincoln in May 2000. He graduated summa cum laude with an honors thesis titled "Far-field and near-surface acoustic fields for a spheroidal particle with arbitrary acoustic wave incidence." He completed his M.S. in Theoretical and Applied Mechanics from the University of Illinois in December 2001, and continued directly into the Ph.D. program in T.A.M. with Prof. Richard L. Weaver as his advisor. He taught several engineering mechanics and mathematics courses at Parkland College while in the Ph.D. program. He has been appointed to the position of Assistant Professor of Physics at Lane College in Jackson, TN.